Proceedings of the 14th UK Conference on Wind Engineering

University of Southampton

4-6 September 2024

14th UK CONFERENCE ON WIND ENGINEERING
University of Southampton
4-6 September 2024

Welcome to 14th UK Conference on Wind Engineering at Southampton!

The full programme can be found on the conference website: https://personal.soton.ac.uk/zxie/WES2024

The 4-page papers accompanying each talk have been registered with permanent DOIs in the format of doi.org/10.5258/WES/P00XX where XX is the Paper ID. Links to each paper are included in the programme.

Location: 4th floor, Centenary Building (B100), Highfield Campus, University of Southampton, SO17 1BJ

- All talks in lecture room 4011
- Posters and refreshments in room 4013

Contact: wes2024@soton.ac.uk

Hosts: Prof Zheng-Tong Xie & Prof Christina Vanderwel, Department of Aeronautical and Astronautical Engineering, University of Southampton

Advisory and Scientific Committee: The Executive Committee of the Wind Engineering Society is acting as the Advisory Committee for the conference. The membership is:

- Mr Stefano Cammelli, WSP
- Dr Bernardo Vazquez, BuroHappold
- Dr David Hargreaves, University of Nottingham
- Mr John Rees, COWI
- Dr Alex To, Arup
- Ms Anna Bagnara, NOVA Fluid Mechanics
- Prof Zheng-Tong Xie, University of Southampton
- Mr Daniel Hackett, RWDI
- Dr Giulio Vita, Ramboll
- Dr Francesco Dorigatti, RWDI
- Dr Mingzhe He, AKT II

The academics listed below also kindly helped review the submitted abstracts:

- Prof Bert Blocken, Heriot-Watt University
- Dr Cung Nguyen, University of Salford
- Prof Christina Vanderwel, University of Southampton

Many thanks for the support from Carlene Cornick, Ruby Wyness, and Kelly Carter in the Department Admin Team; to Tomos Rich and Dominic Clements for volunteering during the event; to the University of Southampton Hospitality Team for organising the venue and accommodation; to the ePrints and Research Data Team at the University of Southampton Library for organising the DOIs to publish the papers; and to the UK Wind Engineering Society for all the provided support.

14th UK CONFERENCE ON WIND ENGINEERING
University of Southampton
4-6 September 2024

Wednesday 4th September, 2024

9:00-9:55	**Registration / Tea and Coffee / Poster Setup**
9:55-10:00	**Welcome & Introduction (Christina Vanderwel and Stefano Cammelli)**
10:00-12:00	**UFM-UKUEQ Mini-Symposium (Chair: Maarten van Reeuwijk, Darren Woolf)**
10:00-10:05	Introduction - *Maarten van Reeuwijk; Imperial College London*
10:05-10:15	Urban Environmental Quality: Challenging Knowledge - *Darren Woolf; Wirth Research*
10:15-10:25	Integrating Urban Environmental Quality in urban design - *Marialena Nikolopoulou; University of Kent*
10:25-10:35	Estimating UEQ in practice - *Rubina Ramponi; Arup*
10:35-10:45	Urban Air Quality and planning. *Steve Moorcroft; AQ consultants*
10:45-10:55	Wind microclimate studies in the UK: nuances, inconsistencies, and current challenges - *Stefano Cammelli; WSP*
10:55-11:05	Using wind compliance to improve UEQ - *Giulio Vita; Ramboll*
11:05-12:00	Panel discussion
12:00-12:15	**In memoriam of John Macdonald (Cung Nguyen and Stefano Cammelli)**
12:15-13:00	**Lunch and Networking**
13:00-14:00	**Keynote – Ian Castro, *University of Southampton* (Chair: Christina Vanderwel) "Porous structures and vortex shedding"**
14:00-14:45	**Session 1 – Atmospheric boundary layer & climate change (Chair: Stefano Cammelli)**
14:00-14:15	Atmospheric turbulence as seen by a moving object (PID 7) - *Peter John Richards, Nicholas Kay, Stuart Norris; University of Auckland*
14:15-14:30	Future winds: a review of the likely impacts of anthropogenic climate change on wind engineering in the UK (PID 9) - *Anna Bagnara, Daniel Hackett, David Hankin, Stefano Cammelli; NOVA Fluid Mechanics Ltd, RWDI, WSP UK*
14:30-14:45	Codification of mean wind and turbulence profiles over the ocean with roughness saturation (PID 27) - *John D. Holmes; JDH Consulting*
14:45-15:15	**Tea and Coffee**
15:15-16:45	**Session 2 – Urban microclimate & wind (Chair: Bernardo Vazquez)**
15:15-15:30	Coupled mesoscale–microscale modelling of airflow at Hong Kong International Airport (PID 4) - *Chang-Chang Wang, Pak-Wai Chan, The Hong Kong Polytechnic University*
15:30-15:45	Large-eddy simulation of a diurnal cycle in a coastal urban environment (PID 42) - *Sam Owens, Owen Beckett, Andy Acred, Maarten van Reeuwijk; Imperial College London, Foster+Partners*
15:45-16:00	Drag Characteristics of a Volumetric Tree Model in Computational Fluid Dynamic Simulations (PID 34) - *Dipanjan Majumdar, Maarten van Reeuwijk; Imperial College London*
16:00-16:15	Introducing BeStPLW: A Benchmark Study on Pedestrian Level Winds (PID 1) - *Giulio Vita, Mingzhe He, Stefano Cammelli; Ramboll UK, AKT II, WSP UK*
16:15-16:30	Wind Microclimate on Balconies: Designing Climate-sensitive Outdoor Spaces (PID 37) - *Jennifer Lowther, Daniel Hackett, A. Cherian, V. RV; RWDI*

14th UK CONFERENCE ON WIND ENGINEERING
University of Southampton
4-6 September 2024

16:45-18:00	**Poster Brief Session (and refreshments)**
19:00-21:00	**Cafeteria Dinner – Arlott Bar and Terrace Restaurant (B38)**

Thursday 5th September, 2024

8:30-9:00	**Tea and Coffee**
9:00-10:00	**Keynote – Goncalo Pedro, *RWDI* (Chair: Zheng-Tong Xie)** **"Deep dive into computation methods for microclimate"**
10:00-11:00	**Session 3 – Pollutant dispersion (Chair: Matteo Carpentieri)**
10:00-10:15	Towards passive scalar reconstruction using data assimilation (PID 45) - *Uttam Cadambi Padmanaban, Bharathram Ganapathisubramani, Christina Vanderwel, Sean Symon; University of Southampton*
10:15-10:30	Towards efficient scale resolving simulation for the prediction of industrial pollutant dispersion applications (PID 23) - *Salvatore Manuel Renda, Apostolos Krassas, Eugene De Villiers, Stefano Capra; ENGYS UK, Ramboll*
10:30-10:45	Pollutant dispersion in a cross-ventilating flow through a scaled building: Wind and water tunnel measurements (PID 40) - *Subhajit Biswas, Paul Hayden, Matteo Carpentieri, Christina Vanderwel; University of Southampton, University of Surrey*
10:45-11:00	Cloud dispersion in complex flows (PID 20) – *Alan Robins, Paul Hayden, Thomas Richards, David Gallacher; University of Surrey, Guy's and St Thomas' NHS Foundation Trust*
11:00-11:30	**Tea and Coffee**
11:30-13:00	**Session 4 – Wind impact (Chair: David Hankin)**
11:30-11:45	Modelling the launch and collision phases of wind-borne debris (PID 10) - *David M. Hargreaves, John S. Owen; University of Nottingham*
11:45-12:00	CROSS-STORM project: developing a numerical-experimental procedure for evaluating the risk of accident on road vehicles due to the strong crosswinds generated by a thunderstorm (PID 44) - *Andi Xhelaj, Carlos Esteban Araya Reyes, Maria Pia Repetto, Luisa Pagnini, Gisella Tomasini; University of Genoa, Polytechnic of Milan*
12:00-12:15	Integrated performance prediction tool for wind-assisted ship design with a routing case study - *Andhini Zurman-Nasution, Suleyman Aykut Korkmaz, Dominic A. Hudson, Stephen R. Turnock, Joseph Banks; University of Southampton*
12:15-12:30	Finite element analysis of low-rise non-engineered timber residential buildings in Dominica under hurricane loads (PID 62) - *Sarah Esper, Dina D'Ayala, University College London*
12:30-14:00	**Lunch and Poster Discussion**
14:00-15:00	**Keynote – Janet Barlow, *University of Reading* (Chair: Zheng-Tong Xie)** **"Across-scale processes in urban environments: the ASSURE project"**

14th UK CONFERENCE ON WIND ENGINEERING
University of Southampton
4-6 September 2024

15:00-16:30	**Session 5 – Across-scale processes in urban environments (Chair: Zheng-Tong Xie)**
15:00-15:15	An analytical solution for a surface energy balance model including water transport - *Maarten van Reeuwijk, Sue Grimmond, Chris Wilson, Sam Owens; Imperial College London, University of Reading*
15:15-15:30	Large scale wind study of the inner city of Rotterdam (PID 18) – *Nick Vlaun, Eric Terry, Actiflow*
15:30-15:45	Flow across a step change in roughness: turbulence statistics estimation via interpretable network-based modelling - *Giovanni Iacobello, Marco Placidi, Shan-Shan Ding Matteo Carpentieri; University of Surrey, University of Oxford*
15:45-16:00	Sensor measurements and large-eddy simulation of point source plumes over a complex urban terrain (PID 52) - *James C. Matthews, Matthew Coburn, M. Anwar H. Khan, Dudley E. Shallcross, Zheng-Tong Xie; University of Bristol, University of Southampton, University of the Western Cape*
16:00-16:30	**Tea and Coffee**
16:30-18:00	**Session 6 – Wind loading and building design (Chair: Michael Graham)**
16:30-16:45	Physical Simulation of the Surface Pressure Field on a 5-Storey Residential Building and Application to Natural Ventilation (PID 26) - *Khrystyna Myroniuk, Vasyl Zhelykh, Yurii Furdas, Mike Jesson, Stergios-Aristoteles Mitoulis; University of Birmingham, Lviv Polytechnic National University*
16:45-17:00	Exploring wind engineering challenges in super-slender buildings (PID 46) - *Stefano Torre, Edoardo Ruffini; NOVA Fluid Mechanics Ltd*
17:00-17:15	Unsteady Loading of Horizontal Axis Wind Turbine Rotors by Atmospheric Turbulence (PID 14) - *J. Michael Graham, Kevin Gouder, Ian A. Milne; Imperial College London, University of Western Australia*
17:15-17:30	CFD Methodology for Air Quality Assessment (PID 60) - *Vincenzo Sessa, Mingzhe He, Steven Daniels; AKTII*
17:30-17:45	Reference pressure for wind load measurements in a turbulent boundary layer (PID 6) - *Roger Hoxey, Peter Richards, Adam Robertson*
19:00 - 22:30	**Banquet Dinner at Chilworth Manor, SO16 7PT** **Coach to depart at 19:00 outside B100, and return at 22:15 to Halls and Highfield Campus**
19:00 -	**Alternative Young Person's Social – Brewhouse & Kitchen, 47 Highfield Ln, SO17 1QD**

14th UK CONFERENCE ON WIND ENGINEERING
University of Southampton
4-6 September 2024

Friday 6th September, 2024

8:30-9:00	**Tea and Coffee**
9:00-10:00	**Keynote – Bert Blocken, *Heriot-Watt University* (Chair: Christina Vanderwel)** **"CFD for case studies environmental wind engineering: have we gotten ahead of ourselves?"**
10:00-11:00	**Session 7 – Tall-building clusters 1 (Chair: Marco Placidi)**
10:00-10:15	Fluid dynamics of Urban Tall-building clUsters for Resilient built Environments (FUTURE) (PID 59) - *Marco Placidi, Matteo Carpentieri, Alan Robins, Zheng-Tong Xie, Davide Lasagna, Janet Barlow, Sue Grimmond, Omduth Coceal; University of Surrey, University of Southampton, University of Reading*
10:15-10:30	Cluster Effects of Tall Buildings (PID 58) - *Saad Inam, Cung Nguyen, Changchang Wang, Davide Lasagna, Zheng-Tong Xie; University of Southampton*
10:30-10:45	Impact of Stably Stratified Boundary Layers on Tall Building Wake (PID 54) - *Abhishek Mishra, Matteo Carpentieri, Alan Robins, Marco Placidi; University of Surrey*
10:45-11:00	Observations of Tall-Building Wakes in Berlin's Urban Boundary Layer Using Two Doppler Wind Lidars - *Matthew Clements, Janet F. Barlow, Sue Grimmond, Daniel Fenner, William Morrison, Andreas Christen; University of Reading, University of Freiburg*
11:00-11:30	**Tea and Coffee**
11:30-13:00	**Session 8 – Tall-building clusters 2 (Chair: Alan Robins)**
11:30-11:45	Modelling wind profiles in heterogeneous urban environments using fractional derivatives - *Omduth Coceal; University of Reading*
11:45-12:00	Flow Over an Array of Very Tall Buildings with Random Heights - *Donnchadh MacGarry, Zheng-Tong Xie, Christina Vanderwel; University of Southampton*
12:00-12:15	Pollutant Dispersion and Bimodality in Tall Building Clusters (PID 55) - *Dianfang Bi, Abhishek Mishra, Marco Placidi, Alan Robins, Matteo Carpentieri; University of Surrey*
12:15-12:45	**Concluding discussions about the FUTURE project (Alan Robins)**
12:45-13:00	**Closing Ceremony (Christina Vanderwel and Stefano Cammelli)**
13:00-14:00	**Lunch**
14:00-15:00	**Optional Lab Visits to the RJ Mitchell Wind Tunnel (B17) and Fluid Dynamics Labs (B185) (walking tour departing from B100 at 14:00)**

14th UK CONFERENCE ON WIND ENGINEERING
University of Southampton
4-6 September 2024

List of Posters

Turbulent transport characteristics of coherent structures in ideal urban morphology based on wind tunnel experiments (PID 2) *Guoliang Chen, Chun-Ho Liu, Ziwei Mo; The University of Hong Kong, Sun Yat-sen University*

Turbulent boundary layers over multiscale urban arrays (PID 3) *Cameron Southgate-Ash, Sue Grimmond, Alan Robins, Marco Placidi; University of Surrey*

Structure of yawed wind turbine wakes in thermally neutral and stable boundary layers (PID 13) *Rose Foster, Phillip Hancock, Marco Placidi; University of Surrey*

Surface Pressure Fluctuations in an Atmospheric Boundary Layer (PID 15) *Joy Schmeer, Marco Placidi and David M. Birch; University of Surrey*

Simulation of atmospheric boundary layer in the wind tunnel facility at University of Bristol (PID 16) *Nada Taouil,H.D. Lim, B. Zang, Mahdi Azarpeyvand; University of Bristol*

Bridging the Gap: Embedding 3D Details into Fast Deep-Learning Model for Pedestrian-Level Wind Prediction (PID 17) *Adam Clarke, Knut Erik, Teigen Giljarhus, Luca Oggiano, Alistair Saddington, Karthik Depuru-Mohan; Cranfield University, University of Stavanger*

Dynamic Calibration of Low-Cost Gas Sensors for Dispersion Experiments (PID 19) *Paul Hayden, David M. Birch; University of Surrey*

Kinematic Similarity for Urban Aerodynamic Wind Tunnel Tests Using Retrofit Atmospheric Boundary Layer Screen Filter (PID 28) *Rakesh, Rayapureddi, Joe, Dillane, Andrew Keppel, Thomas Confrey; South East Technological University, Ireland*

Shading Affects the Latent Heat Flux in Vegetated Urban Areas (PID 32) *Christopher Wilson, Jon Shonk, Sylvia Bohnenstengel, Athanasios Paschalis, Maarten van Reeuwijk; Imperial College London, Met Office*

Small wind ram air turbine blade geometric modification for performance (PID 35) *Kiran S Gadda, Hardit R Saini, Mariana G. Avila Zaya, Nithya Venkatesan, Eldad J Avital; Queen Mary University of London, Vellore Institution of Technology*

A Comparison Study of Structural Wind Tunnel Tests and Code-based Approaches in Evaluating Wind Loads on Tall Buildings (PID 36) *Pietro Manica, Fabio Faseli, Tung Nguyen, Suresh Kumar, John Kilpatrick; RWDI*

The Need for Post-Construction Microclimate Monitoring (PID 38) *Supun Enderage, Jeniffer Lowther, Daniel Hackett; RWDI*

Multi-resolution heterogeneity analysis of urban flows (PID 41) *Jingzi Huang, Maarten van Reeuwijk; Imperial College London*

Dispersion of Passive and Dense Plumes over a Step-Change in Wall Roughness (PID 43) *C. Deebank, M. Placidi, M. Carpentieri; University of Surrey*

Increasing high-fidelity modelling efficiency with automated setup and validation of methodologies (PID 48) *Matthew Coburn, Zheng-Tong Xie; University of Southampton*

Using a virtual Doppler LiDAR and Large Eddy Simulation to quantify wind velocity measurement errors of ground-based Doppler LiDAR (PID 49) *Veronica Escobar-Ruiz, Janet F. Barlow, and Zheng-Tong Xie; University of Reading, University of Southampton*

Introducing BeStPLW: A Benchmark Study on Pedestrian Level Winds

Giulio Vita[1], Mingzhe He[2], Stefano Cammelli[3]
[1]Ramboll UK, Birmingham, United Kingdom, giulio.vita@ramboll.co.uk
[2]AKT II, London, United Kingdom, mingzhe.he@akt-uk.com
[3]WSP UK, London, United Kingdom, stefano.cammelli@wsp.com

1 INTRODUCTION

The interaction between wind and the built environment can significantly alter the experience of pedestrians within the urban fabric of a city [1]. With a growing focus on incorporating recreational outdoor spaces into new developments, designers and developers are often tasked with "shaping" the wind microclimate to ensure the suitability of these spaces whilst minimising impacts on surrounding areas. In this context, high-rise buildings receive special attention from planning authorities due to their potential to detrimentally modify the wind conditions around them. As a result, planners are increasingly becoming aware of the need for early considerations of the expected wind microclimate as part of design proposals and, in the UK, mandate comprehensive wind assessments and design measures to mitigate any identified and significant wind effects [2].

In the UK, despite the introduction of the 'Wind Microclimate Guidelines' by the City of London Corporation back in 2019 [3], a certain degree of interpretation in the execution of pedestrian level wind studies still exists. To gain a better insight into the quality and consistency of wind microclimate studies conducted both experimentally and computationally by wind engineering practitioners, a benchmark study (BeStPLW, short for 'Benchmark Study on Pedestrian Level Winds') led by a sub-committee of WES - the UK Wind Engineering Society [4], will be undertaken. The experimental component of BeStPLW will benefit from funding provided by ERIES - the Engineering Research Infrastructures for European Synergies [5].

The main goal of BeStPLW is to provide a snapshot of the state-of-the-art in the industry. More specifically, BeStPLW will be aimed at: i) providing guidelines on the minimum level of details of the building of interest and of its surroundings; ii) providing guidance on the most suitable layout of surface-mounted wind sensors; iii) providing guidelines on the minimum number of wind directions; iv) quantifying the impact of different post-processing methods used in the industry to obtain 'gust' wind speeds; v) investigating experimental and computational modelling techniques for wind mitigation solutions.

This technical paper represents the first introduction of BeStPLW; it will provide an update on its current status, including details on up-coming engagements with the industry; and it will present a timeline for the delivery of its different 'work packages'.

2 BESTPLW CASE STUDY

One of the trickiest aspects of setting up a benchmark is that a real case study needs to be chosen which is generalisable for practical applications throughout the possible variability of the urban fabric of a city. The city of Manchester represents an appropriate area of study which can arguably be representative of a typical urban area in the UK, i.e. featuring a mix of high-rise and low-rise buildings, open parkland and roadworks. Both clusters of tall buildings, as well as more isolated and exposed buildings of large footprints have in fact the potential to introduce complex adverse wind effects that can cause uncomfortable or even unsafe conditions for pedestrians and the Deansgate area of Manchester provides an opportunity to test all of these aspects.

Figure 1 shows the area taken as a reference, with the Hilton hotel at its centre. We anticipate that at least three (3) surround configurations will be studied (existing scenario, cumulative scenario and existing scenario with the geometry of the Hilton hotel to be replaced by a much more challenging but realistic geometry). We also anticipate that the assessments will be initially conducted in the absence of mitigation solutions and that eventual wind mitigation measures will be studied separately either numerically or experimentally.

DOI 10.5258/WES/P0001

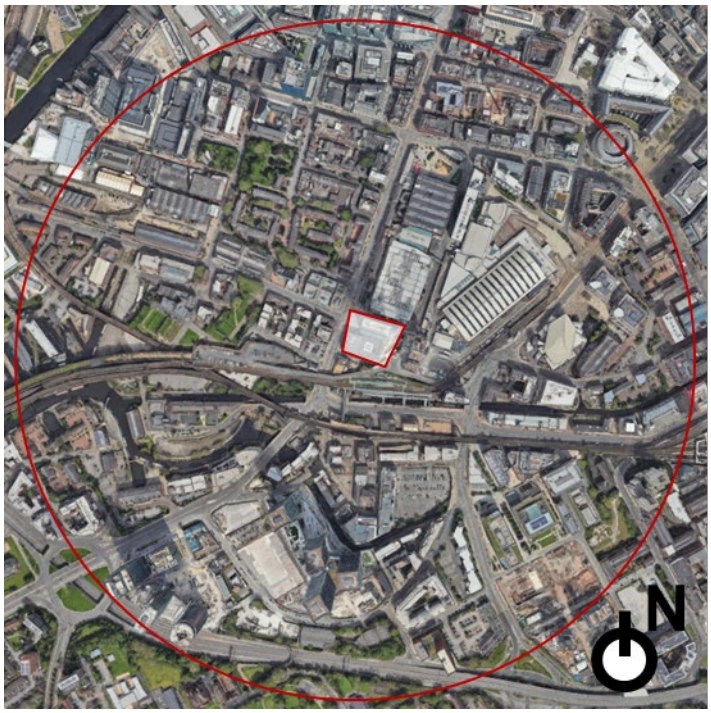

Figure 1. Google Earth aerial view of the study area.

A close-up view of the 3D model of the selected built environment (existing scenario) is shown in Figure 2, providing an appropriate composition of low-, medium- and high-rise buildings as well as complex street canyons. This unique composition has the potential to exhibit complex urban flow phenomena such as downwash from high-rise buildings, flow acceleration from sharp building corners, funnelling between building interference.

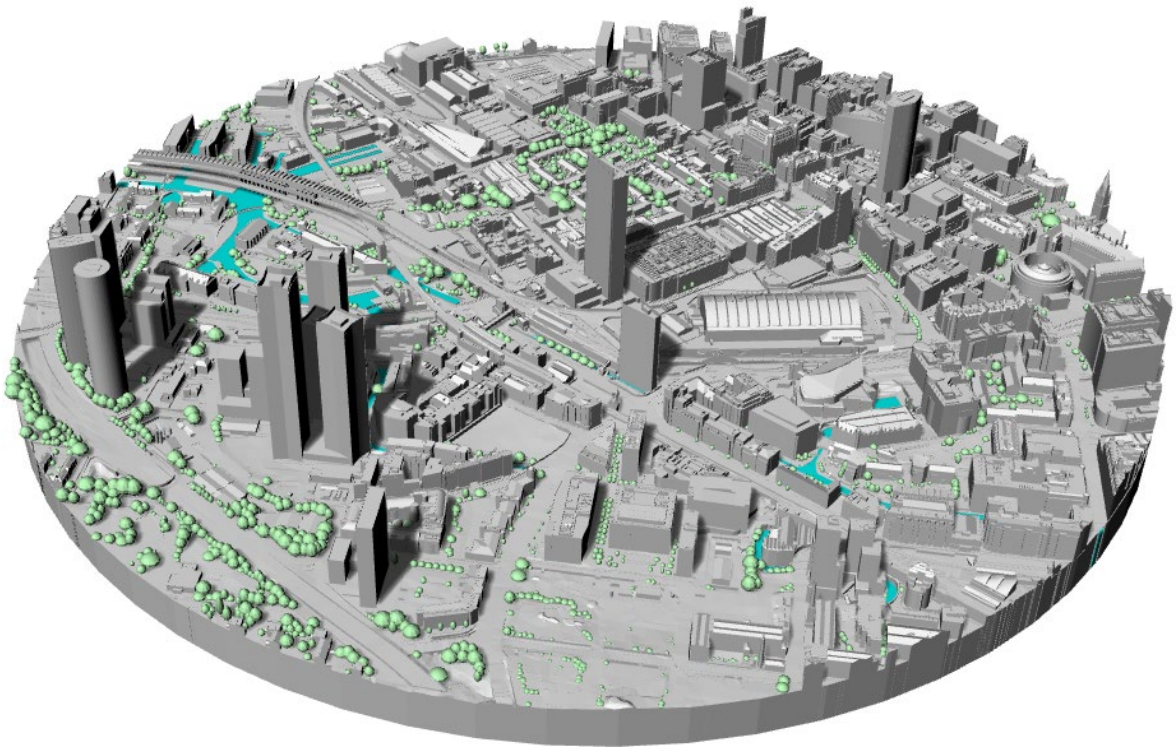

Figure 2. Perspective view of the study area.

DOI 10.5258/WES/P0001

3 APPROACH AND METHODOLOGY

The benchmark is composed of three work packages: (1) wind tunnel testing; (2) computational fluid dynamics (CFD) simulations; and (3) a digital platform for data exchange and management.

3.1 Wind Tunnel Tests

Wind tunnel testing represents a core request in planning applications, both at preliminary and definitive levels of the design. The wind tunnel tests planned for this benchmark study will involve benchmark testing in the atmospheric boundary layer wind tunnel of the Technical University of Eindhoven in the Netherlands.. Discussions with another facility are currently on-going and, if successful, this would give us the opportunity of gathering two independent sets of experimental data.

An urban scaled model, at a geometrical scale of 1:400, will be designed and manufactured to represent the ground geometry and the geometry of the buildings to a suitable level of details which is representative of significant flow structures affecting the pedestrian comfort and safety. It is anticipated that one single exposure will be used in the experiments. Also, if a second wind tunnel facility is engaged, we anticipate that the same physical wind tunnel model will be shipped between the two laboratories to minimise sources of discrepancies.

The pedestrian level wind speed will be measured using the industry-standard Irwin probes placed at multiple locations [5,6].

Multiple wind directions (up to 36 with 10° intervals) will be tested. Data from the Irwin probes will be collected for a sufficient sample time, depending on sampling frequency (typically above 500Hz), to obtain proper statistics for estimating the peak velocities, which will shed light on significant wind gusts affecting pedestrian comfort and safety.

The full set of measurements obtained from the wind tunnel testing campaign will be made publicly available and will also be studied and compared by a sub-committee of WES against the outcome of the CFD simulations.

3.2 CFD Simulations

The geometry and configurations of the wind tunnel model and tests will be replicated numerically to ascertain the limitations of both technologies and most importantly to better understand how they complement each other.

The CFD simulations will primarily focus on identifying best numerical practice and equip planning authorities and third-party reviewers with a defined roadmap to evaluate the work of practitioners proposing a sole numerical test to assess pedestrian safety and comfort, which is allowed for smaller buildings.

A suitable validation procedure could also be scoped in to address the validity of numerical results obtained using low-fidelity CFD methods (such as RANS) in assessing the gust wind speed. Also, a thorough comparison of the results obtained is expected to help WES to come up with suitable minimal quality requirements for CFD simulations in the built environment.

Ultimately the scope of the work is to set out a systematic study on a variety of key parameters to establish best practice or minimal quality requirements for both numerical and experimental tools. The outcome of the work would be a set of CFD results that are accurate for pedestrian wind assessment purposes.

3.3 A Comprehensive Digital Platform

The main ambition of the project is the vision of establishing a digital platform to provide a blind-test benchmarking for industry practitioners who would like to contribute to the wind microclimate assessment market. The main aim of the platform is not to inhibit the growing competition in this field, but to minimise risks associated with poorly planned and poorly executed wind tunnel tests and CFD simulations.

DOI 10.5258/WES/P0001

4 CURRENT PROGRESS AND PLANNED FUTURE WORK

BeStPLW has already been granted funding through the ERIES Projects (Ref: 101058684, Call: HORIZON-INFRA-2021-SERV-01-07).

A contact has been made with the host facility of the "Venturi Lab" at the Technical University of Eindhoven in the Netherlands to plan the work ahead. The wind tunnel testing campaign is expected to start early in 2025. The CFD work has also commenced in terms of choice of the geometry and setting up of the models.

Initial steps have been made towards defining a robust framework for data gathering and data storing but this needs to be finalised in due course. Also, the first steps in advertising this initiative across the industry will commence soon after the 2024 WES Conference and are expected to make use of well-established channels such as LinkedIn.

REFERENCES

[1] Vita, G., Shu, Z., Jesson, M., Quinn, A., Hemida, H., Sterling, M., & Baker, C. (2020). On the assessment of pedestrian distress in urban winds. Journal of Wind Engineering and Industrial Aerodynamics, 203, 104200.

[2] Cammelli, Stefano, and Robin Stanfield. "Meeting the challenges of planning policy for wind microclimate of high-rise developments in London." Procedia engineering 198 (2017): 43-51.

[3] www.cityoflondon.gov.uk/services/planning/planning-application-requirements/microclimate-guidelines

[4] www.windengineering.org.uk

[5] eries.eu/transnational-access

[6] Wu, H., & Stathopoulos, T. (1993). Wind-tunnel techniques for assessment of pedestrian-level winds. Journal of engineering mechanics, 119(10), 1920-1936.

[7] Irwin, H.P.A.H., 1981. A simple omnidirectional sensor for wind-tunnel studies of pedestrian-level winds. Journal of wind engineering and industrial aerodynamics, 7(3), pp.219-239.

DOI 10.5258/WES/P0001

Turbulent transport characteristics of coherent structures in ideal urban morphology based on wind tunnel experiments

Guoliang Chen[1*], Chun-Ho Liu[1], Ziwei Mo[2]
[1] Department of Mechanical Engineering, The University of Hong Kong, 7/F, Haking Wong Building Pokfulam Road, Hong Kong, China
[2] School of Atmospheric Sciences, Sun Yat-sen University, & Southern Marine Science and Engineering Guangdong Laboratory (Zhuhai), Zhuhai, China
* Corresponding author.
*E-mail addresses: glchen97@connect.hku.hk (G. Chen)

ABSTRACT:

Considering the impact of individual roughness elements, turbulence within urban roughness sublayers (RSLs) is characterized by its non-uniformity. This paper employs the phase-space algorithm to uncover coherent structures, serving as a solution approach to investigate the transport mechanism across urban morphology. The drag coefficient *Cd*, a measure of surface roughness, is utilized to examine the influence of (idealized) urban morphology on canopy-level dynamics and ventilation. Wind tunnel experiments are conducted to study the flows and turbulence within urban canopy layers (UCLs) under various aerodynamic roughness conditions.
Keywords: Drag coefficient C_d, Phase-space algorithm, Wind tunnel experiment

1. Introduction

In rapidly developing cities, the air quality has emerged as a significant public concern, particularly when compared to rural areas, due to the high population density (Lawal et al., 2023; Vidanapathirana et al., 2023). The extensive construction and bulky architectural layout in urban areas inevitably hinder the efficient removal of stale air from, or the entry of fresh air into, urban canopy layers (UCLs). As a result, this degradation severely impacts the air quality at street level (Edward, 2009; Leung et al., 2012; Zhang et al., 2022; Liang et al., 2023). Hence, it is crucial to develop an advanced understanding of the dynamics within the atmospheric surface layers (ASLs) over buildings. This understanding is essential for enhancing street-level ventilation and improving air quality (Oke, 1988; Jiménez, 2004; Michioka et al., 2023).

Coherent structures can be detected with the assistance of a range of detection algorithms. Coherent-structure detections, such as U-level (Bogardt and Tiederman, 1986), window average gradient (WAG) (Antonia and Bisset, 1990; Krogstad et al., 1998), variable interval time average (VITA) (Bogardt and Tiederman, 1986), temporal average (TPAV) (Wallace et al., 1977), quadrant (Lu and Willmarth, 1973; Wallace, 2016), and phase-space filtering (Goring and Nikora, 2002), are commonly adopted. Recently, there have been advancements in the conventional phase-space filtering (Goring and Nikora, 2002) by incorporating central differencing (Wu et al., 2005) to analyze 3D physical quantities such as velocity fluctuation, acceleration, and jerk. This approach provides a more comprehensive perspective for studying and understanding the dynamics of turbulent flows.

Building upon the phase-space algorithm proposed by Wu et al. (2022) and conducting wind tunnel experiments with various configurations of roughness elements, this study aims to explore the coherent structures within turbulent flows. Specifically, the focus is on understanding the characteristics of these structures and their role in contributing to the momentum flux over an idealized urban morphology.

2. Wind tunnel experiments

The experiments were performed in an isothermal, open-circuit wind tunnel located at the Department of Mechanical Engineering, The University of Hong Kong, as illustrated in Fig. 1. The test section of the wind tunnel is constructed using acrylic and has dimensions of 6 meters in length, 0.56 meters in width, and 0.56 meters in height. To simulate idealized urban areas, roughness elements were affixed to the entire 6-meter floor of the wind tunnel, facilitating the generation of fully developed turbulent-boundary-layer (TBL)

DOI 10.5258/WES/P0002

flows. Each measurement point had a sampling duration of over 40 seconds, and the sampling frequency was set at 2 kHz.

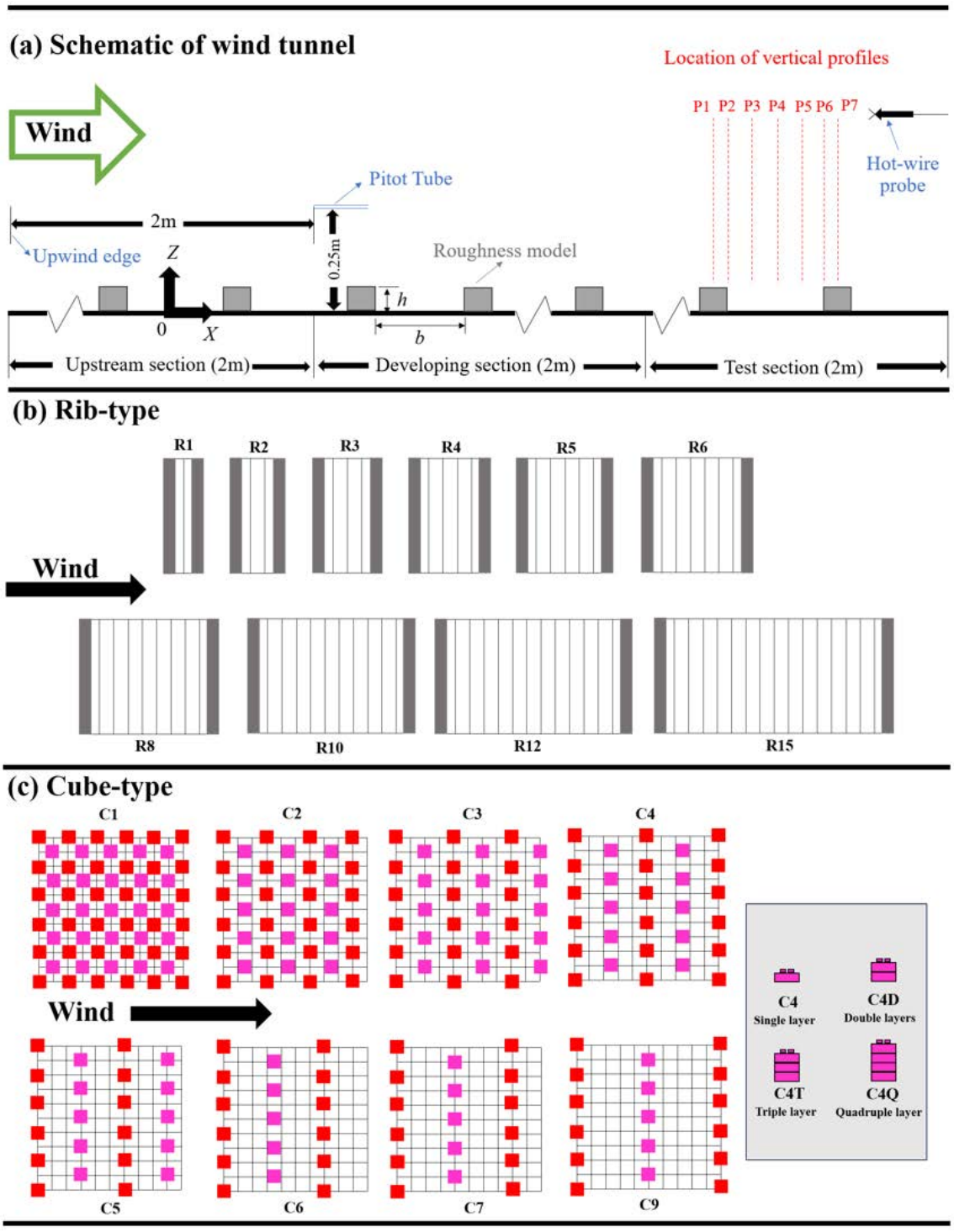

Fig. 1. Configurations of roughness elements employed in the wind tunnel experiments.

3. Results and discussion

When analyzing the data, it was observed that the number of detected coherent-structure data points initially encompassed all data points when k = 0. However, as the

DOI 10.5258/WES/P0002

value of k increased, the number of coherent-structure data points gradually decreased until it reached zero when k = 1 (as shown in **Fig. 2a**). Additionally, the count of discrete turbulent events (defined as consecutive coherent data points) followed a distinct pattern. It started with one event at k = 0, peaked at around k = 0.25, and then decreased to zero when k = 1 (**Fig. 2b**). It is worth noting that in **Fig. 2b**, all data points were contained within the ellipsoid, indicating that no turbulent events were detected.

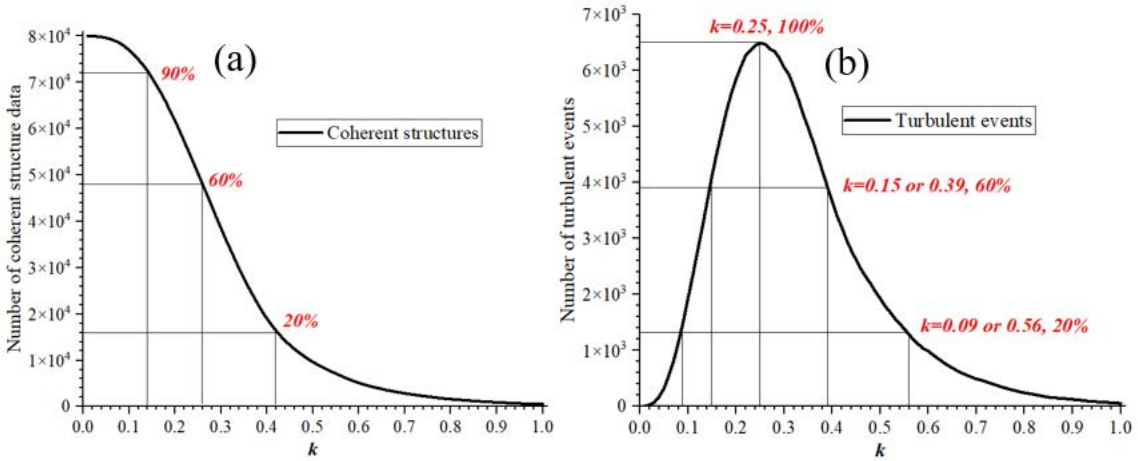

Fig. 2. Coherent-structure data points and the associated turbulent events. Number of detected: (a) coherent structure data points and (b) discrete turbulent events versus the scaling factor k. Measurement location P1 at z = h in R4 case is taken as an example.

Fig. 3 illustrates the relationship between exuberance (η), drag coefficient (Cd), and the scaling factor (k). In the high-drag-coefficient regime (with Cd values ranging from 4.1×10^{-3} to 10.8×10^{-3} in rib-type arrays), the exuberance η is relatively unaffected by changes in the drag coefficient Cd, except for a slight increase (peaking at approximately -0.33 to -0.3) observed between cases R1 and R2. This increase corresponds to a variation of approximately 9% (as shown in **Fig. 3a**). Conversely, in the low-drag-coefficient regime (with Cd values ranging from 3.6×10-3 to 7.9×10-3) in cube-type arrays, the exuberance η is significantly influenced by the drag coefficient Cd. The peaked exuberance values fall within the range of -0.41 to -0.21, representing a substantial change of around 50% (as depicted in **Fig. 3b**).

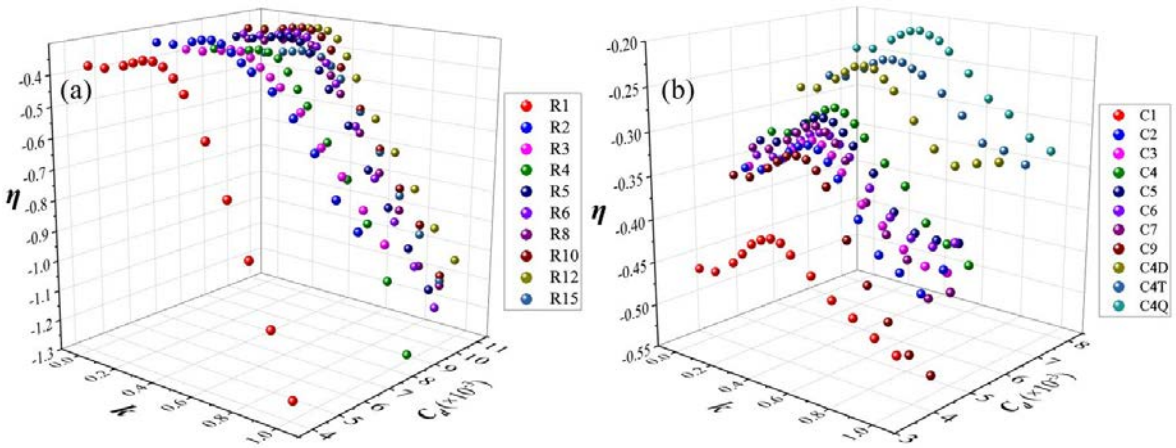

Fig. 3. Correlation among exuberance η, drag coefficient Cd, and scaling factor k for (a) rib-type arrays and (b) cube-type arrays at z = h.

DOI 10.5258/WES/P0002

4. Conclusion

In this study, wind tunnel measurements were conducted on two different idealized urban morphologies. The focus of the research was to investigate the coherent structures detected using the phase-space algorithm and to elucidate the ventilation mechanism of urban canyons. The research findings can serve as valuable references for urban planning and architectural layout. For instance, they suggest that appropriate adjustments, such as increasing building spacing, adjusting building height, and changing building arrangement from aligned to staggered, can significantly improve air transport efficiency. Furthermore, promoting the influence of high-frequency and small-scale motion in turbulence on air circulation can help enhance the air quality within the urban canopy. By implementing these measures, cities can work towards improving air quality and achieving sustainable urban development goals.

REFERENCES

[1] Lawal, O., Ogugbue, C. J., & Imam, T. S. (2023). Mining association rules between lichens and air quality to support urban air quality monitoring in Nigeria. *Heliyon, 9*, e13073.

[2] Vidanapathirana, M., Perera, N., Emmanuel, R., & Coorey, S. (2023). Air pollutant dispersion around high-rise building cluster forms: The case of Port City, Colombo, Sri Lank. *In Environmental Science and Pollution Research, 30*, 94166–94184.

[3] E. Ng. (2009). Policies and technical guidelines for urban planning of high-density cities–air ventilation assessment (AVA) of Hong Kong, *Building and Environment, 44*, 1478–1488.

[4] Leung, K. K., Liu, C. H., Wong, C. C. C., Lo, J. C. Y., & Ng, G. C. T. (2012). On the study of ventilation and pollutant removal over idealized two-dimensional urban street canyons. *Building Simulation, 5*, 359–369.

[5] Zhang, A., Xia, C., & Li, W. (2022). Exploring the effects of 3D urban form on urban air quality: Evidence from fifteen megacities in China. *Sustainable Cities and Society, 78*, Article 103649.

[6] Liang, M., Chao, Y., Tu, Y., & Xu, T. (2023). Vehicle pollutant dispersion in the urban atmospheric environment: A review of mechanism, modeling, and application. *Atmosphere, 14*, 279.

[7] T.R. Oke. (1988). Street design and urban canopy layer climate, *Energy and Buildings, 11*, 103–113.

[8] J. Jiménez. (2004). Turbulent flows over rough walls, *Annual Review of Fluid Mechanics*. 36, 173–196.

[9] Michioka, T., Funaki, R., & Kawai, T. (2023). Effects of building arrays on large-scale turbulent motions within an urban canopy. *Boundary-Layer Meteorology*.

[10] Bogardt, D. G., & Tiederman, W. G. (1986). Burst detection with single-point velocity measurements. *Journal of Fluid Mechanics, 162*, 389–413.

[11] Krogstad, P.-A., Kaspersen, J. H., & Rimestad, S. (1998). Convection velocities in turbulent boundary layers. *Physics of Fluids, 10*,949.

[12] Wallace, J. M., Brodkey, R. S., & Eckelmann, H. (1977). Pattern-recognized structures in bounded turbulent shear flows. *Journal of Fluid Mechanics, 83(4)*, 673–693.

[13] Lu, S. S., & Willmarth, W. W. (1973). Measurements of the structure of the Reynolds stress in a turbulent boundary layer. *Journal of Fluid Mechanics, 60(3)*, 481–511.

[14] Goring, D. G., & Nikora, V. I. (2002). Despiking acoustic doppler velocimeter data. *Journal of Hydraulic Engineering,128(1)*, 117–126.

[15] Wu, B., Bao, H., Ou, J., & Tian, S. (2005). Stability and accuracy analysis of the central difference method for real-time substructure testing. *Earthquake Engineering and Structural Dynamics*, 34(7), 705–718.

[16] Wu, J., Krynkin, A., & Croft, M. (2022) Objective phase-space identification of coherent turbulent structures in 1D time series. *Journal of Hydraulic Research, 60*, 811–825.

DOI 10.5258/WES/P0002

Turbulent boundary layers over multiscale urban arrays

Cameron Southgate-Ash, Sue Grimmond, Alan Robins and Marco Placidi
University of Surrey, Faculty of Engineering and Physical Sciences, Centre for Aerodynamics and Environmental Flow (EnFlo), Guildford, GU2 7XH, United Kingdom

Abstract

Wind tunnel experiments were conducted on multiscale building model arrays immersed in a deep turbulent boundary layer. A reference cuboid model of aspect ratio 3 was used, with two fractal iterations which systemically added smaller model length scales, totalling in three building models and in turn three roughness arrays of varying length scales. Through these fractal iterations, the frontal and plan solidities, λ_f and λ_p respectively, are kept the same to isolate the effects of the additional length scales on the flow structure and the aerodynamic parameters. Three-dimensional Laser Doppler Anemometry measurements were taken to measure the velocity fields along with a pressure tapped model in each array allowing for a direct calculation of the friction velocity, u_τ, and an estimation of the virtual origin, d, using Jackson's [1] interpretation. Preliminary results suggest that d increases with the addition of smaller length scales while the roughness length, z_o shows significant changes across iteration, despite the fixed λ_f and λ_p. The friction velocity calculated from pressure is found to be within 10% of that estimated from the Reynolds shear stress method [2]. The pressure also gives a good approximation for the virtual origin when compared to its evaluation from customary log-law fitting procedures.

1 Introduction

Understanding and modelling the flow field around tall urban environments is becoming increasingly important as more of the world's population begin to live in cities where tall buildings predominate. Despite significant improvements in morphometric methods, models remain relatively poor particularly when assessing more complex geometries with multiple length scales. There has been some shift in research towards multiscale roughness and considering different geometric parameters with a particular focus on predicting the aerodynamic parameters of a roughness surface such as drag and the roughness length, z_0 [3, 4, 5]. Even so, a clear understanding of how smaller length scales can affect atmospheric turbulence around urban arrays is needed.

To explore this, we employ a tall building model array of AR = 3. The model has two fractal iterations obtained using a Minkowski sausage-type generator which add a length scale roughly an order of magnitude lower than the previous totalling in three roughness arrays. Through these iterations λ_f and λ_p are kept constant (as well as the average height and width of the budlings). Herein, we examine how the surface characteristics change with additional length scales via an indirect method, using the Clauser chart method and Reynolds stress approximation, and a direct method, obtaining the shear stress, μ_τ and d with a pressure tapped building model.

2 Experimental facility and details

2.1 Experimental facility and boundary layer development

The experiments were carried out in the University of Surrey Environmental Flow Research Centre (EnFlo) 'Aero' wind tunnel. This tunnel's working section covers 9000 mm (length) x 1060 mm (width) x 1270 mm (height). It is a closed-circuit wind tunnel with a maximum velocity of 40 m s^{-1}. A Pitot-static probe at the tunnel inlet measures the free-stream velocity. The tunnel velocity was set to 10 m s^{-1}, resulting in a Reynolds number of 6×10^4 , based on the building height. Irwin spires, along with floor roughness elements are employed to produce a thick velocity profile similar to that of an urban boundary layer (Fig. 1). The spires have a height of 245 mm and a base width of 35 mm, with a centre spacing of 130 mm. The 2 mm tall and 8 mm wide floor roughness elements are spaced 16 mm apart in a staggered array. These give a boundary layer depth at the building location of $\delta \approx$ 221 mm and, using the approximation $u_\tau \approx \sqrt{u'w'}$ [6], a u_τ = 0.45 m s^{-1}.

DOI 10.5258/SOTON/WES/P0003

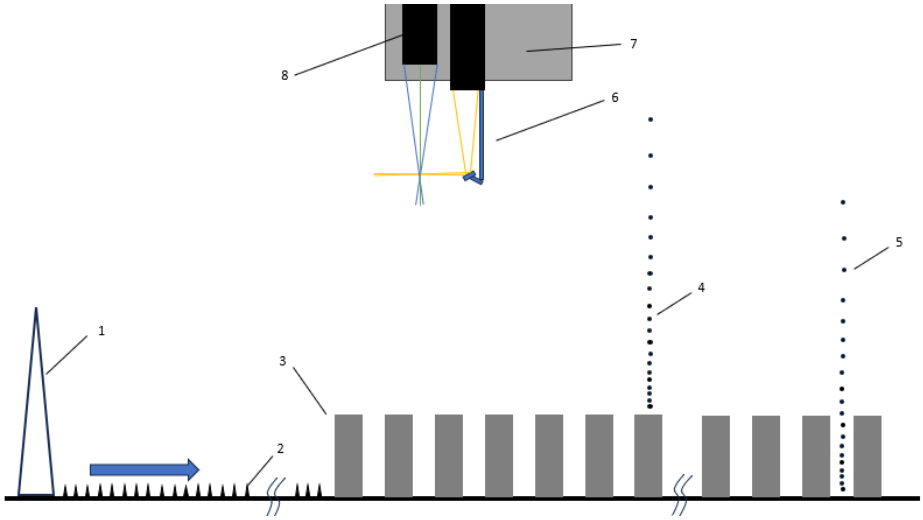

Figure 1: Tunnel side on view with LDA set up showing [1] Irwin spires, [2] floor roughness, [3] building models, [4] streamwise location of vertical profiles, [5] In canopy vertical profile, [6] mirror, [7] LDA probe shroud, [8] LDA probes. Not to scale. [7]

2.2 Rough wall models

A flat-surface tall square cylinder with AR = 3 is used as a reference case. From this form, two iterations of geometric complexity are added, each an order of magnitude more detailed or lower than the previous one. Thus, three building models are used (Fig. 2), all with a mean building height (H_B) 90 mm and width of 30 mm. Through each iteration the frontal and plan area, λ_f (0.5) and λ_p (0.2) respectively, remain the same, isolating the effects of the smaller length scales. Thus, all models have a H_B/δ of 0.41. The building model arrays started 2000 mm downwind of the spires (Fig. 1). The fractal iterations are obtained using a Minkowski Sausage-type generator [8] to decrease the minimum length scale characterising the building at each iteration (see Fig. 2). Although more iterations are possible, the length scales rapidly become smaller than the sensor's spatial measurement resolution rendering any differences undetectable. 3D printed building models, used for drag estimation, have embedded pressure ports using grey resin from i.materlise (Technologielaan 15, 3001 Leaven, Belgium) and the rest of the models were manufactured from laser cut wood.

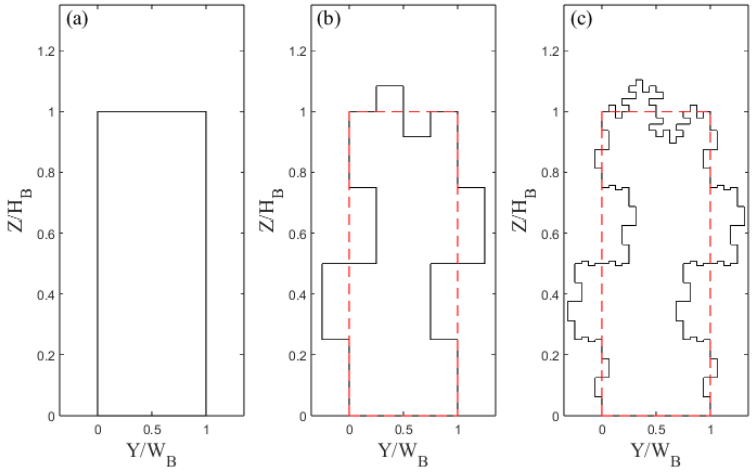

Figure 2 Building models normalised with mean height (H_B) and width (W_B), for (a) zero, (b) first, and (c) second iterations, with average width and height of models (red dashed lines). [9]

DOI 10.5258/SOTON/WES/P0003

2.3 LDA

A three-component Laser Doppler Anemometer (LDA, Fibreflow, Dantec Dynamics, Denmark) is used to simultaneously measure the mean (U, V, W) and fluctuating (u', v', w') velocity components, corresponding to the streamwise (x), spanwise (y) and wall-normal (z) directions, respectively. The laser beams are converged by a 300 mm focal length lens. An acquisition frequency of 500 Hz is set as the minimum target for the flow seeder. Each data point is recorded for 30 s to allow for sufficient statistical convergence, while constraining experiment run time. We define X= 0 mm at the start of the rough wall models, Y = 0 mm at the centre line of the tunnel and Z= 0 mm at the top of the baseboard the rough wall models are placed on. For each array, vertical profiles are taken at several streamwise locations from 0 mm to 4000 mm, from the top of the canopy to Z = 550 mm. Once fully-rough flow is reached, 12 to 18 in-canopy profiles are taken within a repeating unit (depending on model and iteration) to be spatially averaged.

3 Preliminary results

This paper presents some preliminary results for the surface characteristics of each array which come from a manuscript currently in preparation for publication [7]. In spatially-developing flow, z_0 has a dependency on the boundary layer fetch [10], and so to accurately assess the surface characteristics the flow must be fully rough and adjusted to the roughness below. This was determined to occur by a fetch of x ≈ 4000 mm for all building arrays. The surface characteristics for each rough wall are presented in Table 1. The surface characteristics are obtained with 2 separate methods, the first of which is and indirect method where μ_τ is calculated from the Reynolds shear stress and using the suggested correction factor from Cheng and Castro 2002, $u_\tau = 1.12\sqrt{\overline{u'w'}}$. The Clauser chart method is then used where d and z_0 are unknown variables and are found by fitting the viscous scaled spatially averaged streamwise velocity, U^+, to a logarithmic region of the boundary layer [11] (Fig. 3). The second method calculates μ_τ and d directly from a pressure tapped building using the method outlined in [12] for the former and Jackson's (1981) interpretation of d as the point at which the mean surface drag appears to act for the latter. z_0 is then found by again fitting U^+ to the logarithmic region of the boundary layer (Fig. 3).

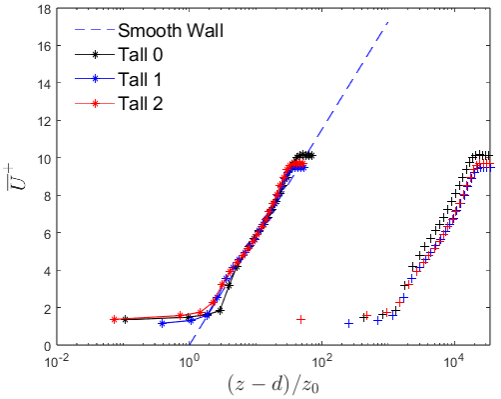

Figure 3 Mean streamwise velocity profiles of Tall arrays. The dotted blue line represents a smooth wall and the crosses the unscaled data. [7]

Table 1 shows that the results from both methods are all within 10% of each other supporting the use of the correction factor for the Reynolds shear stress and Jackson's 1981 interpretation of d as well as the validity of both methods. d shows an increase with fractal iteration which is larger from iteration 0 to 1 than 1 to 2, suggesting that the virtual origin is, at least partly, a function of the maximum height of the buildings. The models show an overall increase in μ_{τ_p}, but this is not fully reflected in μ_τ. z_0 and z_{0_p} increase with each iteration, which is in contradiction to many morphometric methods that would suggest it should remain unchanged given the fixed frontal and plan solidities. Overall, the addition of the smaller length scales had a significant effect on the roughness length and results suggest that this could be an important factor in finding a more accurate morphometric method for complex rough walls.

DOI 10.5258/SOTON/WES/P0003

Table 1 Surface characteristics for each building array iteration. "$_p$" subscript denotes results from direct pressure measurements. [7]

Building Model	d (mm)	d_p (mm)	μ_τ	μ_{τ_p}	z_0 (mm)	z_{0_p} (mm)
Tall 0	60	62	1.02	1.06	7.1	7.0
Tall 1	63	66	1.09	1.12	9.5	9.3
Tall 2	66	67	1.07	1.15	9.8	9.7

4 Conclusion

3D LDA was carried out over rough walls with varying length scales to assess how these affect the surface characteristics. This was done using an indirect method, using the Clauser chat method and the Reynolds shear stress, and a direct method, using a pressure tapped building to calculate μ_τ and d. The compared data from both methods was all within 10% showing good validity. The roughness length scale in both methods was shown to change significantly with the additional length scales highlighting the importance of multiscale information when considering morphometric methods for rough walls modelling.

This paper briefly covered some of the preliminary mean results from the flow. This experiment has also investigated similarity across each of the rough walls as well as changes seen in the fluctuating flow and the spectra which will be covered in future work.

5 References

[1] P. S. Jackson, "On the displacement height in the logarithmic velocity profile," *Journal of Fluid Mechanics,* vol. 111, pp. 15-25, 1981.

[2] R. T. Reynolds and I. P. Castro, "Measurements in an urban-type boundary layer," *Experiments in Fluids,* vol. 45, pp. 141-156, 2008.

[3] M. Kanda, A. Inagaki, T. Miyamoto, M. Gryschka and S. Raasch, "a New Aerodynamics Parametrization for Real Urban Surfaces," *Boundary-Layer Meteorology,* vol. 148, no. 2, pp. 357-377, 2013.

[4] C. Vanderwel and B. Ganapathisubramani, "Effects of spanwise spacing on large-scale secondary flows in rough-wall turbulent boundary layers," *Boundary-Layer Meteorology,* vol. 172, no. 1, pp. 1-16, 2019.

[5] T. Medjnoun, E. Rodriguez-Lopez, A. Ferreira, T. Griffiths, J. Meyers and B. Ganapathisubramani, "Turbulent boundary-layer flow over regular multiscale roughness," *Journal of Fluid Mechanics,* vol. 917, 2021.

[6] I. P. Castro, "Rough-wall boundary layers: mean flow universality," *Journal of Fluid Mechanics,* vol. 585, pp. 469-485, 2007.

[7] C. Southgate-Ash, S. Grimmond, A. Robins and M. Placidi, "Turbulent boundary layers over multiscale urban arrays," *Paper in preperation ,* 2024.

[8] B. B. Mandelbrot and J. A. Wheeler, "The Fractal Geometry of Nature," *American Journal of Physics,* vol. 51, no. 3, pp. 286-287, 1983.

[9] C. Southgate-Ash, A. Mishra, S. Grimmond, A. Robins and M. Placidi, "Wake Characteristics of Multiscale Buildings in a Turbulent Boundary Layer," *Under consideration for publication ,* 2024.

[10] H. Cheng, P. Hayden, A. G. Robins and I. P. Castro, ") Flow over cube arrays of different packing densities," *Journal of Wind Engineering and Industrial Aerodynamics ,* vol. 95, no. 8, pp. 715-740, 2007.

[11] F. H. Clauser, " Turbulent boundary layers in adverse pressure gradients," *Journal of the Aeronautical Sciences ,* vol. 21, pp. 91-108, 1954.

[12] H. Cheng and I. P. Castro, "Near-wall flow development after a step change in surface roughness," *Boundary-Layer Meteorology,* vol. 105, pp. 411-432, 2002.

DOI 10.5258/SOTON/WES/P0003

Coupled mesoscale–microscale (CMM) modelling of airflow at Hong Kong International Airport

Chang-Chang Wang[1*], Pak-Wai Chan[2]
[1]Faculty of Construction and Environment, The Hong Kong Polytechnic University, Hong Kong, China
[2]Hong Kong Observatory, Hong Kong, China
[*] E-mail: wangchangchang026@vip.163.com

1 INTRODUCTION

Coupling mesoscale (several kilometres) and microscale (meters to tens of meters, CMM) models is an important step forward in the microscale turbulence forecasting in the atmospheric boundary layer (ABL). The mesoscale models adopt the physical parameterizations to model the outer flow phenomena while the microscale models resolve the terrain details and microscale flows around buildings/man-made structures. For example, Esparza et al. (2018) firstly proposed multiday dynamic downscaling from numerical weather prediction (NWP) forecasts to eddy-resolving scales with a grid resolution of 25 m and realistically reproduced turbulence levels and peak events at subminute intervals in the daytime ABL. Due to the complex coupling mechanisms of atmospheric flows at several scales, such as street scale (~ 100 m) and city scale (~ 10 km), the development of simulation techniques and tools to resolve these multi-scales is challenging and needed to better forecast and understand these microscale turbulences in the ABL.

At present the operational mesoscale models are unable to predict the details at street scales and the eddy-resolving simulations are still impractical to extend to city scales. On the one hand, several studies have developed the multiscale capabilities in numerical weather prediction (NWP) models (Mirocha et al. 2013; Esparza et al. 2014). On the other hand, with advances in computing power, computational fluid dynamics (CFD), including large eddy simulation (LES), has been performed to provide physical insights into atmospheric turbulence, which can further improve spatiotemporal resolution information (Flores, Garreaud & Muñoz, 2013). Fossum & Helgeland (2020) performed LES of Oslo city using a domain of 150 km^2 at a spatial resolution of 2 m. However, few studies have coupled CFD-LES with mesoscale models to predict microscale turbulence and evaluate its multiscale performance in forecasting realistic atmospheric turbulence.

Hong Kong International Airport (HKIA) is well known for its susceptibility to low-level wind shear, which is a potential hazard for airport during landing and take-off. On average, there are 115 days per year (almost every 3.2 days) with wind shear reported (Hon & Chan 2022). A short-range LIDAR (SRL) facility with a spatial resolution of 30 m and a temporal resolution of 20 s was deployed near aircraft touchdown by the Hong Kong Observatory (HKO) to alert building-induced turbulences (Chan & Lee, 2012). Velocity streaks and tiny anticyclones (~100 m in size) coming out of a building situated at the north part of HKIA were occasionally observed during the routine scanning of the SRL near the airport (Hon et al., 2021). Much less is known, however, about the origin of such vortices. It is supposed to be related to the buildings over there, such as the Passenger Terminal Building (PTB) and the AsiaWorld-Expo (AWE).

This study documents a study of combining meteorological observations and multiscale coupled mesoscale–microscale (CMM) modelling during a tiny anticyclonic vortex event detected by the SRL to investigate the relationship between the anticyclonic vortices and the surrounding buildings such as the PTB and AWE under realistic meteorological conditions.

2 METEOROLOGICAL CONDITIONS

In June 2021, Hong Kong was hit by an active southwesterly monsoonal airstream and a very hot weather warning was issued by the Hong Kong Observatory (HKO) from 16 June 2021 to 21 June 2021. A Doppler Lidar instrumented near the 25RA at HKIA was in operation to monitor low-level windshear on flight runways. At 03:25 UTC (Coordinated Universal Time; 0000 UTC is 0800 HKT; Hong Kong Time), a sequence of anticyclonic vortices was observed downstream of the AWE at the airport in the morning of 17 June 2021. The wind fields by the surface observations in that morning showed that

DOI 10.5258/WES/P0004

moderate southwest monsoon exceeding 6 m/s was prevailing over the south China coast and thus southwesterly flow over the airport area throughout the day. As will be detailed later, this weather condition is quite favorable for the occurrence of anticyclonic vortices.

3 COUPLED MESOSCALE–MICROSCALE MODELLING (CMM) METHODOLOGY

A multiscale numerical framework by coupling large eddy simulation (LES), e.g., the Open Field Operation and Manipulation (OpenFOAM) at a spatial resolution of ~1 m, with a mesoscale model, e.g., the Regional Atmospheric Modelling System (RAMS) at a spatial resolution of 40 m, is developed. In the RAMS simulation, five nested domains are adopted (hereafter, RAMS-run) shown in Fig. 1. The initial and boundary conditions are obtained from NCEP GFS 0.25 Degree Global Forecast Grids Historical Archive. The Smagorinsky scheme is employed for the first two nests, and the Deardorff scheme for the remaining three nests that has been shown to produce reasonable results. The LES simulation domain in Fig. 2 has overall dimensions of 3.20 km (approximately 40 H) × 3.20 km (approximately 40 H) × 1.65 km (approximately 20 H) at a spatial resolution of 8 m. The vertical grid space is initially 1 m and stretches to approximately 2.5 m in the near ground region until twice the height of the tallest building in the simulation domain. Then a coarse grid resolution with approximately 20 m is used until the top of the simulation domain at 1.65 km. The LES and RAMS are coupled through one-way off-line nesting; the initial and time varying boundary conditions are generated from RAMS to provide larger-scale forcing for LES. In the present work, the meteorological fields at 6-*h* separation from 00:00:00 UTC to 06:00:00 UTC on 17 June 2021 are analyzed.

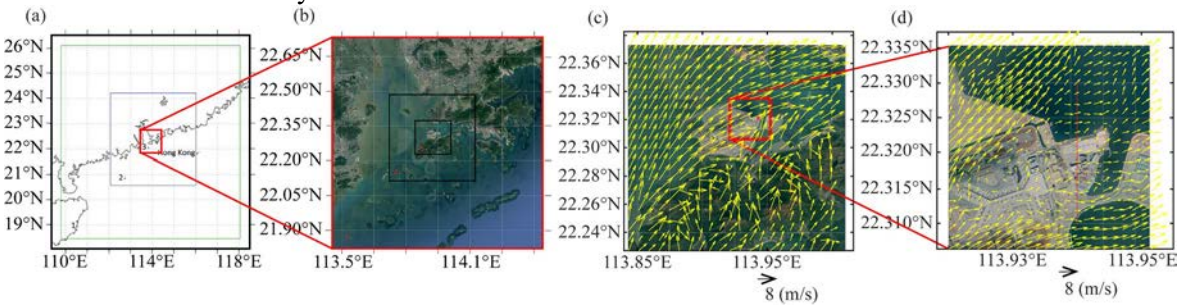

Figure 1, (a-b) The five nested model domains D01-D05 of RAMS for the HKIA site, and calculation domains of (c) the RAMS-run and (b) the LES-run at 40 m height. The color shadings over the land surfaces in (c) and (d) indicate the topography. The red box in (c) is the domain for the LES-run. The arrows in each panel show simulated surface wind vectors at 02:46 UTC on 17 June 2021. The spatial resolution of wind vectors is 800 m in (c) and 160 m in (d).

(a1) 03:26:00 UTC

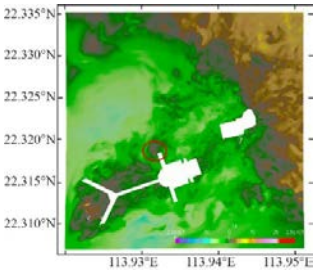

(b1) 02:44:50 UTC

(a2) 03:27:00 UTC

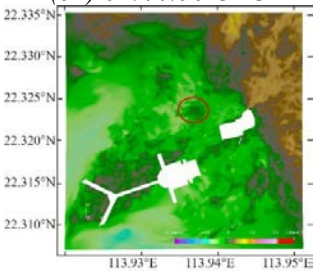

(b2) 02:48:10 UTC

DOI 10.5258/WES/P0004

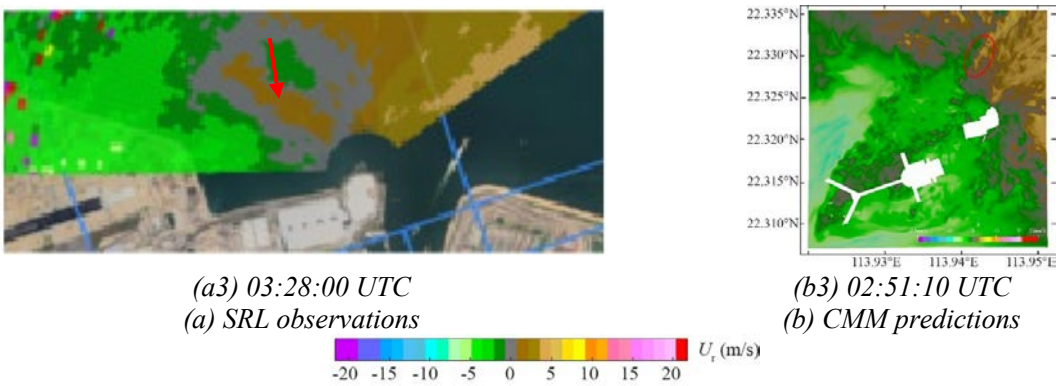

(a3) 03:28:00 UTC
(a) SRL observations

(b3) 02:51:10 UTC
(b) CMM predictions

Figure 3, Comparisons of the time sequence of tiny anticyclonic vortices in the Doppler velocity map: (a) observed by SRL and (b) predicted by the CMM model.

4 COMPARISONS WITH MEASUREMENTS AND DOPPLER LIDAR OBSERVATIONS

Fig. 3 shows the comparisons of SRL observations and simulated Doppler velocity in the LES-run. Comparisons with the SRL observations and wind station measurements testify the performance of the current CMM model.

5 RESULTS AND DISCUSSION

A sequence of anticyclonic vortices simulated by the LES results is shown in Fig. 4. Bot the simulated Doppler velocity images and wind vectors are presented. A tiny vortex first appears on the western side of the PTB at 02:46:30 UTC. It then drifts east-northeastwards following the background southwesterly flow. The anticyclone appears to grow in intensity during the evolution. The size of the anticyclone is growing as well. This kind of microscale anticyclone (i.e., rapid development with rather limited size), also observed by a LIDAR installed nearby, is believed to arise from both the building-induced turbulence and the effect of the Lantau terrain on the rather moderate southwesterly flow.

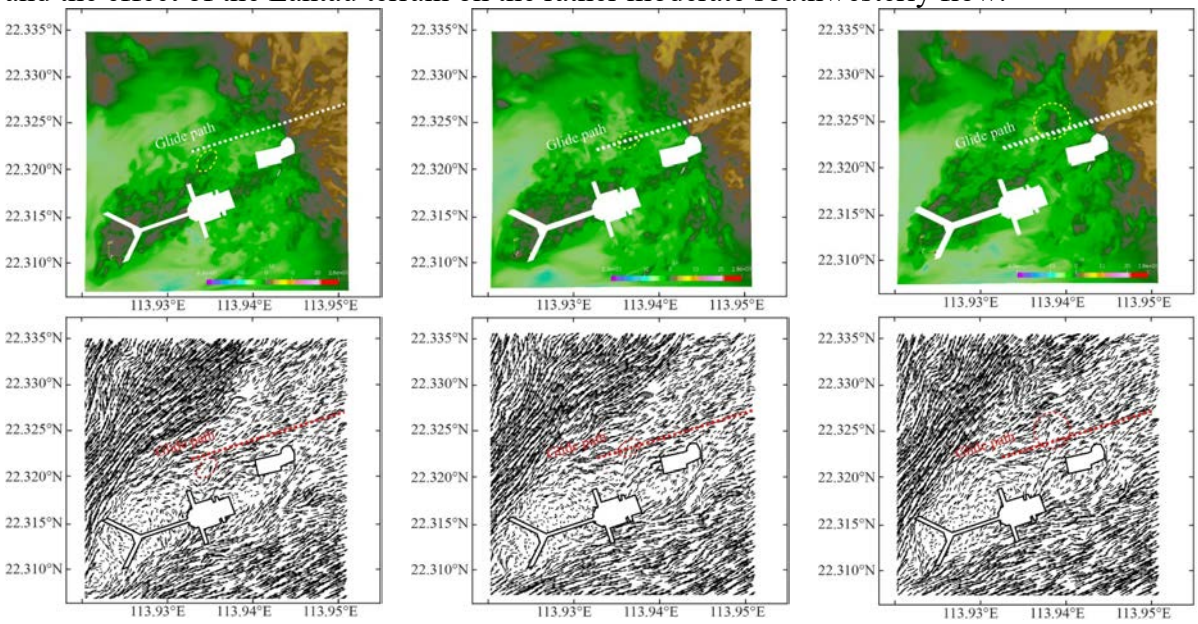

(a) 02:46:30 UTC *(b) 02:47:50 UTC* *(c) 02:49:10 UTC*

Figure 4, A time sequence of simulated Doppler velocity images (up) and corresponding wind vectors based on LES results. The anticyclonic vortices are marked by a yellow circle, and the flight glide path is indicated by dashed white line. Same legend as Fig. 3.

To study the effects of buildings on this microscale anticyclonic vortices, further simulations without the PTB and without the AWE respectively are conducted as shown in Fig. 5. It is found that without

DOI 10.5258/WES/P0004

the PTB and AWE could significantly reduce the intensity of anticyclonic vortices crossing the flight path, illustrating the close relationship between the buildings and this microscale turbulence event. Our study adds evidence that the tiny anticyclonic vortices are a result of the interaction between the background southwesterly flows and the key buildings (i.e., the PTB and AWE) at HKIA, which helps enhance sustainability and resilience of the airport and fulfil the increasing demand for safe aviation services of the city.

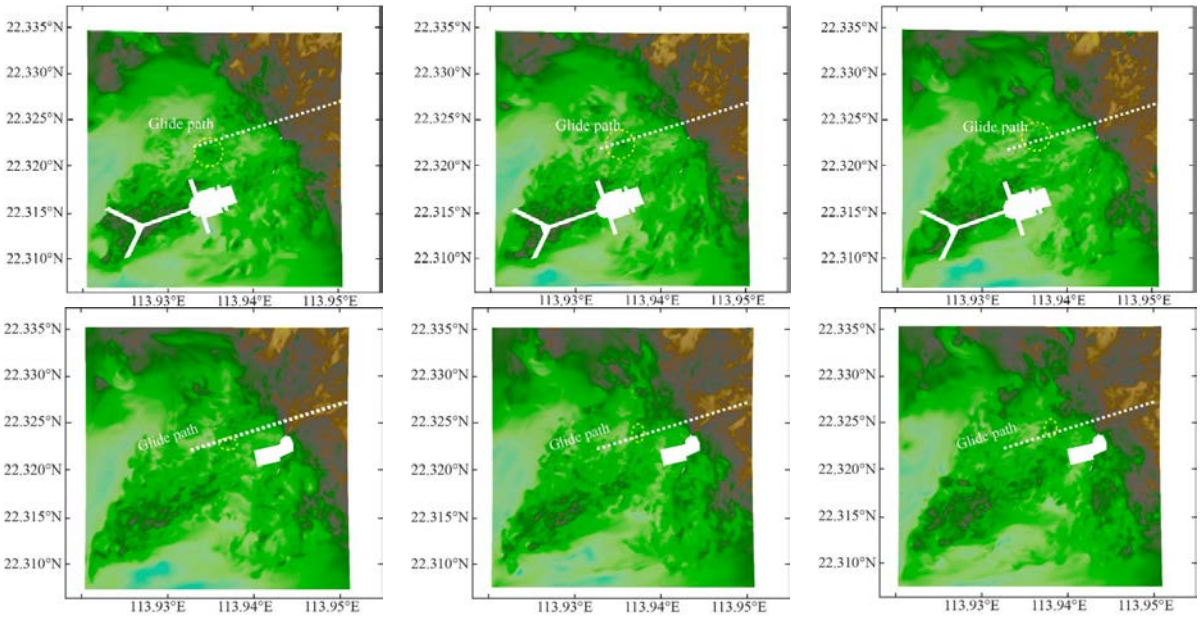

(a) 02:46:30 UTC *(b) 02:47:50 UTC* *(c) 02:49:10 UTC*

Figure 5, A time sequence of simulated Doppler velocity images for simulations without the AWE (up) and simulations without the PTB (down), respectively. Sane legend as Fig. 3.

ACKNOWLEDGEMENT

The authors acknowledge a grant from the Hong Kong Polytechnic University Postdoc Matching Fund Scheme (Grant No. 1-W245), and the finance support from NERC (grant number NE/W002841/1) to present in the WES-2024.

REFERENCES

[1] Muñoz-Esparza D., Kosović B., Mirocha J., van Beeck J. (2014). "Bridging the transition from mesoscale to microscale turbulence in numerical weather prediction models", *Bound. Lay. meteorol.* **153**, 409-440.

[2] Muñoz-Esparza D., Sharman R., Sauer J., Kosović B. (2018). "Toward low‐level turbulence forecasting at eddy-resolving scales", *Geophys. Res. Lett.* **45**, 8655-8664.

[3] Mirocha J., Kosović B., Kirkil G. (2014). "Resolved turbulence characteristics in large-eddy simulations nested within mesoscale simulations using the Weather Research and Forecasting Model", *Mon. Weather Rev.* **142**, 806-831.

[4] Flores, F., Garreaud, R., Muñoz, R.C. (2013). "CFD simulations of turbulent buoyant atmospheric flows over complex geometry: Solver development in OpenFOAM", *Comput. Fluids* **82**, 1-13.

[5] Fossum H.E., Helgeland A. (2020). "Computational fluid dynamics simulations of local wind in large urban areas (20/02365)", *In: Tech. rep., Norwegian Defence Research Establishment (FFI)*.

[6] Hon, K.K., Chan, P.W. (2022), "Historical analysis (2001–2019) of low‐level wind shear at the Hong Kong International Airport". *Meteorol. Appl.* **29**, e2063.

[7] Hon, K.K., Lux, P., Chan, P.W., Ngan, K., Li, Q.S., Wenig, M. (2021), "Statistical analysis of building-induced turbulence at an airport", *Atmósfera* **34**, 491–502.

[8] Chan, P.W., Lee, Y.F. (2012), "Application of short-range lidar in wind shear alerting", *J. Atmos. Ocean. Tech.* **29**, 207–220.

DOI 10.5258/WES/P0004

Reference pressure for wind load measurements in a turbulent boundary layer.

Roger Hoxey, Peter Richards and Adam Robertson

SUMMARY

Within a turbulent boundary layer the static pressure is not spatially constant but exhibits extreme negative pressure fluctuations that contribute to a significant negative mean value in static pressure. The mean static pressure relates to turbulence intensity and varies with height which makes wind load pressure coefficients dependent on the location of reference pressure.

1 INTRODUCTION

Surface pressure measurements were made on the Silsoe 6 m cube some time ago (Richards, et al, 2001) but at that time we were not aware of the influence of static pressure variations associated with eddies in turbulent flow. Measurements of static pressure in the lower part of the atmospheric boundary layer were made on two occasions with full experimental details and analysis given in Hoxey et al, 2021. These eddies, which are a characteristic of turbulent flow, are vortical in structure with a low-pressure core; they exist in sizes from a few millimetres to possibly the boundary-layer thickness.

There are two distinct ways in which static pressure is evident in wind-load measurements. The mean static pressure is spatially depressed and varies with height, following the pattern of turbulence intensity within the boundary layer. This means the reference pressure used as the backing pressure applied to the differential pressure transducers is location dependent and of significance in the evaluation of pressure coefficients. Secondly, the static pressure has a distinct spectral pattern compared to the spectrum of dynamic pressure.

There is limited work with which to make comparisons; the only other full-scale work known of is by Albertson et al 1998 who also found similar spectral properties. Brief reference has been made to wind-tunnel studies on boundary layers at much lower Reynolds Number (Tsuji, et al 2007), but no published work has been found where fluctuating static pressure has been measured in industrial boundary-layer flows, where models are present. The findings have application to all pressure measurements in turbulent flows and specifically to the highly turbulent flows in industrial wind tunnels.

2 MEASUREMENTS IN THE ABL

2.1 Introduction

Measurements were made on the experimental site at Silsoe on a 6 m cube which was mounted on a turntable and could be rotated through 360º (Richards et al 2001, Richards & Hoxey 2012). The approach flow for the measurements reported here were from WSW over open farm land and cut grass extending over 500 m with a typical roughness length z_o of 10 mm. The pressures from surface tapings, together with the simultaneous recording of the 3 components of wind speed using a Gill Instruments symmetrical-head ultrasonic anemometer mounted at a height of 6 m, 18 m upstream of the cube, were recorded. The reference pressure was from a static probe (Moran & Hoxey 1979) mounted near the sonic anemometer at a height of 6 m. The measurements used in this paper are from Run 68 for a WSW wind near normal to the face of the cube, and made at 5 samples per second for a 1-hr period (18,000 data points). With the cube rotated by 90 degrees, the same tapping points were monitored in Run 39 with a similar WSW wind direction, recorded at 4.167 samples per second for 36 minutes (9,000 data points).

On the same site, but on different occasions, measurements of static pressure were made. The data set used here is Run 888 with a similar WSW wind direction, recorded at 10 samples per second for 20 minutes (12,000 data

DOI 10.5258/WES/P0006

points). Static pressure was measured at ground level and at 1, 3 and 6 m heights referenced to a time and spatially-averaged ground-level pressure.

2.2 Characteristics of the ABL wind

Many measurements of the boundary layer at the Silsoe experimental site have been made, for example Richards et al, 2000. For the example runs used here, for a WSW wind, the upstream conditions were similar to when measurements were made of static pressure (Run 888).. An example of the velocity (U_z) at height z and the velocity component turbulence intensities (I_u, I_v and I_w) obtained from the ultrasonic anemometer on the 6 m mast are shown in Table 1. The mean frictional velocity, u_τ was derived from the mean Reynolds stress $-\overline{u'w'} = u_\tau^2$.

Table 1 Mean value statistics derived from the ultrasonic anemometer at 6 m height

	z (m)	*Mean* U_z (m s^{-1})	I_u	I_v	I_w	u_τ (m s^{-1})	$\frac{u_\tau}{U_z}$	*Spectral Index*
Run 888	6	8.61	0.188	0.169	0.082	0.577	0.067	-1.66
Run 68	6	11.70	0.229	0.165	0.097	0.787	0.067	-1.66
Run 39	6	9.45	0.203	0.173	0.078	0.651	0.069	-1.68

In the pressure measurements that follow, wind velocity (U_z) is converted to wind dynamic pressure (q_z) where $q_z = ½\rho U_z^2$ (ρ is air density, a value of 1.226 kg m^{-3} has been used). The spectra of q are shown in Fig. 1; the PSD (Power Spectral Density) is of $S_q(n)/\sigma_q$ for each run (σ_q is the standard deviation of q); dividing by σ_q makes the PSD dimension seconds (s). These spectra follow the expected decay close to $n^{-5/3}$ over the frequency range shown in the inertial subrange, with values of the least-squares fit of the spectral index given in Table 1.

A 10-min record of the measured dynamic pressure and of the static pressure at a height of 6 m are shown in Fig. 2. The static pressure was measured relative to a ground-level pressure tapping but 'true zero' (Hoxey et al 2021) for static pressure at z = 6 m has been applied in place of the backing pressure from the ground tapping. It should be noted that extreme negative peaks in static pressure are often missed as the sampling rate is insufficient with only some evident in Fig. 2. For boundary-layer wind-tunnel flows, an equivalent 'true zero' can be obtained from a sensor placed above the turbulent boundary layer in low-turbulence flow, as used by Tsuji, et al 2007.

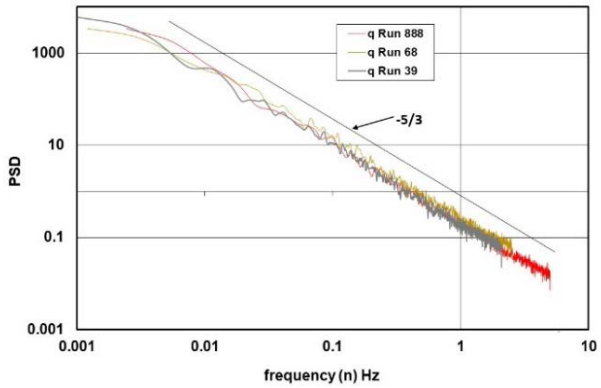

Figure 1 Spectra ($S_q(n)/\sigma_q$) of the wind dynamic pressure at 6 m for the three runs.

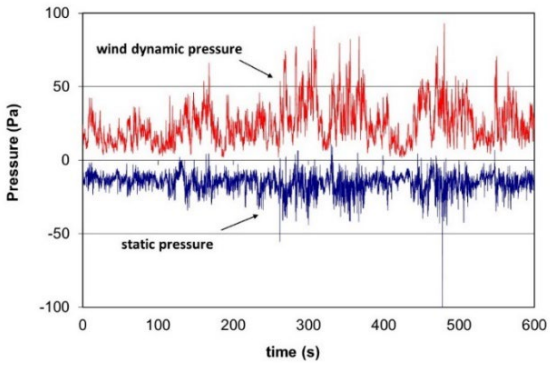

Figure 2 Example of the wind dynamic and static pressure in the ABL at a height of 6 m.

DOI 10.5258/WES/P0006

2.3 Measured values of wind dynamic pressure and of static pressure

The measured mean and RMS values of dynamic pressure (q_z), and of static pressure (p_z) for Run 888 are summarised in Table 2. For Run 888, the mast measurements, p_z are the measured mean static pressure at height z relative to the 'true zero' static pressure (p_t). The derivation of the 'true' static pressure p_t is based on an argument that static pressure excursions are negative. All mean static pressure values are expressed as pressure coefficients (Cp) in terms of the mean wind dynamic pressure at 6 m ($q_{\text{mean 6m}}$). The dynamic pressure turbulence intensity (I_q) is defined as q_{RMS} / $q_{\text{mean 6m}}$.

Table 2 Mean and turbulence intensity of wind dynamic pressure and for Run 888 the mean and RMS of static pressures on the 6 m mast

	z (m)	q_{mean} (Pa)	I_q $q_{RMS}/q_{mean\ 6m}$	p_z-$p_t/q_{mean\ 6m}$	$p_{RMS}/q_{mean\ 6m}$
Run 888	*0*			-0.142	0.029
	1			-0.225	0.055
	3			-0.262	0.062
	6	48.7	0.369	-0.286	0.069
Run 68	*6*	91.3	0.443		
Run 39	*6*	58.5	0.412		

Figure 3 illustrates the sensitivity of static pressure to turbulence which has an impact on the selection of reference pressure when making measurements in boundary-layer flows. This figure includes static pressure measurements on a 10 m mast at 1, 3, 6 and 10 m heights (Hoxey et al, 2021), and show the distribution of static pressure with height. This is consistent with that found by Tsuji et al 2007 for a thin boundary layer on a wind-tunnel floor but as the Reynolds Number and turbulence levels were much lower than at full scale, the magnitude of the pressure coefficients were much reduced.

3.2 Mean surface pressure measurements on the 6 m cube

An example of the measured mean pressure coefficients for the 6 m cube is shown in Fig.4. The example is for a wind near normal to the face of the cube. The coefficients are in relation to the mean dynamic pressure at cube height (6 m) and referenced to a pressure from a static probe (transducer backing pressure) also at cube height, both measured 18 m upstream of the cube.

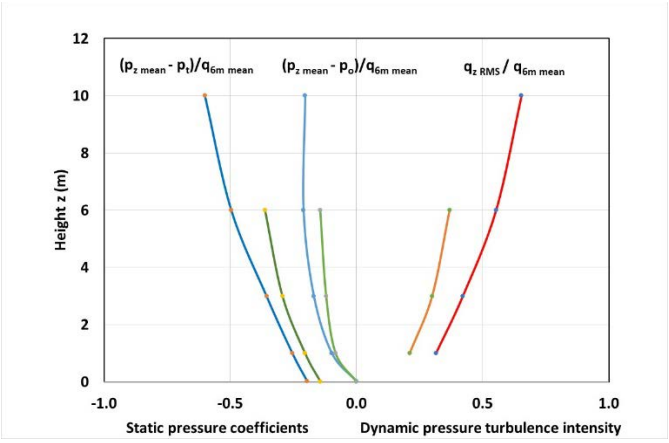

Figure 3 Static pressure coefficients based on $q_{\text{mean 6m}}$: 10 m mast values in blue, 6 m mast values from Run 888 in green. Dynamic pressure turbulence intensity (I_q) for 10 m mast in red and for 6 m mast in orange.

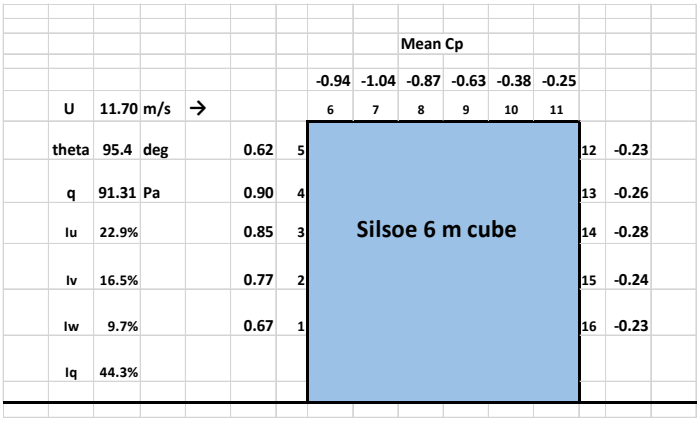

Figure 4 Mean pressure coefficients, and mean wind statistics for Run 68: a one-hour record at 5 samples/s (18000 data points): integers denote tap number. Reference dynamic and static pressure is at cube height sensed at 18 m upstream.

Three example tapping points are presented in Table 3 to illustrate the significance of the location of the

DOI 10.5258/WES/P0006

reference pressure on the evaluation of pressure coefficients. This finding has direct application to all pressure measurement studies in turbulent flows where wind loads are derived relative to a reference pressure from some point in the flow.

Table 3 Mean pressure coefficient for the three example tapping points

	mean Cp relative to static pressure at 6 m	***relative to ground static pressure p_o (-0.144)***	***relative to free stream p_t (-0.286)***
windward wall tap 4	0.903	0.759	0.617
roof tap 9	-0.633	-0.777	-0.919
side wall tap 4*	-0.698	-0.842	-0.984

4 SPECTRAL PROPERTIES OF STATIC PRESSURE

The spectral properties of static pressure fluctuations have been described by Hoxey et al, (2021) and not included in this paper. Surface pressure spectra for the 6 m cube have been examined to show where on the cube surfaces there is evidence of fluctuating static pressure contributing to wind load.

5 CONCLUDING REMARKS

The analysis described above has been developed from measurements of turbulence including static pressure in the ABL. These measurements have shown that turbulent flows consisting of eddies have significant low-pressure centres with a negative mean static pressure which relate to dynamic pressure turbulence intensity. In turbulent boundary layers, the location of reference pressure affects pressure coefficients in wind load experiments.

ACKNOWLEDGEMENTS

The measurements in 2000 were part of the Science Programme conducted at Silsoe Research Institute, and funded by the BBSRC. The measurements in 2015/16 followed full-scale measurements made on the Silsoe site as part of the EPSRC funded Refresh Programme (Ref EP/K031893/1), and formed part of the contribution to the Programme by the University of Birmingham.

DATA AVAILABILITY STATEMENT

The data that support the findings of this study are available from the corresponding author (roger@hoxey.com) upon reasonable request.

REFERENCES

Albertson JD, Katual GG, Pariange MB, Eichinger WE (1998) Spectral scaling of static pressure fluctuations in the atmospheric surface layer: The interaction between large and small scales. Physics of Fluids, Vol **10,** No 7, July 1998.

Hoxey RP, Richards PJ, Quinn AD, Robertson AP, Gough H (2021) Measurements of the Static Pressure near the surface in the Atmospheric Boundary Layer J. Wind Eng. Ind. Aerodyn. Vol **209**, (2021), 104487.

Lim HC, Castro IP, Hoxey RP (2007) Bluff bodies in deep turbulent boundary layers: Reynolds-number issues. J. Fluid Mech, **571**, 97-118.

Moran P, Hoxey RP (1979) A probe for sensing static pressure in two-dimensional flow. J. Phys. E: Sci. Instrum., **12**, 752-3.

Richards PJ, Hoxey RP, Short JL. (2000) Spectral models for the neutral atmospheric surface layer, J. Wind Eng. Ind. Aerodyn. **87**, 167-185.

Richards PJ, Hoxey RP, Short JL (2001) Wind pressures on a 6 m Cube, J. Wind Eng. Ind. Aerodyn., **89** (14-15), 1553-1560.

Richards PJ, Hoxey RP (2012) Pressures on a cubic building—Part 1: Full-scale results. , J. Wind Eng. Ind. Aerodyn., **102** 72-86.

Tsuji Y, Fransson JHM, Alfredsson PH, Johansson AV (2007) Pressure statistics and their scaling in high-Reynolds-number turbulent boundary layers. J. Fluid Mech. (2007), **585**, 1-40.

DOI 10.5258/WES/P0006

Atmospheric turbulence as seen by a moving object

Peter John Richards[1*], Nicholas Kay[1] and Stuart Norris[1]
[1]Department of Mechanical and Mechatronic Engineering, University of Auckland, Auckland, NZ
[*] pj.richards@auckland.ac.nz

1 INTRODUCTION

Research at the University of Auckland has for many years included both wind tunnel and CFD studies of yacht sails, for example the recent study by Matich et al. [1] into unsteady loads on the sails of a TP52 yacht, Fig. 1(a). In recent years, research has also included the effects of turbulent winds on both multi-rotor drones and small fixed-wing Unmanned Aerial Vehicles (UAVs) such as Kahu, Fig. 1(b). Small fixed-wing UAVs tend to operate at low altitudes, under 500 m, and at low speeds, under 25 m/s. Hence, these craft are subjected to higher turbulence intensities than conventional aircraft and operate at lower Reynolds numbers, and so are more susceptible to stalling. With either wind tunnel or CFD modelling of unsteady loads on such craft, it is important to correctly model the turbulence as seen by the moving object. As a result, several important questions arise which will be addressed in subsequent sections.

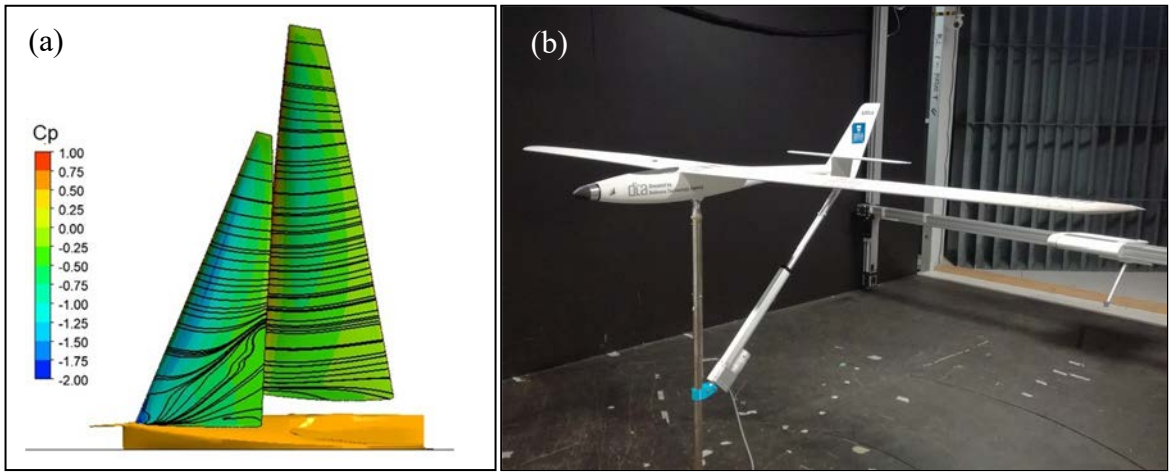

Fig. 1 (a) CFD modelling of a TP52 yacht and (b) Wind tunnel testing of Kahu fixed-wing UAV

2 WHICH COMPONENT OF TURBULENCE IS MOST IMPORTANT?

In many turbulence modelling situations, the default approach is to primarily consider the longitudinal turbulence intensity. However, with lifting surfaces this may not be the most important component. Consider a fixed wing UAV flying with a tail wind as depicted in Fig. 2(a). The turbulent fluctuations of the wind will be primarily determined by the mean windspeed and ground roughness, together with the altitude of flight. However, the UAV's airspeed, V_{Rel} relative to the air around it, will only depend on its trim and the power delivered by the propulsion system. The mean windspeed will not affect the airspeed but will change the ground speed, V_{UAV}. If it is initially assumed that the aircraft motion in response to unsteady loads is small, then relevant fluctuating velocities u',v',w' are those from the wind.

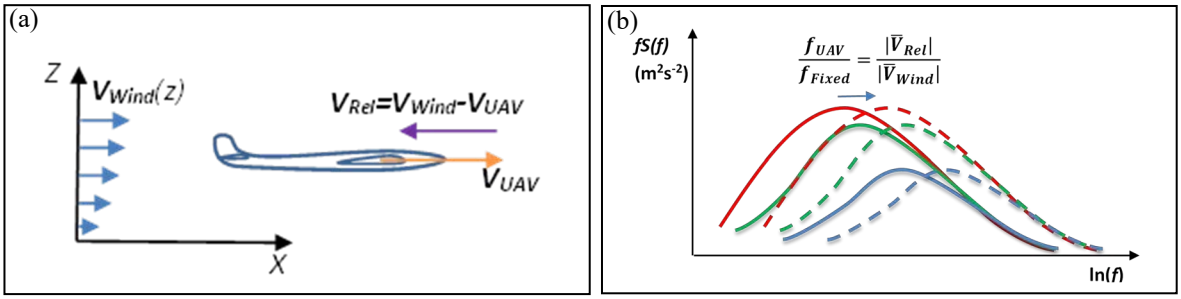

Fig. 2(a) Velocity vectors relevant to a fixed-wing UAV, and (b) Expected effect on turbulent spectra.

DOI 10.5258/WES/P0007

Quasi-steady analysis of the unsteady loads on the UAV, assuming that the turbulence intensities are small and using small angle approximations, results in Eqs. 1 & 2 for the vertical (F'_z) and horizontal (F'_x) fluctuating forces.

$$F'_z = mg\left\{\frac{1}{C_L(\bar{\alpha})}\frac{dC_L}{d\alpha}\frac{w'}{|\bar{V}_{Rel}|} - 2\frac{u'}{|\bar{V}_{Rel}|}\right\} \approx mg\left\{10\frac{w'}{|\bar{V}_{Rel}|} - 2\frac{u'}{|\bar{V}_{Rel}|}\right\} \quad (1)$$

$$F'_x = mg\left\{\left(1 - 2k\frac{dC_L}{d\alpha}\right)\frac{w'}{|\bar{V}_{Rel}|} + 2C_D(\bar{\alpha})\frac{u'}{|\bar{V}_{Rel}|}\right\} \approx mg\left\{0.68\frac{w'}{|\bar{V}_{Rel}|} + 0.056\frac{u'}{|\bar{V}_{Rel}|}\right\} \quad (2)$$

To get an idea of the relative magnitudes, the numerical values given are for Kahu under cruise conditions where $C_L \approx 0.5$, $dC_L/d\alpha \approx 5$, $C_D = C_{D0} + kC_L^2$ with $C_{D0} \approx 0.02$ and $k \approx 0.032$. This suggests the greatest sensitivity is the vertical force responding to vertical turbulence. Even taking into consideration that near the ground the standard deviation of vertical turbulence might only be half that along wind, the vertical fluctuations would still contribute about 86% of the variance of vertical force. Perhaps more surprising is Eq. 2, which shows that the fluctuating horizontal force, while an order of magnitude smaller, is still dominated by vertical wind fluctuations. The conclusion from this analysis is that with lift generating structures it is more important to correctly model turbulence affecting the angle of attack than the along-wind.

3 HOW DOES MOVEMENT AFFECT TURBULENCE INTENSITIES AND SPECTRA?

If Eqs. 1 & 2 are manipulated to give the variances of the forces then these will be essentially functions of the turbulence intensities, such as $I_{w,UAV} = \sigma_w/|\bar{V}_{Rel}|$, when expressed in terms of the airspeed rather than the windspeed. Even with relatively low-speed fixed-wing UAVs the relative airspeed is normally higher than the windspeed: operations cease if the wind gets too high. Thus, the relevant turbulence intensity is lower than for a stationary anemometer. Nevertheless, these turbulence intensities become relatively high during take-off and landing since both the airspeed is lower and the UAV will be near the ground, where the turbulent fluctuations are usually higher.

As depicted in Fig. 2(b), it is suggested that the movement of the UAV does not alter the variances of the velocity fluctuations and so the area under the $fS(f)$ curves remain the same, however the frequencies are all increased by the ratio of the airspeed to the windspeed. A simple analogy for this is to consider a car driving along a bumpy road. The size of the bumps, there distributions both in size and position are unaffected by the car's speed, but the frequency of the vibrations will certainly increase the faster it goes.

In order to support this concept, Fig. 3 shows data from DNS modelling of flow between flat plates. The DNS data was calculated for the standard channel flow problem at a $Re_\tau = 3.95$. A finite volume solver was used within a domain periodic in the streamwise and spanwise direction, having dimensions 6.4 x 2 x 3.2. The problem is non-dimensional both in time and space. The conditions considered are a comparison between a stationary observer and others moving either at the centreplane flow speed ('Full'), or half that ('Half'), either 'With' or 'Against' the flow. Fig. 3(a) shows that as long as there is a significant relative velocity between the observer and the flow the variances of all three turbulent components hardly change. The exception is moving with the flow at the flow speed, which is impossible for a fixed-wing UAV but might be possible for a multi-rotor drone, where the U variance is lower. Fig. 3(b) shows that as expected most of the W spectra, perpendicular to the plates, have similar shape and area but shift in frequency in proportion to the relative airspeed. This is particularly clear on the high frequency end of the spectra where these cut the $fS(f) = 0.05$ line at non-dimensional frequencies of 6, 35, 67, 100 and 135 for relative speeds 0, 0.5, 1, 1.5 and 2 times the centreplane flow speed. Other spectra showed similar patterns.

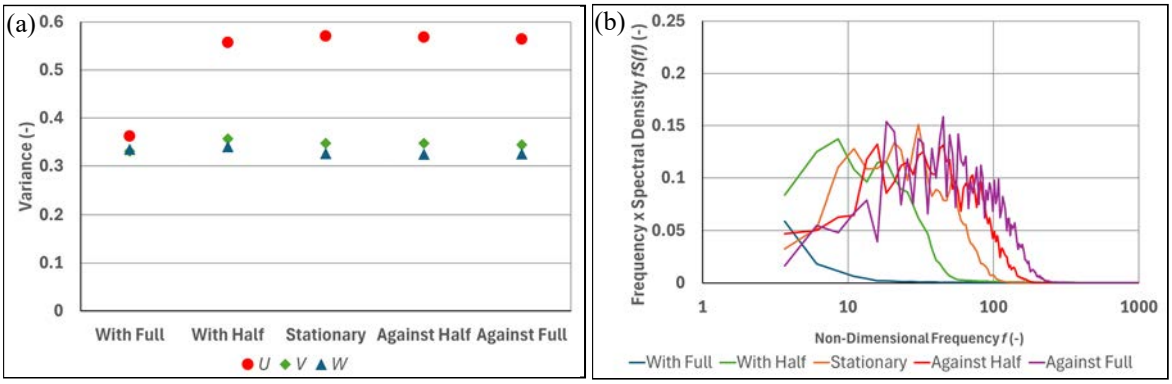

Fig. 3(a) DNS variances for a moving observer, and (b) The corresponding W spectra.

DOI 10.5258/WES/P0007

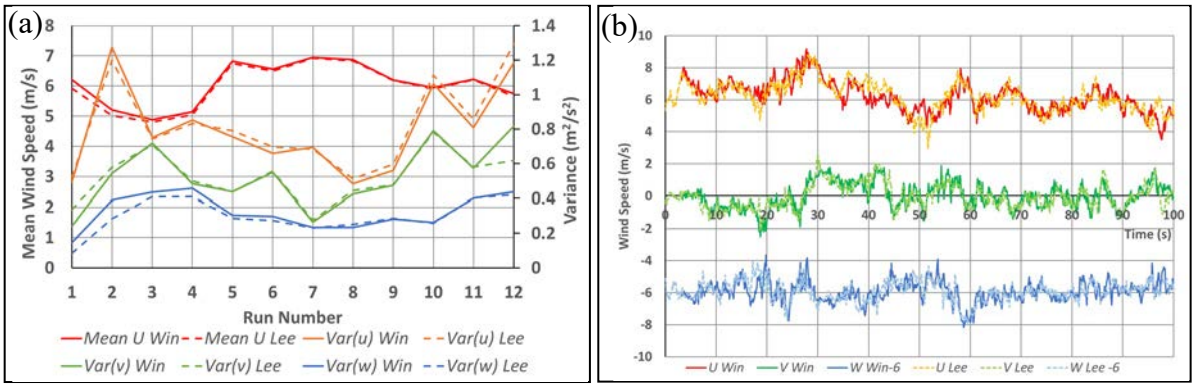

Fig. 4 (a) Mean windspeed and variances for 12 runs, (b) Time series for a separation of 20 m (Run 11), with the windward series delayed 3.2 s

4 HOW REALISTIC IS TAYLOR'S FROZEN TURBULENCE HYPOTHESIS?

One of the simplest approaches to understanding the effects of movement is to assume that Taylor's Frozen Turbulence Hypothesis applies, that is, turbulent eddies are carried past a point with a convective velocity in an essentially frozen state. In reality, the turbulent patterns are constantly changing, both through vortex stretching and the movement of eddies by other eddies, as well as by the mean wind.

To investigate how quickly turbulent patterns change, two Young 8100 ultrasonic anemometers were mounted on 6.5 m high masts and positioned on a flat coastal location in line with the mean wind. Two 300 s records were recorded at 10 samples per second for 6 separation distances of 1, 2, 3, 5, 10 and 20 m. Fig. 4(a) shows the mean wind speed and the three variance recorded at the windward and leeward mast. While there were changes in the conditions over the twelve records, it is clear that on each occasion the two anemometers detected similar conditions. Fig. 4(b) shows the first 100 s of three time series (with the *W* series displaced -6 m/s for clarity) for run 11, with the anemometers 20 m apart. The time series of the windward anemometer is delayed 3.2 s since this gave the highest correlation for all 3 series. It is clear that all the pairs of series are closely related, particularly for fluctuations lasting several seconds, but there are also noticeable changes, most obvious for short duration fluctuations.

Correlation analysis for time delay of all runs showed almost identical delays for each of the three components and these were generally close to that expected, $\tau=\Delta x/\bar{U}$, as shown in Fig. 5(a). Fig. 5(b) shows the peak correlation coefficient as a function of separation distance. As might be expected these are near unity for short separations and decrease steadily with increased distance. It may be noted that the vertical correlations decrease at a higher rate than the other two components. This is probably due to the lower levels of low frequency contribution in the vertical spectra, as seen in Fig. 6(a).

Although there are significant changes in the high frequency variations in the time series, Fig. 6(a) shows that even with a 20 m separation the upwind and downwind spectra are very similar across the whole frequency range. This suggests that while the details of the turbulence are evolving the statistical characteristics remain unchanged. Fig. 6(b) shows the coherence of the *U* time series for frquencies <0.5 Hz. Insufficent data was collected for accurate analysis but this shows a clear pattern of decreasing coherance both with frequency and separation. Similar patterns were observed with the other components.

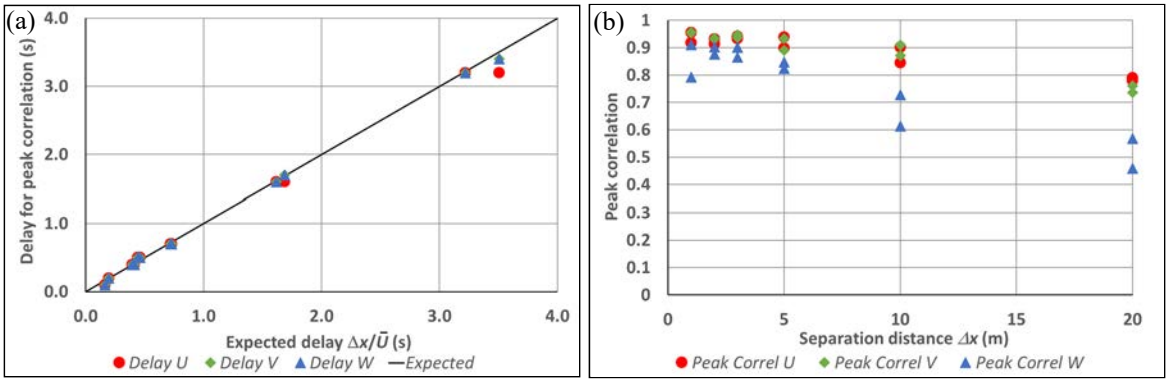

Fig. 5(a)Time delay for peak correlation and (b) peak correlation coefficient

DOI 10.5258/WES/P0007

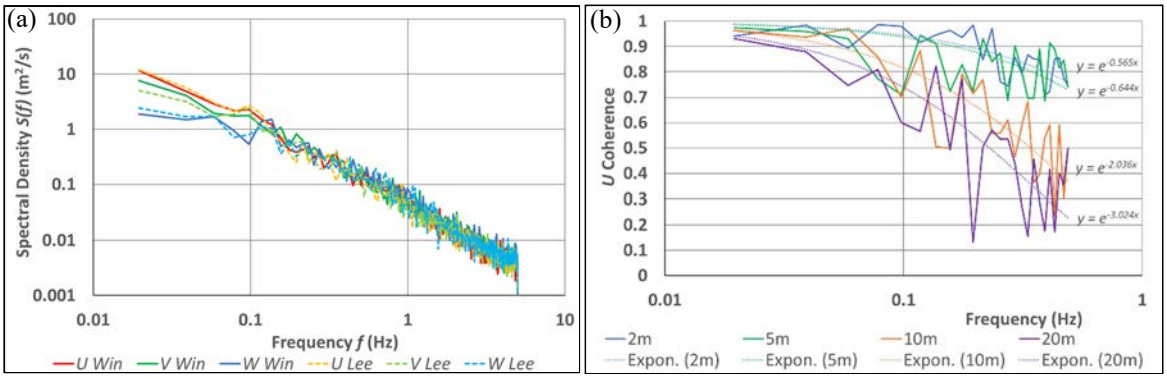

Fig. 6(a) Spectral density comparisons with Δx=20 m. (b) U coherence for selected Δx and f<0.5 Hz.

5. HOW DOES THE CRAFT'S DYNAMIC RESPONSE CHANGE THE SITUATION?

The discussion so far has assumed the craft does not respond to the fluctuating loads, but of course it will. A simple passive 1D model for a UAV responding to vertical wind fluctuations of the form $w'/|V_{Rel}|=A_{Wind}\sin(\omega t)$ shows that the craft will move vertically in response to the wind such that the angle of attack amplitude seen by the wing, A_{UAV}, is given by

$$\frac{|A_{UAV}|}{|A_{Wind}|}=\frac{\omega/\omega_0}{\sqrt{1+(\omega/\omega_0)^2}} \qquad \text{with} \quad \omega_0=\frac{g\frac{dC_L}{d\alpha}}{C_L(\bar{\alpha})\bar{V}_{Rel}} \tag{3}$$

For Kahu at cruise speed $\omega_0\approx5.4$ rad/s. Fluctuations lasting much longer than 1 s are responded to by the UAV moving, which results in a reduced angle of attack amplitude. Therefore, when modelling in the wind tunnel the wind spectrum needs to be reduced by a high pass filter of this form.

6. IS THE DIRECTION OF MOVEMENT RELATIVE TO THE WIND IMPORTANT?

With a yacht sailing upwind, the wing is almost vertical and so it is fluctuations in wind direction which change the angle of attack. Flay and Jackson [2] argue that if direction fluctuations are sufficiently slow the crew will respond and act as a high-pass filter, similar to the UAV passive response. Matich et al. [1] recently modelled a TP52 yacht sailing with the true wind direction varying with a 10s period. In this case the yacht movement and wind are not in the same direction, see Fig. 7(a), but the observed period of the force variations was under 7s, roughly in proportion to the ratio of apparent (relative) to true wind speed.

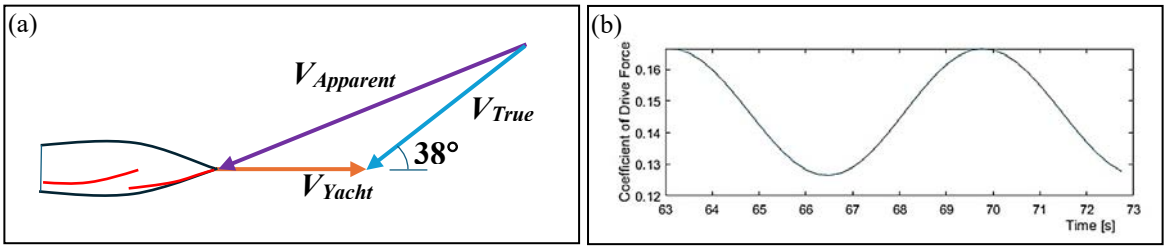

Fig. 7(a) Wind vectors for a yacht. (b) Drive force when the true wind direction varies, period =10s.

7. CONCLUSIONS

When modelling turbulent winds impacting a moving object which has lifting surfaces, it is most important to correctly model the velocity component which alters the angle of attack. Initially it may be assumed that the movement does not change the standard deviation of wind fluctuations but the turbulence intensity should be reduced in proportion to the ratio of airspeed to windspeed, and the frequencies of the spectra increased by this ratio. The dynamic response of the craft may result in high-pass filtering of the turbulence. The direction of movement of the craft relative to the wind is not thought to be significant.

REFERENCES

[1] Matich L. M., Richards P. J. & Norris S. (2024). "Unsteady Upwind Aerodynamics of a Sailing Yacht", *8th High Performance Yacht Design Conference*, Auckland, NZ, 21-22 March.

[2] Flay, R.G.J., Jackson P.S., (1992). "Flow simulation for wind-tunnel studies of sail Aerodynamics", *Journal of Wind Eng. and Ind. Aerodyn.*, Vol. 41-44, 2703-2714.

DOI 10.5258/WES/P0007

Future winds: a review of the likely impacts of anthropogenic climate change on wind engineering in the UK

Anna Bagnara[1], Daniel Hackett[2], David Hankin[1*], Stefano Cammelli[3]
[1]NOVA Fluid Mechanics Ltd, Teddington, UK
[2]RWDI, Milton Keynes, UK
[3]WSP UK, London, UK
[*] E-mail: david@novafluidmechanics.com

1 INTRODUCTION

At the time of writing, hurricane Beryl is raging towards Texas, having ripped through the Caribbean. Beryl is the earliest forming 'Category 5' Atlantic hurricane on record. A single data point is not statistics, but it is clear beyond reasonable doubt – at least to the authors of this technical paper – that our climate is changing, and that these changes will continue into the foreseeable future.

In the field of wind engineering – as in many other disciplines – there is an urgent need to understand the expected changes to our climate and to incorporate such understanding into our assessments. However, while there is broad agreement on the general trend in temperature, for example, the picture for how the wind will change is less clear. A range of local and global factors combine differently depending on the region, resulting in either increases or decreases in mean wind speeds, and more frequent extreme events such as hurricanes, typhoons, tornadoes, and thunderstorms.

Current wind engineering practice (for the purpose of establishing design wind loads, or for predicting the potential impacts on pedestrian comfort and safety, for example) is based on statistical analyses of past weather events. While these methods are well-established, they are implicitly based on an assumption that past climate trends will remain applicable into the future, at least for the operational life of the buildings currently being designed. Considering the predictions that have been made about the impacts of anthropogenic climate change, especially in relation to the magnitude and frequency of extreme weather events, we should accept the possibility that methodologies based solely on the past climate may no longer be valid.

The purpose of this technical paper is to provide a synopsis on the historic and future trends of wind and storm events using scientific articles and grey literature (including projections by the Met Office, the Intergovernmental Panel on Climate Change (IPCC) and others), with respect to their potential impact on wind in the built environment. It goes on to discuss how traditional wind engineering assessments may be affected by climate change, and the potential risks of an inadequate assessment in this regard. Finally, recommendations are made for ways in which these assessments could be adapted to account for the predicted change in the climate of the UK.

The findings of this review will form the basis for a new position paper by the UK Wind Engineering Society (www.windengineering.org.uk). The purpose of the position paper will be to offer relatable, practical guidance in relation to the status of climate change modelling in the UK and the ways in which it could be incorporated into wind engineering assessments.

2 CURRENT UNDERSTANDING

The latest IPCC report from Working Group I [6] on the "The Physical Science Basis" provides an overview of the current understanding with regards to the projected changes to global and regional winds as a consequence of climate change. With respect to mean wind speeds, it is noted that "*…since the 1970s a worldwide weakening of surface wind has likely occurred over land…*", which is also echoed for the regional climate in Europe where "*mean surface wind speeds have decreased…over the past four decades…*". Furthermore, it is projected that "*wind stagnation events may become more frequent…in some areas of Europe…[with] potential consequences for air quality.*" However, there is "*…limited evidence that climate model historical trends are consistent with observed trends*", which is attributed to urbanisation and broader changes in the aerodynamic surface roughness, "*as well as natural variability*".

At the other end of the spectrum, whilst it is noted that "*quantifying the effect of climate change on extreme storms is challenging…*" due to a number of factors including the "*high degree of random variability*"

DOI 10.5258/WES/P0009

and "*constraints in the models' ability to accurately represent the small-scale physical processes…*", the projections indicate that "*…average peak [tropical cyclone (TC)] wind speeds and the proportion of Category 4-5 TCs will very likely increase globally*", albeit that "*…the global frequency of TCs over all categories will decrease or remain unchanged.*" Similarly, there is "*medium confidence that changes in the [wind speeds] of [extra tropical cyclones] will be small, although changes in the location of storm tracks can lead to substantial changes in local extreme wind speeds…*". Finally, it is noted that "*climate models consistently project environmental changes that would support an increase in the frequency and intensity of severe thunderstorms,…but there is low confidence in the details of the projected increase.*"

In terms of Northern Europe specifically (which includes the British Isles), the report concludes that there is a "*…medium confidence of [decreasing mean wind speeds]…*" and a "*…slightly increased frequency and amplitude of extratropical cyclones, strong winds and extratropical storms is projected…by the middle of the century and beyond and for global warming levels of 2°C or higher*". In particular, an increased density of extratropical storm tracks over the UK is projected, albeit with low agreement between models in general.

The UKCP18 [4] projections over land for wind speeds in the UK indicate that "*there are no compelling trends in storminess…over the last four decades.*" Furthermore, whilst "*an increase in near surface wind speeds over the UK for the second half of the 21st century for the winter season…accompanied by an increase in frequency of winter storms over the UK*" is projected, "*…the increase in wind speeds is modest compared to interannual variability*". Furthermore, in their own summary of the current understanding of the UK climate, the Met Office [8] indicate that there will be "*more winter storms, including disproportionately more severe storms*", but that "*summer cyclones will become less frequent*" and that "*smaller scale convective summer storm activity is also projected to increase over the UK in the future*". Acknowledging the projected increase in the strength of tropical cyclones, it is noted that there is the potential for these to "*…retain more strength as they move into subtropical and temperate areas, such as the UK, and have a greater effect here than they do currently.*"

In their review of the future projections for North Atlantic and European Extratropical Cyclones, Zappa & Shaffrey [12] conclude that whilst "*…the total number of North Atlantic cyclones and those of strong wind intensity tend to decrease in response to climate change*", there is an "*…increase in the track density of strong cyclones between the British Isles and Scandinavia*" during the winter months. Furthermore, it is noted that "*weakening of the [Atlantic Meridional Overturning Circulation (AMOC)], might strengthen the storm-track activity over the eastern Atlantic by enhancing the surface atmospheric baroclinicity*", although it is noted that further research on the impact is required. Rahmstorf [10] recently argued that "*…risk of critical AMOC transition is real and very serious, even if we cannot confidently predict when and whether this will happen*". Moreover, there is a "*…much larger risk than previously thought*", in part because the "*…AMOC is generally too stable in climate models*": if the AMOC is "*...too unstable [it will collapse] for the present climate...[and] the model will be "repaired"…[but if] too stable...the present-day climate is correctly reproduced.*" However, Priestley et al. [9] note that "*with a changing climate, it is expected that positive [North Atlantic Oscillation (NAO)] states will become more common…*", which could also lead to "*…more cyclones with higher intensities than neutral or negative phases*", despite "*a positive phase of the NAO strengthen[ing] the AMOC…*" as indicated by Delworth & Zeng [3].

With respect to thunderstorms, whilst Brooks [1] notes that modelling suggests climate change will "*…lead to more frequent environments favorable for severe thunderstorms*", it is concluded that "*…how severe thunderstorms will change in the future is still an open [question].*" Haberlie et al. [5] demonstrate that the regional response (based on a study of the Conterminous United States) of thunderstorms to climate change is complex with "*…an overall increase in convective instability but spatially varying changes in convective inhibition*" meaning that "*regional and seasonal variability is noted in the response of thunderstorm activity…[to] two climate change scenarios.*" However, Brooks [1] notes that "*…it is unclear how well the lessons learned [in the United States] apply to the rest of the world.*"

In more general terms, based on Weibull distributions derived from UKCP09 projections of future mean wind speeds, Manis & Bloodworth [7] indicate a "*…decrease in the future in the probability of wind speeds up to 15 m/s and an increase in the probability of speeds higher than 15 m/s, indicating climate change causing an increase in magnitude and frequency of future extreme storm events.*"

In summary, whilst there is a significant degree of uncertainty about future projections for wind speeds across the UK, the general consensus is that mean wind speeds are expected to decrease and extreme wind

DOI 10.5258/WES/P0009

speeds (both from extra tropical cyclones and thunderstorms) are expected to increase both in frequency and intensity.

3 IMPLICATIONS FOR WIND LOADING

There is a general consensus that the frequency and intensity of extreme wind events in the UK will increase. Consequently, current design wind speeds, which are typically derived from assessments of historical wind records from suitably sited anemometers, may result in reduced resilience of structures subjected to future wind loads. Whilst an increase in design wind speeds could in principle be used to account for future climatic trends, this would require careful consideration as – by leading to designs with a greater carbon footprint due to the requirement for strengthening of the structure – this choice has the potential to accelerate anthropogenic climate change.

Whilst the impact of an increase in synoptic winds on structural design is generally well understood, thunderstorms are very localised and short-duration phenomena, incompatible with the grid size of standard climate models, and cannot be accurately captured by the standard anemometers located at airports that are generally used to determine design wind speeds. Brooks [1] states "*…severe thunderstorm events are typically "target of opportunity" observations. They require the presence of an observer and a system to collect the observations.*" Wind speeds associated with thunderstorm events have the potential to be comparable in magnitude or higher than those generated by strong synoptic events, leading to the documented collapse of many structures around the world, especially low-rise structures (e.g. power grid failure due to pylon collapse). Conversely, tall structures in mixed or thunderstorm dominated climates are likely to be over-designed [11] as codes of practice are based on logarithmic wind profiles that overestimate the wind actions arising from a thunderstorm downburst, which is characterised by a maximum velocity close to the ground. Ongoing research on the effect of thunderstorm downbursts on civil structures aims to enable future codification of these events in order to facilitate safe design. However, the absence of reliable full scale measurements inhibit the assessment of the impact of climate change on these phenomena.

4 IMPLICATIONS FOR WIND MICROCLIMATE

Wind microclimate encompasses two related elements: wind comfort (associated with the typical day-to-day wind conditions that dictate how suitable the wind environment would be for its intended use) and wind safety (associated with infrequent strong winds that might push someone off balance, potentially resulting in injury). With regard to wind comfort, it is expected that current assessment methods will remain valid given that mean wind speeds in the UK are projected to remain broadly unchanged, with potential for a slight reduction in strength. Conversely, the assessment of wind safety will be affected by the projected increase in frequency and severity of winter storms, and thus warrants further consideration as to how this can be accommodated within a robust wind microclimate analysis.

Currently, wind microclimate assessments utilise the probability of occurrence of a given wind speed from a given direction based on their frequency of occurrence in a historical data set. In principle, whilst it is feasible to incorporate the projected increase in strong wind events within these statistics, in practice the choice of climate scenario and associated uncertainties make this difficult, with the potential to be overly conservative in ways that may be detrimental to building design in other respects. Alternatively, the wind safety criteria could be re-examined to determine if there is already sufficient conservatism or otherwise adjust the threshold to account for the projected increase in strong winds. In either case, a more detailed investigation of the wider implications is necessary.

Finally, whilst mean wind speeds are not expected to change significantly, the importance of wind as a component of outdoor thermal comfort (the combination of wind, sunlight, temperature and humidity) becomes increasingly relevant as climate projections point towards increasing temperatures (especially during summer) and increased risk of dangerous heat stress. Maintaining or introducing air flow into an area can be beneficial in offsetting the effects of increasing temperature, and will increasingly need to be considered during the design of new buildings in the UK. Through the adoption of thermal comfort guidelines, such as those of the City of London [2] or similar, and accounting for the projected increase in temperatures, our urban environments might be made more resilient to the changing climate.

DOI 10.5258/WES/P0009

5 CONCLUSIONS

Our climate is changing and we need to change our approach to wind engineering to adapt to, and mitigate, the impacts of that change. However, a significant amount of uncertainty persists in future projections of wind speeds, and among the many questions that need answering, some key topics include:

1) Projections for changes to future winds in the UK are generally modest, although significant uncertainty persists and there are a number of tipping points (e.g. collapse of the AMOC) that could fundamentally alter our climate in ways that have not yet been studied in detail.
2) Whilst there is an encouraging body of ongoing research into thunderstorms, there is an urgent need to codify the results so that they can be applied in design. Furthermore, current climate models are unable to fully resolve thunderstorms, meaning there is significant uncertainty in how these events will evolve as a consequence of climate change.
3) Methodologies for the assessment of new buildings that account for the projected changes to wind conditions need to be developed, ensuring that they are adaptable to changes in the projections, and in such a way as to avoid making the problem worse (e.g. 'over-engineered' solutions with impacts that are more detrimental than those that they mitigate).

Evidently, there is a clear and pressing need for the wind engineering community to be more proactive, both in terms of increasing the resilience of our assessments to account for future winds and, in synergy with the wider design team and all interested parties, being more aware of the impact of those assessments on the global climate.

REFERENCES

[1] Brooks H. E. (2013) "Severe thunderstorms and climate change", *Atmospheric Research*, **123**, 129-138. doi:10.1016/j.atmosres.2012.04.002.

[2] City of London Corporation (2020). "Thermal Comfort Guidelines for Developments in the City of London", London, UK.

[3] Delworth T. L. & Zeng F. (2016). "The Impact of the North Atlantic Oscillation on Climate through Its Influence on the Atlantic Meridional Overturning Circulation", *Journal of Climate*, **29**, 941-962. doi:10.1175/JCLI-D-15-0396.1.

[4] Fung F., Bett P., Maisey P., Lowe J., McSweeney C., Mitchell J. F. B., Murphy J., Rostron J., Sexton D. & Yamazaki K. (2019). "UKCP18 Factsheet: Wind", Met Office Hadley Centre, Exeter, UK.

[5] Haberlie A. M., Ashley W. S., Battisto C. M., & Gensini V. A. (2022). "Thunderstorm activity under intermediate and extreme climate change scenarios", *Geophysical Research Letters*, **49**, e2022GL098779. doi:10.1029/2022GL098779.

[6] Intergovernmental Panel on Climate Change (2021). "Climate Change 2021: The Physical Science Basis. Contribution of Working Group I to the Sixth Assessment Report of the Intergovernmental Panel on Climate Change", Cambridge University Press, Cambridge, United Kingdom. doi:10.1017/9781009157896.

[7] Manis P. & Bloodworth A. G. (2017). "Climate change and extreme wind effects on transmission towers", *Proceedings of the Institution of Civil Engineers - Structures and Buildings*, **170**, 81-97. doi:10.1680/jstbu.16.00013.

[8] Met Office (2021). "Recent trends and future projections of UK storm activity". Available at: https://www.metoffice.gov.uk/research/news/2021/recent-trends-and-future-projections-of-uk-storm-activity (Accessed 25th July 2024).

[9] Priestley M. D. K., Stephenson D. B., Scaife A. A., Bannister D., Allen C. J. T. & Wilkie D. (2023). "Return levels of extreme European windstorms, their dependency on the North Atlantic Oscillation, and potential future risks", *Nat. Hazards Earth Syst. Sci.*, **23**, 3845–3861. doi:10.5194/nhess-23-3845-2023.

[10] Rahmstorf S. (2024). "Is the Atlantic overturning circulation approaching a tipping point?", *Oceanography*. doi:10.5670/oceanog.2024.501.

[11] Solari G., Burlando M. & Repetto M.P. (2020). "Detection, simulation, modelling and loading of thunderstorm outfows to design wind-safer and cost-efficient structures", *Journal of Wind Engineering & Industrial Aerodynamics*, **200**, 104142. doi: 10.1016/j.jweia.2020.104142.

[12] Zappa G. & Shaffrey L.C. (2013). "A Multimodel Assessment of Future Projections of North Atlantic and European Extratropical Cyclones in the CMIP5 Climate Models", *J. Climate*, **26**, 5846-5862. doi: 10.1175/JCLI-D-12-00573.1.

DOI 10.5258/WES/P0009

Modelling the launch and collision phases of wind-borne debris

David M. Hargreaves[1*] and John S. Owen[1]
[1]Faculty of Engineering, University of Nottingham, NG7 2RD, UK
[*] E-mail: david.hargreaves@nottingham.ac.uk

1 INTRODUCTION

It is well documented that debris impact is an important mechanism of damage during severe wind events [1, 2], often contributing significantly to the total losses sustained by the building stock. The investigation of the flight of wind-borne debris (WBD) can be traced back to the work of Tachikawa [3]. Indeed, the Tachikawa number (the ratio of aerodynamic and gravitational forces) is now used to characterise WDB flight [4]. As the study of WDB has developed over the years since, the conditions under which the various types of WDB would become airborne were studied [5], 2D analytical Lagrangian models 3DOF were developed [6], followed by the 3D, 6DOF models, which eventually were incorporated into CFD models [7]. Many of these studies have focussed on debris flight in steady, uniform wind fields, unconstrained by buildings, for example, with corresponding lack of turbulence or intermittency of flow. Experimentally, such work exists [8], but the inclusion of a launch building is something that has not, as yet, been modelled computationally, although Moghim and Caracoglia [9] did look at impact locations close to a tall building.

This paper is a proof-of-concept for the inclusion of the launch scenario in CFD models. One of the reasons this as not been possible until recently is that dynamic meshing techniques that were utilised by Kakimpa et al [7], made it difficult to model the debris close to the building envelope – cells would collapse as the gap became small. Advances in CFD technology, notably Chimera (or overset) meshes, now mean this limitation is no longer an issue. This paper details the modelling approach in 2D, laying the groundwork for the shift to 3D.

2 METHODOLOGY

2.1 Domain and Mesh

A domain, 40 m long and 20 m high was created in the xy-plane using DesignModeler. For the base case, a duo-pitch building of length 5 m, wall height 4 m and a roof angle 30^{o} was created with walls of thickness 0.15 m. On the leeward side, an opening to mimic a failed window was created and on the leeward roof, an opening was created to accommodate the debris. To use the Fluent terminology, this domain was meshed to create the *background* mesh using triangular elements and quadrilateral element in the mesh boundary layers.

The plate debris has a separate domain and mesh, called the *overset* or *component* mesh. This again was built in DesignModeler, with a 0.2 m by 0.02 m plate surrounded by a 1 m by 1 m square domain. The debris was offset and rotated so that it would fit exactly in the roof gap in the background mesh. The initial background and overset meshes can be seen in Figure 1(a). A small gap either side of the plate was necessary to avoid meshing problems. In future work, this gap in the roof will be modelled as a porous region in the background mesh.

2.2 Governing Equations

ANSYS Fluent, version R2024r1 was used throughout. The 2D form of the Navier-Stokes equations were used with the Realisable $k-\varepsilon$ turbulence model with standard wall treatment, which was deemed appropriate for this proof-of-concept study.

2.3 Material Properties and Boundary Conditions

The fluid properties were the default values for air (dynamic viscosity, μ, is 1.79×10^{-5} Pa s and density is 1.225 kg/m^3). The density of the plate, in the base case, was 165 kg/m^3, which is low for a typical roof tile in the UK but was chosen to illustrate the range of flight modes seen in this paper. The mass and moment of inertia of the plate were set appropriately in the 6DOF solver available in Fluent. To reduce

DOI 10.5258/WES/P0010

the jetting effect from the windward window to the gap in the roof, an inertial resistance factor of 1.0×10^4 m^{-1} was applied in a horizontal band at the base of the roof.

A standard ABL boundary layer was applied at the upwind inlet, using the expression language available in Fluent with the *u* component, turbulent kinetic energy and dissipation rates all being functions of height above the ground. All walls were set to smooth no-slip, apart from the ground which was given a roughness height appropriate to a z_0 of 0.01 m. The reference wind speed was 20 m s^{-1} at 6 m reference height for the base case.

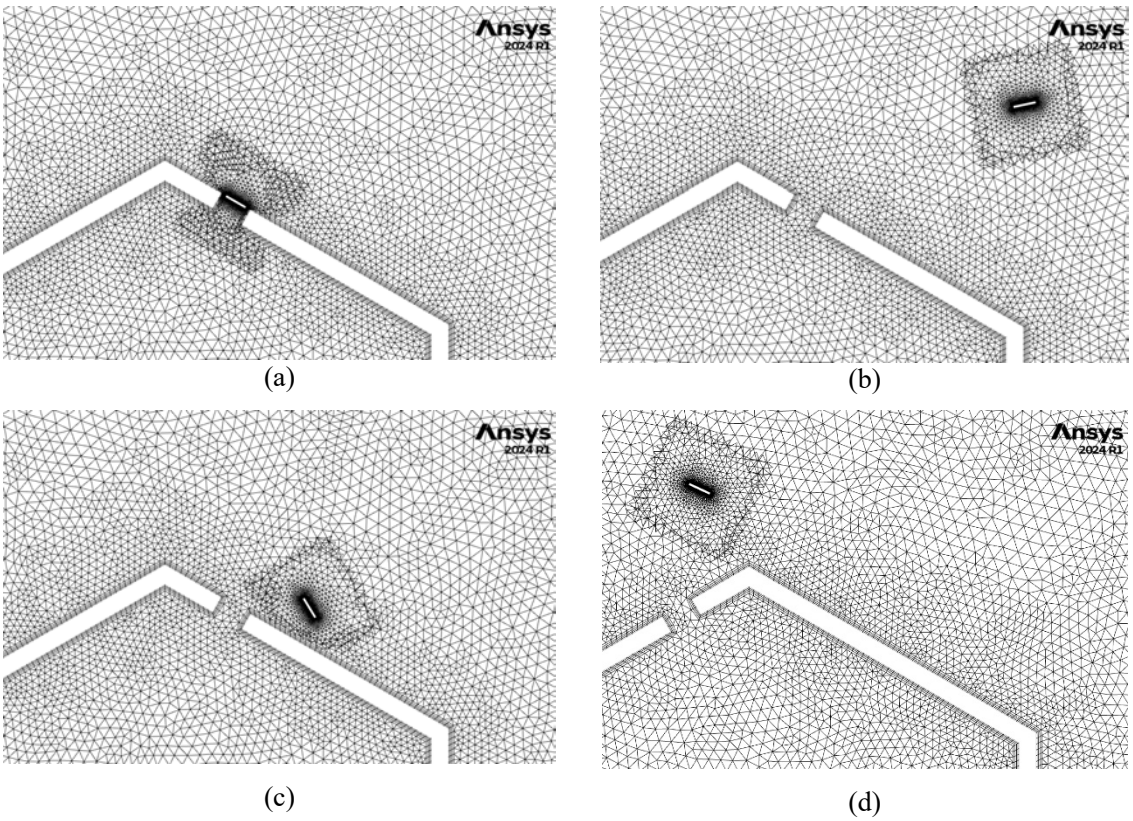

Figure 1: Background and overset meshes: (a) for the base case at release (t=0 s), (b) the base case at t=0.5 s, (c) with an increased internal resistance in the building at t=0.5 s and (d) with a windward face release position at time t=0.15 s.

2.4 Solution

For each case, the flow field for a fixed plate was solved using the transient solver with a time step of 1 ms. Once the lift and drag coefficients on the plate reached stationary values, the simulation was saved. Dynamic meshing was then enabled, and the simulation run on from this release time ($t = 0$ s). A User-Defined Function was written that would terminate the simulation if the plate came withing 1 cm of a wall. In fact, the overset mesh can model the plate going through a wall (and out of the domain) but this was not thought appropriate here. The simulation was saved at this impact point.

3 RESULTS AND DISCUSSION

Rather than attempt to explore the entire parameter space, three scenarios will be addressed, which highlight the breadth of the flight regimes that occur when debris is launched from a building. For context, Figure 2 shows a contour plot of the velocity magnitude from one of the cases prior to launch. Most notable are the flow separation on the windward roof, the larger separation above the leeward roof and the large recirculation zone in the wake of the building, characterised by reverse flow near the ground, travelling back towards the building.

3.1 Wake Flight

The base case set up, with a low internal resistance in the building, causing a positive pressure on the underside of the plate, results in the plate launching into the wake - Figure 1(a) shows the mesh after 0.5 s

DOI 10.5258/WES/P0010

of this flight. As can be seen in Figure 3(a), initially it behaves similarly to a plate in a free stream. However, on entry to the wake, it begins to stall and then is swept back towards the building in the trapped vortex of the wake. Figure 3 also shows the velocity, angular velocity and forces acting on the plate.

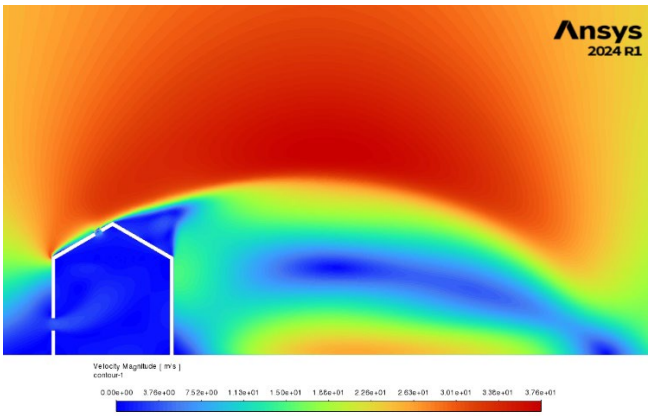

Figure 2: Contours of velocity magnitude in the vicinity of the duo-pitched building. Red corresponds to 37 m/s, with dark blue corresponding to 0.0 m/s.

3.2 Abrupt Flight

With a higher internal resistance in the building, the positive gauge pressure on the underside of the plate is lower and the forces acting on the plate in the early stage of its flight are insufficient for it to reach the high-speed flow above the building and it simply falls under gravity onto the leeward roof – see Figure 1(c).

3.3 Freestream Flight

A plate launched from the windward wall, Figure 1(d), immediately enters the accelerated flow above the ridge of the roof and rapidly flies off into the air. The combination of the rotation of the plate, the vertical component of the wind in this area and the initial launch velocity, causes the plate to rise as it exits the admittedly short domain being modelled here – see Figure 4(a). Figure 4(b), which shows the variation of velocity of the plate and is like that seen in previous work with freestream launches.

4 CONCLUSIONS

From these three simulations and a more comprehensive set of simulations that will be presented at the conference, it is clear that the launch of debris from a building presents a far greater range of flight modes than seen when the debris flies in the free stream. As a result, future work will focus on the move to 3D modelling with LES simulations. However, this brief study opens the possibility of gaining a better understanding of this complex phenomena and to feed into existing and new risk and reliability models.

REFERENCES

1. Grayson, J.M., W.C. Pang, and S. Schiff, *Building envelope failure assessment framework for residential communities subjected to hurricanes.* Engineering Structures, 2013. **51**: p. 245-258.
2. Kareem, A., *Structural Performance and Wind Speed-Damage Correlation in Hurricane Alicia.* Journal of Structural Engineering-Asce, 1985. **111**(12): p. 2596-2610.
3. Tachikawa, M., *Trajectories of Flat Plates in Uniform-Flow with Application to Wind-Generated Missiles.* Journal of Wind Engineering and Industrial Aerodynamics, 1983. **14**(1-3): p. 443-453.
4. Holmes, J.D., C.J. Baker, and Y. Tamura, *Tachikawa number: A proposal.* Journal of Wind Engineering and Industrial Aerodynamics, 2006. **94**(1): p. 41-47.
5. Wills, J.A.B., B.E. Lee, and T.A. Wyatt, *A model of wind-borne debris damage.* Journal of Wind Engineering and Industrial Aerodynamics, 2002. **90**(4): p. 555-565.

DOI 10.5258/WES/P0010

6. Scarabino, A. and P. Giacopinelli, *Analysis of the two dimensional sheet debris flight equations: Initial and final state.* Wind and Structures, An International Journal, 2010. **13**(2): p. 109-125.
7. Kakimpa, B., D.M. Hargreaves, and J.S. Owen, *An investigation of plate-type windborne debris flight using coupled CFD-RBD models. Part I: Model development and validation.* Journal of Wind Engineering and Industrial Aerodynamics, 2012. **111**: p. 95-103.
8. Kordi, B. and G.A. Kopp, *Effects of initial conditions on the flight of windborne plate debris.* Journal of Wind Engineering and Industrial Aerodynamics, 2011. **99**(5): p. 601-614.
9. Moghim, F. and L. Caracoglia, *A numerical model for wind-borne compact debris trajectory estimation: Part 1-Probabilistic analysis of trajectory in the proximity of tall buildings.* Engineering Structures, 2012. **38**: p. 153-162.

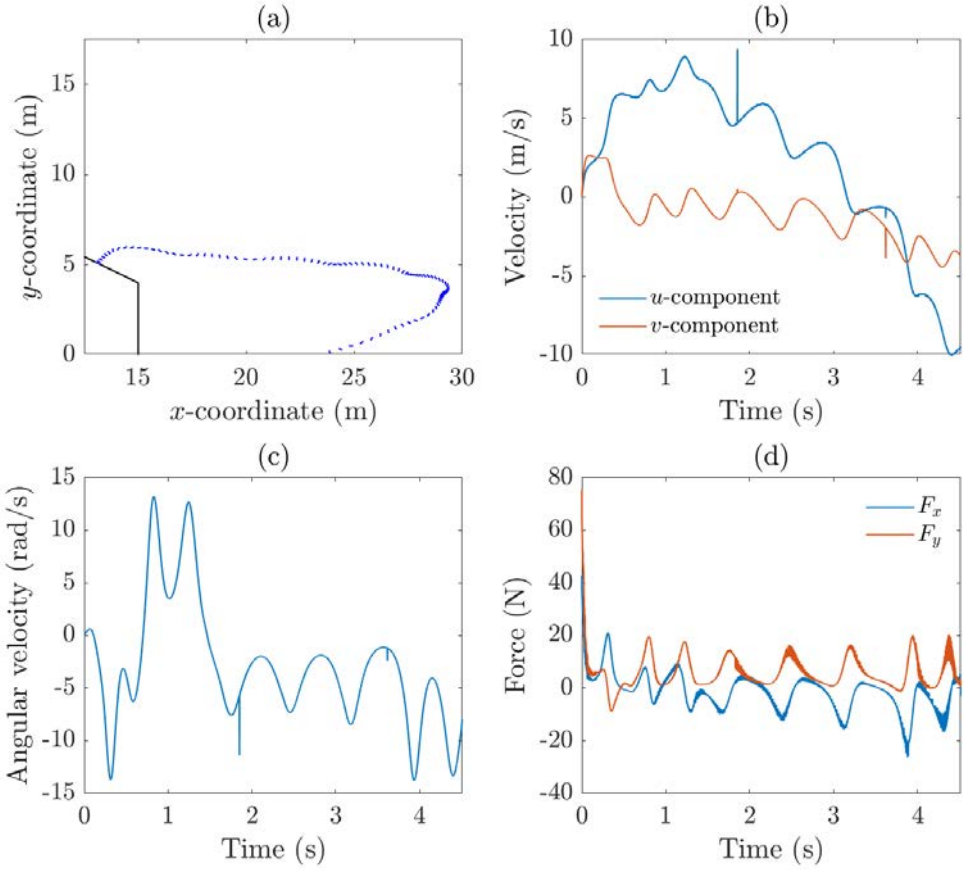

Figure 3: For the base case, (a) flight trajectory and plate inclination, (b) components of velocity, (c) angular velocity and (d) horizontal, F_x, and vertical, F_y, forces acting on the plate.

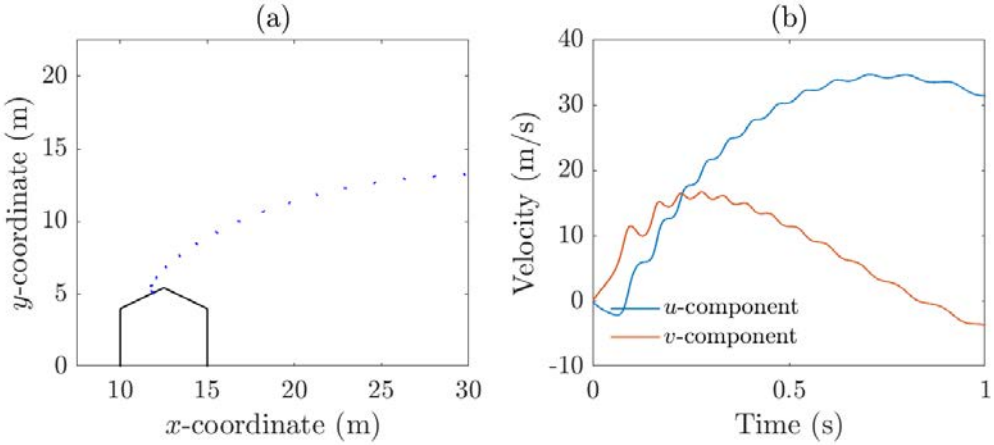

Figure 4: For a windward roof launch, (a) flight trajectory and plate inclination and (b) components of velocity of the plate.

DOI 10.5258/WES/P0010

Structure of yawed wind turbine wakes in thermally neutral and stable boundary layers

Author Name(s): Rose Foster, Phillip Hancock, and Marco Placidi *
School of Mechanical Engineering Sciences, University of Surrey
Guildford, Surrey
* E-mail: m.placidi@surrey.ac.uk

1 ABSTRACT

To investigate variation in the wake structure behind a yawed wind turbine model in different thermal boundary layers, experiments were performed in the Environmental Flow Research Centre (EnFlo) at the University of Surrey. These utilised the 20x3.5x1.5m^3 working section Meteorological Tunnel, which can produce boundary layers of different thermal stabilities. The deep boundary layer used for these experiments had a depth (δ) to turbine hub height (z_{hub} = 300mm) ratio of $\delta/z_{hub} \approx 2$ for the neutral and stable flows, with a bulk Richardson number of $Ri_b \approx 0.2$ and surface Obukhov length $L_{surface} \approx 1$m in the stable case. The turbine was run in these layers at yaw angles of -20 º,0 º, and 20º at a tip-speed ratio of 6. Velocity measurements were taken behind this model using a 3D Laser Doppler Anemometry (LDA) system. This allowed both the time-mean and fluctuating components of the velocity to be captured in the streamwise, lateral, and vertical directions. The measured data sets comprise lateral profiles behind the turbine at z_{hub}, and vertical profiles along the centreline (y = 0), at a series of downstream distances.

The influence of thermal stability on the wake is evaluated across several quantities. First, a reduction of wake growth in stable flows is observed, along with an anti-axisymmetric wake shape. Second, wake recovery is shown to be hindered by stable conditions. Next, yaw is considered by comparing the rotor area averaged velocity across the 6 test cases, showing that a positive yaw performs best. Finally, lateral wake deflection is determined to demonstrate the larger deflections produced by a positive yaw angle.

2 INTRODUCTION

With the onset of climate change a global transition towards clean energy sources is underway. In the UK wind energy is identified as a key contributor towards this, with wind farms expected to produce 50GW of power annually by 2030, half of all renewable production [1]. For this to be achieved not only is new infrastructure of wind farms and power distribution needed, but existing wind farms should be made more efficient. Presently, a key limitation to production is the waking of downstream turbines within a farm, starving downstream turbines and limiting their power output. A promising method to overcome this is yaw control, where the upstream turbine's wake is redirected away from a downstream turbine to both increase the overall power yield and decrease the fatigue loading from wake turbulence. Studies on yaw strategies suggest an increase of 10% in farm power output is possible [2], but to be implemented in practice wake modelling and experimental data are required across a wide range of conditions. Research on yawed turbines has mostly focused on a simplified 2D wake in the lateral plane. Building upon established models of un-yawed turbines that represent the wake velocity deficit as a series of Gaussian curves [3]. However, behind a yawed turbine the formation of the counter-rotating vortex pair (CVP) will distort the wake from an ellipse to a "kidney" shape. Here, the lateral profile will remain in its established Gaussian form, but the vertical profile will not, forming two peaks as it effectively crosses the curled wake twice. Thus, to properly predict the power available to a downwind turbine and the effectiveness of yaw an improved understanding of this vertical plane is needed.

Along with yaw, the experiments herein also consider the impact of thermal stability on the wake. The relationship between stability and wake development is well established; in increasingly stable flows the turbulence intensity is reduced, hindering wake entrainment and slowing the wake's growth and recovery [4]. However, less work has been performed on the impact of stability on yaw, with initial research suggesting that yaw effectiveness can increase in stable flows [5] it is crucial to better quantify how this can be exploited to maximise wind farm efficiency.

DOI 10.5258/WES/P0013

3 EXPERIMENTAL METHODOLOGY

Experiments were undertaken in the Meteorological tunnel at the EnFlo centre. Here, boundary layers of varying thermal stability are generated by a set of heaters that apply a temperature profile at the flow inlet, alongside a series of cooling/heating panels on the floor that maintain the positive/negative thermal gradient. For more detail on how these are used to produce different levels of stability see [6]. Roughness length is controlled by blocks on the floor acting as roughness elements. Boundary layer growth is accelerated by 12 Irwin spires at the front of the working section, each measuring 600mm in height. These ensure the flow is fully developed before it reaches the turbine 10m downstream. A flow speed, $U_{\infty,hub}$, of 1.5ms^{-1} was set for both boundary layers, with upwind flow speed recorded using a sonic anemometer at the tunnel inlet. The resulting chord Reynolds number was around 3x10^5, high enough for Reynolds effects to be somewhat mitigated and comparisons to a full-scale turbine to be possible. Cases for the two stabilities with the varying turbine configurations are outlined in table 1.

The wind turbine used, shown in figure 1a, was of 0.416m diameter with a hub height of 0.3m. Further details of its design can be found in [6]. The turbine was run at a tip speed ratio of 6. For each boundary layer the required RPM was calculated from the mean of the velocity at z_{hub} in an empty tunnel. In the yawed cases a positive angle indicates where the effects of yaw and turbine rotation combine to give a larger wake deflection. Here, this results from a clockwise rotation of the turbine viewed from the front and anti-clockwise yaw angle viewed from above. The turbine's RPM was monitored by a photo-Darlington sensor mounted to the hub, this showed the variation of the RPM to be within ±0.25%.

Wake measurements were taken using LDA, giving both time averages and fluctuations of velocity in the x, y, z directions to determine the values of U, u', V, v', W, w'. Flow seeding was provided by evaporated sugar water, with the level of seeding controlled to give a minimum data rate of 100Hz. Each measurement lasted 3 minutes to ensure that the fluctuating components were accurately captured. Measurements were taken at downstream distances of x/D = 2, 2.7, 5, 6, 8, 10.8, 15.4 to give a good range of data for both the near and far wake. Vertical profile measurements were made between a height of 50mm and 750mm along y = 0. Lateral profiles covered a range between ±810mm at z_{hub}. Each had a spacing of around 20mm. The profiles are illustrated in figure 1b.

Table 1. Overview of setups for which data was taken.

Flow \ Turbine	-20	0	20	None
Neutral	*Case -20N*	*Case 0N*	*Case 20N*	*Case Empty N*
Stable	*Case -20S*	*Case 0S*	*Case 20S*	*Case Empty S*

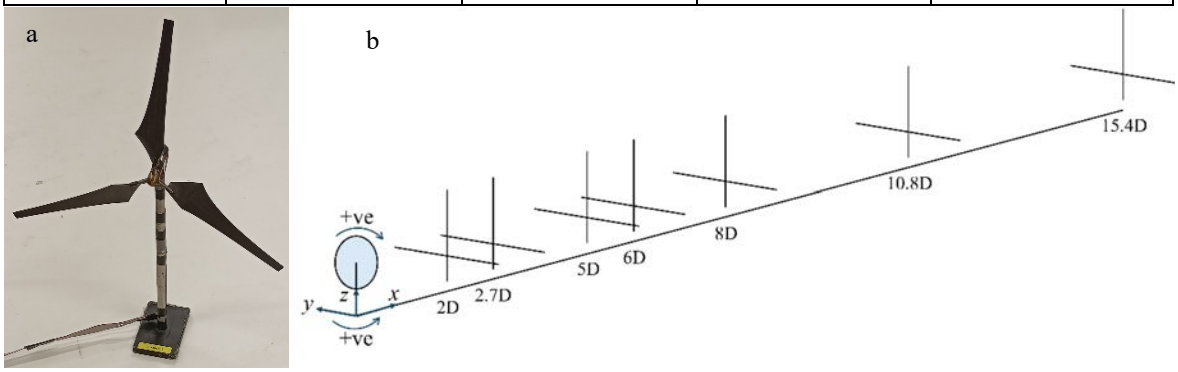

Figure 1. a. Wind tunnel model used for the experiments. b. LDA measurement profile locations.

4 RESULTS

Figure 2a shows the vertical profiles of wake velocity normalised by local free stream velocity, U_{fs}, in the neutral case, with the velocity tending back towards the inflow profile, illustrated in black. Initially, the wake consists of two peaks, due to the turbine acting as an annular disk and not slowing the flow as much near the hub. Downstream, wake mixing blends these peaks into the familiar single peak. For this data set the transition occurs around 6-8D downstream, thus, figure 2b shows the Gaussian curve fitted to velocity deficit from 8D onwards. This deficit has been corrected according to the local free stream velocity, as the turbine's blockage slightly accelerates the flow.

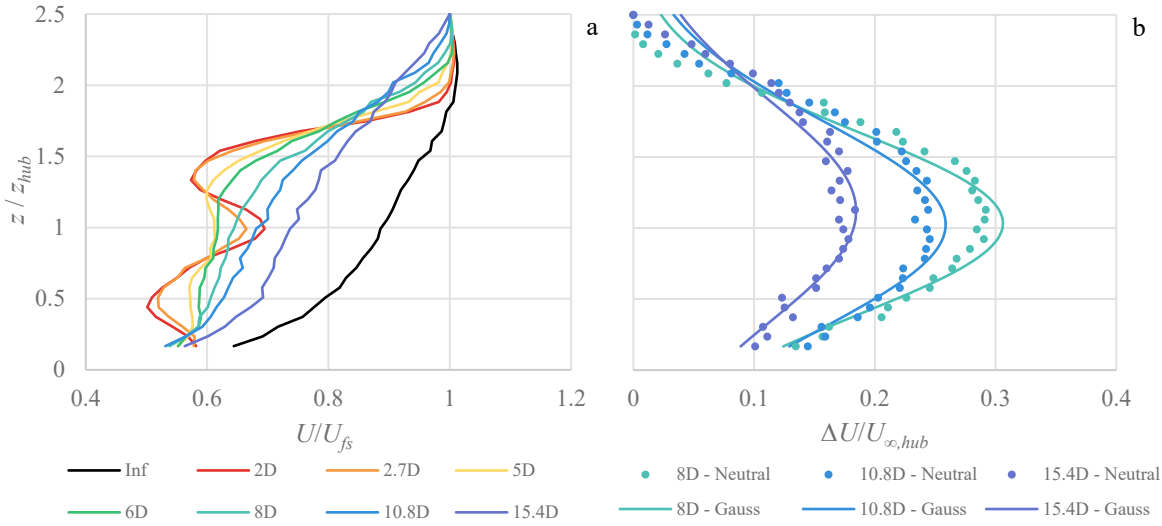

Figure 2. a, Wake velocity of the un-yawed turbine in 0N. b, Corresponding corrected velocity deficits with fitted Gaussian curves.

The same curves were fitted for the lateral profiles of the un-yawed configuration. Each curve giving a wake width and maximum velocity deficit. However, the wake will shift from the hub centre due to both wake meandering and yaw so the profiles measured here will be slight underestimates of the true wake maximum. To correct for this the wake is assumed to be elliptical with zero tilt, as the vertical and lateral profiles are found to suitably overlap at the hub centreline. As such, the width and height of the ellipse can be determined using the standard deviations of the vertical/lateral Gaussian curves to find four non-mirrored points on the ellipse. These are shown in figure 3a. Finally, the true maximum velocity deficit is found from the measured velocity at the curves' overlap point along the hub centreline and the equation of a bi-variate Gaussian distribution. This is shown in figure 3b. As expected, the velocity recovers slower in the stable case, with both cases following a power law relationship.

Figure 3a demonstrates that in neutral flow the vertical and lateral growth behaves roughly the same, so traditional modelling methods are appropriate here. However, in the stable case there is a deviation between the two, with the wake growing faster vertically than laterally, illustrating the need for more refined vertical modelling.

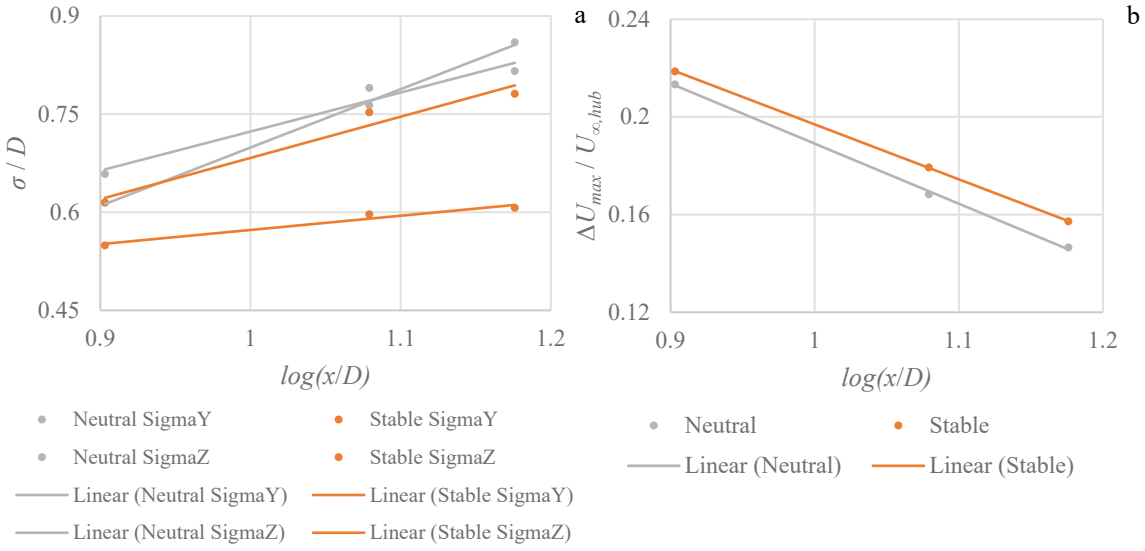

Figure 3. a, Comparison of the corrected wake growth in the two directions across 0N and 0S. b, Recovery of the corrected maximum velocity deficit.

The same approach cannot readily be used for the yawed data, as the CVP distorts the vertical profiles into having two peaks. Instead, comparisons are made by averaging wake velocity across the diameter of a virtual downstream turbine. This is shown for the six cases in figure 4a. For each turbine orientation

DOI 10.5258/WES/P0013

the flow recovers faster in the neutral than in the stable case, again as expected. The benefits of yaw can also be clearly seen here; in both flows wake velocity increases when the turbine is negatively yawed, with a further increase for positive yaw, signifying a higher wind resource is available for downstream turbines in these yawed cases. The wake deflection away from the virtual downwind turbine providing this performance increase is shown in 5b, showing that deflection is maximised in the stable case for a negative yaw, while for a positive yaw the neutral flow gives a slightly higher deflection; it is as yet unclear why this is the case, requiring further scrutiny.

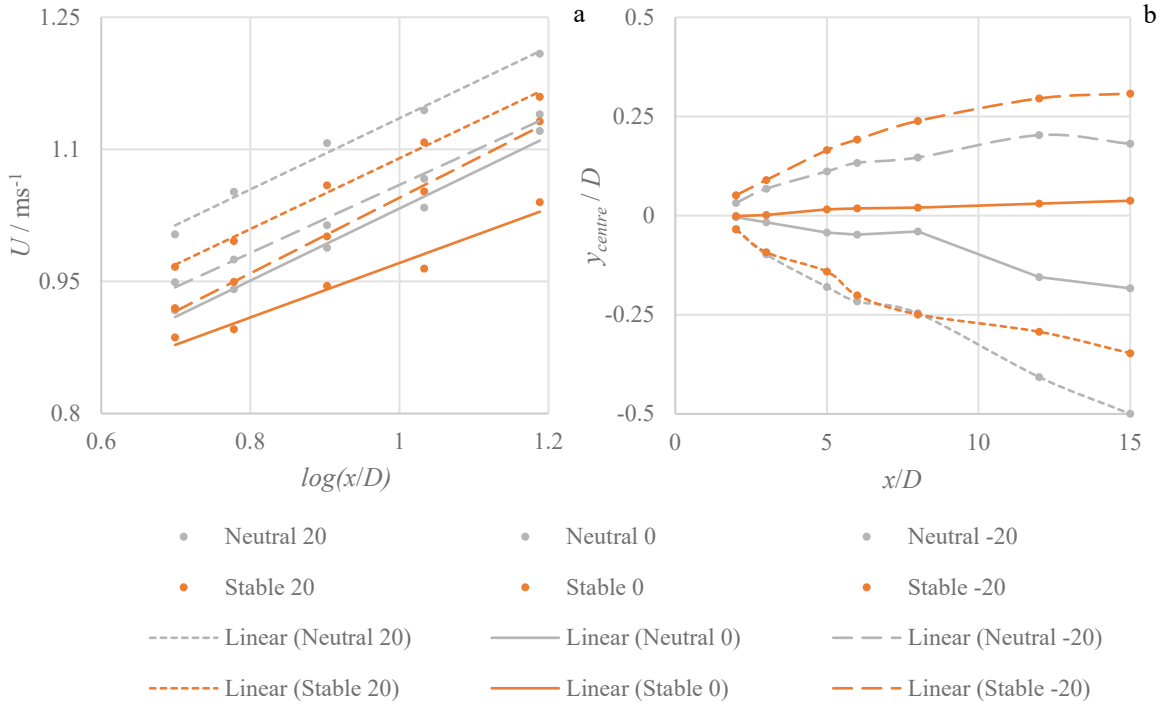

Figure 4. a, Disk area mass-flow averaged velocity in the vertical profile for the three yaw directions in stable and neutral flow. b, Lateral centres of the six cases.

5 CONCLUSIONS

The presented data demonstrates the differences that arise between vertical and lateral wake profiles in different flow stabilities and yaw directions, illustrating the need for alternative modelling approaches to wake flows in the vertical plane. The potential benefits of yaw on wind farm production are explored, highlighting the most effective configurations. Reflecting upon the results of the experiment, the approaches needed for future modelling work are discussed.

6 REFERENCES

[1] UK Government. (2022). *British energy security strategy*. gov.uk/government/publications/british-energy-security

[2] Zong, H., & Porté-Agel, F. (2020). A point vortex transportation model for yawed wind turbine wakes. *Journal of Fluid Mechanics*, *890*. https://doi.org/10.1017/jfm.2020.123

[3] Bastankhah, M., & Porté-Agel, F. (2014). A new analytical model for wind-turbine wakes. *Renewable Energy*, *70*, 116–123. https://doi.org/10.1016/j.renene.2014.01.002

[4] Hancock, P. E., & Pascheke, F. (2014). Wind-tunnel simulation of the wake of a large wind turbine in a stable boundary layer: Part 2, the wake flow.

[5] Vollmer, L., Steinfeld, G., Heinemann, D., & Kühn, M. (2016). Estimating the wake deflection downstream of a wind turbine in different atmospheric stabilities: an LES study. *Wind Energy Science*, *1*(2), 129–141. https://doi.org/10.5194/wes-1-129-2016

[6] Hancock, P. E., & Hayden, P. (2018). Wind-Tunnel Simulation of Weakly and Moderately Stable Atmospheric Boundary Layers. *Boundary-Layer Meteorology*, *168*(1), 29–57.

Unsteady Loading of Horizontal Axis Wind Turbines by Atmospheric Turbulence.

J. Michael Graham[1] , Kevin Gouder[1] and Ian A. Milne[2]
[1]Department of Aeronautics, Imperial College London, London, UK
[2]Oceans Graduate School, University of Western Australia, Perth, Australia.
E-mail: grahamjmr@aol.com

1 INTRODUCTION.

Horizontal Axis Wind Turbines (HAWTs) have continued to increase in size to provide economies of scale and the fluctuating loads resulting from interaction with Atmospheric Boundary Layer (ABL) turbulence have become increasingly challenging. Rotors normally operate at high tip-speed ratio $\Lambda(=\Omega R/U_\infty)$, Ω being the rotor speed, R its radius and U_∞ the free stream wind speed at hub height. The unsteady blade loading is dependent on both the mean shear and, since $\Lambda>>1$, on the streamwise component of the turbulence velocity. Loading calculations are normally either performed stochastically, or increasingly, in the time domain using synthesised time histories and blade element theory assuming mean flow response subject to the rotor blocking effect but the response to turbulence without this modification. However, distortion (ie. stretching and rotation) of the incident turbulence vorticity by the mean upstream flow field of the rotor can, as for other structures in an ABL, significantly intensify the approaching streamwise component of fluctuating velocity and increase its correlation across the rotor disc. Both effects raise the levels of unsteady loading of the rotor. In contrast the blocking potential flow opposing the streamwise component of turbulence lowers turbulence intensity as it does the mean velocity. Recent full-scale field tests have measured turbulence in the induction zone of HAWT rotors using Lidar. The low frequency turbulence (large eddies), was found to be modified significantly in wind flows [1, 2, 3] and tidal flows [4]. Depending strongly on the ratio of the correlation length-scale of the turbulence to rotor diameter and on the below- or above-rated operational condition distortion/ blocking of the flow can amplify or attenuate the unsteady loads. Information on ABL turbulence intensities and length-scales [5] are available for making assessments. When the turbulence length-scale is small compared to the rotor diameter the distortion process satisfies the conditions for Rapid Distortion Theory (RDT) [6] and this theory has been used [7] to compute the turbulence incident on a rotor for a range of rotor resistance. The actuator disc theory for HAWT rotors also applies to porous discs which are often used to simulate turbines and compared with the rotor in the present work.

2 EXPERIMENT

.

2.1 Rotor and Disc Models

A three bladed, 0.5m diameter model rotor was designed to give a near uniform resistance across the rotor disc with wake induction factor $a_0 \approx 1/3$, the optimum power value. Two porous discs laser cut from board, with diameters 0.45m and 0.245m and open area ratios 0.555 and 0.529 respectively to give flow resistance similar to the rotor disc, were tested for comparison. The rotor was operated at a tip-speed ratio of 4.0 giving chord Reynolds 6400 at ¾ radius in a mean wind of 10m/s at 0.375m hub height. Both rotor and porous discs were mounted on short shafts attached to a load cell (Nano17 and Gamma130-10 types being used) and the mean and fluctuating axial forces sampled at 10kHz. The rotor was controlled by a Magtrol torque-RPM sensor and controller to rotate at 1500RPM. The geometric blockage ratio of the models in the working section was 4.3%, 3.5% and 1.0% respectively. No blockage corrections were applied.

DOI 10.5258/WES/P0014

2.2 Simulated ABL and Turbulence Intensities.

The working section of the Imperial College large closed-loop wind tunnel is 3m wide by 1.5m high by 20m long. A 1:400 scale simulation of an ABL with a surface roughness length of 0.01m was generated by a standard set-up [5] using upstream Counihan spires and a fence followed by 15m of development over a roughened floor. Velocity measurements were made using Dantec hot-wire anemometer probes. The mean velocity and streamwise turbulence intensity at the test position are shown in figure 1. The integral correlation length $R_{11}(x)$ at hub height was evaluated from the measured frequency spectrum to be 0.41m assuming Taylor's hypothesis.
These tests were supplemented by tests of the rotor and porous discs in homogeneous turbulence 12 mesh-lengths downstream of a 0.125m square mesh turbulence grid.
At this station the turbulence length-scale was 0.030m with RMS intensity 0.61m/s for a mean wind speed of 10.0m/s. These tests were to evaluate the effect of much smaller turbulence length-scale to rotor diameter ratios.

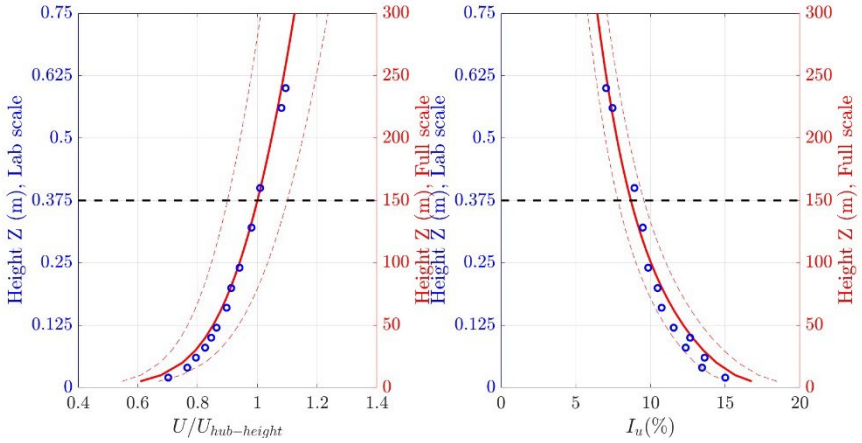

Figure 1 Wind Tunnel Simulated ABL profiles (a) U(z)/U_{hub}, (b) √<u^2>/U_{hub}

2.3 Spectra and Correlations of the Turbulence.

The grid turbulence was found to conform closely to the empirical von-Karman spectrum function $\Phi_{11\infty}$, spectra $S_{11\infty}$ and 2-point correlations $R_{11\infty}$ for quasi-isotropic turbulence [8]:

$$\Phi^{VK}_{11\infty}(\kappa_\infty) = \frac{1}{4\pi U_\infty}\left(1.339 L_{x\infty}\tau^*_\infty/\kappa^{*2}_\infty\right)^2 \frac{\overline{Cu^2}_\infty \kappa^{*4}_\infty}{(1+\kappa^{*2}_\infty)^{\frac{17}{6}}}$$

$$S_{11\infty}(\kappa_{1\infty}) = \frac{4L_{x\infty}\overline{u^2}_\infty}{U_\infty\left(1+\kappa^{*2}_{1\infty}\right)^{5/6}}.$$

$$R_{11}(\Delta r^*) = \frac{1}{\Gamma(1/3)}\left(\frac{\Delta r^*}{2}\right)^{1/3}\left\{K_{1/3}(\Delta r^*) - \Delta r^* K_{2/3}(\Delta r^*)\right\},$$

Here κ_1 is streamwise wavenumber, $\tau^2 = \kappa_2^2 + \kappa_3^2$ and $\boldsymbol{\kappa}^2 = \kappa_1^2 + \tau^2$. $K_{1/3}$, $K_{2/3}$ are Bessel functions and * indicates non-dimensionalisation of wavenumber (κ_j^*) and transverse separation (Δr^*).

However for the ABL turbulence it was found, as has been observed by others, that the transverse horizontal correlation coefficient $R_{11\infty}(\Delta y^*)$ had a much more pronounced negative loop than the vertical coefficient $R_{11\infty}(\Delta y^*)$, figure 2a. This could be better represented, as shown in the figure, by a modified expression for the correlation derived from the empirical spectrum function with an additional term added to that function. With $\eta_0 = 2$ giving the best fit this changes the streamwise wave-number (or frequency) spectrum by a small amount, as shown in figure 2b, to:

DOI 10.5258/WES/P0014

$$S_{11\infty}(\kappa_{1\infty}) = \frac{81 - 15\eta_0/(1+\kappa_{1\infty}^{*2}}{81 - 6\eta_0} S_{11\infty}^{VK}(\kappa_{1\infty})$$

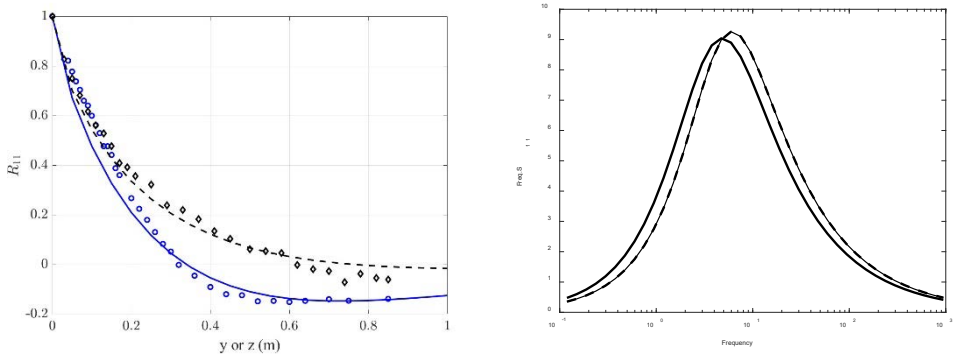

Figure 2(a) measured vertical (♦) and horizontal (o) correlation R_{11} compared with modified empirical formulae. (b) Unmodified (-) and modified (---) von Karman frequency spectrum S_{11}. .

2.4. Distorted turbulence in the induction zone.

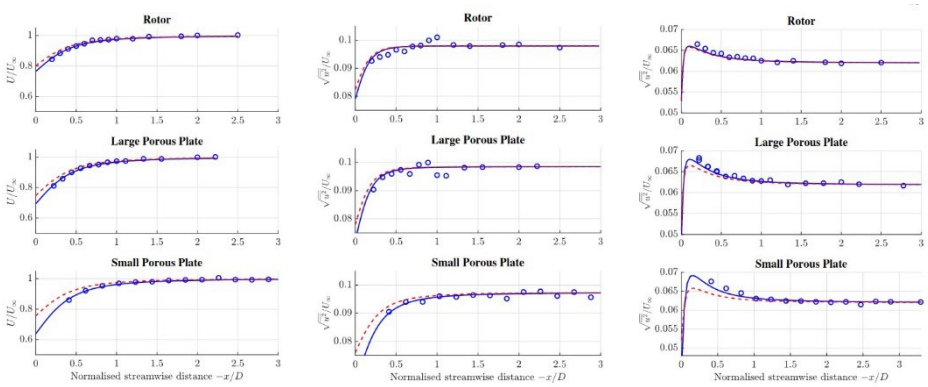

Figure 3(a) Mean flow, (b) u_{RMS} intensity of ABL turbulence, (c) grid turbulence in the induction zone.

Measurements of mean velocity and streamwise turbulence intensity along the upstream axis of each model are compared in figure 3 (a) with mean flow actuator disc theory and in (b) and (c) with distortion theory interpolated for turbulence length-scale to disc diameter ratio between quasi-steady conditions [2] causing no distortion for large scale ratios and large intensification given by RDT [7] for small scales. Distortion occurs over an upstream distance which scales on the body diameter (the scale of the mean flow causing the distortion). The intensities are also affected progressively by blocking potential flow due to disc resistance [9] opposing the streamwise turbulence velocity over a distance which scales on the turbulence length-scale. It is noticeable that the rise in intensity due to distortion is only obvious for the small length-scale grid turbulence, being too small to be seen against the overwhelming blocking reduction effect in the ABL cases.

2.5 Axial force spectra

The time dependent axial force on each disc depends linearly on the instantaneous streamwise velocity of the turbulence incident at the plane of the disc after distortion. It is calculated similarly as for the above blocking effect to which it is related, by interpolating between quasi-steady theory

DOI 10.5258/WES/P0014

and the potential blocking theory [9] as described above. The prominent peaks at ~ 20Hz and 25Hz are due to structural resonance and rotation frequency blade-shear interaction. Considering that these are log-linear spectra the agreement of the computed results with the measured data is good.

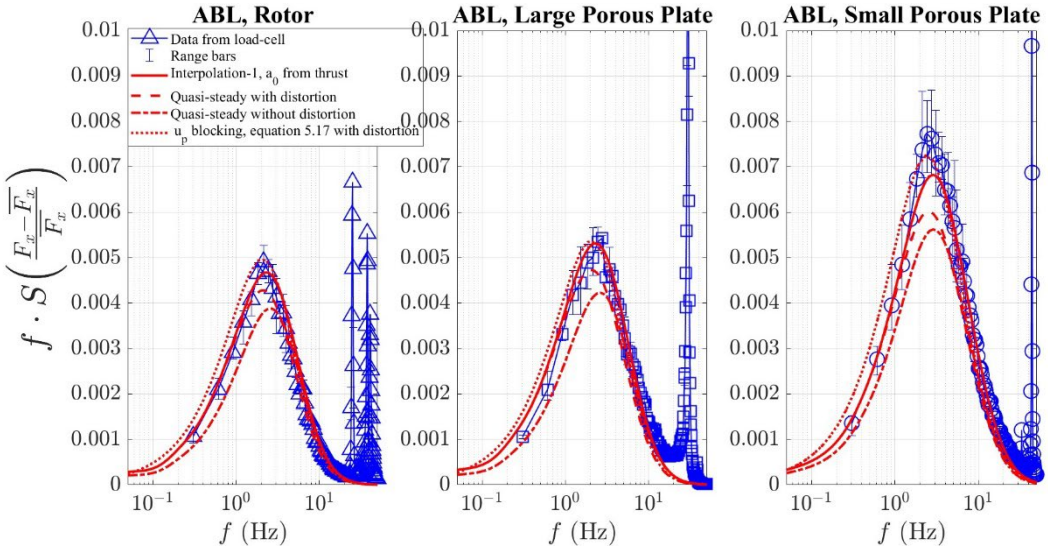

Figure 4 Measured: frequency.PSD of Rotor Axial Force, ABL turbulence, (a) Rotor, (b) Large Porous Plate, (c) Small Porous Plate. Theoretical predictions: (— , ---, -.-., ….).

3. CONCLUSIONS

Induction zone turbulence intensities and axial forces induced by them on a model rotor and two porous discs in a simulated turbulent ABL has been measured and shown to compare well with interpolated formulae which combine quasi-steady theory with small length-scale RDT and a potential back-flow due to blocking. The turbulence in the ABL, unaffected by the discs, has also been studied and a modified empirical spectrum suggested to give a better fit to the horizontal transverse correlation coefficient $R_{11\infty}(\Delta y^*)$.

4. REFERENCES

[1] Pena A., Mann J. and Dimitrov N. (2017) "Turbulence characteristics from a forward facing nacelle Lidar", *Wind Energy Sci*., **2**, 133.

[2] Mann J., Pena A., Troldborg N.J, and Anderson S. (2018) "How does turbulence change approaching a rotor?", *Wind Energy Sci.,* **3**, 293.

[3] Chamorro L. P. (2015) "Turbulence effects on a full-scale 2.5MW horizontal axis wind turbine under neutrally-stratified conditions", *Wind Energy* **18**, 339.

[4] Milne I.A. and Graham J.M.R. (2019) "Turbulence velocity spectra and intensities in the inflow of a turbine rotor", *Jnl. Fluid Mech*. **870**, R3.

[5] ESDU (2002) "Strong winds in the ABL", Rep. **82026** & **85020** IHS Inc, London.

[6] Batchelor G.K. and Proudman I. (1954) "The effect of rapid distortion of a fluid in turbulent motion" , *Quart. Jnl. Mech. App. Math.,* **7,** 83.

[7] Graham J.M.R. (2017) "Rapid distortion of turbulence into an open turbine rotor" *Jnl. Fluid Mech.* **825**, 764.

[8] Deaves D.M. and Harris R.I. (1978) "A mathematical model of the structure of strong winds" *Construction Industry Research and Information Association*, Tech Rep.**76**.

[9] Batchelor G.K. (1960) "Theory of Homogeneous Turbulence", *Cam. Univ. Press.*, **ch.4**, 58.

DOI 10.5258/WES/P0014

Surface Pressure Fluctuations in an Atmospheric Boundary Layer

Joy Schmeer, Marco Placidi and David M. Birch*
Centre for Aerodynamics & Environmental Flow, Faculty of Engineering & Physical Sciences,
University of Surrey
Guildford, Surrey
* E-mail: d.birch@surrey.ac.uk

1 INTRODUCTION

In the wind tunnel simulation of urban canyons, surface pressure measurements remain a very valuable source of information about the flow and provide one of the simplest and most reliable techniques for obtaining estimates of critical turbulence scaling parameters such as the wall shear velocity.

Surface pressures have traditionally only been measured as time-averaged quantities. However, in dispersion studies in particular, there has been much recent attention brought to the importance of peak quantities and their significance to air quality and human health [1]. As a result, there is an increasing need for the capability of making time-resolved surface pressure measurements within a wind tunnel model of a canonical urban canyon-like geometry.

Time-resolved pressure measurements in these conditions pose some particular challenges. First, the problem of physical scale and resolution: in wind tunnels, building models tend to be small. As a result, the only practical way to access the surface pressures are with lengths of hoses connecting pressure taps in the surface to pressure sensors located elsewhere. These lengths of hose inherently distort pressure signals owing to their own internal dynamics [2]. Second, there the problem of the fundamental gain-bandwidth limitation: the maximum dynamic pressures in some environmental wind tunnel tests can be below 0.2 Pa [3], representing just 0.06% of the full-scale range of even the most sensitive conventional pressure transducers.

An instrumentation suite and technique has therefore been developed address these challenges and enable surface pressure measurements to be collected in these conditions, well-resolved in both space and time.

2 METHODOLOGY

2.1 Experimental model and instrumentation

A cube with side length h = 150 mm was selected as the test model, as a canonical representation of urban topography. The five wetted faces of the cube were fitted with 100 pressure taps each, in a 10 × 10, logarithmically-spaced grid. The pressure taps were connected to 512-channel pressure scanner (Surrey Sensors Ltd. model DPS14-160P, having a full-scale range of 160 Pa and an uncertainty of 0.5%FS) by means of ~1.4m lengths of 1 mm ID hose.

The model was tested both in isolation and as an element of a staggered array of cubes with spacing 2h in the EnFlo Atmospheric Wind Tunnel at the University of Surrey, at a free-stream speed of 2.5 m/s. A model atmospheric upstream boundary layer was developed upstream using a combination of Irwin spires and surface roughness, yielding a boundary layer thickness δ = 0.9 m and roughness velocity u_τ = 0.15 m/s (estimated using the Clauser method); more details about the facility are available in [2].

2.2 Dynamic calibration

With the lengths of tubing used, the bandwidth of the pressure measurement system was limited to under 10 Hz [3]. Dynamic calibration was therefore required. A sealed chamber was placed around the cube *in situ*. One wall of the chamber was fitted with a speaker, which could be used to dynamically vary the volume of the chamber, varying the pressure by up to 16 Pa. The chamber was also fitted with a fast pressure sensor (with a bandwidth of 1000 Hz) for use as a reference.

The pressure channels were then simultaneously dynamically calibrated using a discrete Fourier reconstruction technique [4]. Sinusoidal signals at a series of discrete calibration frequencies f_0 were sent to the loudspeaker, and the signal amplitudes were adjusted by a control system to achieve the required peak-to-peak pressures on the reference sensor (as the dynamic response of the speaker system itself was unknown).

DOI 10.5258/WES/P0015

Pressure signals from each of the 500 measurement channels were then compared to the reference pressure in the Fourier domain at each f_0, and a discrete gain $G(f_0)$ and phase shift $\phi(f_0)$ obtained. Continuous functions G and ϕ could then be inferred by third-order interpolation. During measurement, a spectral decomposition of the signals was carried out by fast-Fourier transform (FFT), were rescaled and shifted by $G(f)$ and $\phi(f)$, respectively, and returned to the time domain by inverse FFT. Figure 1 demonstrates the effectiveness of the dynamic calibration process, showing its response to a white-noise pressure signal of peak-to-peak amplitude ~5% of the full-scale range P_{FS}.

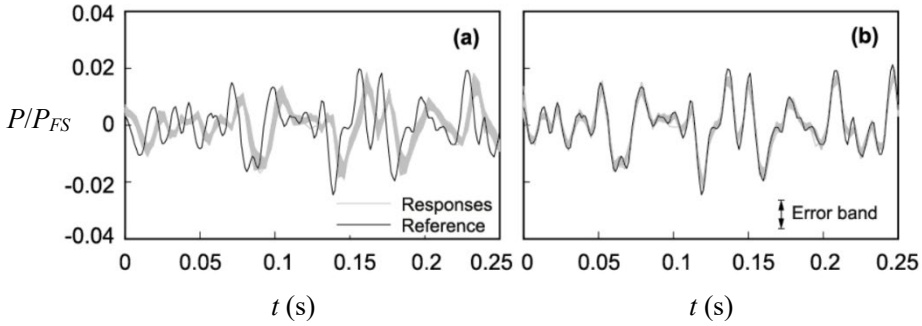

Figure 1: Effectiveness of dynamic calibration for 500 channels. (a), before calibration; (b), after.

Great care was taken to minimize the error band of pressure measurements, including temperature control, a programme of zero measurements and interpolated offsets, and simultaneous characterisation of the reference pressure. The error band reported by the sensor manufacturer is also shown in figure 1(b) as a demonstration of the improvement in sensor performance.

3 RESULTS AND DISCUSSION

3.1 Single cube

Figure 1(a) shows contour maps of the mean pressure coefficient C_P over three faces of the cube at 0º incidence for the case of the single cube in a boundary layer (note that the normalising dynamic pressure was taken at free-stream conditions). The pressure distributions agree well with a number of previously published results from both wind tunnel and field measurements.

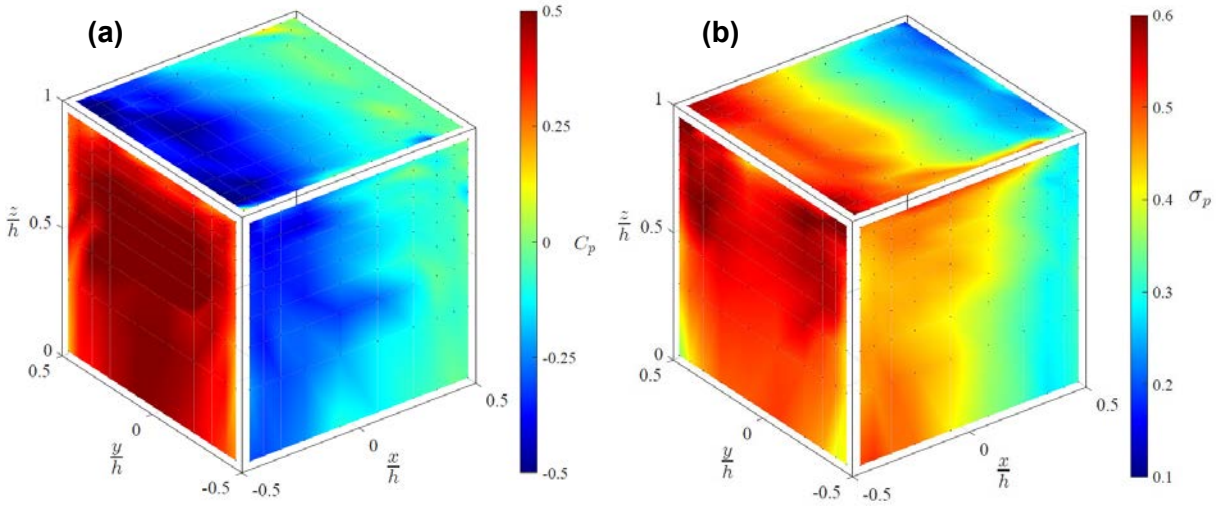

Figure 2: Resuts for a single cube in a boundary layer. (a), mean C_P; (b) standard deviation.

More interesting here, though, is figure 1(b), which shows the standard deviation σ of C_P. High levels of σ on the top corners of the leading face are consistent with the unsteadiness associated with corner vortices; likewise, at the bottom corners of the leading face there is evidence of interaction with the horseshoe vortex. Lines of high σ on the top and sides of the cube, at $x/h \sim -0.4$, are consistent with the

DOI 10.5258/WES/P0015

meandering of separation lines. A weak negative correlation in the area-averaged C_P on the two y-normal faces of the cube demonstrated that the cube could also respond to the spanwise modulation in the mean flow direction.

3.2 Staggered array

Figure 3 shows C_P and σ for the case of the cube in a staggered array at 0º incidence (with the open canyons normal to the flow direction). Although the mean pressures on the cube are substantially reduced relative to the single-cube case; this is expected, as the same free-stream speed was used and the cube was now immersed in a thick roughness sublayer. The peak standard deviation remains high by comparison; fluctuations in C_P are concentrated around the top corner of the leading edge, and are likely the result of intermittent impingement by structures shed from upstream cubes, which are unlikely to penetrate deeper into the roughness array. Interestingly, the flow incidence angle was found to have a marginal effect on the area-averaged magnitudes of σ.

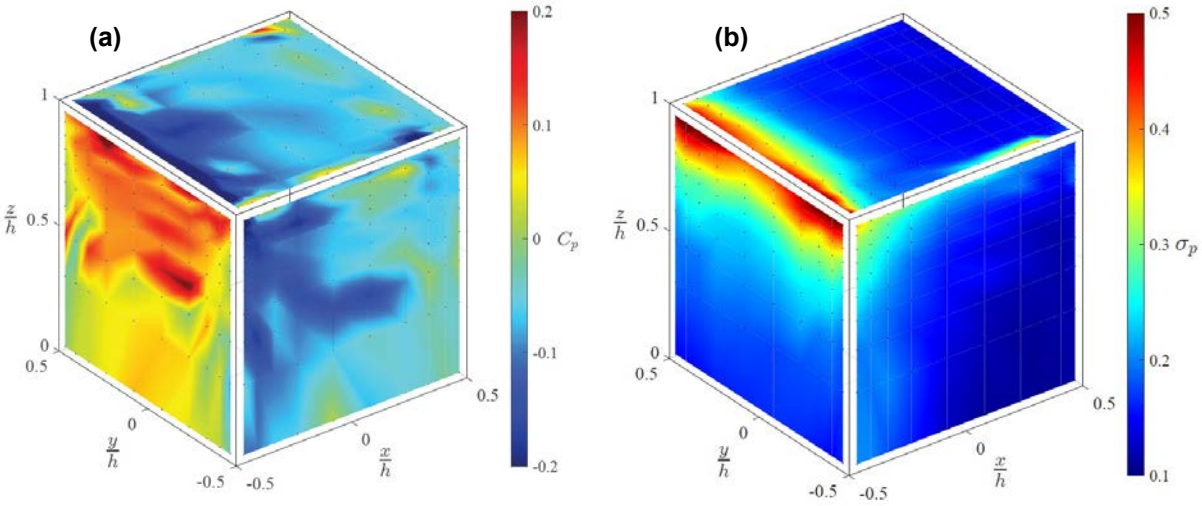

Figure 3: Resuts for a staggered cube array. (a), mean C_P; (b) standard deviation.

3.3 Friction velocity

If the pressure drag on individual roughness elements is assumed to dominate over viscous shear in the net wall shear acting on a rough surface, the shear stress acting on the cube array may be approximated as the area integral of the difference of pressures between the front and the rear faces on a typical cube, normalized by the array repeating element surface area. In the present case, the area-integral method yields a mean u_τ = 0.13 m/s, which compares well with the Clauser estimate.

With the instrumented cube, it is also possible to resolve the time-history of the zero-mean side-shear velocity v_τ, equivalent to the cross-flow wall shear. Figure 4 shows the time-histories of u_τ and v_τ, normalized against U. The streamwise component of wall shear can experience fluctuations with amplitudes as high as three times its mean value, and is indeed negative for some time (as a result of local recirculation). Note that it was assumed in these cases that $u_\tau = (\tau/\rho)^{1/2}$ was computed from the absolute value of τ but retained its sign, as the friction velocity resulting from negative shear would otherwise be undefined.

The side-shear velocity v_τ had a mean value near zero, as expected. However, the distribution was not normal; rather, it was symmetric and bimodal (with peaks at $v_\tau/U \sim \pm 0.05$; see inset). The mechanisms causing this bimodal behaviour were not clear from the evidence available; there was no significant correlation between the area-averaged pressure coefficients on the two sides of the cube (correlation coefficients in C_P were below 0.1).

DOI 10.5258/WES/P0015

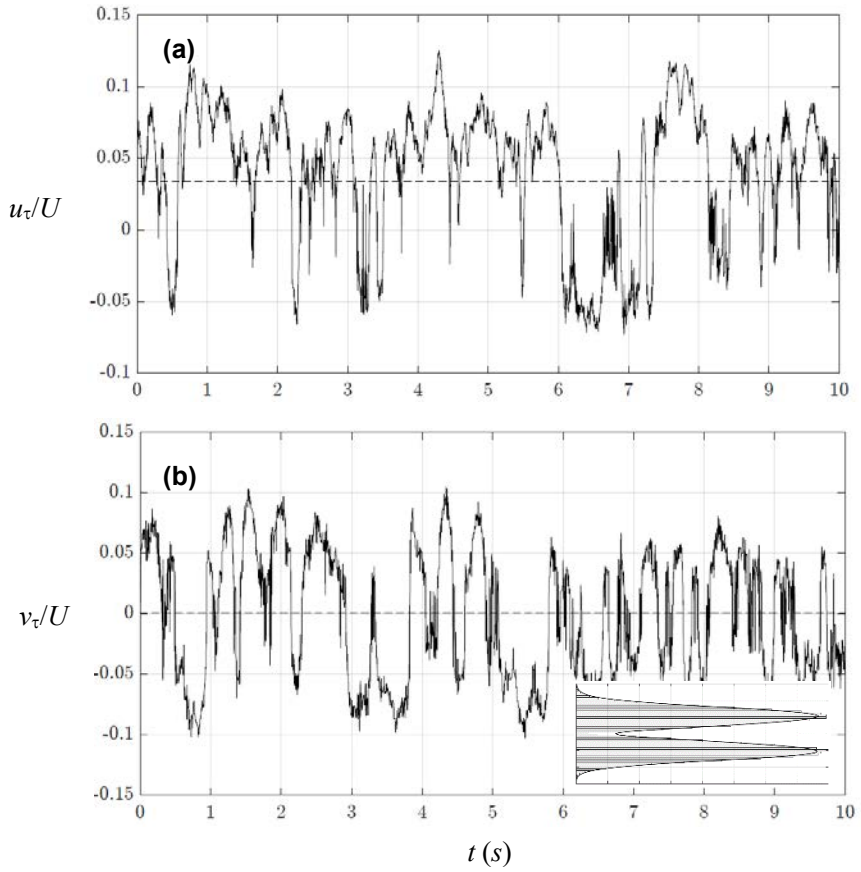

Figure 4: Time history of wall shear velocity. (a), u_τ; (b) v_τ. Inset: probability distribution of v_τ.

4 CONCLUSIONS

Surface pressure measurements were collected on a cube in a boundary layer, both for cases of the individual cube and for a cube in a staggered array commonly used as an approximation of an urban topology. A large number of measurement points and a dynamic calibration process allowed the measurements to be resolved in both space and time.

Results demonstrated that the pressure time-history is rich with information about the flow, including elements of bulk background flow behaviour, meandering of separation points and impingement of coherent structures. For the array case, a time-history of shear stress may also be inferred, demonstrating a clear bimodality in the spanwise component of shear.

REFERENCES

[1] Papp, B. Istok, B. Koren, M, Balczo, M, and Kristof, G. (2024) "Statistical assessment of the concentration fluctuations in street canyons via time-resolved wind tunnel experiments." Journal of Wind Engineering & Industrial Aerodynamics 246 (2024) 105665

[2] Marucci,D. and Carpentieri, M. (2019) “Effect of local and upwind stratification on flow and dispersion inside and above a bidimensional street canyon,” Building and Environment, vol. 156, pp. 74–88, 2019.

[3] Bergh, H. and Tijdeman, H. (1965) “Theoretical and experimental results for the dynamic response of pressure measuring systems,” Netherlands National Aerospace Laboratory, Tech. Rep. TR-F238.

[4] Stefe, M., Svete, A. and Kutin, J. (2016) “Development of dynamic pressure generator based on a loudspeaker with improved frequency characteristics,” Measurement, vol.122, pp. 212–219, 2016.

DOI 10.5258/WES/P0015

Simulation of atmospheric boundary layer in the wind tunnel facility at University of Bristol

Nada Taouil[1,*], H.D. Lim[1], B. Zang[1], Mahdi Azarpeyvand[1]
[1]School of Civil, Aerospace and Design Engineering, University of Bristol
Bristol, UK
[*] E-mail: vv23404@bristol.ac.uk

1 INTRODUCTION

Air pollution studies are critical for understanding the dispersion of pollutants in urban environments and mitigating their adverse health effects. Accurate simulation of these processes in a controlled environment, such as a wind tunnel, is essential for advancing our knowledge and developing effective pollution control strategies. The atmospheric boundary layer (ABL) plays a pivotal role in influencing pollutant dispersion due to its complex flow dynamics and turbulence characteristics. Therefore, replicating the ABL accurately in wind tunnel experiments is crucial for reliable urban air pollution studies.

At the University of Bristol, the new national Boundary Layer Wind Tunnel (BLWT) Facility provides a state-of-the-art platform for such investigations. A number of previous works have reported on characterising new wind tunnel facilities. For instance, Kuznetsov et al. [1] detailed the climatic wind tunnel at the Institute of Theoretical and Applied Mechanics (ITAM), specifically for precipitation and freezing effects, focusing on the streamwise effect of each Counihan method component. Kozmar [2] characterised the Technische Universität München (TUM) boundary layer wind tunnel to replicate rural, suburban, and urban flows. Various methods exist for generating an ABL in a BLWT, including active methods like air injection [3], spires with slats for limited space tunnels [4], and mesh grid and barrier combinations [5]. However, the most widely used approach is Counihan's method [6], with further modifications [7].

Our research began by characterising the wind tunnel's capabilities through baseline measurements of smooth-wall configurations to establish a reference point. The main focus was to generate the ABL using Counihan's method [5], involving a castellated barrier, quarter-elliptic wedge spires, and scaled roughness elements (Lego blocks) to simulate urban surface roughness. We systematically investigated the effects of these components on boundary layer dynamics. Extensive measurements using hot-wire anemometry (HWA) characterised the flow properties, including mean velocity, velocity fluctuations, turbulence intensity, and integral length scales. These measurements were compared with established datasets from sources such as the Engineering Sciences Data Unit (ESDU) [8] and Walshe [9] to validate the flow characteristics and ensure the reliability of our ABL simulations for future wind engineering research.

2 EXPERIMENTAL SETUP

The BLWT at the University of Bristol, spans $30\,m$ and is equipped with 9 axial, with a power requirement of $240\,kW$. Its multi-fan configuration allows for variable operational modes, achieving a steady flow velocity ranging from $0.5\,m/s$ to $35\,m/s$ with low free-stream turbulence levels. The test section measures $2\,m$ in width, $1\,m$ in height, and approximately $18\,m$ in length. It can naturally develop a boundary layer exceeding $200\,mm$ thickness ($Re_x \sim 9.5 \times 10^6$) [14].

For the experimental setup simulating the ABL, components were designed based on [6, 7 ,10], detailed in Figure 1, with $H = 900\,mm$ being the height of vortex generators, with a spacing of $0.6H$, and the height of the castellated barrier is $200\,mm$. The Lego blocks have a height of $60\,mm$, and they were in a staggered pattern with a spacing of $140\,mm$. The instrumentation included Dantec 55P15 single-wire probes for smooth wall configurations, and 55P51 cross-wire hotwire probes for ABL configurations, that were mounted on the linear traverse system SMC-LEFS32 of $1000\,mm$ stroke and a $0.01\,mm$ precision (along *y*-direction). The data acquisition was controlled using Labview. The calibration of the probes was conducted using a 54H10 calibrator and StreamWare Pro v6.00 software. Hotwire measurements were executed using a Dantec Streamline ProSystem equipped with a CTA91C10 module, interfaced with a National Instruments PXIe-4499 module housed in a PXIe-1082Q chassis for data acquisition. Data was sampled at a rate of $2^{16}\,Hz$, with sampling times initially estimated using [11], then optimised based on

DOI 10.5258/WES/P0016

several tests to be 100 s per measurement point. The streamwise distance between the last row of roughness elements and the probe is 700 mm.

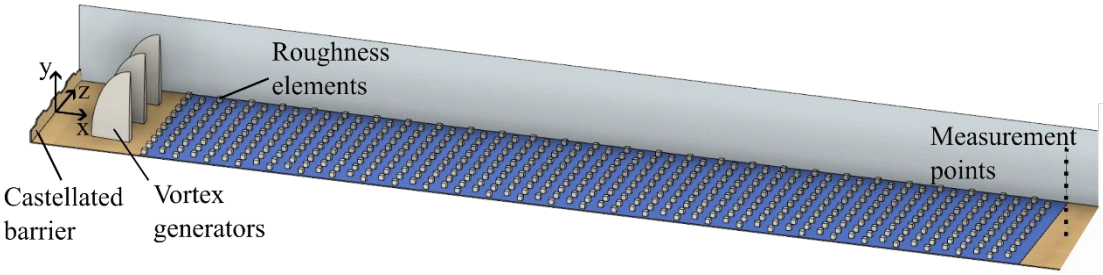

Figure 1: BLWT with arrangement of castellated barrier, vortex generators, and roughness elements .

3 RESULTS AND DISCUSSION

3.1 Empty test section

By measuring the velocity distributions along vertical lines (31 points in total) at *x=15.5 H* downstream of the entrance of the test section, at three different velocities $U_\infty = 10\ m/s$, $15\ m/s$, and $20\ m/s$, the airflow properties in the empty tunnel are evaluated. The mean flow velocities normalised by the free-stream velocity U_∞, turbulence intensities $I_u = \sqrt{\overline{u'^2}}\ /U$, with u' and U the fluctuating and mean velocity at each vertical position, respectively, and the spanwise homogeneity are illustrated in Figure 2.
The boundary layer thickness δ is estimated to be around 200 mm, based on $U = 0.99U_\infty$ at $y = \delta$, in an empty wind tunnel, which is in good agreement with the theory ($\delta = 0.37\ x\ {Re_x}^{-1/5}$). The turbulence intensity in the outer layer is less than 0.3%. The good collapse of the mean velocity profiles and turbulence intensities at different free-stream velocities is an indication of the stability of the wind tunnel performance.
To evaluate the spanwise homogeneity of the flow, we conducted HWA measurements at $z = -400\ mm, 0\ mm, 400\ mm$. The maximum deviation in mean velocity from the centre of the test section was found to be less than 3% of the free-stream velocity, which falls within the acceptable range [12]. This confirms that the flow is spanwise homogeneous.

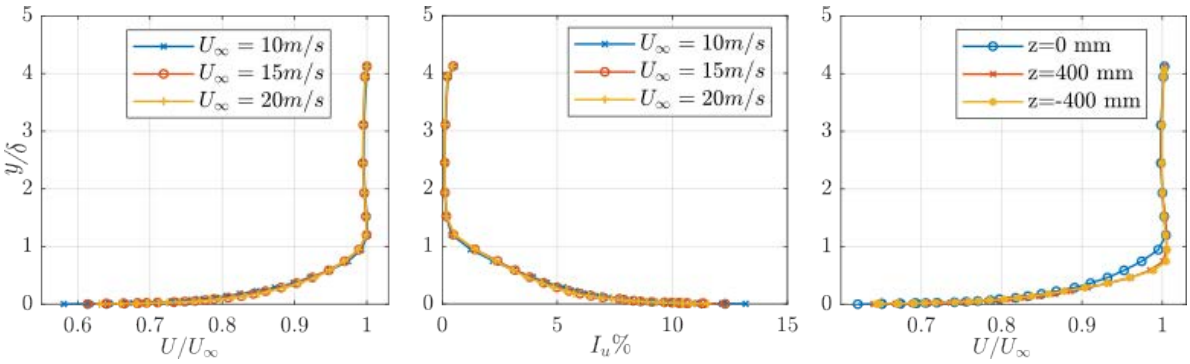

Figure 2: Profiles of (a) Normalised mean velocities at z=0, x=15.5H , (b) Turbulence intensities percentage at z=0, x=15.5H, and (c) Normalised mean velocities in three spanwise positions at x=15.5H .

3.2 Atmospheric boundary layer

Four boundary layer configurations were tested in the BLWT, to further investigate the individual effect of each component of the Counihan's method on the ABL profile parameters. The details of each test are described in Table 1.

Figure 3 shows mean velocity profiles, turbulence intensities, and integral length scales L_{ux} for the four different boundary layers tested. The integral length scales were estimated by calculating the integral of the autocorrelation ($L_{ux} = U \int R_{uu}(t)dt$, with R_{uu} being the autocorrelation) , and then were compared against those calculated using Walshe's method [9], i.e. $L_{ux} = 101\ (y/10)^{\alpha}$, with $\alpha = 0.3$ for urban flows.

DOI 10.5258/WES/P0016

Table 1: Conditions of each Boundary Layer (BL) tested.

BL	*Surface treatment*	U_∞ *(m/s)*	*Location*
BL1	*Vortex generators, roughness elements, and castellated barrier.*	*10*	*z=0 and x=15.5H*
BL2	*Roughness elements and castellated barrier.*	*10*	*z=0 and x=15.5H*
BL3	*Vortex generators and roughness elements.*	*10*	*z=0 and x=15.5H*
BL4	*Vortex generators and castellated barrier.*	*10*	*z=0 and x=15.5H*

As shown in Figures 3(a) & 3(b), and by comparing BL1 and BL4 profiles, the roughness elements effect is more prominent in the near-wall region through introducing higher velocity defect and enhanced turbulent energy in accordance with previous findings [5], and increased integral length scales. The outer region remains relatively comparable for the mean velocity. The effect of vortex generators or castellated barrier is less pronounced, by comparing BL2 & BL3 against BL1, as only a small increase in velocity deficit is observed in the absence of barriers. For the case with no castellated barrier BL3, there is a decrease in the turbulence in the outer region, compared to BL1, as confirmed in Hohman et al. [5], which shows that the castellated barrier improves the turbulence generation.

The effect of the barrier can also be seen in Figure 3(c), where the integral length scales of BL3 are out of the confidence interval of Walshe [9], which highlights its importance in ABL. There is a larger influence in generating turbulent energy with the barrier compared to the vortex generators. Further investigation on their effect on the spanwise homogeneity is necessary.

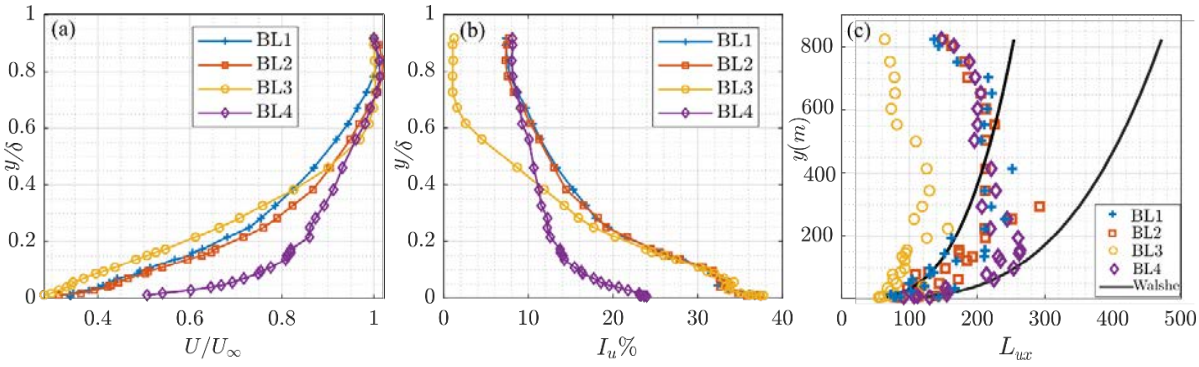

Figure 3: Profiles of the four boundary layers, (a) Normalised mean velocities, (b) Turbulence intensities , and (c) Integral length scales compared to ±30% Walshe confidence interval (y in full scale, with scale 1:800) .

To further investigate the suitability of BL1 as a representation of ABL in urban flow, Figure 4 (a) illustrates the power law, i.e. $U/U_{ref} = ((y-d)/(y_{ref}-d))^{\alpha}$, $with\ U_{ref}$, and y_{ref} being the mean velocity and height at a reference point.The power law exponent reached a value of $\alpha = 0.318$ that is in the range of urban flows according to ESDU [8], with d representing the zero-displacement height. In this study the zero-displacement height was found to be about $d = 9.32\ mm$. The turbulence intensity, shown in Figure 4 (b), is within the 30% confidence interval of the ESDU 85020 [8] up to a height of $300\ m$ in full-scale, which is widely used. The power sepctral density at $y = 255\ mm$, shown in Figure 4 (c), follows the Kolmogorov's $-5/3$ law [13], the spectra has a strong inertial subrange which is useful for structures wind loading future studies.

4 CONCLUSION

The BLWT at the University of Bristol was characterised for simulating urban ABL flows using Counihan's method. Measurements showed effective replication of ABL characteristics, with roughness elements enhancing near-wall turbulence and castellated barriers improving outer region turbulence. Validated against established datasets, the BLWT is considered suitable for urban air pollution and wind engineering research.

DOI 10.5258/WES/P0016

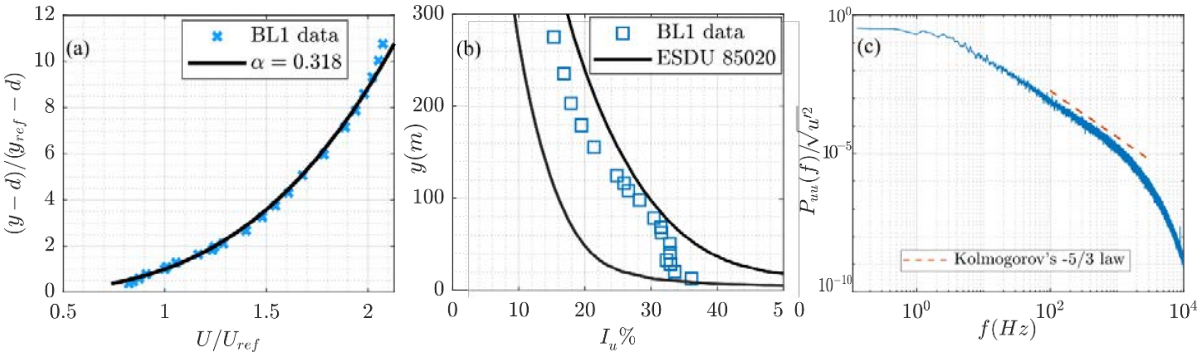

Figure 4: (a) Mean velocity profile compared to the power law with α=0.318, (b) Turbulence intensity compared to ±30% ESDU 85020 confidence interval (y in full scale, with scale 1:800), and (c) Power spectral density of BL1 at y=255 mm.

ACKNOWLEDGEMENTS

This project has received funding from the European Union's Horizon Europe research and innovation program under the MODELAIR project grant agreement No.101072559.

REFERENCES

[1] Kuznetsov, S., Ribičić, M., Pospíšil, S., Plut, M., Trush, A. & Kozmar, H. (2017). "Flow and turbulence control in a boundary layer wind tunnel using passive hardware devices", *Experimental Techniques*, *41*(6), 643–661.

[2] Kozmar, H. (2011). "Characteristics of natural wind simulations in the TUM boundary layer wind tunnel", *Theoretical and Applied Climatology*, *106*(1-2), 95–104.

[3] Schon, J. P. & Mery, P. (1971). "A preliminary study of the simulation of neutral atmospheric boundary layer using air injection in a wind tunnel", *Atmospheric Environment*, *5*(5), 299–311.

[4] Abdelwahab, M., Ghazal, T. & Aboshosha, H. (2022). "Designing a multi-purpose wind tunnel suitable for limited spaces", *Results in Engineering*, *14*, 100458.

[5] Cook, N. J. (1978). "Wind-tunnel simulation of the adiabatic atmospheric boundary layer by roughness, barrier and mixing-device methods", *Journal of Wind Engineering and Industrial Aerodynamics*, *3*(2-3), 157–176.

[6] Counihan, J. (1969). "An improved method of simulating an atmospheric boundary layer in a wind tunnel", *Atmospheric Environment*, *3*(2), 197–214.

[7] Hohman, T. C., Buren, T. V., Martinelli, L. & Smits, A. J. (2015). "Generating an artificially thickened boundary layer to simulate the neutral atmospheric boundary layer", *Journal of Wind Engineering and Industrial Aerodynamics*, *145*, 1–16.

[8] Engineering Sciences Data Unit. (1985). "Characteristics of atmospheric turbulence near the ground, Data Item 85020", ESDU International Ltd, London.

[9] Walshe, D. E. J. (1972). "Wind-excited Oscillations of Structures", National Physical Laboratory, 61-67.

[10] Gartshore, I. S. & De Croos, K. A. (1977). "Roughness Element Geometry Required for Wind Tunnel Simulations of the Atmospheric Wind", *Journal of Fluids Engineering*, *99*(3), 480–485.

[11] Hauptman, Z. (2010). "Characterization of a low-speed boundary layer wind tunnel". *Master's Theses and Capstones*, 549.

[12] Balendra, T., Shah, D. A., Tey, K. L. & Kong, S. K. (2002). "Evaluation of flow characteristics in the NUS-HDB Wind Tunnel", *Journal of Wind Engineering and Industrial Aerodynamics*, 90(6), 675–688.

[13] Kolmogorov, A.N. (1941). "The local structure of turbulence in incompressible viscous fluid for very large Reynolds numbers", *Proceedings of the USSR Academy of Sciences*, 30, 299–303.

[14] University of Bristol. (2024). Hele-Shaw Boundary Layer Wind Tunnel, Boundary layer WT. Available at: https://www.bristol.ac.uk/aerodynamics-research/facilities/boundary-layer/ (Accessed: 31 July 2024).

DOI 10.5258/WES/P0016

Bridging the Gap: Embedding 3D Details into Fast Deep-Learning Model for Pedestrian-Level Wind Prediction

Adam, Clarke.[1*] Knut Erik, Teigen, Giljarhus.[2,3] Luca, Oggiano.[3] Alistair, Saddington.[1] Karthik, Depuru-Mohan[1]
[1]Centre for Defence Engineering, Cranfield University, Defence Academy of the UK, Shrivenham, United Kingdom [2]Department of Mechanical and Structural Engineering and Materials Science, University of Stavanger, Stavanger, Norway [3]Nablaflow AS, Stavanger, Norway
[*] E-mail: adam.p.clarke@cranfield.ac.uk

Keywords: Machine learning, pedestrian comfort, pedestrian-level wind, skywalk, lift-up design, CFD

1 BACKGROUND

In urban areas, pedestrian comfort and safety are paramount considerations in architectural design. Traditionally, studies on pedestrian wind comfort rely on scale model testing or computational fluid dynamics (CFD), which are time-consuming and costly, hindering rapid iteration in early-stage design. This paper presents a deep learning approach for predicting pedestrian-level wind around buildings, focusing on skywalks and lift-up designs. Current research uses 2D projections of geometries, encoding height information to forecast time-averaged velocities at pedestrian height. Our approach embeds 3D details of the skywalks and lift-up designs into the projections, enabling the model to learn flow patterns around these structures and deliver predictions much faster than CFD solutions - We validate our deep learning model's performance on previously unseen configurations, demonstrating its effectiveness in accurately predicting pedestrian-level wind. This approach offers a valuable tool for architects, urban planners, and wind engineers design safer and more comfortable spaces in urban areas.

Lift-up designs provide sheltered outdoor areas beneath elevated buildings, allowing wind to penetrate and ventilate the surrounding areas, improving air circulation and thermal comfort while dispersing pollutants [1–3]. Skywalks enhance pedestrian safety, mobility and provide convenient links between buildings [4]. However, the flow patterns around such structures are often complex with the potential to create difficult conditions for pedestrians.

Recent machine learning approaches to pedestrian-level wind assessments have shown very promising results, with architectures including Convolutional Neural Networks, Generative Adversarial Networks, and Gaussian Process models [5–12]. Despite these advances, current methods use 2D projections of urban morphology, limiting their ability to predict flows around architectural features like bridges or lift-up designs. Weerasuriya, et al trained a neural network to predict flow velocities at discrete locations around isolated lift-up buildings [13] and optimise designs for pedestrian wind and thermal comfort, achieving inference times of less than one minute [14]. Our model can predict the three components of wind across an entire area in fractions of a second, capturing the flow characteristics and interactions between two buildings connected by a skywalk.

2 METHODOLOGY

We developed an automated pipeline to generate 490 unique, simplified geometries, each consisting of two buildings connected by a skywalk, using parametric design ***Figure 1***. The design space for the building geometries includes various dimensions for Building 1, the skywalk, and Building 2. The height (h) for Building 1 and Building 2 ranges from 10 to 100 metres, while the width (w) and depth (d) range from 10 to 80 metres. The distance from the ground (z) is either 0 or 3 metres, and the distance from the datum (y) is set at 0, 10, or 20 metres. The skywalk has fixed dimensions: a height of 3 metres, a width of 20 metres, and a depth of 3 metres. Its distance from the ground (z) is fixed at 6 metres, with the same distance from the datum (y) options as the buildings (0, 10, or 20 metres). We used a Latin hypercube sampling method to select combinations of geometries from the design space. Eight RANS CFD simulations with different wind directions were produced for each geometry using OpenFOAM's steady-state SIMPLE solver with a standard k-ε turbulence model employing the coefficients provided by Hargreaves and Wright [15]. The domain was cylindrical, with a diameter of 1600 m and height of 300 m. The inflow profile was logarithmic with a reference velocity of 5 m/s at 10 m height.

DOI 10.5258/WES/P0017

The CFD data was post-processed into pairs of 256x256 pixel images. The geometry data consisted of two channels containing the heights of the top and bottom of structures. The flow data comprised three channels storing the velocity components 2 m from the ground. The area of one pixel is 0.75 m². The generated data was split into training, validation, and test sets with a ratio of 7:2:1.

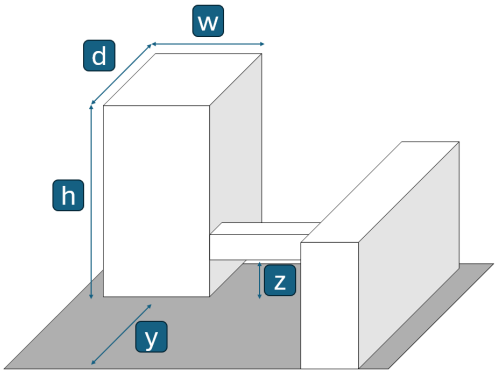

Figure 1, Schematic representation of the geometries.

The model used was an MLP-Mixer modified for this task introduced in [16]. It takes in the two-channel geometry data and returns a three-channel image representing the predicted flow field. A mean squared error (MSE) loss over all pixels was used as the objective function to train the model for 20 epochs, taking approximately 3 hours on a single A100 GPU and achieving a training loss of 0.000052.

3 RESULTS AND DISCUSSION

A test set containing 392 previously unseen geometries was retained to evaluate our deep learning model's performance. The mean inference time for a single image was 0.03 seconds, significantly faster than the CFD solution, which took approximately 4 hours giving the model great potential for uses in optimisation frameworks by facilitating rapid iteration. We used MSE, peak signal-to-noise ratio (PSNR), and structural similarity index (SSIM) to compare the deep learning predictions to the CFD predictions, following the framework introduced in [17]. These metrics provide a good indication of pixel-wise error, image quality, and perceptual error, the ability for humans to make accurate judgment. — These metrics are important in the preliminary design process where results are used to guide direction rather than quantification.

We conducted a series of experiments to determine the optimal set of hyperparameters for this model. We found that reducing patch size and neighbourhood benefits the model. However, the absence of neighbourhood mixing negatively impacts the model's performance, as it removes the ability to consider spatially local information. Conversely, a larger patch size and neighbourhood may introduce unnecessary complexity and noise overwhelming the model. While increasing the model's depth initially aids learning, excessive depth reduces effectiveness, indicating high variance and overfitting. Additionally, increasing the training data size from 30% to 100% of the combined training and validation sets significantly improves model performance. Although the rate of improvement slows between 70% and 100%, the results suggest that further performance gains might be possible with additional training samples.

The best model achieved an average SSIM of 0.991 and PSNR of 42.352 dB, indicating a high degree of similarity and quality when comparing the predictions and the ground truths. Our model captures complex wind flow behaviours around buildings, including downwash on the leading edges, updrafts on the leeward side of lift-up buildings, increased velocity as the wind wraps corners, and reversal of flow direction in the wake regions. ***Figure 2*** illustrates these captured flow features. Additionally, we are able to see that the model correctly predicts decreases in velocity in the vicinity of the skywalk.
To further assess the model's ability to generalise beyond the scope of the training data, we produced additional unseen test samples. These samples included an additional building upwind, designed as either a standard or lift-up structure, to interrupt the approaching flow. The model outputs demonstrated its ability to characterise the resulting flow around the buildings. However, a more in-depth study is

DOI 10.5258/WES/P0017

required to fully understand the extent of this capability, encompassing a variety of building densities, configurations, and morphologies.

One limitation of this study is the use of floating buildings in the CFD simulations for the lift-up design geometries. This simplification omitted the core of the building that would realistically support it. However, the results presented here demonstrate that 2D model inputs can be effectively enhanced by embedding a limited set of 3D information, providing the model with enough context to permit accurate predictions for structural design features such as lift-up structures and skywalks.

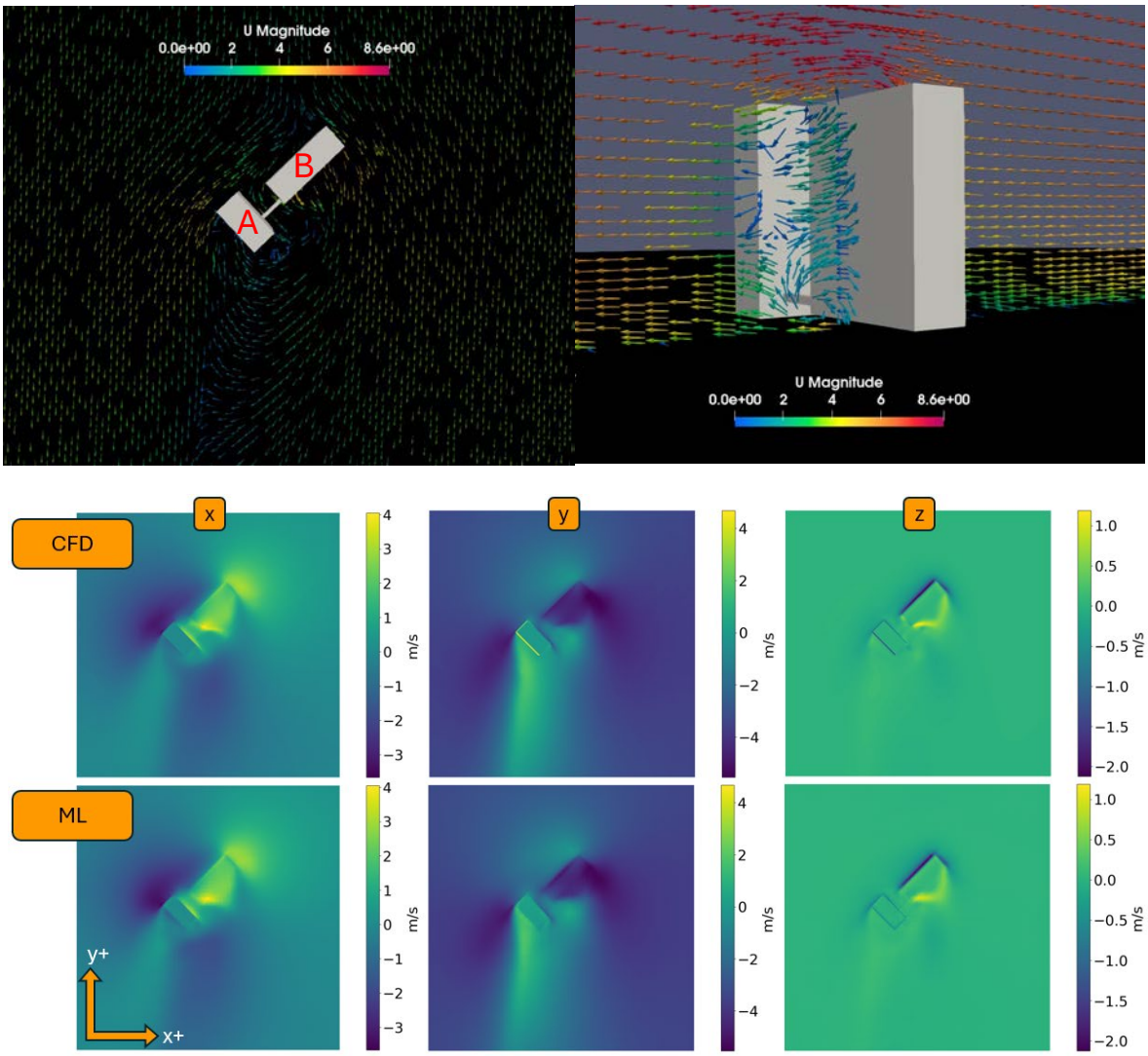

Figure 2, Top: Visualisation of the velocity magnitude computed by the CFD solver for the z-normal plane (left) and x-normal plane (right) for a single geometry with non-lift-up (A) and lift-up (B) buildings. Bottom: Comparison of model predictions and ground-truth for the x-, y-, and z-components of wind velocity for the same geometry.

4 CONCLUSION

This paper demonstrates the capability of a modified MLP-Mixer architecture in predicting pedestrian-level wind flows around lift-up designs and skywalks. The model effectively captures complex flow characteristics and correlates well with CFD solutions across MSE, PSNR, and SSIM metrics. Its high accuracy and rapid inference speed make it a valuable tool for preliminary designs. Further research is needed to explore the model's ability to generalise more complex morphologies. The framework presented here sets a precedent for using surrogate models for structures with intricate design elements such as cantilevers, podiums, and tunnels.

DOI 10.5258/WES/P0017

ACKNOWLEDGMENTS

Mr Clarke is pleased to acknowledge the contribution of the IMechE Whitworth Senior Scholarship Award in supporting this research. This research was supported by funding provided by Cranfield University (https://www.cranfield.ac.uk) and Nablaflow AS (https://nablaflow.io/).

REFERENCES

[1] Y. Du and C. M. Mak, 'Effect of lift-up design on pedestrian level wind comfort around isolated building under different wind directions', *Procedia Eng.*, vol. 205, pp. 296–301, Jan. 2017, doi: 10.1016/j.proeng.2017.09.979.

[2] Y. Du, C. M. Mak, J. Liu, Q. Xia, J. Niu, and K. C. S. Kwok, 'Effects of lift-up design on pedestrian level wind comfort in different building configurations under three wind directions', *Build. Environ.*, vol. 117, pp. 84–99, May 2017, doi: 10.1016/j.buildenv.2017.03.001.

[3] K. T. Tse *et al.*, 'Adopting "lift-up" building design to improve the surrounding pedestrian-level wind environment', *Build. Environ.*, vol. 117, pp. 154–165, May 2017, doi: 10.1016/j.buildenv.2017.03.011.

[4] L. Chen, C. M. Mak, J. Hang, Y. Dai, J. Niu, and K. T. Tse, 'Large eddy simulation study on pedestrian-level wind environments around elevated walkways and influential factors in ideal urban street canyons', *Build. Environ.*, vol. 235, p. 110236, May 2023, doi: 10.1016/j.buildenv.2023.110236.

[5] H. Hoeiness, K. Gjerde, L. Oggiano, K. E. T. Giljarhus, and M. Ruocco, 'Positional Encoding Augmented GAN for the Assessment of Wind Flow for Pedestrian Comfort in Urban Areas', Jan. 04, 2022, *arXiv*: arXiv:2112.08447. Accessed: Oct. 21, 2022. [Online]. Available: http://arxiv.org/abs/2112.08447

[6] A. V. Clemente, K. E. T. Giljarhus, L. Oggiano, and M. Ruocco, 'Rapid pedestrian-level wind field prediction for early-stage design using Pareto-optimized convolutional neural networks', *Comput.-Aided Civ. Infrastruct. Eng.*, vol. n/a, no. n/a, doi: 10.1111/mice.13221.

[7] P. Kastner and T. Dogan, 'A GAN-Based Surrogate Model for Instantaneous Urban Wind Flow Prediction', *Build. Environ.*, vol. 242, p. 110384, Aug. 2023, doi: 10.1016/j.buildenv.2023.110384.

[8] A. U. Weerasuriya, X. Zhang, B. Lu, K. T. Tse, and C. H. Liu, 'A Gaussian Process-Based emulator for modeling pedestrian-level wind field', *Build. Environ.*, vol. 188, p. 107500, Jan. 2021, doi: 10.1016/j.buildenv.2020.107500.

[9] S. Mokhtar, A. Sojka, and C. C. Davila, 'Conditional Generative Adversarial Networks for Pedestrian Wind Flow Approximation', *Soc. Model. Simul. Int. SCS*, vol. SimAUD 2020, p. 8, 2020.

[10] Y. Wu, Q. Zhan, and S. J. Quan, 'Improving local pedestrian-level wind environment based on probabilistic assessment using Gaussian process regression', *Build. Environ.*, vol. 205, p. 108172, Nov. 2021, doi: 10.1016/j.buildenv.2021.108172.

[11] J. Yamaguchi, T. Hasama, Y. Ito, S. Arisaka, and T. Saka, 'Prediction of mean wind velocity in city block area using machine learning by applying LES results to improve RANS results', presented at the 16th International Conference on Wind Engineering, 2023.

[12] B. Kim, D.-E. Lee, K. R. S. Preethaa, G. Hu, Y. Natarajan, and K. C. S. Kwok, 'Predicting wind flow around buildings using deep learning', *J. Wind Eng. Ind. Aerodyn.*, vol. 219, p. 104820, Dec. 2021, doi: 10.1016/j.jweia.2021.104820.

[13] A. Weerasuriya and K. T. Tse, *An ANN-based surrogate model for predicting pedestrian-level wind environment*. 2018.

[14] A. U. Weerasuriya, X. Zhang, B. Lu, K. T. Tse, and C.-H. Liu, 'Optimizing Lift-up Design to Maximize Pedestrian Wind and Thermal Comfort in "Hot-Calm" and "Cold-Windy" Climates', *Sustain. Cities Soc.*, vol. 58, p. 102146, Jul. 2020, doi: 10.1016/j.scs.2020.102146.

[15] D. M. Hargreaves and N. G. Wright, 'On the use of the k–ε model in commercial CFD software to model the neutral atmospheric boundary layer', *J. Wind Eng. Ind. Aerodyn.*, vol. 95, no. 5, pp. 355–369, May 2007, doi: 10.1016/j.jweia.2006.08.002.

[16] A. Clarke, K. E. T. Giljarhus, L. Oggiano, A. Saddington, and K. Depuru-Mohan, 'MLP-Mixer-Based Deep Learning Network for Pedestrian level Wind Assessment', presented at the Climate Informatics 2024, Apr. 2024.

[17] M. Gür and I. Karadag, 'Machine Learning for Pedestrian-Level Wind Comfort Analysis', *Buildings*, vol. 14, no. 6, Art. no. 6, Jun. 2024, doi: 10.3390/buildings14061845.

Large-scale wind study of the inner city of Rotterdam

Actiflow BV, Tramsingel 1, 4814 HB Breda, The Netherlands
Tel + 31 (0) 765 422 220, contact@actiflow.com, www.actiflow.com
Our reference: MUK20240419 Date: July 19, 2024

Introduction

In the Netherlands, most wind studies focus on pedestrian wind comfort near individual high-rise developments. The analysis is carried out according to the guidelines specified in the Dutch standard NEN8100:2006. As the city of Rotterdam is known for its high-rise buildings, the City is familiar with their impact on urban wind patterns. When considering all wind studies performed over the last few years, the City realised that for specific areas of the city, almost no wind studies are available. Furthermore, the question was raised about how to use the wind in the city in a positive way, e.g. for natural ventilation in summer, or to produce wind energy. To answer these questions, the city of Rotterdam turned to Actiflow, a Dutch consulting firm specialising in wind engineering.

Together, the City of Rotterdam and Actiflow decided to perform a wind assessment based on Computational Fluid Dynamics (CFD) simulations for a large area in the city: a region with a diameter of about 5.5 km in which all buildings were modelled explicitly. The project is regarded as a pilot project in which experiments are allowed and the main goal is to gather as much useful information as possible for the city.

3D model

For this project, the starting point is a large 3D model of the selected area in the city of Rotterdam in which all buildings and landscaping are modelled explicitly: see Figure 1. The 3D model of all buildings is generated automatically based on 2D map data and height data from LiDAR scans. The vegetation is modelled automatically based on 2D infrared images, height data and 3D wrapping methods. The model is then manually enhanced with relevant details of high-rise buildings, bridges, and other structures. Structures that cannot be generated by extrusion or those that are missing in the scan data are also added manually.

Figure 1: Visualisation of the 3D CFD model of the inner city of Rotterdam

Computational mesh

In preparation for the CFD simulations, a computational mesh is generated using snappyHexMesh from OpenFOAM v2312. The mesh is a conformal hex-core mesh with polyhedral cells between different levels of refinement. The largest edge length for the mesh is 64 m, with the smallest surface cells having an edge length of 0.25 m.

Edge sizes on the ground plane in the area of interest are 1 m to 2 m wide. Cell sizes on the buildings in the centre of the domain vary between 0.5 m to 4 m, except for the small 0.25 m features mentioned above. Vegetation is modelled using cellZones that are created at the meshing stage, with cell sizes that vary between 0.5 m and 2 m.

Five prismatic layers are requested on all building, ground and bridge surfaces. The buildings have a layer coverage between 80% and 90%. Most ground surfaces have a layer coverage of over 95%. These five prismatic layers have a growth ratio of 1.15 with a final layer thickness of 0.3 m.

The final mesh has 583,381,118 cells and was constructed in 21.5 hours on 1024 cores. Figure 2a shows a 2D cross section of the mesh at 10 m high for the area north of the Erasmus Bridge. Figure 2b shows the mesh in the same cross section, but zoomed in on the area just to the northwest of the bridge.

DOI 10.5258/WES/P0018

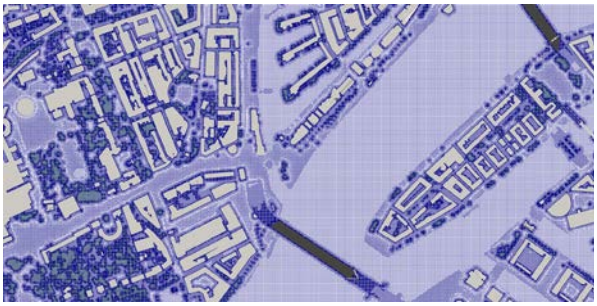

Figure 2a: Impression of the mesh

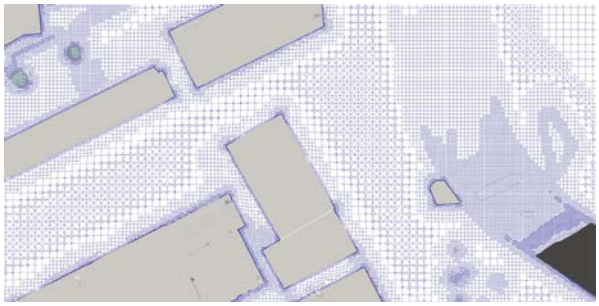

Figure 2b: Impression of the mesh zoomed in

Simulations, settings and boundary conditions

When following the Dutch NEN8100:2006 standard, CFD simulations must be performed for 12 wind directions. A neutral atmospheric boundary layer (ABL) profile was prescribed at the inflow part of the circular domain, while the outflow part was prescribed as a pressure outlet. Turbulence profiles for the ABL were added at the inflow part of the domain, with a zero normal gradient outflow. Turbulence close to walls is modelled using wall functions. On the outer parts of the ground plane, roughness was used to maintain the ABL up to the explicitly modelled inner domain. Turbulence is modelled using the k-omega SST model.

The simulations used simpleFoam, with convergence being determined by monitoring the forces acting on the various bridges. When the drag coefficient of these bridges varied by less than 1 count, results were averaged over the last 500 iterations. The simulations ran on Actiflow's cloud cluster using AWS parallelCluster technology. Each of the 12 simulations required about 4.75 hours running on 1536 cores spread across 16 nodes.

Processing of results with historical wind data

To calculate the wind comfort from the results of the CFD simulations, the velocity fields need to be processed with the local wind data. Initially, two different data sets at 60 m high are produced using an official tool as described in the Dutch NPR 6097 practice guideline (as required by the NEN8100 standard):

1. for a location exactly in the centre of the circular domain, which is located in the Maas River;
2. for a location about 2 km to the north of the centre of the domain, between buildings in the city centre.

When considering both wind statistics, there are some clear differences, mainly in the WSW and SSW directions (see Figure 3). This leads to the conclusion that the wind at 60m high above the city of Rotterdam is influenced by the local roughness of the city.

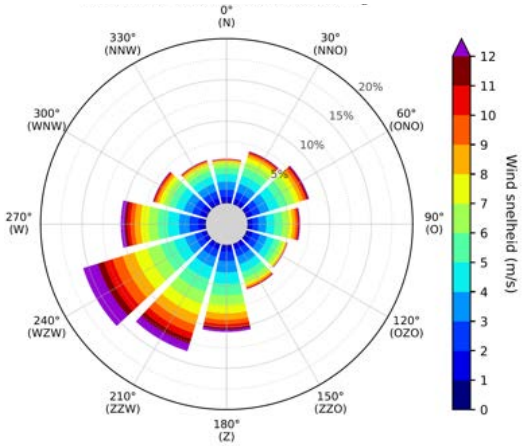

Figure 3a: Wind data for the centre of the domain

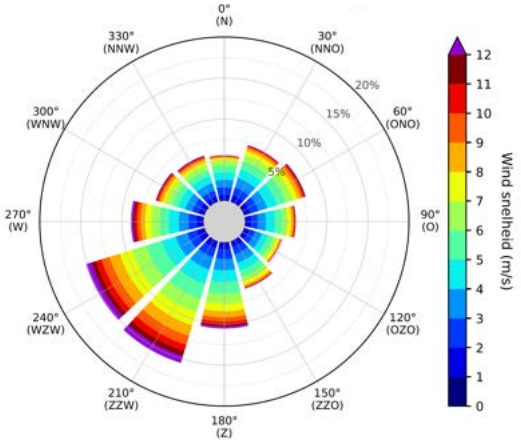

Figure 3b: Wind data for a location 2 km to the north

After processing the simulated velocity fields using both wind data sets, also the resulting pedestrian wind comfort fields show to be significantly different. To determine which result is more realistic, the results are compared with local wind assessments for individual developments, based on CFD, performed by Actiflow and one of its competitors. This comparison shows that both results of this project indicate significantly lower exceedances.

DOI 10.5258/WES/P0018

Based on the insights above it is suggested that, when processing the results with wind statistics for a single location in (the middle of) the computational domain, the local roughness of the city is accounted for twice:

- Once in the local wind data at 60 m coming from the NPR tool, and;
- Once again in the CFD simulations, by simulating the airflow over all buildings in the city explicitly.

When the domain gets larger, the effect of considering the roughness twice becomes more prominent, leading to lower wind speeds and lower exceedance percentages in the wind comfort fields.

To solve the problem above, it is decided to produce a new "combined" wind data set, based on the wind data of 12 different locations along the edge of the computational domain. The local wind data is gathered through the official NPR tool, but as an alternative, another "combined" wind data set is produced based on local wind data from the more recent HARMONIE cycle 40 wind data source as developed by the Royal Netherlands Meteorological Institute (KNMI). See Figure 4 for both combined wind data sets.

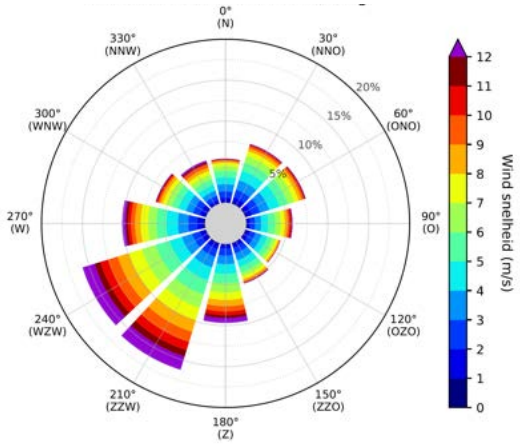

Figure 4a: Combined wind data based on NPR tool

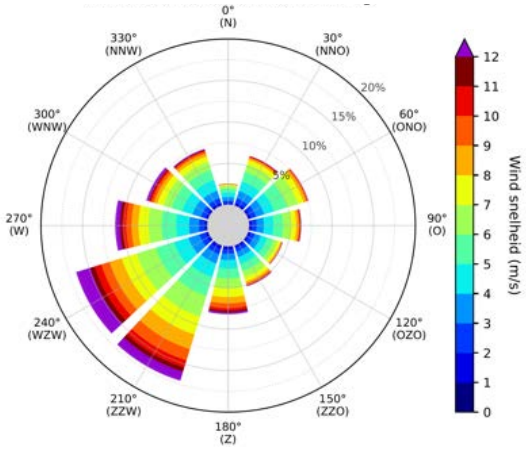

Figure 4b: Combined wind data based on Harmonie

When comparing the results of both "combined" wind data sets, the differences are small and do not significantly influence the result. When comparing the resulting wind comfort fields with the fields processed with the wind data from one single location in the domain, the exceedance rates are significantly higher and much closer to the results of the local wind assessments performed for individual developments in the city. Based on these results, it is decided to use the combined wind data based on the official NPR tool (Figure 4a) for further analysis.

Results

Given the size of the computational domain, not all results can be presented in this 4-page summary. Therefore, only the following results will be presented here: (i) Annual wind comfort according to NEN8100:2006; (ii) Natural ventilation in the city.

Annual wind comfort

The annual wind comfort for the entire domain according to NEN8100:2006 (at 1.75 m above ground level) is presented in Figure 5. Table 1 shows the definition of the wind classes according to the NEN standard.

Exceedance probability (p) (Local wind speed > 5 m/s) (% of the total hours per year)	Wind comfort class	Classification per activity		
		Walking	Strolling	Long-term sitting[a]
p < 2.5 % (< 219 hours)	A	Suitable	Suitable	Suitable
2.5 % ≤ p ≤ 5 % (219-438 hours)	B	Suitable	Suitable	Acceptable
>5 % ≤ p ≤ 10 % (> 438-876 hours)	C	Suitable	Acceptable	Unsuitable
>10 % ≤ p ≤ 20 % (> 876-1752 hours)	D	Acceptable	Unsuitable	Unsuitable
p > 20 % (1752 hours)	E	Unsuitable	Unsuitable	Unsuitable

Table 1: wind classes according to NEN8100:2006

DOI 10.5258/WES/P0018

The presence of the Maas River is clearly visible in the result. When considering Figure 5 in more detail, it can be seen that large parts of the city have class A or B categories, indicating a calm wind climate.

Wind classes C, D and E are typically found on bridges and in areas with high-rise buildings like the central station area and "Kop van Zuid", as could be expected. Both areas are indicated in Figure 5 by blue circles. However, also some regions that are not regarded as high-rise regions appear to have windy conditions, which was not expected at first. This mostly occurs in areas close to the borders of the River, indicated by red circles. As these areas were not regarded as high-rise areas, the city did not request any wind assessments for new developments in these areas until now.

Figure 5: wind comfort according to NEN8100:2006

Natural ventilation

The natural ventilation is expressed as the probability of exceeding 2 m/s (see Figure 6), where low exceedance (poor natural ventilation) is indicated in red, while high exceedance (good natural ventilation) is indicated in blue. A probability of 50% is indicated in grey.

When neglecting the River area, in large areas of the city the natural ventilation is rather poor. When considering the ventilation of pollutants due to traffic in the most high-density roads (as indicated in black), the probability of exceedance ranges between 10% and 60%. In places where buildings are close to each other, the ventilation is poor, while in more open spaces, the ventilation can be considered acceptable.

When the urban climate is considered, the result of this analysis should be combined with information about solar shading and the use of building materials to draw any conclusions. For example, regions with low natural ventilation, but with lots of trees, might still have a good climate. The City of Rotterdam has more information about vegetation and solar shading in the city and will combine all information with the goal to have a better insight in the urban climate.

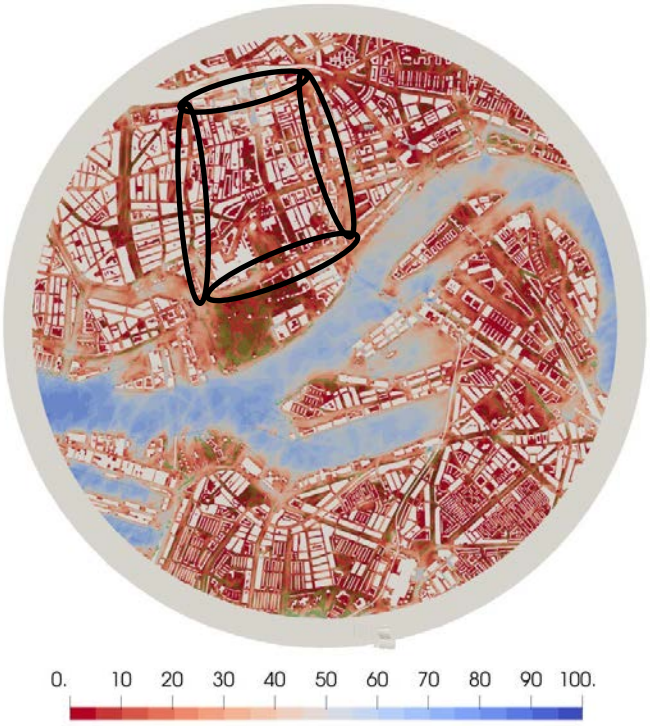

Figure 6: Probability of exceedance of 2 m/s

Besides the results shown in this summary, Actiflow's presentation at the UK Wind Engineering Conference will include more detailed information about the results, and will include among others:

- Wind comfort according to the LDDC Lawson Comfort Criteria
- Potential for wind energy production in the city
- An example of a real-time wind map of the city

DOI 10.5258/WES/P0018

Dynamic Calibration of Low-Cost Gas Sensors for Dispersion Experiments

Paul Hayden and David M. Birch*
Centre for Aerodynamics & Environmental Flow, Faculty of Engineering & Physical Sciences,
University of Surrey
Guildford, Surrey
* E-mail: d.birch@surrey.ac.uk

1 INTRODUCTION

Simulating pollutant dispersion in a wind tunnel is normally achieved using passive tracer gases. Currently, the only available technology for measuring gas concentration with sufficient bandwidth for time-domain correlations is the fast-flame ionization detector (FFID), which is able to measure hydrocarbon concentrations down to low PPM, with bandwiths up to 200 Hz. This is a complex and costly instrument with a large probing head and bulky umbilical, making it unsuitable for rake-type arrangements. In addition to its large size, the probing head generates waste heat and exhaust gas, and can therefore be very intrusive.

On the other hand, platinum-catalyst pellistor sensors for hydrocarbon concentration are a mature technology; commonly used in safety applications, they are inexpensive and readily available from a number of commercial suppliers. Although commercially available pellistors are quite small (~20 mm diameter) compared to FFID heads, they have a fairly large sampling volume and a very low bandwidth (as low as 0.02 Hz).

A technique has therefore been developed to dynamically calibrate pellistor sensors, in order to provide a much less intrusive alternative to FFID for tracer gas measurement in turbulent flows. In addition, the small size and low cost of pellistor probes would enable the deployment of spatially-resolved rakes of concentration probes, providing otherwise unavailable simultaneous spatial correlations and significantly reducing required wind tunnel run times.

2 METHODOLOGY

A commercially-available ATEX-compliant pellistor sensor having a sensitivity of ~3mV/1000 PPM, an RMS signal noise of ±8 PPM and a bandwidth of 0.06 Hz to 0.12 Hz (figure 1a) was fitted with a sealed plenum chamber (of volume ~150 mm^3) with an inlet and exhaust that allowed the sample gas to flow evenly over the 14-mm diameter sensing surface. The plenum was fed with a mixture of clean air and a 15,000 PPM propane-air tracer solution (at a total flow rate Q < 1.5 L/min), and a computer-controlled servovalve was used to control the mixture ratio. Great care was taken to balance the back pressure in the gas systems, and to ensure complete mixing upstream of the sensor. The resultant tracer concentration C could then be controlled via the servovalve to provide an arbitrary, time-varying $C(t)$ in the plenum. The sampling tube from a FFID probe (Cambustion model HFR400) was also inserted into the plenum, in order to provide a reference concentration C_{ref}. in the plenum. The sampling tube had an inner diameter under 1 mm and was ~300 mm long; although it is understood that the length of the FFID sampling tube causes a signal time shift (which is typically calibrated out), the absolute timing of the concentration signals were not relevant in this case.

Analogue signals from the pellistor and reference FFID were acquired simultaneously using a typical 16-bit data acquisition system, and no analogue signal conditioning or filtering was used for the pellistor.

2.1 Dynamic calibration

A dynamic calibration of the pellistor was then carried out using a discrete spectral reconstruction technique often applied for pressure-based measurement systems [1]. The servovalve was actuated to provide the plenum with a concentration that varied nearly sinusoidally in time (figure 1b), with amplitudes adjusted as required to ensure consistent peak concentrations. The spectral energies of the signals $C(t)$ and $C_{ref}(t)$ were compared over a narrow band around the forcing frequency to obtain the gain G and phase shift ϕ at each forcing frequency f_0 (figure 2). As would be expected for a low-

DOI 10.5258/WES/P0019

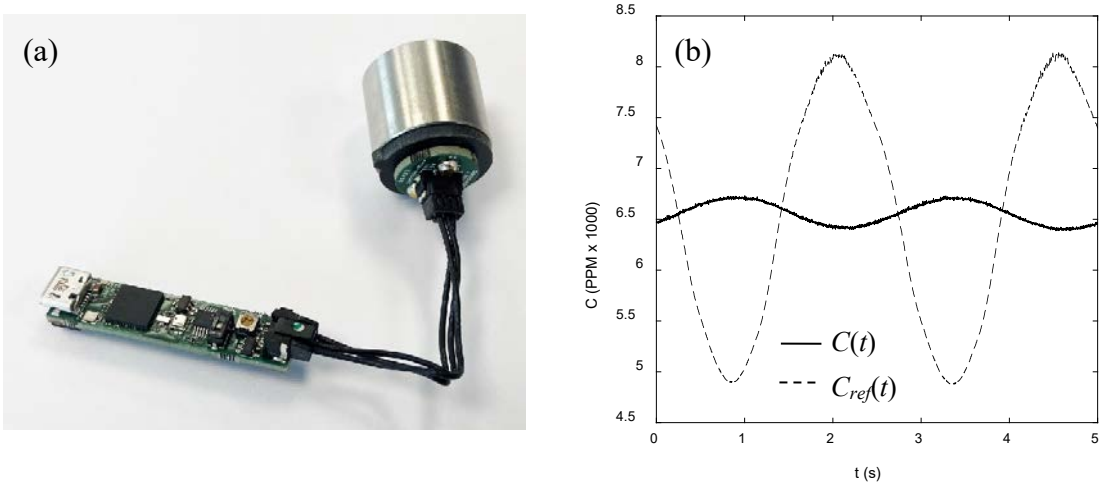

Figure 1: (a), Pellistor sensor system; (b), calibration signal.

bandwidth instrument, G decreases rapidly with increasing f_0, to a minimum of $G \sim 0.004$ at $f_0 = 2$ Hz. It should be noted that this high level of gain also resulted in the signal noise being amplified to a level equivalent to ±2000 PPM at 2 Hz. Continuous functions $G(f)$ and $\phi(f)$ were then inferred by third-order interpolation.

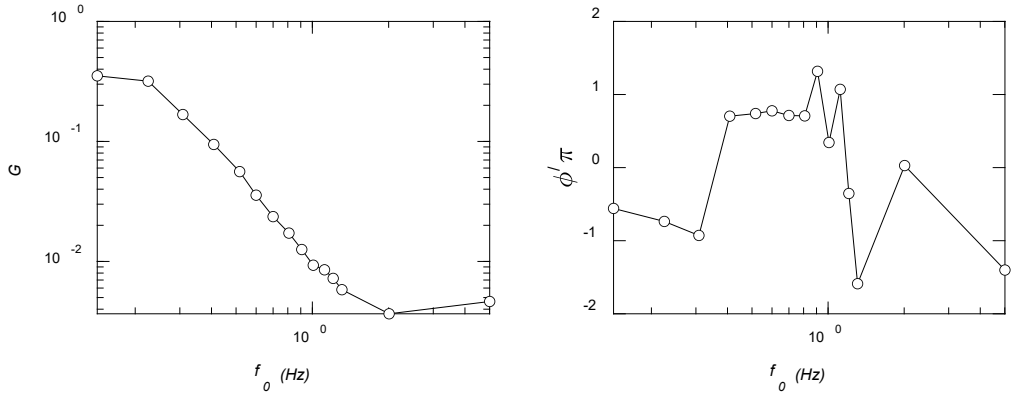

Figure 2: Dynamic calibration results. Left, gain; right, phase shift.

During measurement, the spectral decomposition of the pellistor signal was obtained by fast-Fourier transform (FFT); the amplitudes were rescaled by $G(f)$ and phases were shifted by $\phi(f)$. The signal was then low-pass filtered at 1.7 Hz, and the filtered time-domain signal was reconstructed by inverse FFT.

3 RESULTS AND DISCUSSION

To test the effectiveness of the dynamic calibration, the concentration in the plenum was varied arbitrarily in time using a test signal $C(t)$ which was designed particularly to challenge the pellistor. Figure 3 compares the resultant C_{ref} with both the raw pellistor signal and the dynamically calibrated signal. The process of dynamic calibration yielded a significant improvement in the time response of the pellistor, reducing the mean square error $\varepsilon = \text{mean}(C\text{-}C_{ref})^2/C_{ref}^2$ from 0.11 to 0.0071 over the range shown. A high-frequency 'ringing' in the calibrated signal remains, as a result of the poor signal-to-noise ratio at higher frequencies.

Figure 4 compares the same dynamically calibrated signal and reference concentration in the spectral domain. Again, the two agree very well for $f < 1.5$ Hz. Over the range 1.5 Hz $< f <$ 1.66 Hz, the poor

DOI 10.5258/WES/P0019

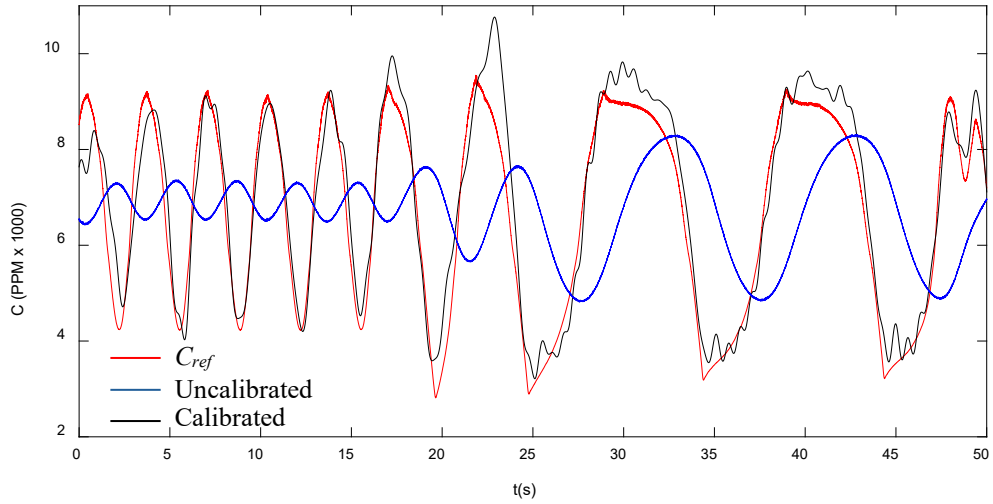

Figure 3: Response of dynamically calibrated pellistor to an arbitrary signal.

signal-to-noise ratio results in a weaker agreement, as the amplification of signal noise begins to dominate. For $f > 1.66$ Hz, the pellistor signal becomes vanishingly small as a result of the low-pass filter applied.

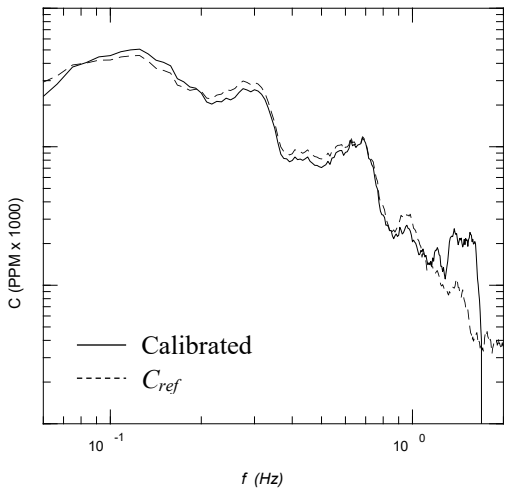

Figure 4: Spectral comparison of C and C_{ref} following dynamic calibration.

The good agreement shown here demonstrates that it is indeed possible to significantly improve the time response of low-cost pellistor sensors by applying a discrete-frequency dynamic calibration techniques developed for use with ultra-low range pressure sensors. Given that no analogue signal pre-conditioning was applied, these results demonstrate that the bandwidth of a pellistor sensor can be increased by at least a factor of 14, to 1.66 Hz.

4 CONCLUSIONS AND FUTURE WORK

Although the bandwidth remains too small for a dynamically-calibrated pellistor sensor to entirely replace FFID for time-domain tracer concentration measurements, there are some atmospheric wind-tunnel tracer concentration measurement applications in which the bandwidths of interest are very low, with frequencies of interest of order 10 Hz [2]. In stratified wind tunnels particularly the time-scales can be even lower [3]. Furthermore, because of their low cost and size, rakes of pellistor sensors are a

DOI 10.5258/WES/P0019

tractable means of acquiring mean concentration field data without the extensive time required for pointwise scans, offering a powerful complementary capability to conventional FFID. On the other hand, a bandwidth of 1.6 Hz is sufficient to yield well-resolved time-domain measurements in field applications.

The results shown here were based on raw (unconditioned) signals from a pellistor sensor developed for explosion safety purposes. With appropriate analogue signal pre-conditioning (gain and filter), it is expected that the signal-to-noise ratio of the sensor can be significantly improved at higher frequencies, and the usable bandwidth increased. Furthermore, the response time of the pellistor may be dominated by the effect of the anti-explosion porous shield covering the catalyst, through which the sample gas must diffuse. It is possible that the time response may be further improved by modifying the design of the plenum.

REFERENCES

[1] Stefe, M., Svete, A. and Kutin, J. (2016) “Development of dynamic pressure generator based on a loudspeaker with improved frequency characteristics,” Measurement, vol.122, pp. 212–219, 2016.

[2] Papp, B. Istok, B. Koren, M, Balczo, M, and Kristof, G. (2024) "Statistical assessment of the concentration fluctuations in street canyons via time-resolved wind tunnel experiments." Journal of Wind Engineering & Industrial Aerodynamics 246 (2024) 105665

[3] Marucci,D. and Carpentieri, M. (2019) “Effect of local and upwind stratification on flow and dispersion inside and above a bidimensional street canyon,” Building and Environment, vol. 156, pp. 74–88, 2019.

DOI 10.5258/WES/P0019

Cloud dispersion in complex flows

Author Name(s): Alan, Robins[1]; Paul Hayden[1]; Thomas Richards[1]; David Gallacher[2]
[1] Department Mechanical Engineering Sciences, University of Surrey, Guildford, UK
[2] Medical Physics Department, Guy's and St Thomas' NHS Foundation Trust, London, UK
[1] E-mail: a.robins@surrey.ac.uk

1 INTRODUCTION

Recent experimental work, say in the last 50 or so years, with short duration emissions can be conveniently divided between field work in the USA at the US Army Dugway Proving Ground and in Oklahoma City, and wind tunnel simulations in Europe. Both have used urban or urban-like sites and open terrain. A full list of references to this work, summarised below, is to be found in [6].

Experiments at the Dugway site, an open area of low surface roughness, used passive emissions from a source at height 2.5m and were conducted over downwind fetches between about 200 and 1200 m under a wide range of atmospheric conditions, from very unstable to moderately stable stratification from Ensemble sizes varied from order 20 in the early work to order 200 in the later work, where off-centreline data was used to increase the ensemble size. Relevant work in Oklahoma City took place in 2000. Data from 10 fast-response tracer samplers were used to examine crosswind and along-wind spread, the decay of tracer concentrations, and the retention of tracer. Three to six puffs were released in each of ten experimental periods and dispersion studied over fetches up to about 1 km. A detailed wind tunnel study using a 1:300 scale model of the Oklahoma field site was also carried out, using emission durations between 0.3 and 2s and reference velocities in the range from 2.4 to 4.2ms^{-1}. The experiments investigated the validity of standard puff scaling parameters, using ensembles of order 200 to 400 to ensure good convergence of statistical properties.

The work described here begins with Robins and Fackrell [1], a wind tunnel study of the dispersion of short duration, ground level emissions in a deep turbulent boundary layer, modelling the atmospheric boundary layer. This focused of comparison with the analytical theory developed by Chatwin [2]. Next, we have the DAPPLE project that ran from 2002 to 2010 and treated short range dispersion in central London [3]. In addition to a series of 15-minute releases in the field, a set of wind tunnel experiments was carried out to examine cloud dispersion and the causes of variability. Some simple correlations were developed for cloud travel time, rise and fall time and advection speed, as functions of fetch in the near field. Further wind tunnel cloud dispersion studies were carried out in the DIPLOS project, where the underlying geometry was a regular array of cuboids. DNS simulations of these experiments have been reported in [4] and shown to agree well with the wind tunnel data. Most recently, wind tunnel studies of cloud dispersion in the presence of a surface mounted cube were reported in [5], the ADMLC project.

1.1 Objectives

In this paper, we address the short-range dispersion of pollutant clouds emitted from elevated sources, using wind tunnel data from the projects referred to above [1, 3, 4, 5]. The objective is to use the concentration measurements to describe the structure of the dispersing clouds and to develop simple scaling rules that reduce the data to universal forms and can therefore be used in a predictive manner. The methodology follows that described in [6].

First, a comment on the structure of dispersing clouds. Where the emission duration exceeds the time of flight ($T_s > T_{flt}$), the cloud has a plateau region and we might term this as being plume-like (but with end regions of course). Further downwind, where $T_{flt} \gg T_s$, the structure becomes puff-like as longitudinal spread has fully eroded the plateau region. How quickly this is established depends on the level of ambient turbulence and shear, and most importantly the emission duration. Between the two limiting regions, there is an intermediate regime, where the form should perhaps be simply referred to as a cloud.

DOI 10.5258/WES/P0020

2 DISPERSION STUDIES

[1] demonstrated the key difference between the puff and plume regimes, characterised cloud structure and development and showed their alignment with Chatwin theory [2]. We now extend the empirical side of that work to complex flows in the presence of, first a single large cube and, second an array of obstacles.

2.1 Cloud dispersion around a cube

The work was carried out in a neutrally stable boundary layer, simulated by use of Irwin spires and a rough surface. The friction velocity and roughness length were $0.055U_{ref}$ and $0.001H$, respectively, where U_{ref}, the reference speed, was 2ms^{-1} and H, the boundary layer depth, 1m.

The cube, side h = 0.24m, was located with the centre of its base at the coordinate origin and, in the work described here, was orientated so that the oncoming flow as normal to the front face. Emissions were made from a source of height 0.06m, located 0.6m up of the cube centre. Large numbers of clouds were released in each case studied to ensure low standard errors in derived results, such as dosage; typically, the number of cloud emissions in an ensemble, N, was N = 200-399 for an emission time, T_e = 0.05s; 170-399 for 0.1s; 150-200 for 0.25s; 120-250 for 0.5s; 100-120 for 1.0s. These emission times allowed the full range of cloud behaviour to be observed.

Concentration measurements were made with either a Cambustion HFR400 or HFR500 Fast Flame Ionisation Detector (FFID) that had a spatial resolution of the order of 1 mm and a frequency response of about 200 Hz, the output being sampled at 400 Hz. Concentrations, C, and dosages, D, were made dimensionless as C^* and D^*:

$$C^* = \frac{CU(h)h^2}{q} \qquad D^* = \frac{DU(h)h^2}{T_e q}$$

where h is the building height, q the tracer emission rate and T_e the emission duration.

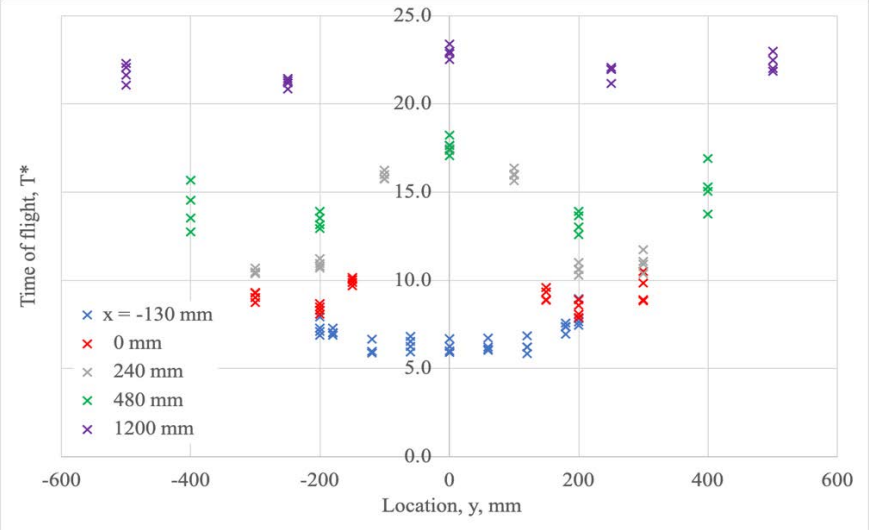

Figure 1. The dimensionless travel time, T, for the 2 ms^{-2} experiments.*

Fig. 1 demonstrates the distortion of the cloud as it passes around the cube and moves downwind. It shows mean time of flight results, determined from moments of the ensemble averaged concentration time series in clouds of emission durations: 0.1, 0.25, 05 and 1s. The profile at x = 240mm passes through the near wake of the cube and clearly shows the hold-up of the clouds in that region. This is equally pronounced at x = 480mm, but has largely disappeared at the furthest downwind profile, x = 1200mm. No distinction in emission duration has been made in plotting the results. T^*, has been adjusted to remove effects of the initial time origin offset, t_o, and the duration of the emission, T_e.

$$T^* = \frac{U_{ref}\left(T_{flt} - t_o - T_e/2\right)}{H}$$

DOI 10.5258/WES/P0020

A useful empirical formulation for the near wake residence time is that used in ADMS [14]. Time series from the near-wake region, shown in Fig. 2, confirm that this holds in the cases here. The figure shows results at two reference speeds and two emission durations – concentrations have been normalised and profiles overlapped according to time of flight.

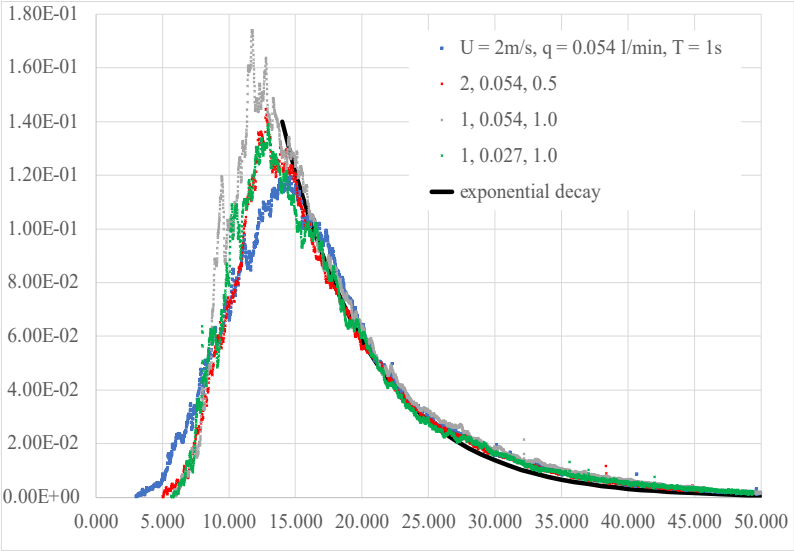

Figure 2. Normalised concentration time series from the near wake for a range of reference speeds, emission durations and emission rates. The thick, black line is the empirical exponential decay relationship from ADMS [7].

The dataset enables the relationship developed in [6] between dimensionless plume concentrations and cloud doses to be demonstrated for a much more complex flow, namely that:

$$D = C.T_e$$

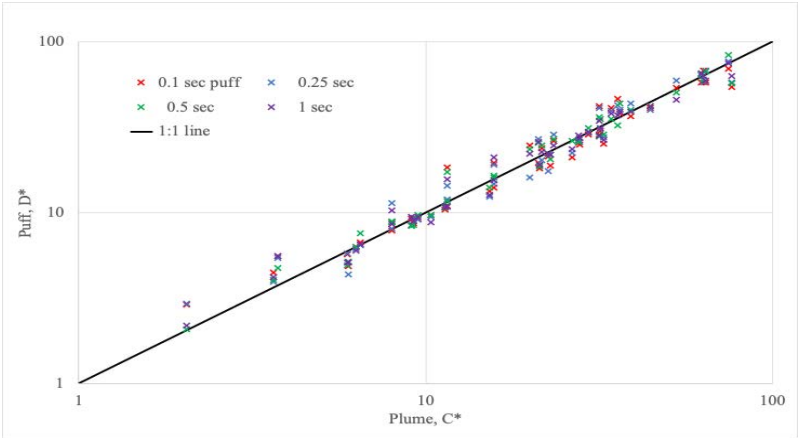

Figure 3. Scatter plot of dimensionless cloud dosage and plume concentrations.

2.2 Cloud dispersion in obstacle arrays

Finally, we show a further demonstration for a complex flow, this from the DIPLOS study [4], Fig. 4, using a large, regular array of cuboids. The source was at ground level at $x = y = 0$, diameter = h, the block height; the cloud release duration was T_e = 0.3s. Mean dosage profiles were formed from 47, 47, 49 individual runs, implying a standard error in the means of about 10%. The averaging time for the mean plume concentration was 150s, implying a standard error of about 5% in the central part of the plume.

DOI 10.5258/WES/P0020

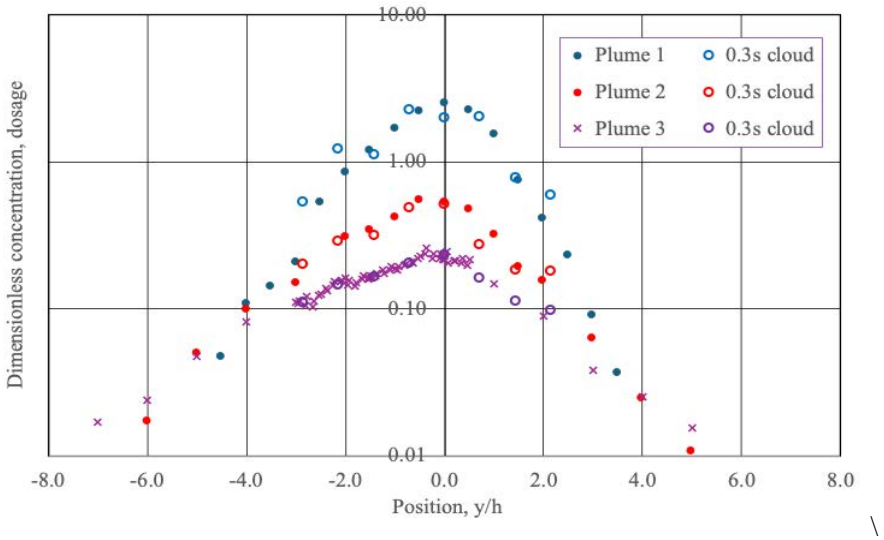

Figure 4. Lateral profiles of dimensionless mean concentration and dosage at x/h = 1, 7, 15, z/h = 0.5 in the DIPLOS array; h = block element height.

3 CONCLUSIONS

This work continued the theme of [6], demonstrating the correspondence between dimensionless cloud dosage and plume concentration in complex flows. The result provides a simple means of estimating dosage from a passing cloud from prediction of plume dispersion.

The work also demonstrated the distortion of pollutant clouds as they interact with obstacles. Here, the imposition of an additional time scale from the near wake has been highlighted.

REFERENCES

[1] Robins, AG and Fackrell, JE, 1998. An experimental study of the dispersion of short duration emissions in a turbulent boundary layer. Transactions on Ecology and the Environment vol 21, 697-707.

[2] Chatwin, PC, 1968. The dispersion of a puff of passive contaminant in the constant stress region. Quart. J. R. Met. Soc., 94, 350-360.

[3] Wood, CR, Arnold, SJ, Balogun AA, Barlow JF, Belcher, SE, Britter, RE, Cheng, H, Dobre, A, Lingard, JJN, Martin, D, Neophytou, MK, Petersson, FK, Robins, AG, Shallcross, DE, Smalley, RJ, Tate, JE, Tomlin, AS and White, IR, 2009. Dispersion experiments in central London - The 2007 dapple project. Bull. Amer. Meteor. Soc., July 2009, 955-969.

[4] T Auerswald, K Klippel, TG Thomas, EV Goulart, M Carpentieri, P Hayden, D. Hertwig, N Reis Jr., A Robins and O Coceal, 2024. Effect of Flow Variability on Dispersion of Continuous and Puff Releases in a Regular Street Network. BL Met 190, 20.

[5] Woodward, H, Gallacher, D, Robins, A, Seaton, M and ApSimon, H, 2020. A review of the applicability of Gaussian modelling techniques to near-field dispersion. In Atmospheric Dispersion Modelling Liaison Committee Report, ADMLC-R11, (January 2021). https://www.gov.uk/government/groups/uk-atmospheric-dispersion-modelling-liaison-committee-admlc#publications..

[6] Robins, A, Hayden P, Gallacher, D, Pace, S, Chaloupecka, H, 2021. Variability in the Short-Range Dispersion of Passive, Short-Duration Emissions. Annals of Biostatistics & Biometric Applications 2021 4(1) ABBA.MS.ID.000584.

[7] Robins, AG, Apsley, DD, CERC, 2023. Modelling of building effects in ADMS. ADMS Paper P16/10Y/23, https://www.cerc.co.uk/environmental-software/technical-specifications.html.

DOI 10.5258/WES/P0020

Towards efficient scale resolving simulation for the prediction of industrial pollutant dispersion applications

Salvatore Manuel Renda[1*], Apostolos Krassas[1], Eugene De Villiers[1], Stefano Capra[2]
[1] *ENGYS UK, Studio 20, Royal Victoria Patriotic Building, John Archer Way, London SW18 3SX*
[2]*Ramboll Denmark, Hannemanns Allé 53, Copenhagen, 2300*

[*] *E-mail: s.renda@engys.com*

1 INTRODUCTION

Urban areas face significant challenges in managing gaseous pollutant emissions, which have direct implications for public health and urban planning. Predicting and managing the dispersion of pollutants is crucial for designing sustainable cities. In this context, Computational Fluid Dynamics (CFD) constitutes a powerful tool that can offer accurate predictions and provide insights on the mechanisms that drive dispersion.

The suitability of different computational methodologies for urban physics modelling applications has been a topic of extensive research and discussion over the last decades [1], [2]. In this context, our recent study [3] assesses how a Large Eddy Simulation (LES) model compares to the industry workhorse Reynolds Averaged Navier Stokes (RANS) turbulence modelling approach in predicting contaminants' dispersion over the Tokyo's Polytechnic University Atsugi campus. The numerical data were compared to wind tunnel experimental measurements available in literature [4]. The results of the study outlined the predominance of high-fidelity LES modelling in accurately reproducing complex flow patterns and predicting concentration distributions. However, one of the main outcomes was that the computational cost entailed in conducting LES simulations might be excessive in an industrial context where fast turnaround times are key, thus making RANS a more viable solution. The question that naturally arises from these observations is how can scale resolving simulations become more cost-effective.

Focused on addressing this point, the scope of the current study is to explore how the use of an implicit low dissipative pressure-velocity block-coupled solver, optimized to run at increased time-step size can impact the turnaround times and accuracy of scale resolving simulations.

2 METHODOLOGY

2.1 Numerical setup & data organizing

The study was aimed at replicating the wind tunnel experiment [4]. A 14 million cells hex-dominant mesh was created using HELYX®, an open-source CFD simulation software, and the Finite Volume Method (FVM) was used for solving the governing equations. A time-dependent inflow velocity profile, obtained by performing a LES precursor simulation of the actual wind tunnel geometry was used as inlet boundary condition. More details concerning spatial discretization, numerical setup and data organizing methodology can be found in [3].

2.2 CFD experiment outline

To sufficiently assess and quantify the potential benefits of the block-coupled solver, the performance of two segregated algorithms, namely PISO (Pressure-Implicit with Splitting of Operators) and transient SIMPLE (Semi-Implicit Method for Pressure Linked Equations), are also evaluated. The standard PISO algorithm operates by performing a predictor step to estimate the velocity field and then applying multiple corrector steps to adjust the pressure field and correct the velocity to ensure mass conservation. PISO is known to be particularly effective for transient simulations, as it provides better convergence and accuracy by repeatedly refining the solution within each time-step. The transient SIMPLE algorithm incorporates the iterative pressure correction of PISO with the robust handling of non-linearities typical of SIMPLE. For each time-step SIMPLE allows for multiple outer corrector steps similarly to PISO but can also performs additional inner iterations to stabilize the solution, making it suitable for transient scale resolving simulations with complex flows at larger time-steps. This hybrid approach of SIMPLE generally offers a balance between accuracy and computational efficiency, especially for cases where

DOI 10.5258/WES/P0023

the flow exhibits significant transient behaviour or requires higher stability in the numerical solution. A known limitation for both these standard segregated pressure-velocity approaches, is the tendency to introduce relatively high numerical dissipation in the solution, as a result of discretization schemes, matrix preconditioning and the form of the momentum interpolation algorithm.

Contrary to the segregated algorithms, the block-coupled solver, as the name implies, solves the pressure and velocity fields simultaneously through coupling the momentum and continuity equations into a single block-matrix. This matrix is solved implicitly, meaning that the solution depends on both the current and the previous time-step. Through inherently enforcing mass conservation, this coupling offers enhanced stability thus allowing for larger time-steps and reduced corrector steps compared to the explicit methods.

At the outset of this study, an iterative process of fine-tuning and optimization of the convergence parameters of all three solvers was conducted. This process indicated that the PISO and transient SIMPLE algorithm reached optimal performance when operating under 3 pressure correction steps, whereas the block-coupled solver could perform well on just a single outer corrector step. Four time-steps were considered, namely 0.0005s, 0.001s, 0.002s and 0.003s, to evaluate the dependence of the results, leading to a total of 12 runs. All simulations were performed at ENGYS using 256 cores on an in-house high-performance computing cluster equipped with EPYC 9354 (Genoa) processors.

2.3 Measured quantities

The main quantity of interest, as defined in the original experiment [4], was the dimensionless concentration C/C_0, with C denoting the local concentration, and C_0 the reference concentration defined according to Eq. (1):

$$C_0 = \frac{q}{U_H H^2} \tag{1}$$

where q denotes the gas emission rate and U_H and H denote the reference velocity and reference height respectively. This quantity was measured at 15 probe locations. The predictions of these values were monitored at the corresponding locations inside the computational domain and were used for evaluating the accuracy of the simulations.

3 RESULTS

The results of the study can be summarized in Figure 1, Figure 2 and Figure 3. Figure 1 shows the Normalized Mean Square Error (NMSE) for the various algorithms at different time-steps. NMSE is defined based on the Eq. (2) below:

$$\mathrm{NMSE} = \frac{\overline{(C_o - C_p)^2}}{\overline{C_o C_p}} \tag{2}$$

where C_o denotes the observed value, C_p the numerically predicted value, n the number of predictions and the overbar symbol '-' denotes the average over the entire dataset. The plot highlights that SIMPLE and Coupled compare well with experiments in terms of mean concentration even at larger time-steps, whereas the accuracy of PISO tends to deteriorate.

Figure 2 shows the normalised mean concentration and its standard deviation obtained by different algorithms at all 15 measurement locations and at different time-steps. These graphs offer a more detailed comparison of the mean concentration predictions obtained by each algorithm. At the same time, they provide insights regarding the standard deviation of the predicted values. Finally, Figure 3 shows the runtimes times for each algorithm for all time-steps. This comparative graph underlines how PISO algorithm and the block-coupled solver are consistently faster than SIMPLE.

DOI 10.5258/WES/P0023

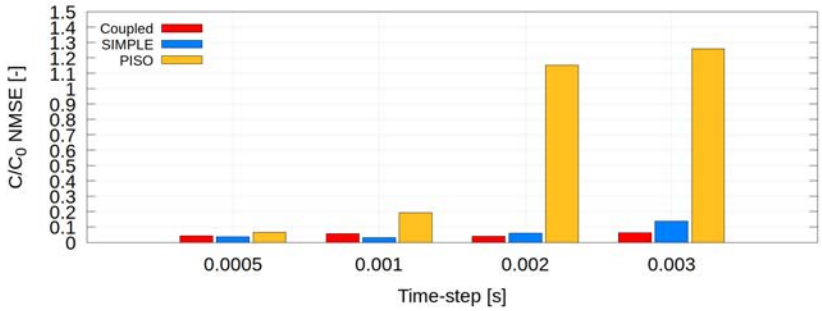

Figure 1. Comparison of the dimensionless concentration predictions' NMSE, for PISO, SIMPLE and Coupled solver for each time-step size.

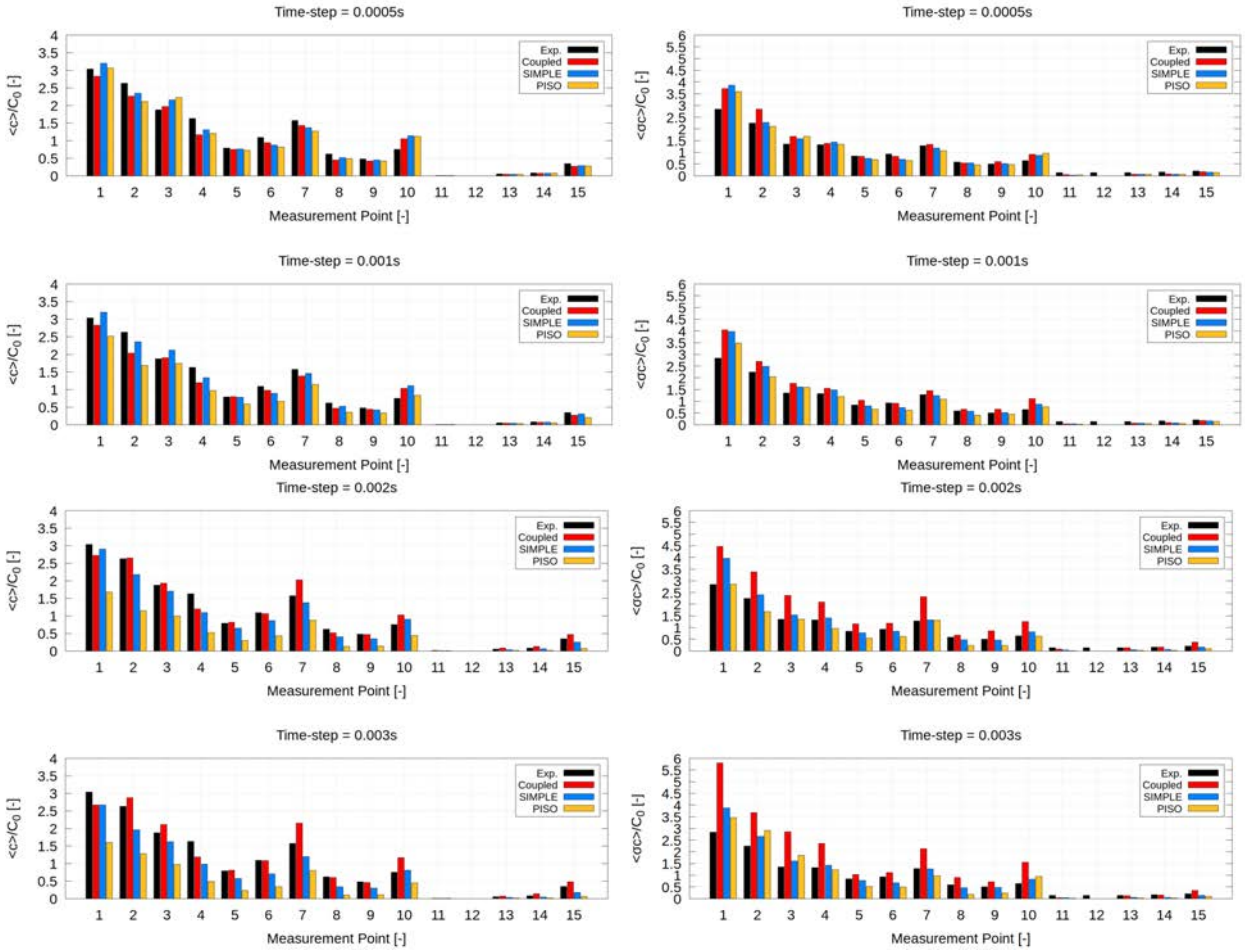

Figure 2. Mean normalized concentration (left column) and standard deviation (right column) at each measurement point for Coupled, SIMPLE and PISO at each time-step size.

DOI 10.5258/WES/P0023

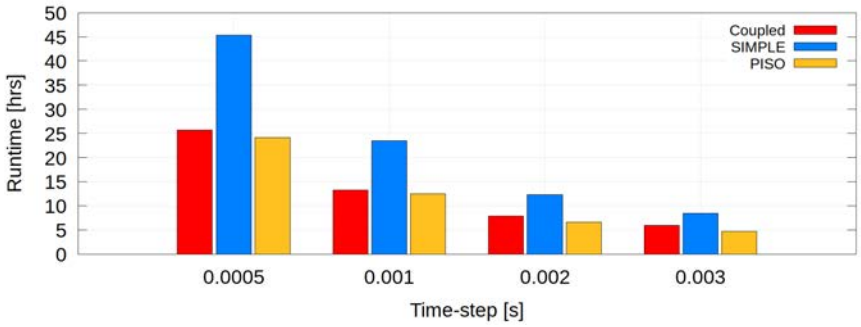

Figure 3. Comparison of the runtimes for Coupled, SIMPLE and PISO solver at different time-step sizes.

4 CONCLUSIONS & DISCUSSION

Results obtained so far indicate that although PISO yields the fastest turnaround times, the compromise in accuracy becomes significant as the time-step size increases. At the same time, SIMPLE yields consistently accurate results but at the cost of consistently being slower than PISO and coupled. The block-coupled solver, on the other hand, provides reasonably accurate predictions, comparable to those obtained by SIMPLE, but at a cost similar to PISO. The speed-up achieved through running coupled over segregated SIMPLE ranges from 43% to 30%. These observations underline how the block-coupled solver offers a good balance between accuracy and computational cost, which renders it as the most efficient approach and the overall best choice in the context of accurately predicting mean concentrations. However, it should be noted that, although the block-coupled solver offers good predictions of the mean concentration, the standard deviation of its predictions is consistently higher when compared to the segregated SIMPLE and PISO algorithms, especially for higher time-steps (i.e. 0.002s and 0.003s). Further investigations are required in this regard.

The conclusion that emerges from this study is that through significantly reducing the computational cost while simultaneously maintaining prediction accuracy in terms of mean quantities as compared to segregated algorithms, the implicit block-coupled solver can turn the scale resolving LES simulation from an impracticable to a more viable approach when running at larger time-steps. However, through coarsening the time-step size, resolution is sacrificed when looking at standard deviations. As such, a compromise in accuracy must be expected as a trade-off when trying to shorten the runtimes. The suitability of the block-coupled solver as an approach for obtaining high levels of accuracy at reduced computational cost depends on the nature of a particular study. If the objective is to predict mean concentration values, then the proposed solver constitutes a more efficient alternative to the standard segregated algorithms. However, if there is interest in accurately reproducing the whole transient nature of the flow, then sufficiently fine time-steps are a requirement, in which case there is less benefit to be gained from the block-coupled solver.

5 REFERENCES

[1] B. Blocken, "LES over RANS in building simulation for outdoor and indoor applications: A foregone conclusion?" *Building Simulation,* vol. 11, pp. 821-870, 2018.

[2] P. Gousseau, B. Blocken, T. Stathopoulos and G. van Heijst, "CFD simulation of near field pollutant dispersion on a higher-resolution grid: a case study by LES and RANS for a building group in downtown Montreail," *Atmospheric Environment,* vol. 45, pp. 428-438, 2011.

[3] A. Krassas, S. Renda, S. Mijorski, E. de Villiers and S. Capra, "Evaluating numerical models for the prediction of pollutant dispersion over Tokyo s' Polytechnic University campus," *Wind Engineering and Industrial Aerodynamics,* vol. 251, 2024.

[4] T. Tachibana, R. Yoshie, S. Nakayama, T. Kishida, K. Miyashita and R. Sasaki, "Comparison between field measurement and wind tunnel experiments of gas dispersion in an urban area and verification of similarity law.," *Wind Engineering and Industrial Aerodynamics,* vol. 47, pp. 39-52, 2022.

DOI 10.5258/WES/P0023

Physical Simulation of the Surface Pressure Field on a 5-Storey Residential Building and Application to Natural Ventilation

Khrystyna Myroniuk[1,2*], Vasyl Zhelykh[2], Yurii Furdas[2], Mike Jesson[1] and Stergios-Aristoteles Mitoulis[1]
[1]Department of Civil Engineering, University of Birmingham
Birmingham, UK
[2]Department of Heat and Gas Supply and Ventilation, Lviv Polytechnic National University
Lviv, Ukraine
[*] E-mail: k.myroniuk@bham.ac.uk

1 INTRODUCTION

A large proportion of existing residential structures incorporate a natural channel ventilation system. This ventilation approach offers several benefits, primarily its capacity to function without requiring energy consumption. However, this method is susceptible to external aerodynamic conditions and lacks controllability, and consequently it is currently difficult to predict how well it will operate and presents challenges to systematic study of the issue. Additionally, its effectiveness can diminish following alterations to the building, such as insulation upgrades (thermal retrofitting).

2 MAIN PART

2.1 Literature review

For a comprehensive understanding of the interaction between buildings and wind, and the impact of wind forces on their stability and functional characteristics, it is advisable to conduct research using wind tunnel models. This approach facilitates the precise determination of pressure values on the building surface under varying wind speeds and turbulent flow conditions [1–3]. Such studies are instrumental in identifying critical pressure values that pose significant risks to the structural integrity of buildings [4–6]. Furthermore, aerodynamic experiments provide insights into wind effects from various directions, considering the correlation between wind speed and flow turbulence [7–9], which is particularly crucial for the design of high-rise structures [10].

Another critical aspect is the influence of natural obstacles, building dimensions, and adjacent structures on the pressure distribution on a building's surface. Scientific research indicates that external factors, such as neighboring buildings or natural features, can significantly alter the direction and magnitude of wind pressure [5]. Various geometric dimensions and their spatial arrangement can also create complex aerodynamic conditions, depending on the density of the surrounding structures [11]. The interaction between buildings affects the pressure distribution and associated aerodynamic phenomena [11,12].

Computer modeling emerges as a cost-effective method for studying aerodynamic phenomena, including the evaluation of natural and hybrid ventilation, and is essential for analyzing wind effects on buildings [13,14]. Determining the aerodynamic coefficient helps in understanding the extent of wind impact on buildings [7]. The results of computer simulations are particularly vital when assessing the impact of wind on high-rise buildings and structures of various architectural configurations [15,16]. The interaction between buildings and the assessment of external elements, such as topography and natural features, also play a significant role [13,14]. This methodology allows for the modeling of urban microclimates and the estimation of harmful substance concentrations in residential areas [3].

While computer simulations are powerful tools, they do not always capture all aspects of the real environment. Therefore, it is crucial to compare the results of computer simulations with data obtained from aerodynamic experiments [17].

2.2 Experimental part

This study presents findings from experimental research on the surface pressure coefficient distribution across the roof of 5-story residential building, using a model of an actual building in the city of Lviv, Ukraine. A 1:300 scale model was fabricated and placed on a 2-metre diameter platform within the atmospheric boundary layer (ABL) wind tunnel at the University of Birmingham's Civil Engineering

DOI 10.5258/WES/P0026

Laboratory. The scaling matches the scale of the ABL flow generated within the tunnel. Pressure coefficients have been measured over the roof of the model for three cases: an isolated building with a surrounding, flat, 1m (300m full-scale) fetch; the building at the centre of a 300m (full-scale) radius model of the city; the building as part of the city but with the model modified to include a small parapet which runs around the edge of the roof (Fig. 1). The primary objective of these measurements was to assess the performance of ventilation channels under wind flow conditions and to identify critical zones that pose a threat to the operation of the natural ventilation system. These research findings are highly pertinent for formulating recommendations for the efficient operation of passive ventilation systems in existing buildings within densely constructed areas. This is particularly relevant for buildings that have undergone thermal retrofitting.

Figure 1, three series of measurements were carried out: 1 - a house without parapet; 2 - a house with a parapet; 3 - a house without surrounding buildings.

The physical emulation of wind-induced loads on residential structures involves examining house models within a wind tunnel, a facility designed to replicate wind forces on buildings. This method uses the pressure coefficient "c" to determine the relationship between excess static pressure at specific points on the building's surface and the dynamic wind pressure. While frequently employed, synthesizing data from these experiments is challenging due to the diverse configurations and placements of buildings in residential areas.

$$\pm c = \frac{P}{\frac{\rho \cdot v^2}{2}} \quad (1)$$

Around the exhaust ventilation duct outlets, building aerodynamics may lead to the formation of zones of positive pressure. This phenomenon poses a critical threat to the functionality of natural exhaust ventilation systems, as it fosters the potential for reverse air flow within the channels, consequently causing the accumulation of hazardous concentrations of harmful substances within the premises. The negative impact on the operation of exhaust ventilation channels increases with the magnitude of the positive pressure coefficient.

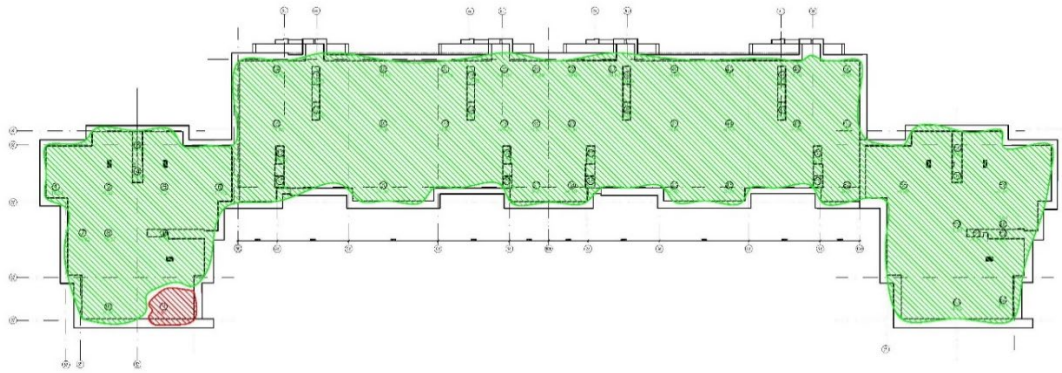

a) an isolated building with a surrounding, flat, 1m (300m full-scale) fetch

DOI 10.5258/WES/P0026

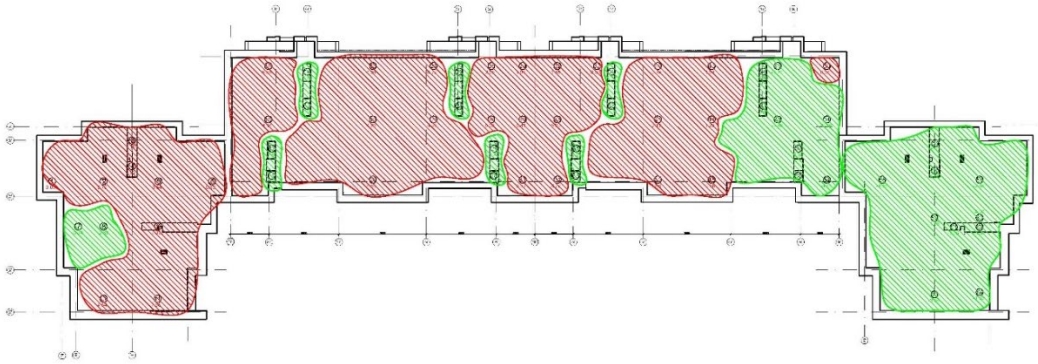

b) the building at the centre of a 300m (full-scale) radius model of the city

Figure 2, pressure distribution on the roof surface: the red zone shows the zone where there is excess pressure, the green zone indicates the rarefaction zone

The findings highlight the importance of including the surrounding buildings in the model. With an open fetch negative pressure coefficients occur around the existing ventilation outlets, which will aid ventilation, but when surrounding buildings are included the surface pressure coefficient increases to +1.0, and as high as +5.5 when the parapet is included. These positive pressures occur for wind directions between south-westerly (270°) to westerly (305°).

3 CONCLUSIONS

The experimental results serve as a foundation for enhancing the design methodology of new buildings and thermal retrofitting of existing ones, particularly focusing on optimizing natural ventilation in medium-rise buildings in densely populated urban areas. This approach is crucial for significantly improving the quality and efficiency of contemporary building design.

Studies on the aerodynamics of external wind influence on the ventilation of residential buildings help identify critical points on the building's roof surface under wind pressure. These findings enable the development of new, efficient, and environmentally friendly ventilation technologies that align with modern construction needs and foster comfortable and healthy living conditions. Thermally retrofitted residential buildings often face challenges with traditional external air inflow due to their tightness. Therefore, implementing appropriate ventilation systems is vital not only for maintaining indoor air quality but also for optimizing energy consumption. Passive ventilation systems present a promising solution, utilizing natural forces and innovative technologies to facilitate air exchange while minimizing energy consumption.

REFERENCES

[1] An L-S. & Jung S. (2024). "Experimental investigation on influence of terrain complexity for wind pressure of low-rise building", *Journal of Building Engineering,* **83,** 108350.

[2] Moravej M., Irwin P., Zisis I., Chowdhury A. G. & Hajra B. (2017). "Effects of roof height on local pressure and velocity coefficients on building roofs", *Engineering Structures,* **150,** 693–710.

[3] Vita G., Shu Z., Jesson M., Quinn A., Hemida H., Sterling M. & Baker C. (2020). "On the assessment of pedestrian distress in urban winds", *Journal of Wind Engineering and Industrial Aerodynamics,* **203,** 104200.

[4] Abdelfatah N., Elawady A., Irwin P. & Chowdhury A. (2020). "A study of aerodynamic pressures on elevated houses", *Wind and Structures,* **31,** 335–50.

[5] Chauhan B. S., Chakrabarti A. & Ahuja A. K. (2022). "Study of wind loads on rectangular plan tall building under interference condition", *Structures,* **43,** 105–30.

[6] Myroniuk K., Furdas Y., Zhelykh V. & Yurkevych Y. (2024). "Examining Wind Flow's Impact on Multi-Storey Buildings: A Quest for Quality Improvement", *Production Engineering Archives,* **30,** 57–66.

[7] Huang Y., Ou G., Fu J. & Zhang H. (2023). "Prediction of mean and RMS wind pressure coefficients for low-rise buildings using deep neural networks", *Engineering Structures,* **274,** 115149.

DOI 10.5258/WES/P0026

[8] Huang J., Gu M. & Gao Y. (2021). "Blockage effects on aerodynamics of isolated tall buildings under uniform turbulent", flows *Journal of Wind Engineering and Industrial Aerodynamics,* **212,** 104607.

[9] Wang X. J., Li Q. S. & Yan B. W. (2020). "Full-Scale Measurements of Wind Pressures on a Low-Rise Building during Typhoons and Comparison with Wind Tunnel Test Results and Aerodynamic Database", *J. Struct. Eng.,* **146,** 04020196.

[10] Kikuchi T., Ohtake K., Takahashi Y., Watanabe H., Hidari K., Tanabe S. & Nobe T. (2024). "Comparison of wind pressure coefficients between wind tunnel experiments and full-scale measurements using operational data from an urban high-rise building", *Building and Environment,* **252,** 111244.

[11] Kim W., Tamura Y., Yoshida A. & Yi J-H. (2018). "Interference effects of an adjacent tall building with various sizes on local wind forces acting on a tall building", *Advances in Structural Engineering,* **21,** 1469–81.

[12] Nagar S. K., Raj R. & Dev N. (2021). "Proximity effects between two plus-plan shaped high-rise buildings on mean and RMS pressure coefficients", *Scientia Iranica, 29*, 990-1005.

[13] Blocken B. (2018). "LES over RANS in building simulation for outdoor and indoor applications: A foregone conclusion?", *Build. Simul.,* **11,** 821–70.

[14] Chen G., Hang J., Chen L. & Lin Y. (2023). "Comparison of uniform and non-uniform surface heating effects on in-canyon airflow and ventilation by CFD simulations and scaled outdoor experiments", *Building and Environment,* **244,** 110744.

[15] Elshaer A., Aboshosha H., Bitsuamlak G., El Damatty A. & Dagnew A. (2016). "LES evaluation of wind-induced responses for an isolated and a surrounded tall building", *Engineering Structures,* **115,** 179–95.

[16] Feng C., Gu M. & Zheng D. (2019). "Numerical simulation of wind effects on super high-rise buildings considering wind veering with height based on CFD", *Journal of Fluids and Structures,* **91,** 102715.

[17] Zhao Y., Li R., Feng L., Wu Y., Niu J. & Gao N. (2022). "Boundary layer wind tunnel tests of outdoor airflow field around urban buildings: A review of methods and status", *Renewable and Sustainable Energy Reviews,* **167,** 112717.

DOI 10.5258/WES/P0026

Codification of mean wind and turbulence profiles over the ocean with roughness saturation

John D. Holmes[1*]
[1]JDH Consulting
Mentone, Victoria, Australia
[*] *john.holmes@jdhconsult.com*

1 INTRODUCTION

Reliable and robust models of strong winds over the open seas and oceans are essential for structural design and operation of structures such as offshore oil and gas platforms, and their renewable energy counterparts – offshore wind turbine towers. These models should include wind speeds expected in the extreme winds of tropical cyclones, including hurricanes and typhoons. In this paper, a revised model for strong winds over the open oceans is proposed, incorporating saturation or 'capping' of the surface roughness and the related turbulence intensity.

Although the length of the extended abstract does not permit a full discussion here, full details of the proposed and other wind models in design codes and standards for offshore structures, are given in a report and submitted paper (Holmes, [1]).

2 HISTORY AND BACKGROUND

Charnock [2] used dimensional arguments in applying the classic logarithmic law to the atmospheric boundary layer over water surfaces. The Charnock relation can be written in the form of an effective, velocity-dependent, roughness length (Eq. (1)):

$$z_o = \frac{a{u_*}^2}{g} \tag{1}$$

where a is the more common form of Charnock's 'constant'. u_* is the friction velocity, and g is the gravitational constant.

Subsequent research has usually replaced the roughness length z_0 with the closely-related surface drag coefficient, $C_{d,10}$, normalized by the mean wind speed at a height of 10 metres above the water surface, $\overline{U}_{10}$. The Charnock relation of Eq. (1) leads to a relation between $C_{d,10}$ and $\overline{U}_{10}$ which is close to linear over a wide range of wind speeds; an example is shown in Fig. 1. This graph illustrates an important characteristic of over-water winds compared with those overland – a dependency of roughness parameters, and hence wind profiles, on the wind speed itself.

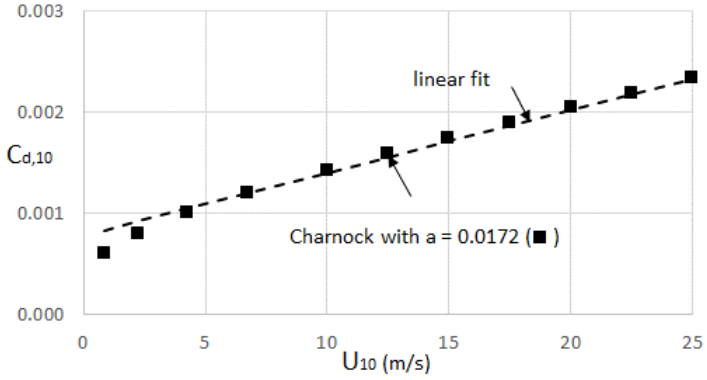

Figure 1, Surface drag coefficient versus mean wind speed - linear fit to Charnock model

Many measurements of wind drag and profiles of open water were made up to about 1990, for wind speeds up to about 20 m/s, and usually with linear $C_{d,10}$ versus $\overline{U}_{10}$ fits. However, virtually none were made over the open ocean and for a range of wind speeds relevant to the design of offshore structures.

DOI 10.5258/WES/P0027

In an attempt to rectify this, the Norwegian state oil company (Statoil) sponsored extensive tower measurements from the island of Frøya, between 1988 and 1989. Measurements of mean wind speeds and turbulence were made from three different towers, for heights up to 100m. The sites were exposed to gales from the west and south-west over the Atlantic Ocean. The sites and instrumentation on Frøya were discussed by Andersen and Lovseth [3], and the results were summarized by Andersen and Lovseth [4].

Powell *et al*. [5] analysed wind profiles from dropwindsonde measurements by the National Hurricane Center of the United States, obtained from aircraft flying into Atlantic hurricanes. The trajectories of the probes were tracked using GPS satellites enabling wind profiles to be obtained, based on the dropwindsondes moving with the local wind speed. Although there are questions about the response of the probes to atmospheric turbulence, averaging the profiles over many drops enables mean wind profiles in the strong winds of hurricanes to be assessed. In an attempt to

Saturation, or 'capping', of the surface drag coefficient and roughness length was identified by Powell *et al*. [5]. Although there was some scatter in the values obtained, the data indicates a levelling off, and even a reduction, in the surface drag coefficient, for mean wind speeds greater than about 30m/s. Powell *et al*. noted: "*surface winds above hurricane force (34 m/s) create streaks of bubbles on the sea surface combined with patches of foam 20-50m wide caused by steep wave faces breaking and being sheared off by the wind. As the wind approaches 50 m/s, the sea becomes completely covered by a layer of foam*". Images in the paper show large areas of near-flat white water corresponding to low surface roughness.

3 PROPOSED MODEL OF SURFACE DRAG COEFFICIENTS AND TURBULENCE FOR STRONG WINDS

Unlike those in international standards, the proposal here is for a model that is suitable for both extra-tropical and tropical synoptic-scale storms. However, it is not an appropriate model for non-synoptic, convective, windstorms that may occur in tropical and sub-tropical oceans.

The proposed model is essentially a 'fine tuning' of the model in ISO 19901-1 [6], with extension to wind speeds in excess of the Frøya data, and incorporating capping of the surface drag coefficient and roughness length at a mean wind speed, $\overline{U}_{10}$, of 25 m/s. Some modification and capping of the ISO expression for turbulence intensity is also proposed.

3.1 Surface drag coefficient and mean profile

The proposed model for surface drag coefficient is given by Equation (2):

$$\begin{aligned} C_{d,10} &= 0.000525[1 + 0.1505\,\overline{U}_{10}] \qquad \overline{U}_{10} \leq 25\ m/s \\ C_{d,10} &= 0.0025 \qquad \overline{U}_{10} > 25\ m/s \end{aligned} \tag{2}$$

The first equation coincides with that in the ISO Standard, but there is no wind-speed limit in [6]. Fig. 2 shows Eqs. (2) (solid black line), plotted with the Frøya data. The version in ISO 19901-1 is shown dashed in Fig. 2.

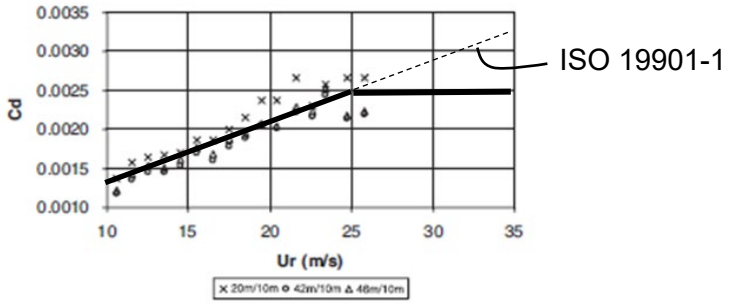

Figure 2, Proposed surface drag coefficient versus mean wind speed – Eqn. (2) versus Frøya data

DOI 10.5258/WES/P0027

The agreement of the data in Fig. 2 with Eq. (2) is good, if the data influenced by near-shore conditions (shown by '×'in the Figure) are ignored. As noted by Andersen and Løvseth [4]: *"..for the highest wind speeds the data indicate saturation."* This is represented in Eqs. (2) by a constant value of $C_{d,10}$ of 0.0025 for wind speeds above 25 m/s.

The logarithmic law, Eq. (3), can be used to give a relation between roughness length and surface drag coefficient, Eq. (4). k is von Karman's Constant (~0.4), and $C_{d,10} = \frac{{u_*}^2}{{\bar{U}_{10}}^2}$.
Together with Eqs. (2), these define the mean velocity profile above ocean surfaces up to a height of at least 100m.

$$\bar{U}_z = \frac{u_*}{k} \ln \frac{z}{z_0} \tag{3}$$

$$\sqrt{C_{d,10}} = \frac{k}{\ln\left(\frac{10}{z_0}\right)} \tag{4}$$

From Eqs. (2) and (4), the saturated value of roughness length, z_0, for wind speeds exceeding 25 m/s, is 3.35 mm.

3.2 Turbulence intensity

25 m/s is an appropriate value of $\bar{U}_{10}$ for capping the surface drag coefficient, as shown in Fig. 2, and logically the turbulence intensity should also be capped at that wind speed. Then the proposed equations for turbulence intensity become:

$$I_u = 0.06[1 + 0.050\,\bar{U}_{10}]\left(\frac{z}{10}\right)^{-0.22} \qquad 10\ m/s \le \bar{U}_{10} \le 25\ m/s$$

$$I_u = 0.135\left(\frac{z}{10}\right)^{-0.22} \qquad \bar{U}_{10} > 25\ m/s \tag{5}$$

The first of Eq. (5) is a modification of that in the ISO Standard [6] with '0.050' replacing the value of '0.043' in [6]. The ISO equation for turbulence intensity is also uncapped, as it is in the surface drag coefficient versus $\bar{U}_{10}$ function.

The I_u versus height relation in Eq. (5) is compared with the available recorded data at high wind speeds (> 25 m/s) in Fig. 3. This figure includes some unpublished data from oil platforms in the Atlantic during hurricanes, values derived from gust factors during the land-falling of Tropical Cyclone 'Yasi' on the Queensland coast [7], values recorded by Shiotani and Arai [8] on the coast of Shikoku Island, Japan, during landfall of typhoons, and recent data from gales in the North Sea recorded at the FINO1 and FINO3 meteorological towers, (Jeans, [9]). The agreement with Eq. (5) in Fig. 3 is very reasonable, allowing for the scatter in the measurements, the scatter to be expected as the data are all based on individual 10- or 60- minute samples.

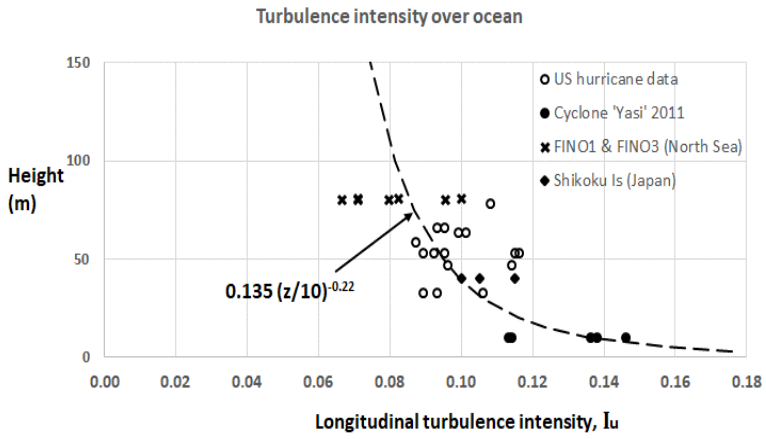

Figure 3, I_u vs. z – Eqn. (5b) compared with recorded data for $\bar{U}_{10}$ > 25 m/s

DOI 10.5258/WES/P0027

Another comparison is shown in Fig. 4, in which recorded turbulence intensities at an average elevation of 46m (+/-13m) are plotted as a function of mean speed at 10m. Eq. (5), with capping at $I_u = 0.0965$ for $\overline{U}_{10} \geq$ 25m/s provides a good fit to the data. Based on Figs. 3 and 4, Eq. (5) gives a better fit to recorded data on turbulence intensity than those in current codes and standards.

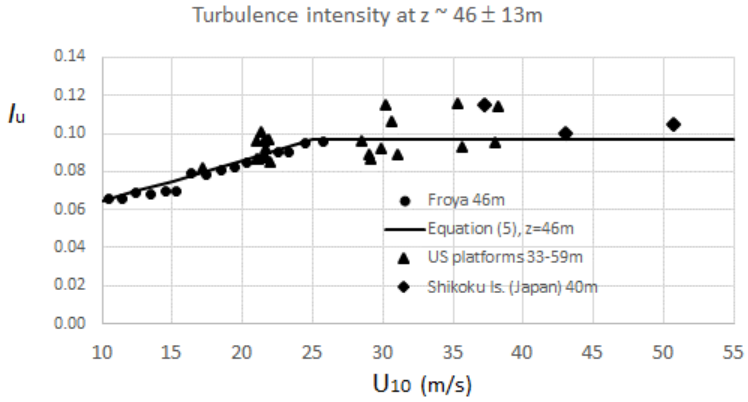

Figure 4, I_u vs. $\overline{U}_{10}$ - *Eq. (5) compared with recorded data at ~ 46m height*

4 CONCLUSIONS

Based on the good-quality wind data recorded on the coast of the island of Frøya (Norway) in the 1980s, and supported by later dropwindsonde profiles in hurricanes, this paper shows that 'capping' of the surface drag coefficient becomes apparent at a mean wind speed, at 10m height, of about 25 m/s. The upper limit of the surface drag coefficient is about 0.0025.

Revised models are proposed for surface drag coefficients, aerodynamic roughness lengths and turbulence intensities for design of offshore structures, valid for all mean wind speeds, incorporating the observed 'capping' beyond a threshold of 25 m/s. The proposed model for longitudinal turbulence intensity is well supported by individual measurements from gales and tropical cyclones (including hurricanes and typhoons) at several different locations.

REFERENCES

[1] Holmes, J.D. (2024), *Mean wind and turbulence profiles over the ocean with roughness saturation*, JDH Consulting Report 24/1R, July 2024, (manuscript submitted to *Wind and Structures*).
[2] Charnock, H. (1955), "Wind stress on a water surface", *Quart. J. Roy. Met. Soc.* **81**, 639-640.
[3] Andersen, O.J., and Løvseth, J.L. (1995), "Gale force maritime wind. The Frøya database", *J. Wind Eng. Ind. Aero.* **57**, 97-109.
[4] Andersen, O.J., and Løvseth, J.L. (2006), "The Frøya database and maritime boundary-layer description", *Marine Structures.* **19**, 173-192.
[5] Powell, M.D., Vickery, P.J., and Reinhold, T.A. (2003), "Reduced drag coefficients for high wind speeds in tropical cyclones", *Nature* **422**, 279-283.
[6] International Organization for Standardization (2015), Petroleum and natural gas industries – Specific requirements for offshore structures. Part 1 Metocean design and operating considerations, International Standard, ISO 19901-1:2015, ISO, Geneva, Switzerland.
[7] Holmes, J.D. (2017), "Roughness lengths and turbulence intensities for wind over water", *9th Asia-Pacific Conference on Wind Engineering*, Auckland, New Zealand, December 3-7.
[8] Shiotani, M. and Arai, H. (1967), "Lateral structures of gusts in high winds", *2nd International Conference on Wind Effects on Buildings and Structures*, Ottawa, Canada, September 11-15
[9] Jeans, G. (2023), "Converging profile relationships for offshore wind speed and turbulence intensity", *Wind Energy Science Discussions.* Preprint, *doi.org/10.5194/wes-2023-35*.

DOI 10.5258/WES/P0027

Kinematic Similarity for Urban Aerodynamic Wind Tunnel Tests Using Retrofit Atmospheric Boundary Layer Screen Filter

Rakesh, Rayapureddi[1*]; Joe, Dillane[1]; Andrew, Keppel[1] and Thomas, Confrey[1]
[1]Department of Aerospace and Mechanical Engineering, South East Technological University
Kilkenny Road, Carlow, Ireland, R93 V960
[*] E-mail: rakesh.rayapureddi@postgrad.setu.ie

1 INTRODUCTION

Wind tunnel experiments provide a controlled environment for investigating urban airflow patterns and their impact on pollutant dispersion at reduced scales, making urban environment research cost-effective. To conduct realistic urban wind tunnel experiments, it is crucial to achieve geometric, dynamic, and kinematic similarities with the actual model. For urban aerodynamics studies, boundary layer (BL) wind tunnels are commonly used as they are designed to replicate the natural wind structure by covering a considerable length of the wind tunnel's floor with a material of suitable roughness. However, this method requires a long test chamber to form the BL and often results in an uneven boundary profile along the horizontal space, making it less feasible for realistic urban studies [1].

Atmospheric Boundary Layer (ABL) characteristics inside a wind tunnel can be produced either actively, using controllable devices like oscillating spires and multiple fans, or passively, by introducing flow conditioners such as spires, roughness elements, and screens. Recent studies have focused on improving techniques for replicating natural wind characteristics and forming the atmospheric boundary layer (ABL) in wind tunnels with short test sections [1,2,3]. These studies primarily employed passive approaches, extending the test section length and incorporating spires and roughness elements to create an ABL flow field. Pires [3] found that spires and thin screens were the most efficient passive devices for forming the boundary layer with minimal area required.

Based on previous results from ABLs characterization in wind tunnels, the need for generating velocity profiles that adhere to natural wind flow in short test sections was identified. Therefore, the main goal of this study is to replicate ABL characteristics within the wind tunnel using a flow filter screen and to improve the quality of passively regulated airflow methods, facilitating realistic urban wind dispersion analysis.

2 THEORY CALCULATIONS

Atmospheric boundary layer is composed of a mean wind speed and an overlaid fluctuation due to the turbulence that varies based on topography of terrain. The wind speed within the urban inertial sublayer is uniform in the horizontal direction and it is almost windless in the vertical direction, and the wind speed in the horizontal direction varies only with the height. For describing the lower part of the boundary layer, known as the Prandtl layer, the logarithmic law of the wall suggested by Thuillier and Lappe [1] is generally used.

The variation of the mean horizontal velocity, $\overline{u(z)}$ with height, z can be represented by Eq. 1,

$$\frac{\overline{u(z)}}{u^*} = \frac{1}{\kappa}\ln\left(\frac{z+z_0}{z_0}\right) \quad (1)$$

Where, $u^*$is Frictional velocity, κ is von Karman constant and z_0 is aerodynamic roughness height.

In urban aerodynamic studies, *Re* of airflows in the wind tunnel is much lower than that of actual atmospheric flows. Thereby, *Re* of full-scale and model-scale cannot be equal. Therefore, the wind tunnel experiments must be conducted at the critical *Re* where the Reynolds independence theory is valid. Plate [4] introduced the *Re*-independence criteria for flow over an urban model in terms of Roughness Reynolds (Re_Z) Eq. 2,

$$Re_Z = \frac{u^* Z_{0,Model}}{\nu} > 5 \quad (2)$$

The value of $z_0$depends on the atmospheric stability and surface roughness of topographic features. Proper scaling of ABL wind properties ensures that the flow characteristics in the wind tunnel are representative

DOI 10.5258/WES/P0028

of those in the full-scale urban environment. Therefore, it is necessary to replicate these conditions in wind tunnels to study urban aerodynamics under realistic scenarios.

3 METHODS

This work has been carried out in the open subsonic wind tunnel located in the EngCore department at South East Technological University (SETU). The cross section of this wind tunnel is 304x304 mm with the length of 650 mm testing chamber. The wind tunnel has two pitot tube measuring devices to record the dynamic pressures positioned at 200 mm and 550 mm from honeycomb screen respectively.

In order to achieve the boundary profile similar to ABL, a new screen filter has been designed to passively regulate the free stream airflow within the wind tunnel test chamber. This screen functions as a flow manipulator, transforming the upstream flow exiting the honeycomb into a logarithmic flow profile. The ABL screen comprises a grid of slots with widths increasing logarithmically, as shown in Fig. 1. Initially, the velocity profile of the free-flow wind in the test section is recorded at different fan speeds to serve as a baseline for comparison with the velocity profiles after the ABL screen is introduced.

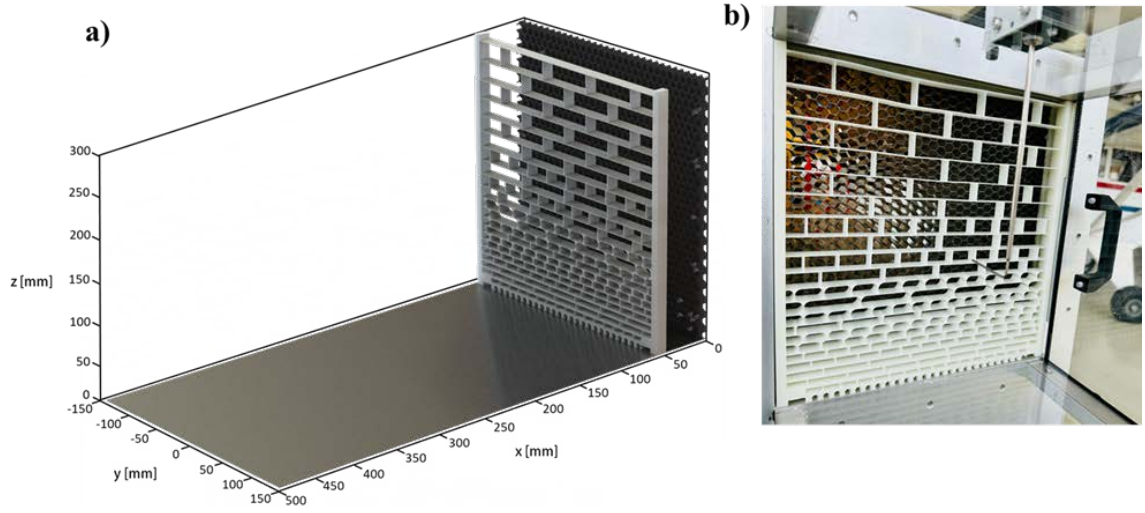

Figure 1, a) Position of the ABL screen in the test chamber; b) 3D-printed model for experiments

The ABL screen measures 300x300 mm and comprises 21 vertical rows with variable slot configurations. The height of each pair of adjacent vertical rows is determined by Eq. 3, while the width of the horizontal slots in each row are designed to produce a uniform velocity at each layer. The primary objective of this ABL screen design is to restrict flow near the ground and gradually reduce blockage to enhance vertical fluid flow, thereby replicating the natural wind profile. Slot widths in each row are adjusted according to the velocity profile observed near the test section. Additionally, 5 mm diameter holes at the bottom accommodate skin friction effects near the wind tunnel's bottom wall.

$$D(n) = 5 + \sum_{k=1}^{n} \ln(k) \tag{3}$$

Where, $D(n)$ is the width of rows; and row number$n \in (2,4,6,8,10)$.

The dynamic pressure of the airflow in wind tunnel was measured with a standard pitot tube manometer, and the respective velocities were calculated based on the dynamic pressure readings. The procedure resulted in calibration errors below 2%, which are typical of pitot tube applications. The experimental uncertainty in the measurement of ambient conditions is 0.5%. This result is an uncertainty of < 5% in the estimation of the Reynolds number, with the confidence interval of 95%.

4 RESULTS AND DISCUSSION

The CFD simulations are performed on the wind tunnel model to analyze the flow structure after introducing the designed mesh screen. A uniform velocity distribution is observed in the test chamber as shown in the Fig. 2. The ABL was fully developed at x=150 mm, showing an even velocity horizontally at each layer in the wind tunnel, due to different slots at each row on the screen.

DOI 10.5258/WES/P0028

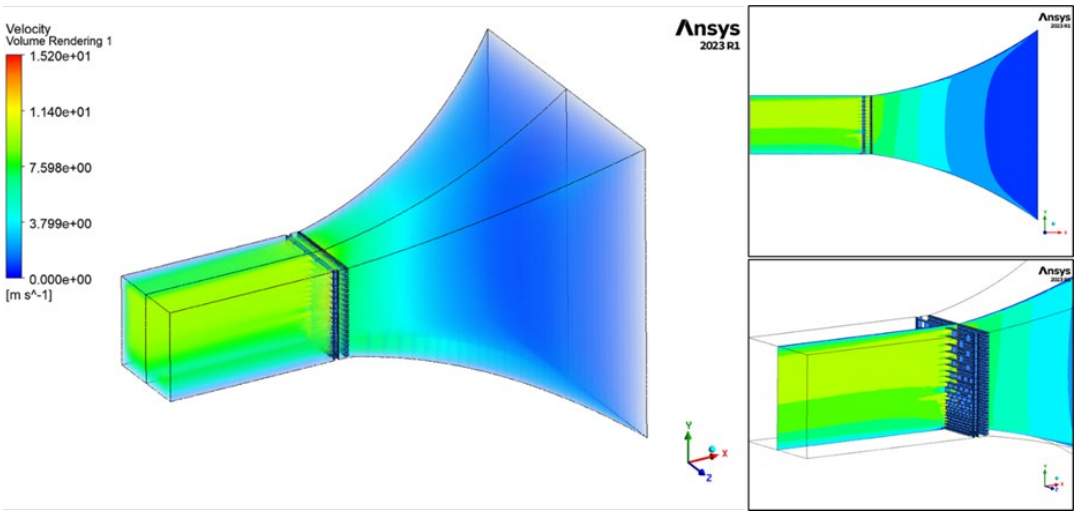

Figure2, Velocity distribution in the wind tunnel at free stream velocity of 8.5 m/sec

Three different fan speeds were selected for the experiments: 8.5 m/s, 17.7 m/s, and 35 m/s. The frictional velocity and effective roughness height of the developed flow structure were obtained by fitting wind profiles on a semi-logarithmic scale. The analysis yields the model aerodynamic surface roughness length $Z_{0,m}$=0.0005m and the friction velocity u^*= 0.152 m/s at the mean freestream velocity $\bar{u}$ = 8.5 m/s; $Z_{0,m}$= 0.00055m and u^*= 0.164 m/s at $\bar{u}$ = 17.7m/sec; $Z_{0,m}$=0.0008m and u^*= 0.195m/s at $\bar{u}$ = 35m/sec. Table 1 summarizes the experimental values of aerodynamic roughness height (Z_o) and roughness Reynolds numbers (Re_z) at different free stream velocities after retrofitting the developed ABL screen. The effective roughness heights showed nonsignificant differences at low and medium fan speeds. However, the frictional velocities and roughness heights after introducing the ABL screen fell within the recommended theoretical ranges for dense urban region aerodynamic studies at all fan speeds [5,6]. The critical Reynolds number condition defined by Plate [4] (Re_z>5) is satisfied for the medium and high-speed conditions, which indicates that the flow replicated the natural wind conditions in the test section. Additions of roughness elements are required at low fan speed to improve the flow characteristics near the ground level as Re_z is very close to critical value.

Table 1, Airflow parameters and Re inside wind tunnel test section at different fan speeds

Wind Speed (m/sec)	**Dynamic Pressure (mm H_2O)**	**Roughness height ($z_{o,m}$)**	**Frictional velocity(U^*) m/s**	**Roughness Reynolds**
8.5	5	0.0005	0.152	5.14
17.7	20	0.00055	0.164	6.09
35	75	0.0008	0.195	10.54

Variations in mean and turbulent flow profiles along the spanwise direction were used to ensure the development of the ABL. To evaluate the results in relation to real ABLs, the mean flow profile was compared to theoretical log-law profiles. Fig. 3 presents the developed velocity profiles after introducing the ABL screen, compared with free flow wind profiles and the theoretical log-law profile at different speeds. Introducing the ABL screen resulted in significant changes in velocity profiles across all cases. A good agreement was observed between the experimental mean flow characteristics and the theoretical log-law profiles representing the urban boundary layer, particularly near the ground surface levels at all three fan speeds. Therefore, the present study suggests that the mean flow characteristics of the ABL can be effectively simulated in a short wind tunnel using the ABL screen device. Nevertheless, the turbulence characteristics within the test section can be controlled by adjusting the slot dimensions on the ABL screen according to the terrain conditions of the targeted urban study region.

DOI 10.5258/WES/P0028

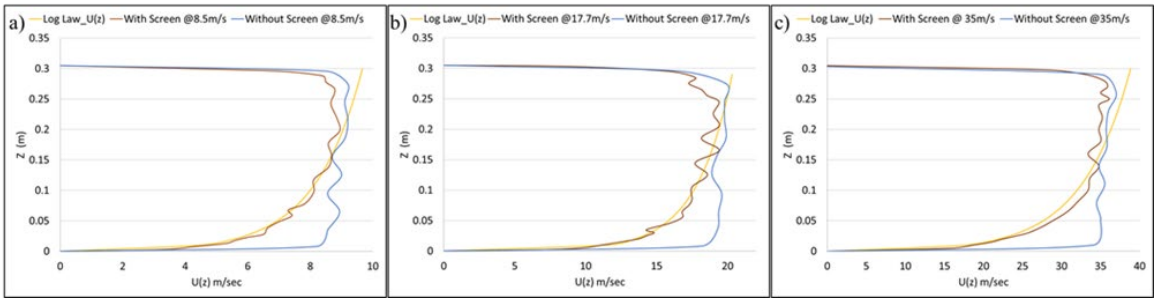

Figure3, Velocity profile inside wind tunnel compared with theoretical log profile and free flow wind profile at: a)8.5m/sec; b)17.7m/sec; c)35m/sec

5 CONCLUSION

In this study, atmospheric boundary layers (ABL) over a generic urban terrain were simulated in a subsonic wind tunnel using the ABL screen flow modifier technique. Initially, the velocity profile properties in the test section of the empty wind tunnel were evaluated at different wind speeds. The goal was to replicate ABL characteristics within the shortest possible wind tunnel extension and with minimal pressure loss, achieving a velocity profile similar to natural wind for realistic urban wind dispersion analysis. This was accomplished by passively regulating airflow using an ABL screen positioned near the inlet. To generate ABL flow characteristics, a screen filter with vertically varying height rows and a grid of slots was proposed. The screen's effectiveness was validated through wind tunnel tests with a 3D-printed screen.

The effective roughness height and frictional velocity in the test section after introducing the ABL screen show good agreement with theoretical values typically used to represent the ABL over urban terrain. Additionally, a uniform wind velocity distribution throughout the test section, adhering to the logarithmic law near the ground, is achieved with the developed screen. The main characteristics of wind in an ABL are well reproduced in these experiments, demonstrating the potential of using the ABL screen flow modifier technique to generate the atmospheric boundary layer in wind tunnels with short test sections. To meet the requirements of wind engineering applications in short wind tunnels, further experimental studies are needed, particularly to address the inadequacy of the generated turbulence intensity in the upper part of the boundary layer. Nonetheless, the ABL screen used here is suitable for reproducing ABLs over nearly flat terrains with low-height dense urban areas.

REFERENCES

[1] Thuillier, R. H., and U. O. Lappe. "Wind and temperature profile characteristics from observations on a 1400 ft tower." Journal of Applied Meteorology and Climatology 3.3 (1964): 299-306.

[2] Blessmann, J. "Simulation of the Natural Wind Structure in an Aerodynamic Wind Tunnel." Ph. D. thesis, Instituto Tecnológico de Aeronáutica (ITA), São José dos Campos, SP, Brazil (1973).

[3] Pires, Luciana Bassi M., et al. "Simulations of the atmospheric boundary layer in a wind tunnel with short test section." Journal of Aerospace Technology and Management 5 (2013): 305-314.

[4] Plate, Erich J. Wind tunnel modelling of wind effects in engineering. Elsevier, 1982.

[5] Wiernga, Jon. "Representative roughness parameters for homogeneous terrain." Boundary-Layer Meteorology 63 (1993): 323-363.

[6] Davenport, Alan G., et al. "Estimating the roughness of cities and sheltered country." Preprints, 12th Conf. on Applied Climatology, Asheville, NC, Amer. Meteor. Soc. Vol. 96. 2000.

DOI 10.5258/WES/P0028

Shading Affects the Latent Heat Flux in Vegetated Urban Areas

Christopher Wilson[1*], Jon Shonk[2], Sylvia Bohnenstengel[2], Athanasios Paschalis[1] and Maarten van Reeuwijk[1]
[1]Imperial College London
[2]Met Office
[*]cew216@ic.ac.uk

1 INTRODUCTION

1.1. Motivation

It is a well-established fact that the world is undergoing rapid climate change and that this is leading to an increase in extreme weather events. Particularly there have been increases in warm-weather extremes [1] and urban areas are particularly vulnerable to such events. The urban heat island effect (UHI) is the well-documented phenomenon that temperatures in urban areas can be several degrees warmer than those in the surrounding rural areas. This means that cities are more susceptible to heatwaves than rural areas [2] the consequences of which can range from costly and inconvenient to fatal for those living in urban areas. When this is taken into consideration along with the fact that over 50% of the global population inhabits cities [3] (a figure that is predicted to rise throughout the 21st century) there is a pressing need to be able to understand and accurately model the urban microclimate and meteorology

1.2. Surface Energy Balance (SEB)

The surface energy balance (SEB) describes the way an urban area exchanges energy with the surrounding atmosphere, and it plays a key role in determining both the local microclimate and meteorological forcings. In this work the SEB of a surface is modelled as follows:

$$Q^* = H + E + G \tag{1}$$

where Q^* is the net radiative flux incident on the surface, H and E are the sensible and latent heat fluxes going from the surface into the atmosphere and G is the conductive heat flux away from the surface into the ground and buildings.

1.3 The Urban Surface

Urban areas are inherently heterogeneous and complex environments consisting of a wide range of materials. Surface variability impacts range of processes involved in urban atmospheric interaction; for example, the transport of heat and moisture [4], radiative interactions and momentum exchanges between the air and the urban surface. Given the complex nature of the urban surface land-surface models (LSMs), used for weather forecasts, tend to employ simplifications, often approximating the geometry as infinite canyons, parameterizing the flow and reducing radiative calculations to two dimensions. It has been shown that such models tend to struggle to accurately predict the latent heat flux and that models that decouple the buildings and vegetation perform worse across all of the fluxes. It has also been shown [5] that models that reduce the urban surface to an infinite canyon perform poorly in terms of partitioning the radiative energy across the urban surface – the ramifications for the SEB being evident.

This work aims to investigate the impact that shading has on the SEB in vegetated urban areas and hence quantify the uncertainty associated with fluxes calculated by LSMs that do not account for realistic shadow-casting effects.

2 METHOD

Two cases are simulated, both considering the same vegetated urban area but with different solar zenith angles and therefore different shade distributions. The SEBs arising from these two cases are compared.

DOI 10.5258/WES/P0032

2.1 Setup

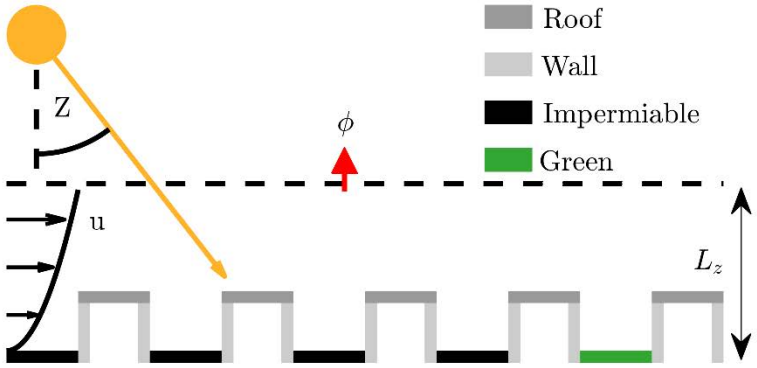

Figure 1, Schematic representation of the simulations.

Figure 1 shows how the simulations are setup, the solar zenith angle (Z) is fixed, a constant flow rate (u) is enforced such that the plane averaged streamwise velocity is 4 ms^{-1}, the domain height (L_z) is 384 m and the surface comprises of roofs, walls impermeable floor material (roads and pavements) and green spaces. The simulations experience a constant forcing and so are in a statistically steady state. This means the fluxes exhibit turbulent fluctuations about a constant mean.

The two zenith angles used are Z = 45° (case 1) and Z = 0° (case 2) which correspond to mod afternoon and midday respectively. Reducing the zenith angle by 45° will increase the total radiative power incident on the surface by a factor of $\sqrt{2}$ which will significantly alter the buoyancy and turbulence. As this work focuses only on the distribution of shading this effect is negated by reducing the solar irradiance by $\sqrt{2}$.

2.2 Geometry

Figure 2 shows the geometry that is used in this work. The geometry is 1152 x 768 x 384 m^3 and is formed of 6 copies of a unit tile – this is done to reduce computational requirements. The geometry was produced using an urban landscape generator (ULG) similar to that presented by Sützl et al. [6]. The urban area is constructed such that it has morphometric indicator values that are within the ranges defined by Yu et al. [7] for mixed-type residential and commercial zones.

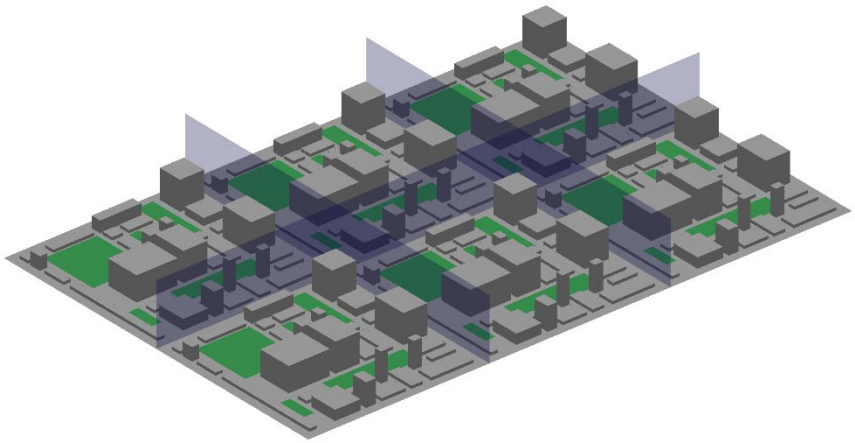

Figure 2, the urban geometry used, the blue planes highlight periodicity.

DOI 10.5258/WES/P0032

2.3 uDALES

The simulations are run using the urban Dutch Large Eddy Simulation code (uDALES), a Fortran based large eddy simulation (LES) model that includes a two-way coupled SEB scheme [8]. Building on the work presented Grylls et al. [9] the code has been extended to allow for the simulation of radiatively forced convective boundary layers in periodic domains.

3 RESULTS

Figure 3 shows the area averaged SEB fluxes for both cases normalised by their values in case 1.

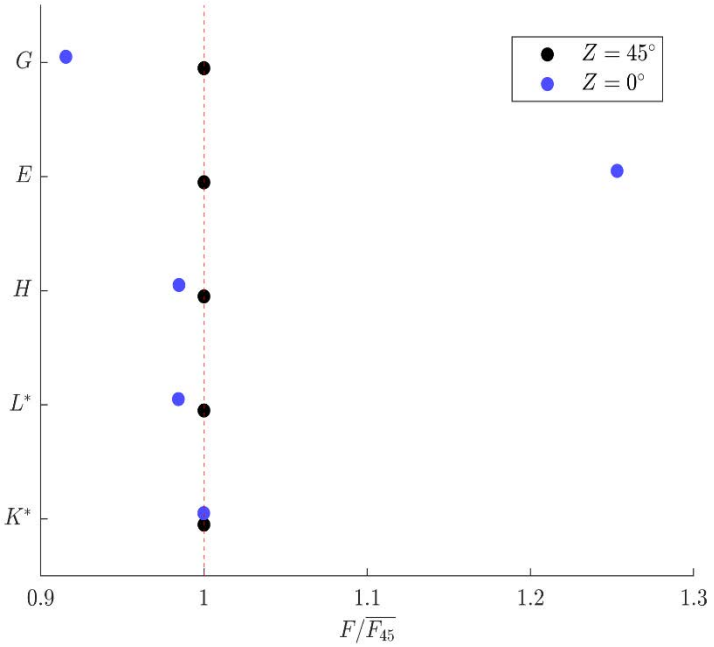

Figure 3, area averaged SEB fluxes for both cases, normalised by their case 1 values.

By definition, the Z = 45° results are 1 for each of the fluxes. There is almost no change in K^* when Z = 0°, as discussed, the incoming shortwave is adjusted however this should not mean that there is no change in K*. When increasing the zenith angle more of the walls will be in direct sunlight and more of the roads and green space will be shaded. Additionally, there will be more reflections of direct shortwave between buildings as the walls are in general more illuminated than when the Sun is directly overhead. As a result, even though the total incident shortwave is the same we would still expect some change in K*. That the values are very similar suggests that the changes in shading, reflections and sunlit albedo happen to balance out. Both L^* and H decrease by about 3% with the Sun directly overhead, G decreases by around 8% and E increases by approximately 25%. This suggests that E is sensitive to the distribution of shading and may explain why LSMs which simplify the geometry, and therefore do not correctly partition the radiative fluxes, tend to struggle to accurately reproduce E. That the other fluxes vary significantly less may suggest that they are not affected by the shading distribution, however, as the result has only been shown for one geometry and one pair of zenith angles it might be coincidental. It is possible that the combination of surface materials and the shape of the geometry used in this work are such that the changes in the fluxes across the surface almost exactly balance out. Furthermore, if the similarity in K* is not seen in other geometries then we would definitely expect larger variations in the other fluxes because K* is the most significant energy supply to the balance. For example, as the zenith angle increases less of the wall surface area is shaded but more of the floor is in shade. The same argument does not apply for E because green spaces only exist on the floor and so as Z increases the amount of green space that is in the shade can only increase.

DOI 10.5258/WES/P0032

4 CONCLUSIONS

The SEB data obtained from running the two cases with different zenith angles highlights that shading plays a significant role in determining E, the average value varying by 25%. In this instance K* is essentially unchanged which is likely a coincidence of the materials and geometry used, with various effects cancelling out. Whilst such cancelling out may also contribute to reducing the changes in the other fluxes it is certain that if K* varied significantly then the other fluxes would too. To investigate this further a greater range of geometries and zenith angles should be investigated.

REFERENCES

[1] Perkins-Kirkpatrick, S. E. & Lewis, S. C. (2011), 'The joint uk land environment simulator (jules), model description – part 2: Carbon fluxes and vegetation dynamics', Geoscientific Model Development 4(3), 701–722.

[2] Kleerekoper, L., van Esch, M. & Salcedo, T. B. (2012), 'How to make a city climate-proof, addressing the urban heat island effect', Resources, Conservation and Recycling 64, 30–38. Climate Proofing Cities.

[3] Zhang, X. Q. (2016), 'The trends, promises and challenges of urbanisation in the world', Habitat International 54, 241–252.

[4] Piringer, M., Grimmond, C. S., Joffre, S. M., Mestayer, P., Middleton, D. R., Rotach, M. W., Baklanov, A., De Ridder, K., Ferreira, J., Guilloteau, E. & et al. (2002), 'Investigating the surface energy balance in urban areas — recent advances and future needs', Urban Air Quality - Recent Advances p. 1–16.

[5] Schoetter, R., Caliot, C., Chung, T.-Y., Hogan, R. J. & Masson, V. (2023), 'Quantification of uncertainties of radiative transfer calculation in urban canopy models', Boundary-layer meteorology 189(1-3), 103–138.

[6] Sützl, B., Rooney, G. & Van Reeuwijk, M. (2021-Feb), 'Drag distribution in idealized heterogeneous urban environments', Boundary-Layer Meteorology.

[7] Yu, T., Suetzl, B. & Van Reeuwijk, M. (2023-Jul), 'Urban neighbourhood classification and multiscale heterogeneity analysis of greater london', Environment and Planning B: Urban Analytics and City Science.

[8] Owens, S. O., Majumdar, D., Wilson, C. E., Bartholomew, P., and van Reeuwijk, M.: A conservative immersed boundary method for the multi-physics urban large-eddy simulation model uDALES v2.0, EGUsphere [preprint], https://doi.org/10.5194/egusphere-2024-96, 2024.

[9] Grylls, T., Suter, I. & Van Reeuwijk, M. (2020-Aug), 'Steady-state large-eddy simulations of convective and stable urban boundary layer', Boundary-Layer Meteorology.

DOI 10.5258/WES/P0032

Drag Characteristics of a Volumetric Tree Model in Computational Fluid Dynamic Simulations

Dipanjan Majumdar[1*] and Maarten van Reeuwijk[1]
[1]Department of Civil and Environmental Engineering, Imperial College London
London SW72AZ, United Kingdom
[*] E-mail: d.majumdar@imperial.ac.uk

1 INTRODUCTION

Trees play a crucial role in urban environments, offering potential solutions to significant challenges like urban air quality and the urban heat island effect by modifying the local exchanges of momentum, radiation, moisture, heat and pollution. Given the multi-fold impact of trees on urban ecosystem, they must be included in the microscale models of urban environment to obtain an accurate prediction of the urban wind flow [1]. The assessment of trees' impact on urban areas is often investigated through urban microclimate models relying on either wind tunnel experiments with small-scale tree models [2, 3] or volumetric source models in computational fluid dynamics (CFD) simulations [4]. However, it remains unclear how to map the aerodynamic characteristic of model trees in experiments or of large urban trees in CFD simulations accurately.

Often in CFD based micorscale urban models, trees are modelled following a 'grey scale' approach [4], *i.e.*, neither the tree effects are entirely parameterized as done in mesoscale models, nor is the tree behaviour resolved going in the level of tree branches and leaves. Instead, trees are modelled as porous volumetric blocks using a volumetric source/sink term (S_{u_i}) in the momentum equation. This source/sink term accounts for the combined inertial and viscous losses introduced by the presence of the tree, and has a quadratic dependence on the local wind velocity as given by [5],

$$S_{u_i} = -aC_d^V |u_i| u_i \tag{1}$$

where u_i indicates wind velocity, a is the leaf-area density defining the one-sided surface area of leaves over the volume of air that they are present in [6], and C_d^V is the volumetric drag coefficient. The flow turbulence due to the tree-air interactions is resolved using appropriate turbulence models. Notably, a and C_d^V are the two main parameters required as inputs to perform a CFD simulation with a tree canopy.

In contrast to CFD simulations, wind tunnel experiments with model trees compute the bulk drag coefficient C_d based on the bulk drag force measured using the force measuring instruments. The bulk drag coefficient is defined as

$$C_d = \frac{2F_D}{\rho U_\infty^2 A_F} \tag{2}$$

where F_D indicates the bulk drag force, ρ is wind density, U_∞ is the streamwise free stream velocity, and A_F is the projected frontal area. Another important quantity often measured in wind tunnel experiments, that in a way represents the aerodynamic resistance of a tree, is the aerodynamic porosity (α) defined as the ratio of volume flux going through the tree to the volume flux entering at the windward plane of the tree canopy [7],

$$\alpha(x) = \frac{\iint_{A_F} \bar{u}(x,y,z)\, dy\, dz}{\iint_{A_F} \bar{u}(0,y,z)\, dy\, dz} \tag{3}$$

where $\bar{u}$ is the mean streamwise wind speed, and x, y, z indicate the coordinate directions.

As listed above, the CFD simulation with a tree canopy requires a and C_d^V as inputs whereas the wind tunnel experiments with model trees measure the quantities C_d and α. However, a direct correlation between these is yet to be achieved. Note that C_d being defined based on a two-dimension projected area, is different from the volumetric coefficient C_d^V. Thus it is not clear what values for a and C_d^V to use as inputs to replicate the aerodynamic characteristics of an experimental model tree in a corresponding CFD simulation accurately. The present study aims to establish a connection between the two set of parameters

DOI 10.5258/WES/P0034

in an appropriate manner such that both the CFD and wind tunnel model trees yield comparable aerodynamic traits. To this regard, a simplified canopy model for the flow inside a vegetation canopy is proposed in Section 2 and the supporting results are presented in Section 3. Finally, the main findings are concluded in Section 4.

2 ANALYTICAL MODEL FOR THE FLOW INSIDE A VEGETATION CANOPY

A simplified steady-state Reynolds-averaged horizontal momentum equation considering only the horizontal advection, the pressure gradient, and the source/sink term modelling the tree drag can be written as

$$\bar{u}\frac{\partial \bar{u}}{\partial x} + \frac{\partial \bar{p}}{\partial x} = -aC_d^V \bar{u}^2 \tag{4}$$

where $\bar{p}$ indicates mean pressure upon density. Here, we consider a homogeneous vegetation canopy of length L, width W and canopy height h, with the base of the canopy being at a height of h_0 from the ground; see in Fig. 1. Averaging Eq. 1 over the canopy frontal area gives,

$$\frac{dU^2}{dx} + \frac{2}{c}\frac{dP}{dx} = -2aC_d^V U^2 \tag{5}$$

where $U = (Wh)^{-1}\iint_{A_F} \bar{u}\, dA$, $P = (Wh)^{-1}\iint_{A_F} \bar{p}\, dA$, and c is a shape factor defined such that $cU^2 = (Wh)^{-1}\iint_{A_F} \bar{u}^2\, dA$. In order to be able to obtain a closed form solution for Eq. 5, a key assumption is made at this stage that the pressure gradient inside the tree canopy evolves in the same way as the inertial term, *i.e.*,

$$\frac{2}{c}\frac{dP}{dx} = \beta\frac{dU^2}{dx} \tag{6}$$

where β is a coefficient assumed to be independent of x and accounts for all the complex three dimensional flow phenomena not considered in the flow governing equations above (Eqs. 4 and 5). The results will show that this assumption works reasonably well; although other parameterisations are conceivable, this one stands out for its simplicity. Additionally, the leaf area density and the volumetric drag coefficients are combined to a single quantity which we define as the drag length $\ell_d = (aC_d^V)^{-1}$. Substituting these assumption into Eq. 5, one can obtain the equation for the bulk flow inside a tree canopy as

$$(1+\beta)\frac{dU^2}{dx} = -\frac{2}{\ell_d}U^2 \tag{7}$$

which has a closed form solution given by,

$$U^2 = U_0^2\, e^{-\frac{2}{1+\beta}\cdot\frac{x}{\ell_d}} \tag{8}$$

where U_0 is the average streamwise wind speed at the windward plane of the canopy, *i.e.*, $U_0 = U|_{x=0}$ assuming the vegetation canopy starts at $x = 0$. From Eq. 7, the aerodynamic porosity can be derived following Eq. 3 and is given by,

$$\alpha^2 = \frac{U^2}{U_0^2} = e^{-\frac{2}{1+\beta}\cdot\frac{x}{\ell_d}} \tag{8}$$

This Eq. 9 is the key equation that describes the evolution of bulk flow inside the tree canopy. This simplified analytical model finds an exponential decay of the bulk flow inside the canopy along its length.

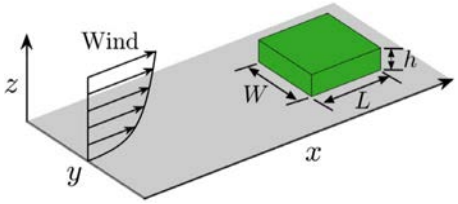

Figure 1, schematic diagram showing a simplified tree canopy model

DOI 10.5258/WES/P0034

Note in Eq. 9, the aerodynamic porosity α in the left hand side can be directly measured in a wind tunnel experiment by measuring the velocity field at the windward and leeward plane of the tree canopy. On the other hand, the drag length ℓ_d in the right hand side of Eq. 9 is directly related to the input parameters a and C_d^V required in the CFD simulations. Thus the Eq. 9 establishes the direct interconnection between the wind tunnel experiments and CFD simulations. We propose the drag length ℓ_d to be the main parameter that dictates the bulk aerodynamic signature of a vegetation canopy. For a tree canopy in a wind tunnel experiment and in a CFD simulation (of same length scale) to be of comparable aerodynamic traits, the drag length must remain the same in both these situations.

3 VALIDATION OF THE PROPOSED ANALYTICAL MODEL

The credibility of the proposed analytical model for the bulk flow inside a vegetation canopy (Eq. 9) is tested through a series of large eddy simulations. The simulations are performed using uDALES [8] which is a multi-physics micro-climate modelling framework for urban environment. It performs the large eddy simulation of the incompressible Navier-Stokes equations within the Boussinesq approximation. Grylls and van Reeuwijk [4] included trees in the uDALES framework, modelling the drag, shading, evaporation and deposition. Trees are modelled in uDALES as rectangular blocks, and the source/sink term defined in Eq. 1 is applied to the grid points that fall within the volumetric tree blocks. In the present simulations, a rectangular tree block is considered with $L \times W \times h = 4.5 \times 4.5 \times 6.5$ m^3, being inspired by the dimension of the model tree used in the wind tunnel experiments of Fellini et al. [3]. The base of the tree block is at $h_0 = 2$ m height from the ground, hence the crown of the tree is at a height of $h_{ref} = h_0 + h = 8.5$ m from the ground. A comprehensive parametric study is performed covering wide ranges of C_d^V and a values, summarized systematically in Table 1 along with the resulting C_d and α_L $(= \alpha|_{x=L})$ computed from the simulation outputs. Note in Table 1, the individual values of the input parameters C_d^V and a are not important and are interchangeable; the output aerodynamic properties are primarily governed by the combined drag length ℓ_d. All the cases C11 - C15 results in the same C_d and α_L as dictated by $\ell_d = 5$ m in these cases, though a and C_d^V took values of various combinations. This finding corroborates the theory proposed in Section 2. Moreover, it is observed that a decrease in drag length increases C_d and decreases α_L.

Next, the contour plots of mean streamwise wind velocity and the turbulent kinetic energy at the mid-span vertical plane are presented in Figs. 2a and 2b respectively, for a typically chosen case form Table 1. Presence of tree canopy slows down the incoming flow as it enters into the canopy. Both flow velocity and TKE decay towards the leeward side of the canopy. Similar trend is seen for all remaining cases as well, and therefore not repeated here only for the sake of brevity. For a quantitative representation, the variation of aerodynamic porosity along the length of the tree canopy is shown in Fig. 2c. Note that the evolution of α obtained from the simulation results indeed reflects an exponential decay agreeing well to

Table 1, parameter space: cases C1-C5 vary C_d^V, C6-C10 vary a, C11-C15 vary both C_d^V and a such that ℓ_d remains constant, and C16-C20 are representative limiting ℓ_d cases

Type	C_d^V	a [m^2/m^3]	ℓ_d [m]	C_d	α_L	Type	C_d^V	a [m^2/m^3]	ℓ_d [m]	C_d	α_L
C1	0.1	1.0	10	0.657	0.61	C11	0.1	2.0	5	0.893	0.43
C2	0.15	1.0	6.67	0.804	0.48	C12	0.15	1.33	5	0.893	0.43
C3	0.2	1.0	5	0.893	0.43	C13	0.2	1.0	5	0.893	0.43
C4	0.25	1.0	4	0.954	0.37	C14	0.25	0.8	5	0.893	0.43
C5	0.3	1.0	3.33	0.998	0.32	C15	0.3	0.67	5	0.893	0.43
C6	0.2	0.5	10	0.657	0.61	C16	0.0	0.0	∞	0.0	1.0
C7	0.2	0.75	6.67	0.804	0.48	C17	0.2	0.1	50	0.189	0.91
C8	0.2	1.0	5	0.893	0.43	C18	0.15	0.5	13.33	0.55	0.69
C9	0.2	1.25	4	0.954	0.37	C19	0.3	2.0	1.67	1.1	0.15
C10	0.2	1.5	3.33	0.998	0.32	C20	0.3	3.0	1.11	1.127	0.07

DOI 10.5258/WES/P0034

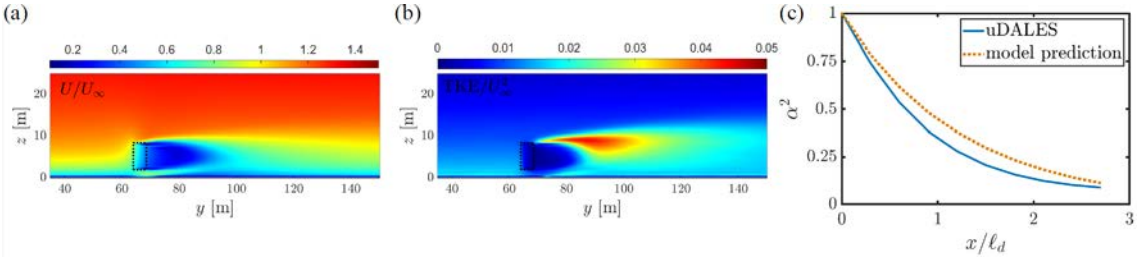

Figure 2, contour of mean (a) streamwise velocity and (b) turbulent kinetic energy at the mid-span vertical plane for the case C3, and (c) the corresponding evolution of aerodynamic porosity inside the canopy

Eq. 9 derived in Section 2, thus establishing the credibility of the proposed theoretical model. An appropriate value of the coefficient β in Eq. 9 is estimated by extracting $\alpha^2(x)$ inside the canopy such that the simulation output result best fits Eq. 9.

4 CONCLUSIONS

The current study contributes towards better understanding of the interplay between volumetric tree modelling parameters and the drag behaviour of wind tunnel tree models. It reveals that the aerodynamic characteristics of the tree model does not depend on the individual modelling parameters C_d^V and a, but the combined drag length ℓ_d defined in this work plays the pivotal role in determining C_d and α. The present work proposes a simplified analytical model for the evolution of bulk flow inside a tree canopy, and derives an equation for aerodynamic porosity as it evolves along the length of the canopy. This theoretical model provides a direct interlinking between aerodynamic porosity, which is a measurable quantity in wind tunnel experiments, and the volumetric tree modelling input parameters required in CFD simulations. Drag length ℓ_d is the novel parameter defined here to act as the bridge between experimental and simulation approaches, leading to potential equivalences in aerodynamic characteristics of the tree models used in these approaches. This establishes a practical mean for emulating an experimental tree model/natural tree to reproduce the corresponding drag behaviour in CFD simulations accurately.

REFERENCES

[1] Salim M.H., Schlunzen K.H. & Grawe D. (2015). "Including trees in the numerical simulations of the wind flow in urban areas: Should we care?", *J. Wind Eng. Ind. Aerod.* **144**, 84–95.

[2] Manickathan L., Defraeye T., Allegrini J., Derome D. & Carmeliet J. (2018). "Comparative study of flow field and drag coefficient of model and small natural trees in a wind tunnel", *Urban For. & Urban Green.* **35**, 230-239.

[3] Fellini S., Marro M., Del Ponte A.V., Barulli M., Soulhac L., Ridolfi L. & Salizzoni P. (2022). "High resolution wind-tunnel investigation about the effect of street trees on pollutant concentration and street canyon ventilation", *Build. Environ.* **226**, 109763.

[4] Grylls T. & van Reeuwijk M. (2021). "Tree model with drag, transpiration, shading and deposition: Identification of cooling regimes and large-eddy simulation", *Agric. For. Meteorol.* **298**, 108288.

[5] Finnigan J. (2000). "Turbulence in plant canopies", *Annu. Rev. Fluid Mech.* **32**, 519–571.

[6] Oke T.R., Mills G., Christen A. & Voogt J.A. (2017). *Urban climates*. Cambridge University Press, Cambridge.

[7] Guan D., Zhang Y. & Zhu, T. (2003). "A wind-tunnel study of windbreak drag", *Agric. For. Meteorol.* **118**, 75–84.

[8] Owens S.O., Majumdar D., Wilson C.E., Bartholomew P. & van Reeuwijk M. (2024). "A conservative immersed boundary method for the multiphysics urban large-eddy simulation model udales v2. 0", *EGUsphere* 1–33.

DOI 10.5258/WES/P0034

Small wind ram air turbine blade geometric modification for performance

Kiran S Gadda[1], Hardit R Saini[1], Mariana G. Avila Zaya[1], Nithya Venkatesan[2], Eldad J Avital[1*]
[1]School of Engineering and Materials Science, Queen Mary University of London UK
[2]School of Electrical Engineering, Vellore Institution of Technology, Chennai India
[*] E-mail: e.avital@qmul.ac.uk

1. INTRODUCTION

Wind energy is one of the main pillars of renewable energy policy worldwide. Various installations of different size are used from small turbines in urban settings to large off-shore structure. The common with all of them that they fixed to the ground (on shore or seabed) or sometimes on floating platforms. Hence in terms of aerodynamic design extracting maximum power P from the incoming wind is the primary point. The drag experienced by the turbine which (due to historial reasons of being develop from the propeller design) is referred as thrust *T*. It is considered to be less crucial for stationary grounded application and is mainly required for the structural design of the turbine.

However, recently interest has grown at small airborne wind turbines as attached to aircraft or stationary airships in order to provide additional power to the air vehicle, which may transmitted to the ground in case of an airship. We will call this kind of turbine ram air turbine (RAT) [1]. On the face it, such turbine does not make sense as always it is efficiency will be less than one, meaning the loss of thrust for the aircraft due the drag caused by the small turbine will require power compensation from the engine higher than the power the turbine can give the aircraft. However, there are instances when power is so needed and/or slowing down the air vehicle is acceptable in order to get that additional power. Nevertheless, in this concept of extracting power from the wind the drag experienced by the turbine (which we note as *T*) has to be considered as important as the power P. We can normalise both to yield coefficients of power and thrust C_P and C_T respectively as follows:

$$C_P = \mathrm{P}/(0.5\rho \mathrm{A V}^3)\,,\; C_T = \mathrm{T}/(0.5\rho \mathrm{A V}^2), \tag{1}$$

where ρ is the air density, *A* is the cross-section area covered by the turbine's rotor, V is the incoming wind speed towards the turbine (taken as low enough for incompressible flow assumption).

There has been strong interest to increase C_P using passive or active aerodynamic control means. For example, we can use the simple installation of Gurney Flap (GF) illustrated in Fig 1 named after the F1 race car driver who introduced the flap in 1971 to increase the lift *L* produced by the spoiler of the car. Hence, this small modification has strong potential to increase the power production for a lift based turbine, as our group argued for a vertical axis wind turbine [2].

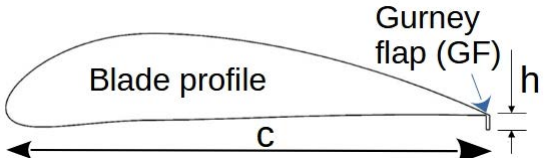

Figure 1, illustration of a Gurney Flap (GF) mounted perpendicular at the trailing edge of the blade profile, where c is the profile's chord length and h is the GF's height.

However, the GF will also increase the drag *D* caused by the profile as surely it will enhance flow separation around the trailing edge (T.E). This does not prevent the C_P to increase due to the GF demonstrated by the following blade element momentum (BEM) analysis and Fig 2 for a horizontal axis wind turbine (as commonly in RAT design). Taking that the resultant force acting in the rotation plane as caused the aerodynamic forces lift *L* and drag *D*: $F_Q = \mathrm{L}\cdot\sin\phi - D\cdot\cos\phi$. Assuming high tip speed ratio $TSR = \Omega R/V$ (see Fig 2 for definitions), linear aerodynamics and a simplistic model of constant drag coefficient C_D we get for the maximum possible C_P [3];

$$(C_P)_{\max} = \frac{\sigma(\mathrm{TSR})^3}{4}[2\phi_t C_{L_t} - C_D], \tag{2}$$

DOI 10.5258/WES/P0035

where

$$C_L = \mathrm{L}/(0.5\rho \mathrm{U}^2 c)\,,\ C_D = \mathrm{D}/(0.5\rho \mathrm{U}^2 c)\,,\ \sigma = \mathrm{b}\bar{c}/(\pi \mathrm{R}). \quad (3)$$

The speed U is defined in Fig 2, b is the number of blades (b=2 for our RAT) and $\bar{c}$ is the mean geometric chord length of the blade. The subscript t relates to the blade's tip condition where we neglected tip losses in Eq (2).

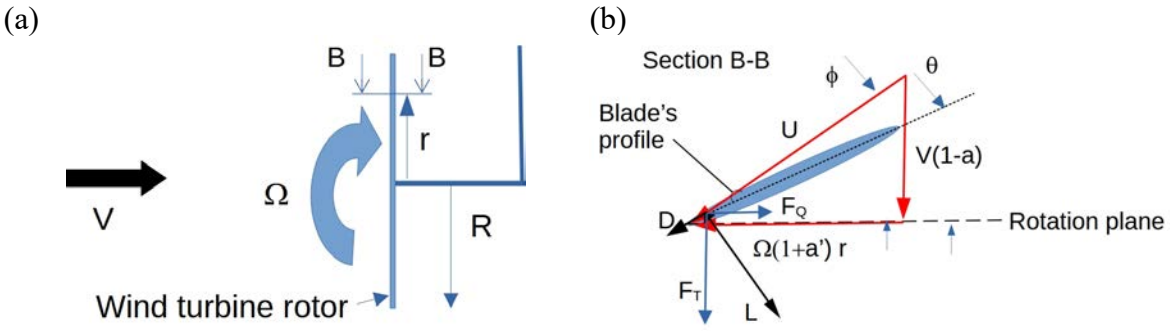

Figure 2, illustration of a blade element method analysis of a horizontal axis ram air turbine (RAT) configuration, where a and a' are the axial and tangential induction factors.

Since the aerodynamic efficiency of a profile C_L/C_D is so high (above 10) then even when the GF causes a higher percentage increase in C_D than in C_L, it will still lead to an increase in C_P by Eq. (2) as long as the flow angle ϕ_t does not change much (it relates to the pitch angle θ_t through a quadric equation). However, the force contributing to the thrust T of the turbine is $F_T = \mathrm{L}\cdot\cos\phi + \mathrm{D}\cdot\sin\phi$ by Fig 2 and for TSR>>1, $\phi \ll 1$ rad and thus $F_T \simeq L$. Hence T will increase due an increase in the profile's lift caused by the GF. Nevertheless, if we manage to keep the ratio C_P/C_T as similar to the (clean) configuration without the GF, then increasing C_P using a GF (or any other blade) modification will still be highly useful. This is the aim of this paper. We started looking at this using a combination of 2D computational fluid dynamics (CFD) and BEM for a generic RAT, showing that it is possible to achieve such improvement if the GF is implemented only partly near the blade's hub [1]. Here, we extend this study by using additional wind tunnel test results and known optimisation procedures for the blade's twist angle to maximise C_P.

2. METHODOLOGY

The methodology follows the BEM approach. The aerodynamic forces acting on the blade profile due to the incoming wind were studied using three methods and then were fed into the freeware qblade that calculated the turbine's coefficients C_P and C_T using the BEM method [4]. For the 2D profile aerodynamic calculations we used Xfoil as implemented in qblade [4], computational fluid dynamics (CFD) based on RANS and wind tunnel tests. Xfoil proved itself sufficiently accurate for the clean profile (i.e. with no GF) in pre-stall conditions, while the flow separation around the profile's T.E. caused by the GF led to distortion in the Xfoil's results. The 2D CFD-RANS calculations were pursued using the Ansys software, where a structural C grid was used along with the SST k-omega RANS model. Second order upwind and central schemes were used for the convection and diffusion terms respectively. A velocity inflow condition was used along with a pressure outlet as an outflow condition. The overall computational domain size was (26x26)c, where symmetry conditions were used on the upper and lower sides of the computational domain. Grid point clustering was used near the profile, leading to a y^+<1 for the first grid point above the profile's skin. For further details on this CFD approach, the reader is referred to Ref [2].

The wind tunnel tests were pursed in the open suction wind tunnel AF100. As in the CFD and Xfoil calculations, the Reynolds number was matched with that experienced by the blade's profile. The incoming velocity was measured through a pitot tube and the blade model was put on a balance to measure the lift and drag. The model stretched from wall to wall of the work section, but cautiously it did not touch the walls. This led to a very minor secondary flow through the less than 1 mm gap between the wall and the model (as compared to the model's chord length of 127 mm), which mildly increased the drag. Measurements were averaged along a period of time and repeated several times to remove any temporary fluctuations.

DOI 10.5258/WES/P0035

3. RESULTS AND ANALYSIS

A two-blade RAT was studied with the profile NACA8318 [1, 5]. Its geometry and twist angle are illustrated in Fig 3. The chord length *c* was uniform along the blade's span yielding a Reynolds number Re_C (as based on c) varying from about 218k 25% away from the hub to close to 700k near the tip at mid range TSR of about 4. This means the blade exhibits laminar aerodynamics near the hub, while turbulent aerodynamics near the tip.

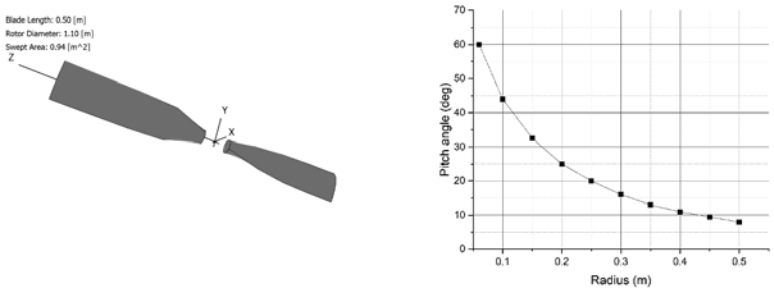

Figure 3, the RAT's studied geometry and its pitch angle variation along the blade's span.

The lift and drag coefficients variations with the angle of attack (AoA) for Re_C=218k which corresponds to the condition of the blade profiterole about 25%*R* away from the hub are shown in Figure 4 for the clean profile and those with GF (where *h*/*c* is noted by its percentage). These are the CFD results. All configurations show a region of linear aerodynamic followed by a stall. The slope of the lift coefficient is mildly below the familiar one for high Reynolds number (~0.1 1/deg) but also the wind tunnel test for the model with GF3% yielded a similar lift coefficient (although mildly higher, pointing to a deficiency of the RANS model at low Reynolds numbers). As Re_C was increased above 400k (making the profile dominated by turbulent aerodynamics) the C_L slope got very close the 0.1 1/deg value. The installation of the GF increases the lift coefficient but also increase the drag. This occurs due to the enhanced flow separation near the profile's trailing edge. It also hastens the occurrence of stall, as relative to the geometric AoA (i.e. as relative to the chord line) shown in Fig 4.

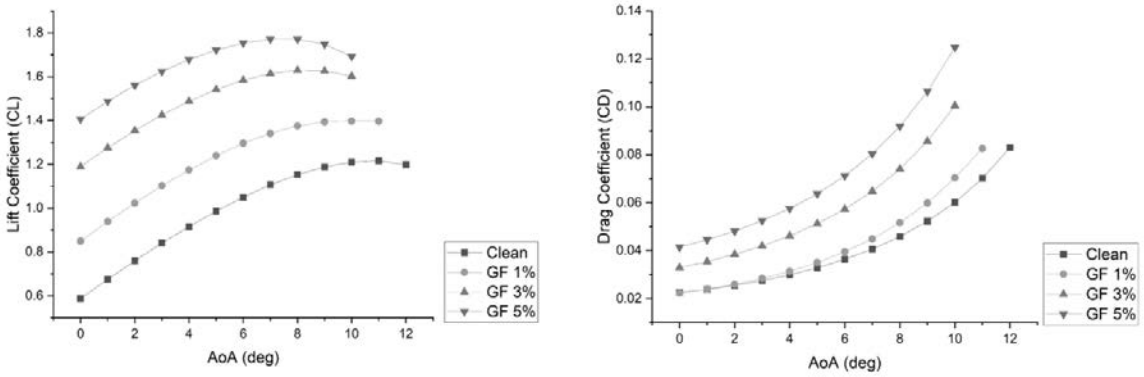

Figure 4, the variations of the lift and drag coefficients with the angle of attack (AoA) for the clean NACA8318 profile and its modifications with installed GF, where the GF height to chord length ratio (h/c) is noted in percentages and Re_C=218k. The results were produced using CFD-RANS.

To better understand the effect of the GF, we show the flow contours around the clean profile and its modified version with GF 3% at AoA=9 deg. Both profiles show noticeable flow separation near the trailing edge, but the one with the GF has a larger flow separation above the upper surface and also a small flow separation on the lower surface just in front of the GF. This results in a longer wake of flow separation beyond the profile and hence the higher drag coefficient, and earlier stall caused by the GF. Nevertheless, one should note that at low AoAs < 4 deg, all the profiles with GF modification showed higher aerodynamic efficiency (C_L/C_D) than the clean profile (i.e. no GF modification)

Finally, we present in Fig 6 the variations of C_P and C_P/C_T with TSR. It is seen that when using GF of 3% the TSR of the maximum C_P increases as well as the value of C_P. Hence, the ratio of C_P/C_T can also increase. Furthermore, the original configuration of the RAT [5] as illustrated in Fig 3, seems to have been

DOI 10.5258/WES/P0035

optimised for its twist angle (yielding a variation close to 1/*r* as seen in Fig 3), but not for its chord length variation. Using the Betz BEM optimisation algorithm [4] we managed to further improve the C_P and C_P/C_T behaviours for TSR around 4.

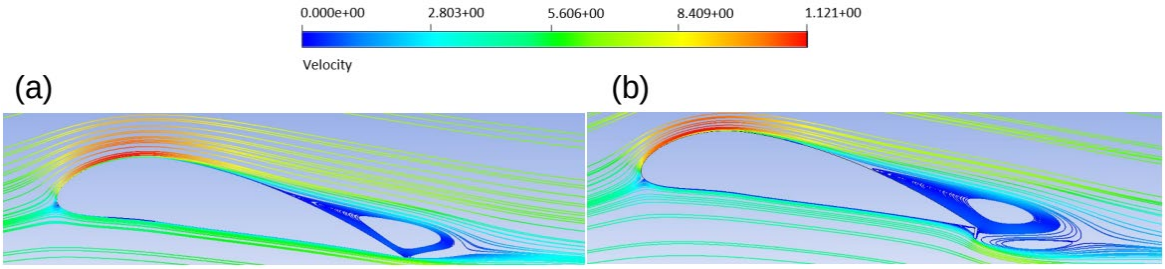

Figure 5, the flow regime around (a) the clean NACA8318 and (b) its modification with GF h/c=3% at AoA=9 deg as computed by the CFD-RANS and where the rest of the conditions are as in Fig 4. The velocity magnitude values have been normalised.

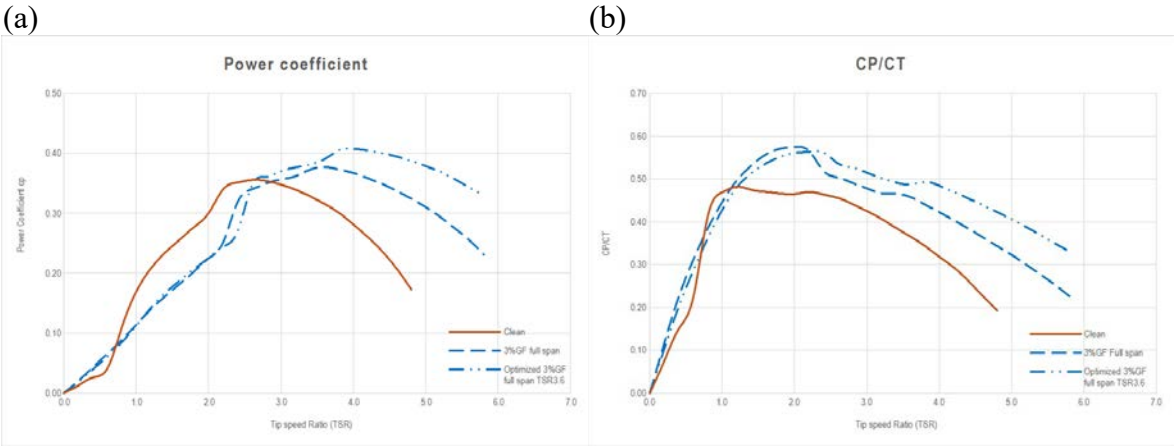

Figure 6, the variations of (a) C_P (b) C_P/C_T ratio with TSR for the original RAT configuration and its modification with GF installation of h/c=3% along with a Betz-BEM optimisation around TSR=3.6.

4. CONCLUSIONS

A small horizontal axis wind turbine was studied for its aerodynamic performance in context of its power *P* production and also thrust *T* (i.e .the actual drag it causes). It was argued that while in terrestrial implementations the importance is usually put on *P* and *T* is mostly important for structural considerations, *T* becomes as important as *P* for performance in airborne installation. It was also argued that enhancing *P* by increasing the lift produced by the blade will also very likely increase *T.* Hence, the focus of the aerodynamic design should be on the coefficient C_P and the coefficients ratio of C_P/C_T. It was shown that a Gurney flap (GF) installation has the potential to increase C_P and also C_P/C_T which can be attractive for further design. Further experimental tests and computations will be carried out to verify these results and also study other variations of GF as slotted ones.

REFERENCES

[1] Zayas M.G. & Avital E.J. (2023) "Computational analysis of the effects of Gurney Flaps on commercial Ram Air Turbine performance" AIAA paper 2023-76568, Regional student conference

[2] Yan Y, Avital E, Williams JJR & Cui J (2020) "Performance Improvements for a Vertical Axis Wind Turbine by Means of Gurney Flaps", *J Fluid Eng* **142**, 021205

[3] Ai K, Wang M, Wang D, Wang H, R Cao R & Avital E (2021) "Numerical study of a generic tidal turbine using BEM optimization methods", *China Ocean Eng* **35**(3), 344-351

[4] Qblade.org (2024) "Qblade Documentation v2.0.7", https://docs.qblade.org/

[5] Bolaños M. (2020) "Optimización aerodinámica del rotor de la turbina RAT de un avión comercial" MSc dissertation, Facultad, unpublished, https://hdl.handle.net/20.500.12930/2485

DOI 10.5258/WES/P0035

A Comparison Study of Structural Wind Tunnel Tests and Code-based Approaches in Evaluating Wind Loads on Tall Buildings

Pietro Manica, Fabio Faseli, Tung Nguyen, Suresh Kumar, John Kilpatrick
RWDI
Milton Keynes, UK
pietro.manica@rwdi.com

1 INTRODUCTION

Wind loading is one of the key lateral forces acting on tall buildings, and mostly becomes dominant as the height increases. It governs the structural design of high-rise buildings in the UK and affect various critical elements such as shear walls, cores, and the layout of columns. Having a good estimate of wind loads acting on a building is critical to optimise the structural design, allowing efficient usage of materials and contributing to the overall reduction of embodied carbon.

Lateral wind-induced loads acting on tall buildings are named as along-wind loads and across-wind loads. As the name depicts, along-wind loads act in the direction of wind, while across-wind loads act in the direction perpendicular to wind. Across-wind loads are not well addressed in many standards due to its inherent complexity and left to the wind tunnel to determine.

Building codes and standards tend to focus on along-wind loads which are often used for the design of tall buildings at the preliminary stage. When the buildings have regular geometry and located in typical terrain conditions, the wind loads estimated based on codes could be reasonably similar to those derived from wind tunnels unless there are peculiar structural dynamic effects. RWDI possesses one of the world's most extensive portfolios of data from structural wind tunnel tests. Drawing upon its extensive database of wind response data, RWDI conducted studies to compare wind loads achieved by undertaking site-specific wind tunnel tests against values obtained using analytical code-based approaches.

In the first study, the along-wind loads of three buildings were estimated using Canadian (NBC 2015), American (ASCE 7-22), Australian (AS/NZS 1170.2:2021), and European (EN 1991-1-4:2005) standards and were compared with wind tunnel results. There are differences between the standards, and the European standard was found to be very conservative. Further explanations of the differences are provided in this paper.

In the second study, the peak overturning moments of ten prominent tall buildings in the UK were estimated from structural wind tunnel tests and compared against values based on the UK National Annex to Eurocode (NA to BS EN 1991-1-4:2005). Wind tunnel testing resulted in approximately 35% reduction in lateral wind loads, which could benefit structural design and optimization for material savings.

2 RESULTS OF INTERANTIONAL STANDARDS

2.1 Comparison of Loads

Three samples of wind tunnel-tested buildings have been chosen for comparison for this study. Along-wind loads have been estimated based on the chosen standards and compared against the wind tunnel results. Note that the influence of wind directionality is not accounted for in these comparisons. Buildings located in typical code-specified terrain conditions without dense immediate surroundings have been selected to mimic the isolated condition scenario. In some cases, across-wind loading is dominant, however for this study only the maximum along-wind loading has been compared.

The details of the buildings, and the estimated along-wind loads based on various standards and wind tunnel tests are provided in Tables 1 to 3. Fig. 1a to 1c show the pictures of the buildings in the wind tunnel and their axis system.

DOI 10.5258/WES/P0036

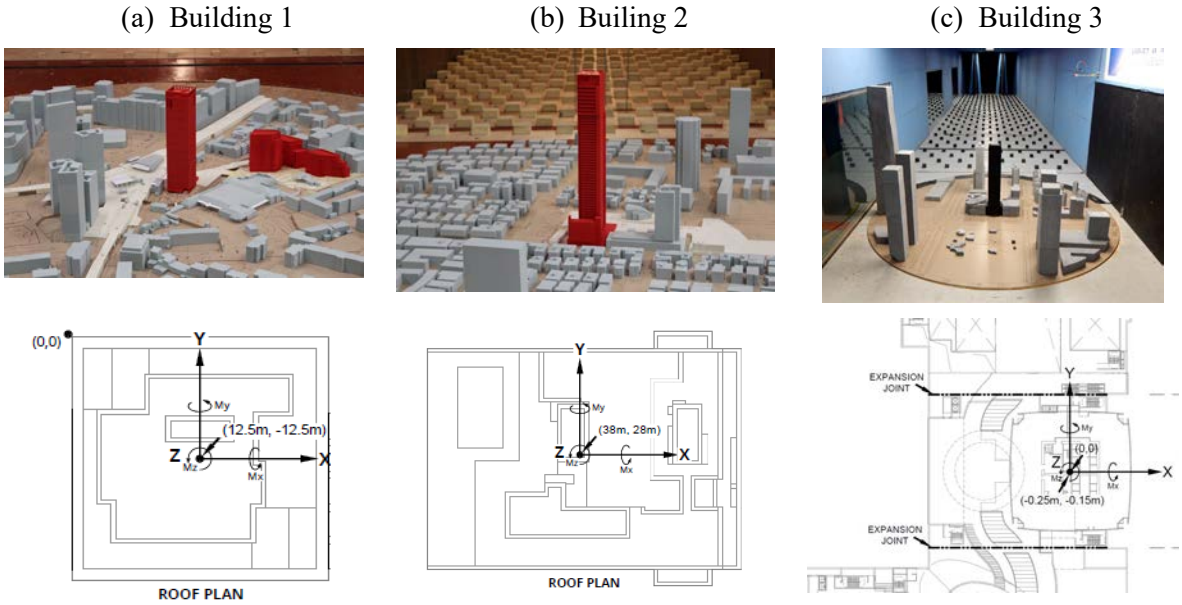

Figure 1, Wind tunnel model and the structural axes.

Table 1, Comparison of non-directional peak along-wind loads – Building 1.

	X	Y
Wind Speed (m/s)	21.5	
Terrain Category	III	
Height (m)	113.5	
Width (m)	23.3	23.7
Frequencies (Hz)	0.26	0.24
Damping (%)	2	

	Peak Along Wind Loads			
	My (Nm)	Mx (Nm)	Fx (N)	Fy (N)
NBC	1.27E+08	1.32E+08	2.04E+06	2.11E+06
ASCE 7-22	1.36E+08	1.41E+08	2.28E+06	2.34E+06
AS/NZS 1170.2	1.69E+08	1.75E+08	2.83E+06	2.92E+06
EN 1991-1-4	2.07E+08	2.14E+08	3.51E+06	3.64E+06
Wind Tunnel	1.31E+08	1.24E+08	2.03E+06	1.86E+06

Table 2, Comparison of non-directional peak along-wind loads – Building 2.

	X	Y
Wind Speed (m/s)	30	
Terrain Category	II	
Height (m)	191.23	
Width (m)	27.2	27.2
Frequencies (Hz)	0.21	0.21
Damping (%)	2	

	Peak Along Wind Loads			
	My (Nm)	Mx (Nm)	Fx (N)	Fy (N)
NBC	1.27E+09	1.74E+09	1.25E+07	1.70E+07
ASCE 7-22	1.15E+09	1.65E+09	1.16E+07	1.64E+07
AS/NZS 1170.2	1.27E+09	1.78E+09	1.28E+07	1.78E+07
EN 1991-1-4	1.73E+09	2.46E+09	1.70E+07	2.40E+07
Wind Tunnel	1.30E+09	1.74E+09	1.11E+07	1.70E+07

Table 3, Comparison of non-directional peak along-wind loads – Building 3.

	X	Y
Wind Speed (m/s)	25.5	
Terrain Category	III	
Height (m)	277	
Width (m)	46	46
Frequencies (Hz)	0.145	0.152
Damping (%)	2	

	Peak Along Wind Loads			
	My (Nm)	Mx (Nm)	Fx (N)	Fy (N)
NBC	3.17E+09	3.11E+09	2.04E+07	1.90E+07
ASCE 7-22	2.94E+09	2.88E+09	1.97E+07	1.82E+07
AS/NZS 1170.2	3.42E+09	3.32E+09	2.31E+07	2.11E+07
EN 1991-1-4	4.43E+09	4.29E+09	2.91E+07	2.65E+07
Wind Tunnel	2.47E+09	3.22E+09	1.59E+07	1.89E+07

In general, the NBC (Canadian) and ASCE (American) loading are the closest to the wind tunnel results. AS/NZS (Australian) standard-derived loads are somewhat higher than the wind tunnel results, but noticeably, the EN (European) standard always predicted the highest of all.

DOI 10.5258/WES/P0036

While NBC considers the dynamic pressure at half the height for determining leeward pressure, all the remaining standards use the dynamic pressure at full height. Note that NBC uses mean hourly speed, ASCE uses 3-sec gust speed, AS/NZS uses 0.2-sec gust wind speed, and EN uses 10-min mean wind speed for the prediction. Appropriate conversion factors have been used to convert the 10-min mean speed provided in Tables 1 to 3 to speed relative to other averaging times.

3 SOURCES OF DIFFERENCES

The main sources of differences in the results from the different building codes are attributed to differences in the wind velocity profiles, the external pressure coefficients and the gust factors.

3.1 Wind Velocity Profile

Wind velocity profiles scaled to basic wind speed at 10m for the above project site have been found different between the standards. As an example, a comparison of the mean and gust profiles is shown in Fig. 2 for Category III (Exposure B). Though gust speeds are in reasonable agreement between EN and AS/NZS regardless of the unknown averaging time with EN, mean speed profile corresponding to EN stands out compared to the remaining standards.

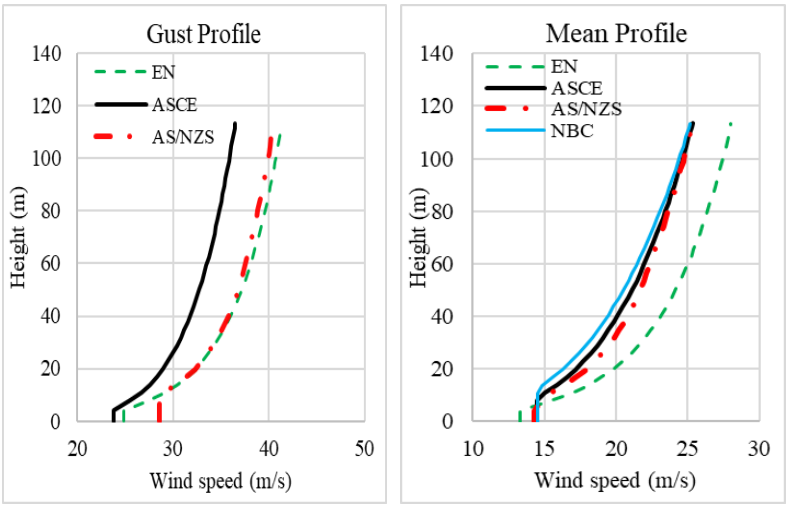

Figure 2, Comparison of wind speed profiles – Category III.

3.2 External Pressure Coefficients

For the prediction of along-wind loads, external pressure coefficients play an important role as well. For the specified building in this paper, the variation in combined windward (Cpw) and leeward (Cpl) external pressure coefficients is provided in Table 4. Once again, EN standard value is higher than the remaining standard.

Table 4, Combined external pressure coefficients.

		NBC		ASCE 7-22		AS/NZS 1170.2		EN 1991-1-4	
		X	**Y**	**X**	**Y**	**X**	**Y**	**X**	**Y**
Building 1	C_{pw}-C_{pl}	1.30	1.30	1.30	1.30	1.17	1.17	1.50	1.50
Building 2	C_{pw}-C_{pl}	1.30	1.30	1.25	1.30	1.13	1.17	1.39	1.60
Building 3	C_{pw}-C_{pl}	1.30	1.30	1.30	1.28	1.17	1.15	1.53	1.45

3.3 Gust Factor

A comparison of the gust factor between the standards is shown in Table 5. NBC's gust factor calculations are based on mean-hourly speed, while the remaining standards are based on gust speed.

Table 5, Comparison of gust factors.

	NBC		ASCE 7-22		AS/NZS 1170.2		EN 1991-1-4	
	Gx	**Gy**	**Gx**	**Gy**	**Gx**	**Gy**	**Gx**	**Gy**
Building 1	2.17	2.21	0.90	0.91	1.01	1.02	0.92	0.93
Building 2	2.13	2.29	0.99	1.05	1.08	1.14	1.01	1.06
Building 3	2.10	2.07	0.94	0.93	1.03	1.03	0.93	0.93

D

4 RESULTS OF THE UK NATIONAL ANNEX TO EUROCODE

To further investigate the impact on the structural design of using the Eurocode and its UK National Annex (UK NA), ten prominent high-rise buildings in the UK were select to cover a range of height and surroundings, with relatively simple geometry and dynamic characteristic. The buildings are between 72 m and 162 m and are located in suburban to urban areas. Wind-induced loads were first determined by undertaking code-based analytical wind analysis and then compared against the results from specific wind tunnel testing conducted at RWDI's facility. The comparisons of the peak overturning moments are shown in Fig. 3. Included in this Figure are also the minimum reduction obtained by comparing corresponding components of the base moment. On average, undertaking WT studies could lead to a reduction of 35% in structural wind loads, with instances where a 50% reduction was observed.

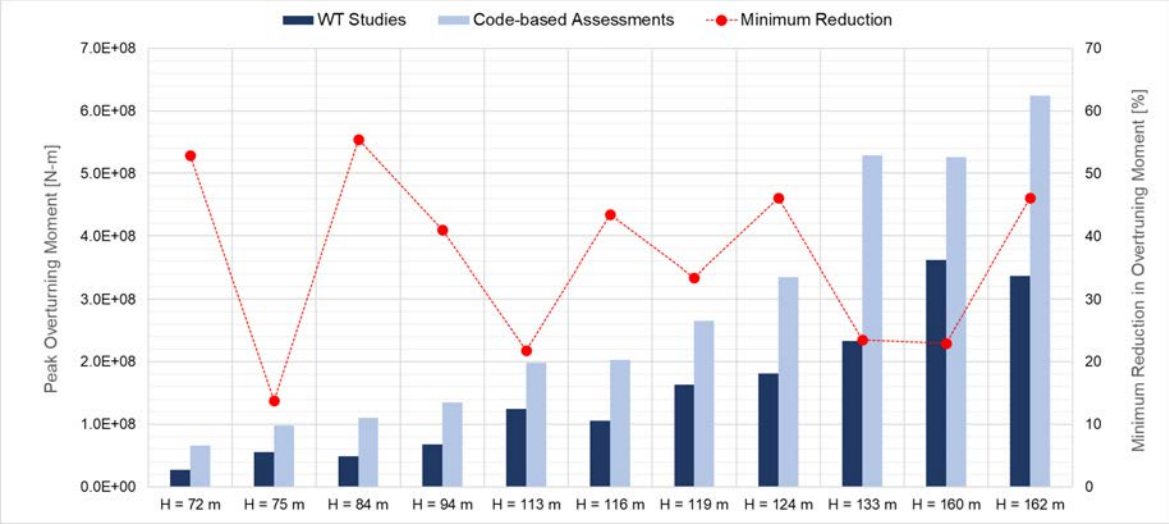

Figure 3, Histograms of the peak overturning moments obtained from the code-based and WT studies.

5 CONCLUSION

Boxy isolated tall buildings are still upcoming around the world, and many are initially designed based on the existing regional standards. Only a few of them are considered for wind tunnel tests, especially in developing nations. Considering the standard's prominent role in the design of such structures, the notable differences among them are alarming and shall be rectified. Besides, considering the increasing effort to reduce carbon emissions, having a more accurate assessment of wind loads becomes more critical than ever not only to optimising building structural systems and delivering safe and fit-for-purpose buildings, but also to reducing unnecessary construction materials and embodied carbon.

REFERENCES

[1] ASCE 7-22 (2022). *Minimum Design Loads and Associated Criteria for Buildings and Other Structures.* New York: American Society of Civil Engineers.

[2] AS/NZS 1170.2:2021 (2021). *Structural design actions, Part 2: Wind actions.* Joint Australian/New Zealand Standard, Third Edition.

[3] British Standard Institution. BS EN 1991-1-4:2005. Eurocode 1 (2005). *Actions on Structures: general Actions: wind actions.* London: BSI.

[4] British Standard Institution. NA to BS EN 1991-1-4:2005. UK National Annex to Eurocode 1 (2008). *Action on Structures: general actions: wind actions.* London: BSI.

[5] Kwon, D.K., and Kareem, A., 2013. "Comparative study of major international wind codes and standards for wind effects on tall buildings". *Engineering Structures*, **51**, 23-35".

[6] NBC 2015 (2015). *National Building Code of Canada: User's Guide, Structural Commentaries (Part 4 of Division B)*. National Research Council of Canada.

[7] Zhou, Y., Kijewski, T., and Kareem, A., 2002. "Along-Wind Load Effects on Tall Buildings: Comparative Study of Major International Codes and Standards." *ASCE Journal of Structural Engineering,* **128**, 788-796.

DOI 10.5258/WES/P0036

Wind Microclimate on Balconies: Designing Climate-sensitive Outdoor Spaces

Lowther, J., Hackett, D., Cherian, A., RV, V.
RWDI
Milton Keynes, UK
jeniffer.lowther@rwdi.com, daniel.hackett@rwdi.com

1 INTRODUCTION

Wind microclimate assessments in the UK (and elsewhere throughout the world) are required to demonstrate that wind conditions are safe and suitable for thar area's intended uses. In principle, this should apply to both public spaces around buildings and the private amenity spaces within a new design (such as balconies and terraces), however the latter of these has historically received less attention than the public realm. However, in the UK, the design of balconies and terraces has become increasingly important in the past few years due to the desire of urban planners to provide enjoyable amenity spaces at elevated private areas as well as public realm. The BSI's 'Guide to the design of balconies and terraces'[1] specifically includes a section on designing for an appropriate wind environment. It is therefore important that these spaces are robustly assessed during design, in much the same way as the public realm at ground level.

There are several constraints to the assessment of balconies in the wind tunnel, such as the physical size of these areas, fitting instrumentation into the wind tunnel model and achieving a suitable coverage of balcony locations with a limited amount of instrumentation. As a result, the critical limitation of appropriate balcony instrumentation is not only achieving the necessary accuracy but also doing so efficiently, such that the service is feasible for building designers and developers to undertake. Computational Fluid Dynamics (CFD) methods are a potential alternative, however these suffer from their own distinct limitations (including the need for a very fine mesh resolution around the relatively small balcony features, within an overall domain size of the order of a kilometer). Specific local guidelines (such as in the City of London[2]) prescribe the particular use of one or other method (and sometimes both), meaning that both kinds of methodology must be capable of robustly assessing balconies and terraces.

As part of a wind microclimate assessment, it is likely that wind mitigation measures will also need to be tested. Where wind mitigation is required to alleviate unsuitable wind conditions, options for potential measures are restricted due to the size of the space, as well as the balcony being a private amenity area where tenants can opt to adapt non-permanent features such as provided landscaping. As a result, wind mitigation measures typically involve adaptation of the balustrade design; either by increasing the height or modifying the porosity. Therefore, consideration of instrumenting or simulating these small balcony areas also needs to factor the interaction of balustrades of varying heights and porosities, which will dramatically alter the wind characteristics within the space.

Over several years RWDI has conducted research into measurement techniques and methodologies at balcony locations, with the intention of improving our practices for balcony assessments. These assessments include consideration of different instrumentation which may be used at balconies, as well as the optimal approach to use specific instrumentation at balconies. RWDI are conducting further work with the aim of understanding the accuracy of wind microclimate assessments at balconies further, however these are not completed at this time.

2 EXISTING LITERATURE

Existing literature on the assessment of wind conditions at balconies is extremely limited, particularly with a focus on the wind microclimate within the balcony area. The majority of papers focus on the mean, rms and peak surface pressures around the balcony. Furthermore, of the studies which considered the mean wind velocity at the balcony, of which a summary of existing research can be found in Xing Zheng (2021)[3] none of these studies were undertaken using wind tunnel assessments. The majority of wind tunnel assessment which consider balconies specifically use pressure taps to assess wind pressures (such as Zhu, 1988[4] and Martura, 1998[5]) which is not applicable to wind microclimate assessments.

DOI 10.5258/WES/P0037

Furthermore, of the studies reviewed, few consider the impact of balustrades as part of the assessment. As balustrades design is often the only option for wind mitigation measures when wind conditions are found to be unsuitable, the impact of balustrades is a key factor for effective balcony assessments. (Xing Zheng, 2021) demonstrate the importance of the consideration of balustrades having compared balconies of different depths and balustrade heights as well as the number of separations along the balcony space (modelled as a long balcony extending the length of the façade). Regarding balustrade height specifically, it was noted that including a 1m tall solid balustrade along the balcony would result in an increase in Cp, however a further increase of the balustrade height to 2m would reduce Cp. This highlights that the impact of balustrade on the wind conditions within and around the balcony is not linear, and therefore when conducting research at balconies not only should balustrades be considered but several heights of balustrade should be assessed.

3 COMPARISON OF INSTRUMENTATION TECHNIQUES (METHODOLOGY)

There are currently no guidelines that pertain specifically to the best approach for instrumentation at balconies for wind microclimate assessments. Instrumentation such as cobra probes or hotwires are often used as it is assumed that this will produce a more accurate result; however, the practical limitations of using these instruments include an increase in testing time and a reduction in the number of balcony locations which can feasibly be assessed to fit project timescales. Furthermore, these will typically increase the cost of the assessment for the client. Alternatively, Irwin probes[6] are also used within balcony spaces which is more time and cost effective, as well as meaning more balcony locations could be assessed. However, Irwin probes were initially developed for use at ground level spaces where there would (in theory) be a local, well-formed boundary layer, and were not investigated at balconies. There is therefore some uncertainty as to whether it is appropriate to use Irwin probes in these spaces. The aim of RWDI's research was to a) understand if different instrumentation methods would produce different results, b) determine if the most efficient instrumentation method (Irwin probes) are adequate for balcony assessments and c) if any precautions or consideration are required for the balcony instrumentation methodology.

3.1 Comparison of Instrumentation

The comparison of instrumentation tests were conducted using an existing wind tunnel model used for a pedestrian level wind microclimate assessment. The intention was to use a "real case" scenario which would be more realistic in terms of balcony design, the surrounding context of the assessment buildings and the practical benefits and limitations of testing with particular instrumentation, compared to a simplified model. At the instrumented balconies it was important to ensure the readings were taken at the same location within the balcony space, meaning the tip of the Irwin probe, the tip of the cobra probe ad the centre of the hotwire needed to be places in approximately the same location.
Up to ten balconies were assessed for each model tested. It was important to ensure several types of balcony location were assessed to ensure that different flow fields would be accounted for. Therefore, corner balconies were assessed both upwind and downwind of the prevailing wind direction (i.e. the direction where winds occur most frequently based on meteorological data, such as southwest in most of the UK), and balconies within chamfers were also instrumented for this assessment (see Figure 1).

As discussed above, there are significant time constrains when using cobra probes or hotwires for balcony testing, and as the purpose of the assessment was to compare measured wind conditions between the two options of instrumentation rather than conduct a complete assessment, the testing time was optimised by testing the most significant angles at each balcony which would contribute most significantly to the overall wind conditions. Several wind angles were selected for each balcony to be measured based on the wind exceedances noted in the Irwin probe assessment. The stand and support of the hotwire were located such that they would not interfere with the wind flow, which also meant the hotwire did not have to be repositioned for each angle.

As the design of the Proposed Development used for these tests is not currently in the public domain, images of the wind tunnel model cannot be shared.

DOI 10.5258/WES/P0037

3.2 Instrumentation of Irwin Probes in varying orientations and configurations

To assess the wind conditions on the balconies, a 1:300 scale model of a square tower of dimensions 500mm tall and floor plan of 190mm2 were constructed. The model was symmetrical with wall mounted probes on one side and floor mounted probes on the opposite side.

The wind tunnel model was instrumented with 48 sensors in total. Locations 13 to 30 were wall mounted, and locations 31 to 48 were floor mounted. Both the sides included 18 sensors each – three rows each having six balconies. At each level, three locations would be projecting balconies and three locations would be recessed. The size of the balconies were 12mm2 to incorporate the sensor. The tip of the brass tubes of the sensors were placed in such a manner that the wall and floor mounted sensors are measured at the exact same location irrespective of how the sensors were mounted.

Control probes (locations 1 to 12) at the grade level were used on the disc to check its repeatability between various iterations.

Wind speeds were measured for 36 directions in 10-degree increments. Therefore, the wall and floor mounted results could be compared at 0° and 180°, 10° and 190°, etc (wall and floor mounted respectively), as the cube and probe layout were symmetric. A profile matching a suburban surrounding area was used to provide a more likely turbulent environment. However, no surrounding buildings were included as the intention was to assess the balcony measurements with no other influence. The wind tunnel test was conducted for the following configurations:

- Configuration 1: No balustrades (representative of very porous railings)
- Configuration 2: Solid balustrades 1.2m
- Configuration 3: Solid balustrades 1.5m

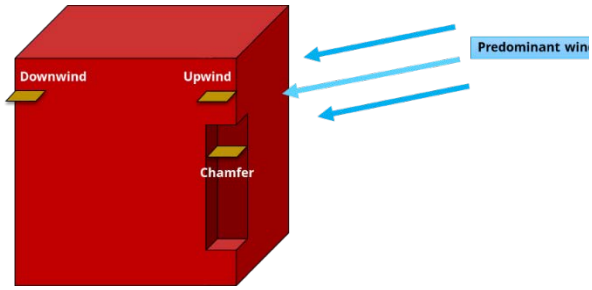

Figure 1: Diagram of notable balcony location types

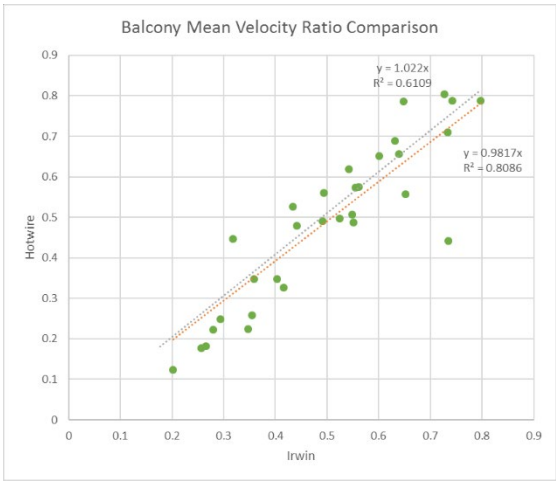

Figure 2: Comparison of mean velocity ratios from the hotwire and Irwin probe

4 COMPARISON OF RESULTS

Cobra probes were found to be impractical to use for balcony assessments. Despite being more robust that hotwires, the size of the instrument means it is extremely difficult to measure in the correct space for the balcony. This would lead to results which were too windy and, although embracing the most conservative methodology for balcony assessments in lieu of knowing the most accurate method is useful, the wind conditions were unrealistic.

Hotwires and Irwin probes were more apt for assessments in the small balcony spaces, however testing using hotwires took more for both acquisition and set up. The comparison of results showed that there was no consistently conservative option between hotwires and Irwin probes, and furthermore for the

DOI 10.5258/WES/P0037

majority of balcony locations there was a strong correlation between the instrumentation methods. The results were similar enough that when processed using the Lawson Comfort Criteria[7] the overall wind conditions would remain the same. Therefore, it is recommended that, if used appropriately, Irwin probes are just as suitable for balcony assessments as alternative instrumentation options.

The appropriate method for instrumentation of Irwin probes at balconies was also investigated. The results indicated that wall mounted probes are preferable in many cases, however it is important to consider several features of the balcony when installing any instrumentation such as balustrades, projecting/recessed designs and location on the building. For example, the assessment at recessed corner balconies may be more conservative if instrumented in the floor depending on how high up the building the balcony is located, which corner the balcony is located on and if there is a balustrade. In these scenarios an experienced wind engineer would need to consider the balcony features in addition to the prevailing wind direction to determine the most appropriate method for installing the Irwin probe.

5 CONCLUSIONS

Due to the significant gaps in available research for the assessment of wind microclimate at balconies there currently are no informative procedures and methodologies to advise on these assessments. Of the research conducted with a focus on wind microclimate, there is little consideration for the inclusion of balustrades, the location of the balcony on the building, or the practicality of the assessment for the purposes of industry. RWDI has undertaken several studies to understand the difficulties of assessing balconies as part of a wind microclimate study, and to work towards improving our methods. This is an area of limited current research and will be the focus of ongoing work with the potential to develop practical guidelines following further assessments. The aim of the guidelines would be to outline what methods should be used for efficient and precise results which the wind consultant can be confident would not underpredict the overall wind conditions. Further research is required to determine the most accurate methods for balcony assessments.

Based on the comparison of instrumentation there is no clear conservative options between using hotwires and Irwin probes. However, due to the practicality of using Irwin probes in comparison to hotwires, our recommendation would be that Irwin probes are more effective when used for wind microclimate assessments. The ease of use and ability to test more balconies more efficiently not only saves cost for the client but also means a wider selection of balconies can be considered. Methods for the most effective and appropriate use of Irwin probes within balconies were also assessed. In many cases wall mounting the Irwin probe within the balcony is preferable, as this will give the more conservative and/or sensible results.

5.1 REFERENCES

[1] BSI (2020). BS 8579:2020 Guide to the design of balconies and terraces. London (UK). British Standards Institution

[2] City of London (2019). Wind Microclimate Guidelines for Developments in the City of London. London (UK). City of London.

[3] Xing Zheng, H. M. (2021). CFD Analysis of the Impact of Geomterical Characteristics of Building Balconies on Near-Facade Wind Flow and Surface Pressure. Building and Environment.

[4] Zhu, T. S. (1988). Wind Pressures on Buildings with Appurtenances. Montreal, Quebec: Journal of Wind Engineering and Industrial Aerodynamics, 31.

[5] Martura, E. (1998). Effects on Surface Roughness for Wind Pressure on Glass and Cladding of Buildings. Journal of Wind Engineering and Industrial Aerodynamics.

[6] Irwin, P. (1980). A Simple Omnidirectional Sensor for Wind-Tunnel Studies of Pedestiran-Level Winds. Ottawa Ontario (Canada): National Research Council of Canada, National Aeronautical Establishment.

[7] Lawson, T. (2001). Building Aerodynamics. London: Imperial College Press.

DOI 10.5258/WES/P0037

The Need for Post-Construction Microclimate Monitoring

Author Name(s): Supun Enderage[1*], Jeniffer Lowther[2*], Daniel Hackett[3*]
[1]Rowan Williams Davies & Irwin Inc
Milton Keynes, UK
[*] E-mail: Supun.Enderage@rwdi.com, Jeniffer.Lowther@rwdi.com. Daniel.Hackett@rwdi.com

1 ABSTRACT

This paper presents the findings of wind monitoring conducted for a proposed high-rise development with the aim to compare the pedestrian wind comfort conditions measured at the site with the wind conditions predicted in the wind tunnel assessment.

The comparison reveals consistent pedestrian wind comfort results between the site monitoring and the wind tunnel assessment. This indicate site monitoring post-construction confirm the building is performing as they were predicted to during the design stage. Site monitoring is useful to confirm that wind mitigation measures are providing the important benefits that they were designed to, to reassure the designers, planning authorities and the future residents of the new development. Furthermore, site monitoring post-construction would allow the wind consultant to assess the viability of any wind mitigation measures designed at the design stage and where necessary replace and evaluate the effectiveness of any alternative measures that are feasible.

2 INTRODUCTION

In recent years, the importance of assessing the wind microclimate around buildings (especially around proposed new high-rise schemes) has gained significant attention. Undertaking a wind microclimate assessment demonstrates the impacts that the proposed massing of the building would have on the users of the spaces at and around the building, for the purpose of ensuring a safe and comfortable wind environment. Awareness of wind microclimate when designing a usable urban space have increased over the years, as local boroughs now require a new proposed scheme to undertake a detailed microclimate assessment (either via the Wind Tunnel or Computational Fluid Dynamics (CFD) method). Another indication of the growth in awareness and importance of microclimate is the adoption of Wind Microclimate guidelines in Leeds (1) and City of London (2).

Wind Microclimate assessments are conducted during the design stage and post planning and primarily use Wind Tunnel and CFD assessment to predict and evaluate the wind microclimate in urban environments and often both methods are used in complementary ways to ensure accurate and comprehensive wind assessments. And where necessary, the effectiveness of any required wind mitigation measures can be assessed and confirmed during the assessment process.

Though the wind conditions expected around a development can be predicted accurately and mitigate areas where building-induced wind issues would cause discomfort using the two methodologies described above, validation of the predicted wind microclimate post-construction tends to occur very rarely (based on the experience of the authors).

Often developments complete construction several years following the wind microclimate assessment. As such, post-construction on-site monitoring of the wind microclimate is important to validate wind tunnel/CFD predictions in real-world conditions. It can identify any unexpected wind patterns as changes could occur during the years of construction to the assumed surrounding context at the time of design and if any discrepancies are found then necessary modifications can be made to the built environment and can confirm (or disprove) the effectiveness of any wind mitigation measures implemented based on predicted wind conditions at the design stage.

To this end, this paper investigates the methods which can be implemented for on-site monitoring and the usefulness of post-construction on-site monitoring, using a real case study undertaken by RWDI in which monitoring data has been compared against wind tunnel measurements for the same development.

DOI 10.5258/WES/P0038

3 SITE MONITORING PROCESS

RWDI was initially appointed by the developer to conduct a wind microclimate assessment of the Development at the design stage, using wind tunnel-based methodology and where conditions windier than suitable for the intended uses were identified, wind mitigation measures which would be expected to provide beneficial shelter were recommended.

When the construction of the Development was close to completion and following feedback from the design team on windy conditions experienced within the Development, RWDI performed a wind monitoring study for the new Development.

Prior to the site visit, the measurement locations were determined based on the information received form the design team, current usages within the Development and the wind conditions predicted from the wind tunnel analysis during the design stage.

RWDI visited the Development site, during a period that was determined based on the wind conditions ideal for wind speed measurements, based on the meteorological data forecasted by the nearest meteorological station.

During the site visit period, wind speeds were acquired at various locations across the site. This included the predetermined locations based on the wind tunnel assessment as well as locations chosen from the real observations during the site visit.

Figure 1, example of monitoring equipment setup on site

In order to acquire accurate data, the anemometers were secured to the ground to avoid accidental impacts due to harsh weather conditions and vandalism and regular checks were conducted to ensure measuring equipment were functioning as intended.

4 ON-SITE MONITORING DATA VALIDATION

During the site visit, it was noted that the surrounding existing buildings and the design of the Development itself had changed since they were initially tested in the wind tunnel. The differences were deemed significant to alter the winds approaching the site and the local building induced wind interactions. As such, an updated wind tunnel assessment for the current design of the Development and the updated surrounding context was completed to validate the on-site measurements.

On-site measurements were taken at a café space at ground level (Location 1), passageways within the buildings (Locations 2 and 3), 1st floor terrace (Location 4) and on upper-level balcony location (Location 5), as shown in Figure 2.

Wind speeds measured on-site were categorised in accordance with the RWDI Criteria (3-8) wind threshold, as indicated in Figure 3. As per the RWDI Criteria, an area is deemed to have acceptable wind conditions for the intended use when suitable wind conditions persist for at least 80% of the time. For example, the terrace amenity (Location 4) measured wind conditions suitable for sitting use for 86% of the time during the measured period, which is consistent with the wind conditions predicted in the wind tunnel model (Figure 4). As per RWDI Criteria this terrace is expected to have conditions suitable for its intended amenity use.

DOI 10.5258/WES/P0038

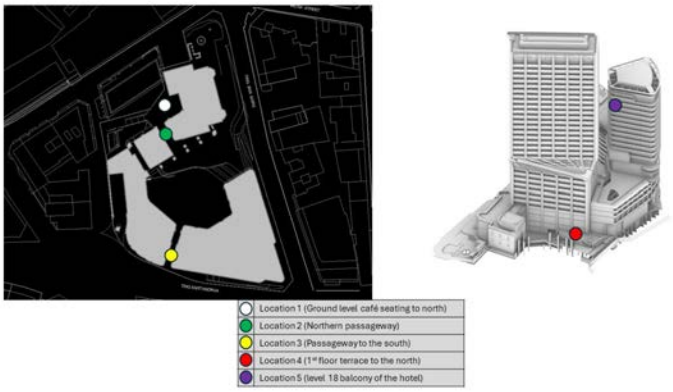

Figure 2, wind monitoring locations

During the measuring period, Location 1 measured wind conditions suitable for sitting use for 62% of the time. The wind tunnel assessment predicted that this area would be expected to have wind conditions suitable for sitting use for at least 80% of the time. Even though, the site monitoring indicated the majority of the time during the measured period this space would have suitable sitting use conditions, this indicated a potential limitation of the precision of short-term monitoring. As such, conducting the monitoring exercise over a longer period is expected to be beneficial to acquire more accurate wind speed measurements.

Comfort Category	Location 1	Location 2	Location 3	Location 4	Location 5
F of Sitting	62%	0.46%	80.4%	86.1%	0.3%
F of Standing	24%	0.13%	14.2%	10.5%	0.2%
F of Strolling	9%	0.13%	4.5%	2.3%	0.4%
F of Walking	3%	0.46%	0.7%	0.9%	1.8%
F of Uncomfortable	1%	98.8%	0.1%	0.1%	97.4%

Figure 3, wind speeds measured at the site (categorised as per the RWDI Criteria)

During the site monitoring visit, it was noted how the existing wind mitigation measures (specifically, the trees around the site) would perform in windy conditions. It was noted that young plants would not thrive in a windy environment. These observations have been taken into consideration when designing the necessary measures to increase the shelter to isolated areas with building-induced high winds.

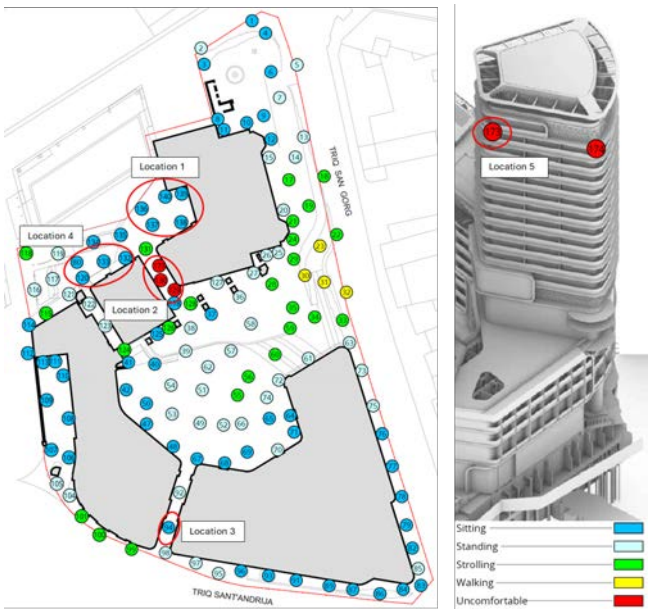

Figure 4, predicted wind conditions from the wind tunnel assessment

DOI 10.5258/WES/P0038

5 CONCLUSION

This study investigated the methods and importance of on-site monitoring post construction. The site monitoring visit following the feedback from the design team was effective to identify local building-induced wind patterns around the Development and to note any changes to the surrounding context compared to the wind tunnel model assessed during the design stage. The visit was useful to identify how the existing wind mitigation measures (trees around the site) would perform in windy conditions. These observations were helpful when designing the necessary measures to increase the shelter to isolated areas with building-induced high winds. Furthermore, it should be noted that conducting a long-term monitoring assessment would be beneficial to acquire more accurate data.

The results of this monitoring assessment show a good correlation between the wind speeds measured during the site visit with the wind conditions predicted during the wind tunnel assessment. As such, it can be concluded that the wind conditions predicted during the wind tunnel/CFD assessment during the design stage can be validated through on-site monitoring post-construction.

REFERENCES

[1] Leeds City Council (July 2021). Draft Wind & Micro-climate Toolkit for Leeds.
[2] City Of London (August 2019). Wind Microclimate Guidelines For Development In The City Of London.
[3] ASCE Task Committee on Outdoor Human Comfort (2004). Outdoor Human Comfort and Its Assessment, 68 pages, American Society of Civil Engineers, Reston, Virginia, USA.
[4] Williams, C.J., Hunter, M.A. and Waechter, W.F. (1990). "Criteria for Assessing the Pedestrian Wind Environment," Journal of Wind Engineering and Industrial Aerodynamics, Vol. 36, pp. 811-815.
[5] Williams, C.J., Soligo M.J. and Cote, J. (1992). "A Discussion of the Components for a Comprehensive Pedestrian Level Comfort Criteria," Journal of Wind Engineering and Industrial Aerodynamics, Vol. 41-44, pp. 2389-2390.
[6] Soligo, M.J., Irwin, P.A., and Williams, C.J. (1993). "Pedestrian Comfort Including Wind and Thermal Effects," Third Asia-Pacific Symposium on Wind Engineering, Hong Kong.
[7] Soligo, M.J., Irwin, P.A., Williams, C.J. and Schuyler, G.D. (1998). "A Comprehensive Assessment of Pedestrian Comfort Including Thermal Effects," Journal of Wind Engineering and Industrial Aerodynamics, Vol.77&78, pp.753-766.
[8] Williams, C.J., Wu, H., Waechter, W.F. and Baker, H.A. (1999). "Experiences with Remedial Solutions to Control Pedestrian Wind Problems," Tenth International Conference on Wind Engineering, Copenhagen, Denmark.

DOI 10.5258/WES/P0038

Pollutant dispersion in a cross-ventilating flow through a scaled building: Wind and water tunnel measurements

Subhajit Biswas[1*], Paul Hayden[2], Matteo Carpentieri[2] and Christina Vanderwel[1]
[1]Department of Aeronautical and Astronautical Engineering, University of Southampton, UK
[2]Centre for Aerodynamics and Environmental Flow, University of Surrey, UK
E-mail: s.biswas@soton.ac.uk

1 INTRODUCTION

In urban environments, pollutants can originate from both indoor and outdoor sources [1]. Consequently, when it comes to modelling pollutant dispersion, numerous studies have concentrated on scalar dispersion in outdoor environments (e.g., [2]) as well as indoor environments (e.g., [3, 4, 5]). The indoor environment poses health challenges due to various sources of pollutants, such as volatile organic compounds and particulate matter, and could be life-threatening in cases such as potential gas leaks and airborne transmission of infectious diseases. Since humans spend most of their time indoors, maintaining a healthy and sustainable indoor environment would be very critical for human health. In such scenarios, cross-ventilation could help to keep a healthy indoor environment [6].

To date, most experimental studies on flow and pollutant dispersion for outdoor and indoor environments predominantly utilize wind tunnel facilities, while the use of water tunnels for similar studies remains relatively limited. Drawing motivation from this, we perform a series of experiments examining pollutant transport in a cross-ventilating flow through a scaled-down hollow building (a hollow cube) in a *water tunnel* with an indoor scalar (Rhodamine dye) source. Subsequently, the findings are compared with sets of analogous experiments performed in a *wind tunnel*, with the model building being equipped with an indoor gaseous (Propane) scalar source. Our comparative approach aims to establish the consistency and reliability of dispersion measurements across two experimental arrangements by evaluating and comparing the flow dynamics and scalar dispersion.

2 EXPERIMENTAL METHODOLOGY

Two different experiments were conducted and then compared results from the University of Southampton water tunnel (see Figure 1(a)) and the University of Surrey EnFlo wind tunnel (Figure 1(b)). The condition of a turbulent atmospheric boundary layer was created using a series of roughness elements placed upstream as shown in Figure 1 (for details, see [2, 7]).

The water tunnel experiments involved a cube of height H_1 = 100 mm (approximately 40:1 to full scale) with a reference water speed at the cube height of $U_{Ref,1}$ = 0.45 m/s, resulting in a Reynolds number of $Re = U_{Ref,1} H_1/\nu \approx 50{,}000$; here, $U_{Ref,1}$ is the oncoming mean streamwise velocity at the cube's height, measured without the cube in the test section. On the other hand, the wind tunnel experiments were performed using a hollow cube of height H_2 = 300 mm (approximately 13:1 scale to a full-scale room) with a reference wind speed at the cube height of $U_{Ref,2}$ = 2.5 m/s, resulting in the Re ($=U_{Ref,2} H_2/\nu$) being the same as in the water tunnel. Both setups benefited from spires and roughness to condition the oncoming boundary layer to have a depth of $\delta/H \approx 3$ (H=cube height). The hollow (acrylic) cubes had two opposite openings (0.35H x 0.35H) in the windward and leeward façade, with about 10% area-based porosity (see Figure 2(a)). Before beginning experiments involving the cube, the incoming boundary layer was characterized without the model in the test section, as shown in Figure 2(b) are the wall-normal (z/H) profiles of the normalised mean stream-wise velocity ($\overline{U}/U_{Ref}$) from both the experimental facilities; here, $\overline{U}$ is the time-averaged stream-wise velocity.

2.1 Water tunnel measurements

The water tunnel setup facilitated *Rhodamine 6G dye* injection at the floor of the building, essentially replicating a ground-level passive scalar source with negligible effects on the flow (similar to [2, 4]). The aqueous solution of the dye (Schmidt number, Sc=2500$\pm$300) with concentrations (C_S) of 1 mg/L was injected at a constant flow rate of Q_S=7 mL min^{-1} (see Figure 1(a)). The two-dimensional maps of the

DOI 10.5258/WES/P0040

velocity (U) and the scalar concentration (C), within the cube were captured simultaneously through Particle Image Velocimetry (PIV) and Planar Laser-Induced Fluorescence (PLIF), in the streamwise plane (x-z) along the centreline of the building. For the PIV measurements, the flow was seeded with $50\ \mu m$ polyamide seeding particles. For both the PIV and PLIF measurements, the illumination was provided by a 100 mJ Nd:YAG double-pulsed laser with an emission wavelength of 532 nm, and appropriate filters were used in two cameras to separate the PIV and PLIF signals.

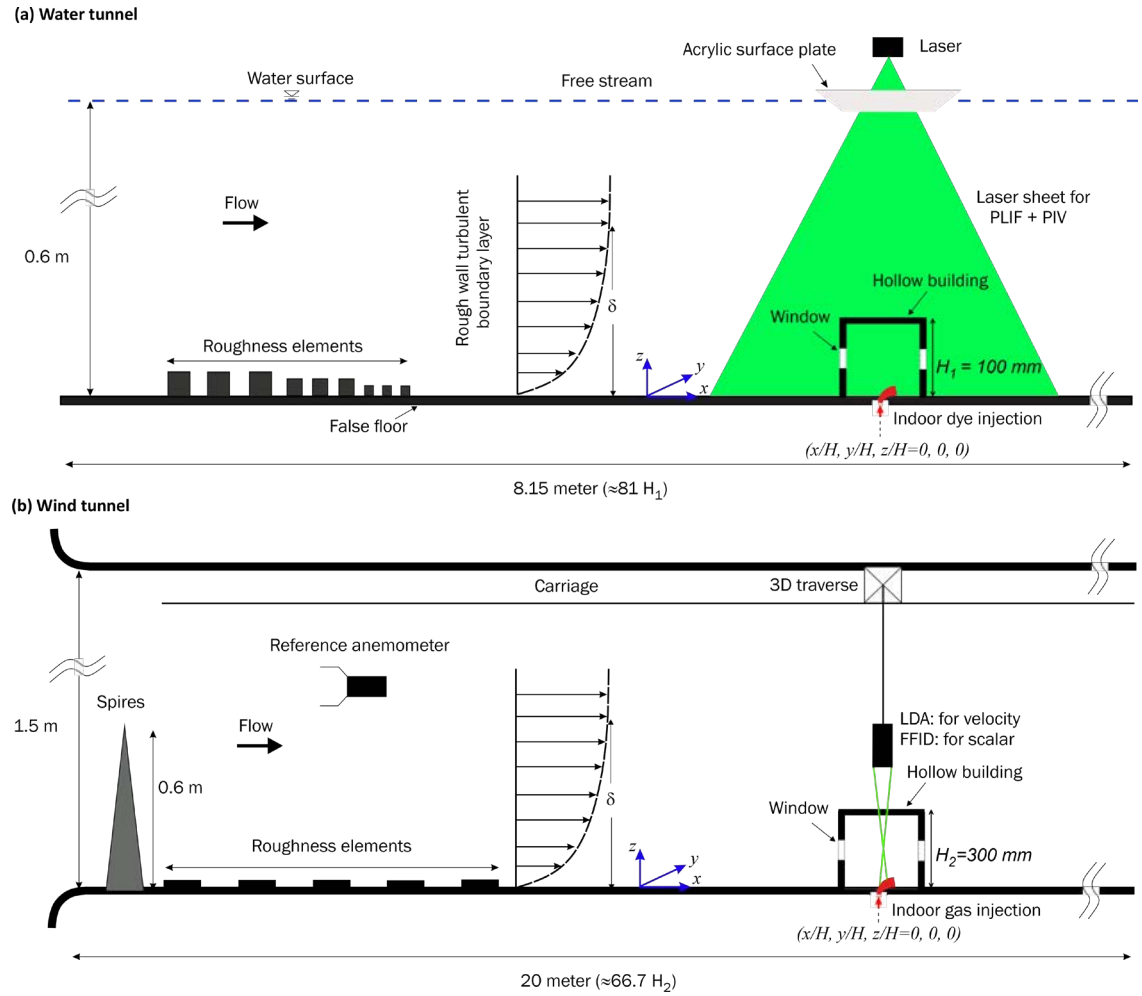

Figure 1. *(a) Schematic of the side-view of the experimental setups showing the hollow building inside the turbulent boundary layer in: (a) the water flume facility at the University of Southampton, and (b) the Enflo wind tunnel facility at the University of Surrey.*

2.2 Wind tunnel setup

The *EnFlo* wind tunnel facility (see Figure 1(b)) at the University of Surrey [7] is a suck-down tunnel with a large working section measuring 20m in length, 3.5m in width, and 1.5m in height. The flow was seeded with micron-sized sugar particles, and the flow velocity was measured using a Dantec two-component laser Doppler anemometer (LDA). For scalar, a mixture of Propane gas and air was used as the tracer ($Sc \approx 1.5$), released from ground level. The flow rate of the gas mixture (Q_S) was about 0.021 l min^{-1}, at a concentration (C_S) of about 15,000 ppm. Tracer concentration measurements were performed using a *Cambustion Fast Flame Ionization Detector* (*FFID*) with a frequency response of 200 Hz.

3 RESULTS AND DISCUSSIONS

Turbulent flows around cubes are characterized by phenomena like separation, re-circulation, and vortex shedding. Introducing openings in such configurations results in an unsteady internal flow. In the present configuration, the internal flow involves a jet penetrating the cube and two re-circulation regions (R_{up}, R_{low}) adjacent to the upper and lower walls, as delineated in Figure 3(a) showing the streamwise time-averaged velocity ($\overline{U}/U_{Ref}$) in the centre-plane (x-z), from water tunnel measurements. Following this,

DOI 10.5258/WES/P0040

the scalar concentration map ($C^* = \overline{C}\,AU_{Ref}/C_SQ_S$; here, $A=H^2$) in Figure 3(b) shows a notable accumulation of scalar in the re-circulation regions near the top and bottom walls of the cube, with relatively higher scalar strength near the bottom wall; here, C and $\overline{C}$ are the instantaneous and time-averaged scalar concentrations.

The results from the water tunnel measurements are compared with the wind tunnel (Figure 4(b,c,d)), in terms of the wall-normal (z/H) profiles for the mean velocity, scalar and variance ($\overline{c'c'}AU_{Ref}/C^2_SQ_S$; here, $c'=C-\overline{C}$), at different locations (P_1, P_2 & P_5) as illustrated in Figure 4(a). The magnitude and the wall-normal variation in velocity and the scalar measured at these locations along the streamwise centre plane are found to be substantially similar [Figure 4(b,c,d)] across the water tunnel and wind tunnel, thus establishing universality in the methodologies and measured quantities. In addition, be noted that the present water tunnel measurements have been performed only in the centre plane. To help quantify the out-of-plane variations in $\overline{C}$, the wind-tunnel measurements performed at two out-of-plane locations (P_3 & P_4) clearly show [Figure 4(c(ii))] a lower scalar buildup than the centre plane and the nearly uniform wall-normal (z/H) scalar concentration implies a relatively well-mixed scalar in these regions in comparison with the centre plane.

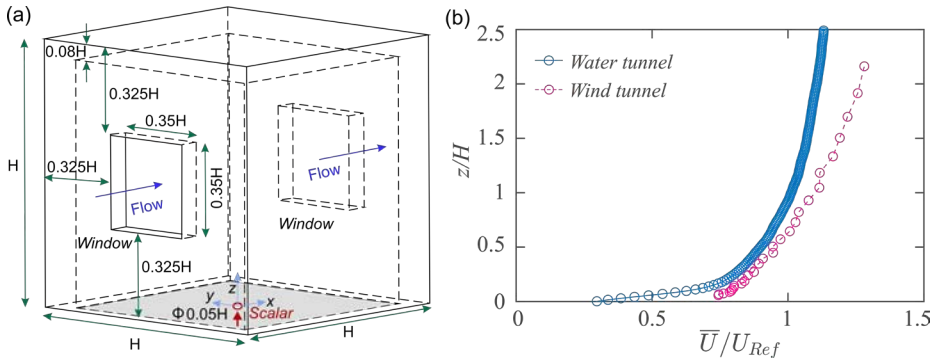

Figure 2 (a) Schematic showing the 3D view of the hollow building model. The dye is injected from a hole flush mounted at the centre of the floor (x/H,y/H,z/H=0,0,0). (b) The base flow mean stream-wise velocity ($\overline{\boldsymbol{U}}/\boldsymbol{U_{Ref}}$) is shown along the wall-normal direction (z/H), measured in the water and wind tunnel test section (at x/H=-1, y/H=0) without the cube.

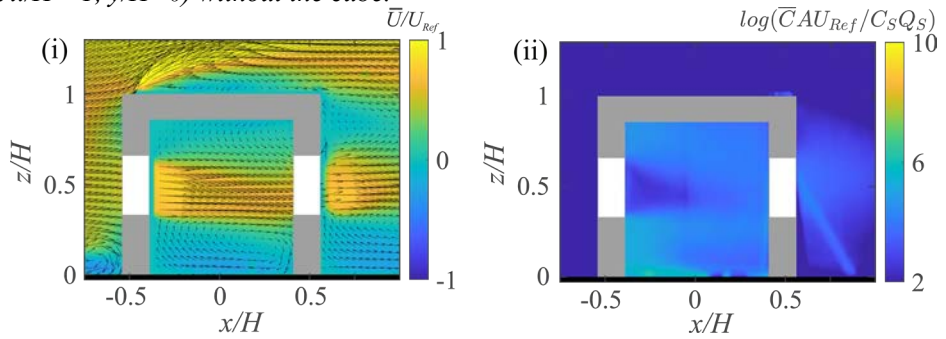

Figure 3. Time-averaged (a) vector map in the streamwise centre plane (x-z) overlaid with streamwise velocity ($\overline{\boldsymbol{U}}/\boldsymbol{U_{Ref}}$), and (b) scalar concentration map ($\overline{\boldsymbol{C}}AU_{Ref}/C_SQ_S$, in natural logarithmic scale), all obtained in the water tunnel. Flow is from left to right.

To summarise, the present work experimentally investigated a cross-ventilating flow through a hollow cube with an indoor scalar source, immersed in a rough-wall turbulent boundary layer. The primary focus was on comparing the water tunnel PIV and PLIF measurements for indoor velocity and velocity, with the wind tunnel measurements using LDA and FFID. The in-plane scalar (dye) field from the water tunnel shows scalar accumulation in re-circulation regions, with the peak concentration being around the source and the upstream near-ground corner. These magnitudes of water velocity and scalar (dye) and their spatial variations are considerably close to the air velocity and gas concentration from wind tunnel experiments.

DOI 10.5258/WES/P0040

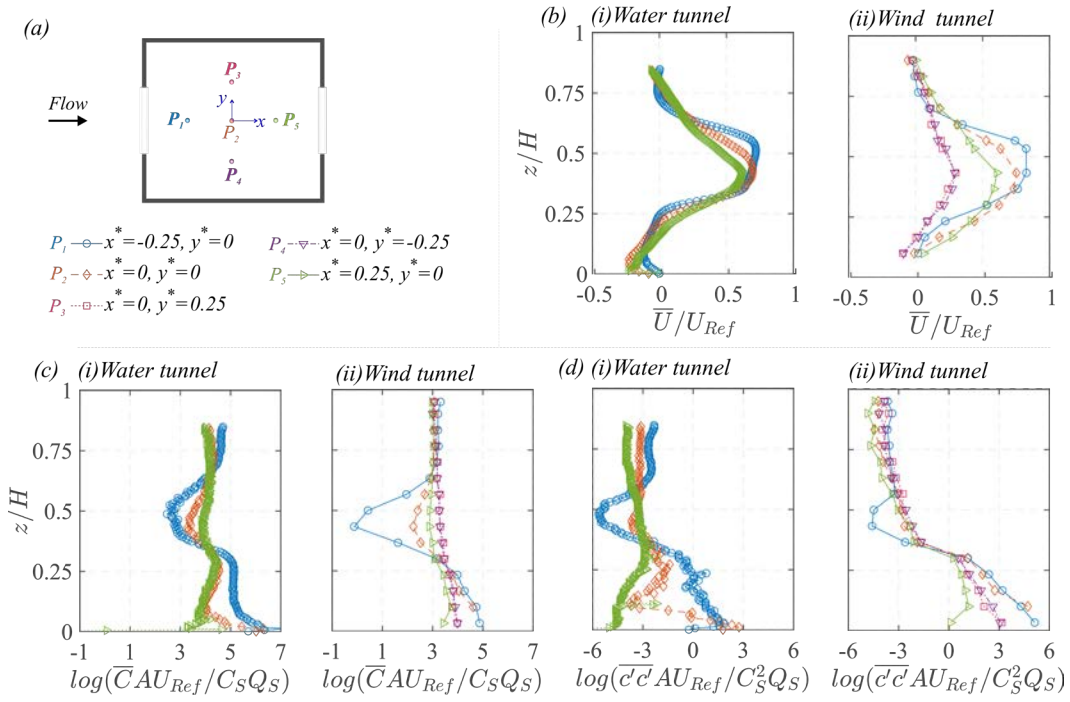

Figure 4. (a) A top-view schematic (x-y plane) showing the x-y coordinates of the different indoor locations (P_1 to P_5) where the wall-normal (z/H) profiles for indoor velocity and concentration are obtained; here, x=x/H, y*=y/H and z*=z/H. (b,c,d) Wall-normal (z/H) profiles of the indoor mean stream-wise velocity ($\overline{\boldsymbol{U}}/\boldsymbol{U_{Ref}}$), mean concentration ($\overline{\boldsymbol{C}}AU_{Ref}/C_SQ_S$) and concentration variance ($\overline{\boldsymbol{c'c'}}AU_{Ref}/C^2{}_SQ_S$), at different locations, as illustrated in 'a'. In 'b, c & d', the water tunnel and wind tunnel measurements are shown in 'i' and 'ii', respectively.*

The substantial similarities in the results obtained from both water tunnel and wind tunnel experiments affirm the validity and reliability of both experimental setups in simulating the scalar dispersion in such urban flows with reasonable accuracy. This gives us confidence in the use of both wind tunnel and water tunnel methodologies as complimentary experimental approaches for studying pollutant dispersion in complex atmospheric boundary layer conditions.

REFERENCES

[1] R. E. Britter and S. R. Hanna, "*Flow and dispersion in urban areas*,"Annual review of fluid mechanics, vol. 35, pp. 469--496, 2003.
[2] H. Lim, D. Hertwig, T. Grylls, H. Gough, M. v. Reeuwijk, S. Grimmond and C. Vanderwel, "*Simulation, Pollutant dispersion by tall buildings: laboratory experiments and Large-Eddy simulation*," Experiments in Fluids, vol. 63, p. 92, 2022.
[3] Y. Tominaga and B. Blocken, "*Wind tunnel analysis of flow and dispersion in cross-ventilated isolated buildings: Impact of opening positions*," Journal of Wind Engineering and Industrial Aerodynamics, vol. 155, pp. 74--88, 2016.
[4] S. Biswas and C. Vanderwel, "*Indoor-outdoor pollutant exchange in a flow through a hollow cube submerged in a turbulent boundary layer*," Thirteenth International Symposium on Turbulence and Shear Flow Phenomena (TSFP13), pp. 1--6, 2024.
[5] S. Biswas and C. Vanderwel, "*Flow through a hollow cube in a turbulent boundary layer: Towards understanding indoor pollutant dispersion*," Flow (In Press), 2024.
[6] M. J. Finnegan, C. A. Pickering and P. S. Burge, "*The sick building syndrome: prevalence studies*," British medical journal Clinical Research ed., vol. 289, p. 6458, 1984.
[7] M. Placidi, P. E. Hancock and P. Hayden, "*Wind turbine wakes: experimental investigation of two-point correlations and the effect of stable thermal stability*," Journal of Fluid Mechanics, vol. 970, p. A30, 2023.

DOI 10.5258/WES/P0040

Multi-resolution heterogeneity analysis of urban flows

Jingzi Huang[1*] and Maarten van Reeuwijk[1]
[1]Department of Civil and Environmental Engineering,
Imperial College London, London SW7 2AZ, UK
[*] E-mail: jingzi.huang17@imperial.ac.uk

ABSTRACT
Whether or not urban form or urban flow is perceived to be heterogeneous is dependent on the measurement resolution. In this study, we construct flow fields at various resolutions via a coarse-graining operation using a square spatial convolution filter. We use these fields to explore multi-scale aspects of heterogeneity with the aim preparing for developing scale-aware parameterisations for numerical weather prediction (NWP). The case we studied involves neutral flow around a staggered array of cubes with random heights. We coarse-grain the Reynolds-averaged velocity $\overline{u}$ using seven different filter lengths to analyse the filtered velocity field at these different resolutions. By exploring the multi-resolution properties of these fields, for example, by examining the tile-based variances (which represent the heterogeneity) as a function of the resolution at different heights, we highlight that the conventional spatially averaged value is not representative to describe the high-resolution field.

1. INTRODUCTION

Heterogeneity represents spatial variation and is dependent on the measurement resolution. Higher resolution would provide more detailed information about urban surface properties but would also require more computational resources [1, 2]. It can be quantified by measuring the variance of a system property [3]. The current numerical weather prediction (NWP) is usually interested in the spatially average of properties over an entire horizontal plane, ignoring the variance within the plane. This is a concession primarily because that the current resolution equipped in the NWP is of $O(1\ \mathrm{km})$, which is not able to resolve all the details especially within the canopy region [4]. Indeed, in the canopy region, the heterogeneity and variance are apparent [5, 6], so that the spatial average becomes less representative. Therefore, understanding the heterogeneity evolves with the resolution is important and would be benefit to the parameterisations of the unresolved parts in the numerical simulation under different resolutions.

In the present study, a Multi-Resolution framework is used to analyse heterogeneity. In the Multi-Resolution framework, starting from an original-resolution field, a series of low-resolution fields is obtained through a coarse-graining operation, which reduces the resolution by a factor of two using spatial average in a square filter. Then, the heterogeneity of the resolved and unresolved fields at different resolutions is explored. The paper is organized as follows: Sect. 2 introduces the background equations and simulation details; Sect. 3 provides the results showing how the velocity field evolves with the different resolutions and Sect. 4 remarks on the conclusions.

2. METHODOLOGY AND NUMERICAL DETAILS

Inspired by the volume-averaging framework of [7, 8], and considering that in numerical weather predications, the computational cells are much wider than they are high, particularly near the surface, we employ a two-dimensional superficially area-averaging framework by defining a two-dimensional masking function $\mathcal{A}(\boldsymbol{x}_\perp)$ as the area averaging kernel on the horizontal x-y plane with the area A, the masking function is 1 within the averaging domain and 0 outside of it, with this notation, the superficial (area) average of an arbitrary scalar $\varphi(\boldsymbol{x})$ is given as

$$\tilde{\varphi}(\boldsymbol{x}) = \frac{1}{A}\int_{\Omega} \mathcal{A}(\boldsymbol{x}_\perp - \boldsymbol{y}_\perp)\varphi_f(\boldsymbol{y}_\perp, z)\,\mathrm{d}\boldsymbol{y}_\perp\,, \tag{1}$$

where $\Omega(\boldsymbol{x})$ is the whole domain of interest, however, only the scalar within its fluid subdomain is integrated, e.g., $\varphi_f(\boldsymbol{x})$.

Then, we define the superficially spatial average over the entire x-y plane whose area is A_T

$$\langle\cdot\rangle = \frac{1}{A_T}\int_{\Omega_f} \cdot\,\mathrm{d}A\,, \tag{2}$$

and note that $\langle\varphi\rangle = \langle\tilde{\varphi}\rangle$. Hereafter, we refer to $\varphi(\boldsymbol{x})$ as the 'original' field and $\tilde{\varphi}(\boldsymbol{x}, L)$ as the 'filtered' field.

The case we studied involves neutral flow around a staggered array of cubes with random heights, where the width and mean height are both $h_m = 10$ m [6]. The case was simulated using uDALES, an open-source large-eddy simulation model for urban environments [9]. Periodic lateral boundary conditions are used, with a free-slip boundary condition at the top. The flow is forced by a constant kinematic pressure gradient $\mathcal{F}_u = 4.1912 \times 10^{-3}\ \mathrm{ms}^{-2}$. The domain size is $L_x \times L_y \times L_z = 16h_m \times 16h_m \times 10h_m$, and the number of grid cells is $N_x \times N_y \times N_z = 256 \times 256 \times 256$. The initial velocity profile is uniform. In this study, the averaging kernel $\mathcal{A}$ is a square with the lengths of $L = 1.25\ \mathrm{m}, 2.5\ \mathrm{m}, 5\ \mathrm{m}, 10\ \mathrm{m}, 20\ \mathrm{m}, 40\ \mathrm{m}, 80\ \mathrm{m}$, respectively.

DOI 10.5258/WES/P0041

3. RESULTS

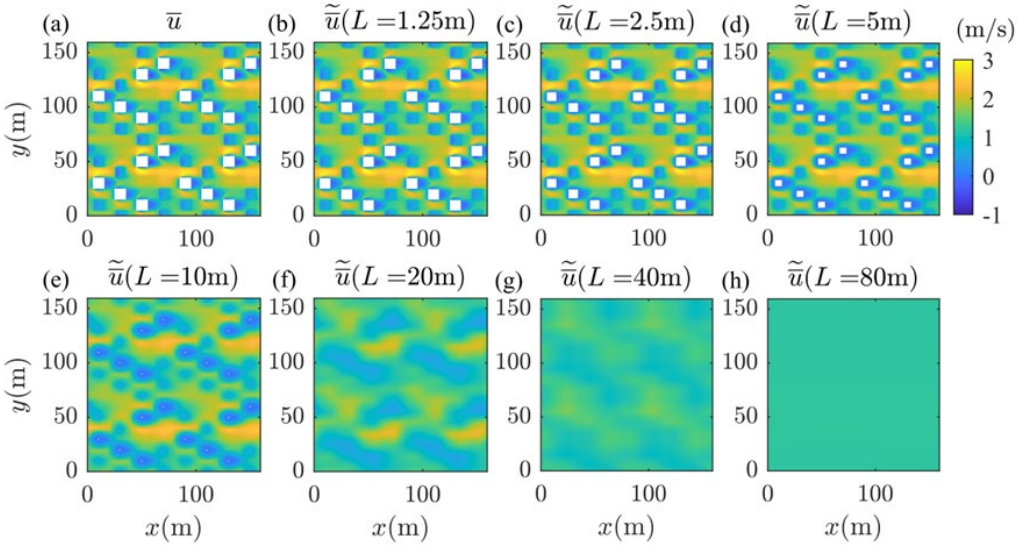

Figure 1, The horizontal plane of Reynolds-averaged velocity $\overline{u}$, (a) with the original resolution of the simulation, (b-h) spatial averaged under different filter lengths, at the mean building height level $h_m = 10\ m$. The white boxes represent the building.

To note the building area (solid subdomain), we define a solid indicator $\varepsilon(\boldsymbol{x})$ which is 1 only at the building area and 0 anywhere else. Substituting $\varphi = \varepsilon$ and $\overline{u}$ into the spatial average Eq.1, we obtain the filtered field for the building $\tilde{\varepsilon}(\boldsymbol{x})$ and for the fluid velocity $\widetilde{\overline{u}}(\boldsymbol{x})$ with different filter lengths (resolutions), which are shown in figure 1. First, the filtered building area $\tilde{\varepsilon}$ can range between 0 to 1 depending on the location of the filter, note that, $\tilde{\varepsilon} = 1$ only when the whole filter emerges within the building area, in which case the filtered velocity $\widetilde{\overline{u}}$ does not exist. Therefore, in this field figure, only the loci ε (or $\tilde{\varepsilon}$) is 1 are labelled as white boxes to remark the absence of the velocity. With the increase of the filter length, the area of these white boxes gets smaller and finally vanishes in the large filter length, which indicates that for the low resolution, the building and its relevant properties, e.g., the drag force, are not resolved and will induce the uncertainties to the flow dynamics.

Second, figure 1 shows the Reynolds-averaged wind velocity $\overline{u}$ from its original resolution (figure 1a) to its filtered average $\widetilde{\overline{u}}$ with different filter lengths (figures 1c-h) at the mean building height $h_m = 10$ m. As expected, the figures clearly show that as the filter length grows (i.e., the resolution decreases), the fluid velocity field becomes more homogeneous, less variance and heterogeneity can be observed, indicating that more information becomes unresolved.

To quantify the heterogeneity in a field, we are interested in the between-cell variance $V_\varphi(z, L)$, over the horizontal plane, which is defined as

$$V_\varphi(z, L) = \frac{1}{L_x L_y} \iint \left(\varphi(\boldsymbol{x}, L) - \langle\varphi\rangle(z, L)\right)^2 \mathrm{d}x\mathrm{d}y\,. \tag{3}$$

Substituting $\varphi = \overline{u}$ and $\widetilde{\overline{u}}$, we obtain this between-cell variance of the streamwise velocity varying with filter lengths and plot it with the averaged streamwise velocity $\langle\widetilde{\overline{u}}\rangle$ (or $\langle\overline{u}\rangle$, they are identical) in the figure 2. To show the variance clearly, the plot is only restricted within the canopy region (reminding that, the maximum building height is $1.8h_m$), above the canopy region, not shown here, we observe very small variances for all the filter lengths, and the averaged velocity profiles gradually fits the log-law.

Figure 2 shows that horizontal slab averaged velocity $\langle\widetilde{\overline{u}}\rangle$ and $\langle\overline{u}\rangle$ are independent of the filter lengths. However, as the filter length gets smaller (i.e., the resolution gets higher, looking from figures 2h to 2a), the velocity variance $V_{\widetilde{\overline{u}}}$ becomes significant, and it suggests that for high resolutions, e.g., figures 2(a, b), the average is unlikely to represent the detailed distribution of the velocity field. Among the low resolutions, for example, from figures 2h to 2f, even if we increase the resolution by a factor of 4, the variance remains very low, indicating that the heterogeneity it captures is still not ideal. This indicates that for the current NWP (usually has a low resolution of $O(1\ \text{km})$), our attempt to increase the resolution may not induce a significant improvement.

Therefore, to investigate how the variance evolves with the resolution, we plot the between-cell variance of the filtered (resolved) velocity $V_{\widetilde{\overline{u}}}$ at four specific heights against different filter lengths, for a comparison we also plot the variance on the original velocity field $V_{\overline{u}}$ which is independent of resolution. On the other hand, we denote an unresolved velocity $\overline{u}'''(\boldsymbol{x}, L) = \overline{u}(\boldsymbol{x}) - \widetilde{\overline{u}}(\boldsymbol{x}, L)$, and also calculate and plot the variance within the unresolved

DOI 10.5258/WES/P0041

velocity field $V_{\overline{u}}'''$, as shown in figure 3, and by definition $V_{\overline{u}} = V_{\widetilde{\overline{u}}} + V_{\overline{u}}'''$. We are also interested in the tile-based variance $\Delta V_{\widetilde{\overline{u}}}(\boldsymbol{x}, L)$ --- the tile-based variance represents the change of the between-cell variance between the two neighbour resolutions, e.g., $\Delta V_{\widetilde{\overline{u}}}(5\ m) = V_{\widetilde{\overline{u}}}(10\ \mathrm{m}) - V_{\widetilde{\overline{u}}}(5\ \mathrm{m})$.

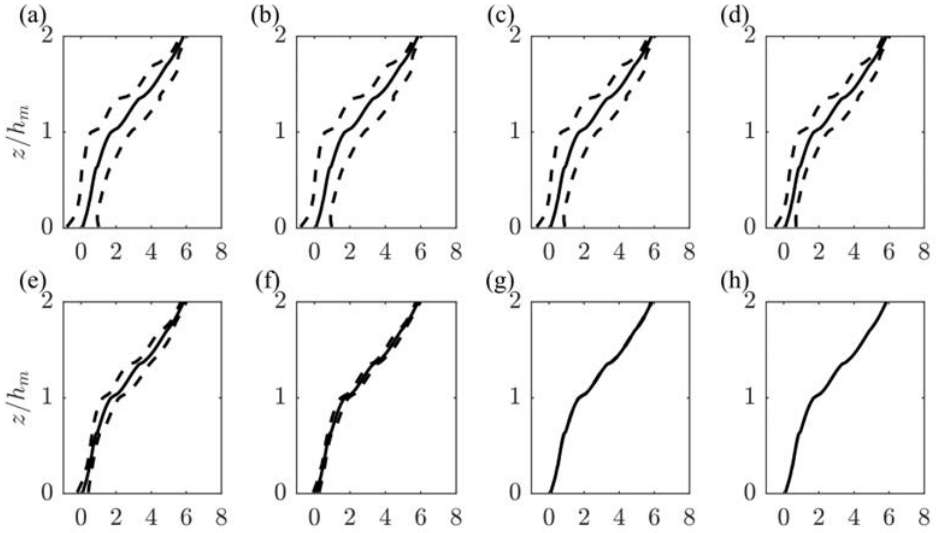

Figure 2, (a-g) The slab averaged filtered velocity $\langle\widetilde{\overline{u}}\rangle$ (solid line), varying with the filter length for filter length L = {1.25, 2.50, 5, 10, 20, 40, 80} m*, respectively, (h) is the slab averaged velocity in the original field. The dashed lines mark the upper and lower bound of the variance around the average, i.e., $\langle\widetilde{\overline{u}}\rangle \pm V_{\widetilde{\overline{u}}}$. The height is only shown up to the canopy region.*

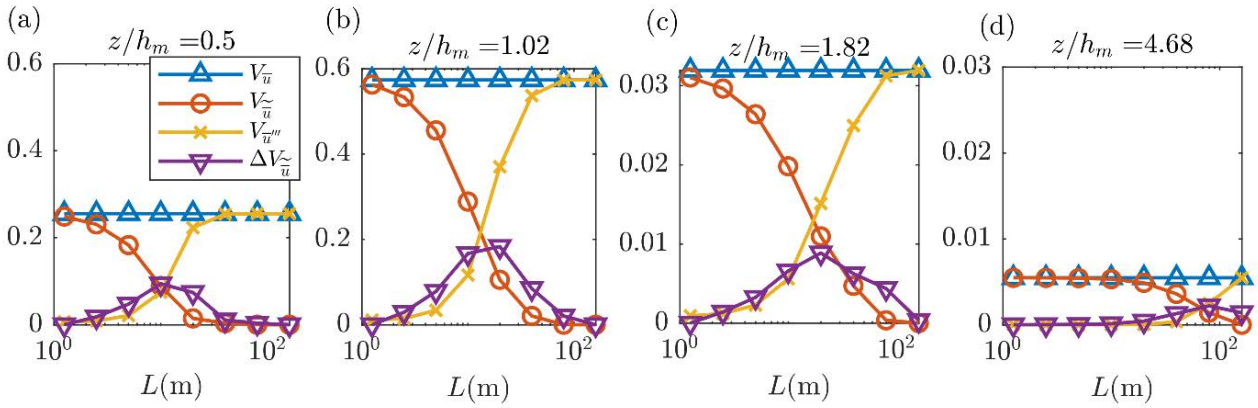

Figure 3, The between-cell variance of the original velocity $V_{\overline{u}}$, the filtered (resolved) velocity $V_{\widetilde{\overline{u}}}$ and the unresolved velocity $V_{\overline{u}}'''$ and the tile-based variance of the resolved velocity $\Delta V_{\widetilde{\overline{u}}}$, evolving with the filter length at four different heights.

In terms of the variance of original velocity field $V_{\overline{u}}$, the figure shows that, in the canopy region (figures 3a-c), $V_{\overline{u}}$ at the mean building height (figure 3a) is relatively larger than that at the half mean-building height and the maximum building height (figures 3b and 3c, respectively), which is primarily due to the morphology change. However, in the roughness sublayer, $V_{\overline{u}}$ becomes much smaller due to the absence of the building. The variance is expected to be even closer to zero above in the inertial sublayer. In terms of the resolved and unresolved velocities, the figure shows that, in the canopy region, with the filter length grows (resolution lows), the variance of the resolved velocity $V_{\widetilde{\overline{u}}}$ decreases and that of the unresolved velocity $V_{\overline{u}}'''$ increases --- again reassure that in the lower resolution, more information becomes unresolved instead of being resolved. However, in the roughness sublayer, the variances seem less sensitive to the change of filter length, indicating that the no-building region has a lower requirement on the resolution than the building region (e.g., canopy region).

The tile-based variance of the filtered velocity field $\Delta V_{\widetilde{\overline{u}}}$, represents the proportion of between-cell variance that becomes resolved by increasing the resolution. Figures 3(a-c) show this variance as a function of the filter length,

DOI 10.5258/WES/P0041

which peaks around the length $10\ \mathrm{m} - 20\ \mathrm{m}$ implying that there is a significant increasing unresolved part when the resolution changes over $10\ \mathrm{m} - 20\ \mathrm{m}$. Note that this filter length is roughly where the variances of resolved and unresolved between-cell variance cross over. Practically, this change suggests that, for low resolution for example $L = 80\ \mathrm{m}$, the effort should be made to at least increase the resolution by approximately 8 times (to $L = 10\ \mathrm{m}$), to have a practically significant improvement.

4. CONCLUSIONS

A Large-Eddy simulation was performed over a staggered array of cubes with random heights and the heterogeneity was investigated by a multi-resolution analysis. The variances of the streamwise velocity fields showed that, in the canopy region, although the resolutions do not affect the horizontally spatial averaged velocity over the plane, the higher the resolution, the more heterogeneity, making the averaged velocity become less representative. The variances also indicated that, in the relatively low resolution that is used in NWP, much information is unresolved which needs to be modelled. For example, we observed that the building (solid) part is not resolved in the low resolutions, which suggested that the drag of the building is not captured. As drag plays an important role in wind momentum, developing a numerical model that considers heterogeneity could be a future work.

ACKNOWLEDGEMENTS.

The support of the ARCHER2 UK National Supercomputing Service (project ARCHER2-eCSE05-3) and the NESRC highlight grant ASSURE: Across-Scale ProcesseS in Urban Environment (NE/W002868/1) is acknowledged.

DECLARATION OF INTERESTS.

The authors report no conflict of interest.

REFERENCES

[1] Cadenasso ML, Pickett STA & McGrath B. (2013). “Ecological heterogeneity in urban ecosystems: reconceptualized land cover models as a bridge to urban design. In: Pickett STA, Cadenasso ML and McGrath B (eds)”. *Resilience in Ecology and Urban Design: Linking Theory and Practice for Sustainable Cities*. Dordrecht: Springer, pp. 107–129.

[2] Cadenasso ML, Pickett STA & Schwarz K. (2007). “Spatial heterogeneity in urban ecosystems: reconceptualizing land cover and a framework for classification”, *Frontiers in Ecology and the Environment* 5: 80–88.

[3] Fitch PJR, Lovell MA, Davies SJ. (2015). “An integrated and quantitative approach to petrophysical heterogeneity”, *Marine and Petroleum Geology*. **63**, 82–96.

[4] Sutzl B.S., Rooney G.G. & van Reeuwijk, M. (2020). “Drag distribution in idealized heterogeneous urban environments”, *Boundary-Layer Meteorology.* **178**, 225–248.

[5] Coceal O, Thomas TG & Belcher SE. (2007). “Spatial variability of flow statistics within regular building arrays”, *Boundary-Layer Meteorology*. **125**, 537–552.

[6] Xie Z.-T. & Castro I. P. (2008). “Efficient generation of inflow conditions for large eddy simulation of street-scale flows”, *Flow, turbulence and combustion*, **81**, 449–470.

[7] Whitaker S. (1999). “The method of volume averaging”, *Theory and applications of transport in porous media*, Kluwer Academic Publishers.

[8] Schmid M., Lawrence G.A., Parlange M.B. & Giometto M.G. (2019). “Volume averaging for urban canopies”, *Boundary-Layer Meteorology.* **173**, 349–372.

[9] Owens S. O., Majumdar D., Wilson C. E., Bartholomew P., & van Reeuwijk M. (preprint). “A conservative immersed boundary method for the multi-physics urban large-eddy simulation model uDALES v2.0”, *EGUsphere*

DOI 10.5258/WES/P0041

Large-eddy simulation of a diurnal cycle in a coastal urban environment

Sam Owens[1,2*], Owen Beckett[2], Andy Acred[2], Maarten van Reeuwijk[1]
[1]Department of Civil and Environmental Engineering, Imperial College London
[2]Specialist Modelling Group, Foster+Partners
London, UK
[*]sam.owens18@imperial.ac.uk

1 INTRODUCTION

Urban areas tend to exhibit microclimates, i.e. small-scale variation of environmental conditions in the urban canopy layer (UCL), which can directly influence people's experience in terms of wind and thermal comfort [1]. The principal thermal forcing to the urban surface, which is thermally coupled with the UCL, is the diurnal cycle of solar radiation, with the surface energy balance (SEB) dictating heat transfer and storage [2]. An important factor influencing the evolution of the SEB is thermal inertia: the fact that surface temperature changes tend to be delayed and damped compared to the solar forcing [3].

This study involves simulating an urban environment with a hot, arid climate in order to provide insight into the microclimatic processes contributing to thermal comfort. The case consists of a set of buildings that are located by the coast (Fig. 1). The buildings are situated on underlying terrain, and there is a substantial section of terrain where there are no buildings. This enables a comparison of the microclimate of the built environment with that of the open terrain.

2 METHODOLOGY

The model used in this study is uDALES v2.0 [4]: a large-eddy simulation (LES) model with a two-way coupled 3D SEB scheme. The governing equations for the flow are discretised on a Cartesian computational grid, but the immersed boundary method (IBM) uses a geometry representation that is unstructured, i.e. the surface is not necessarily aligned with the grid. This is a unique feature of the model in comparison to other LES tools with SEB modelling capabilities, and it means that it can faithfully capture radiative transfer for realistic (non-grid-aligned) geometries. The geometry is specified using an STL that was obtained from a CAD model for a realistic masterplan (Fig. 1).

A precursor simulation is used to generate an inflow boundary condition that is characteristic of the marine boundary layer at the site. The main simulation uses data from a nearby weather station for the inflow air temperature and radiative forcing to the surface. The simulation is carried out for several days in order to capture the effect of thermal inertia.

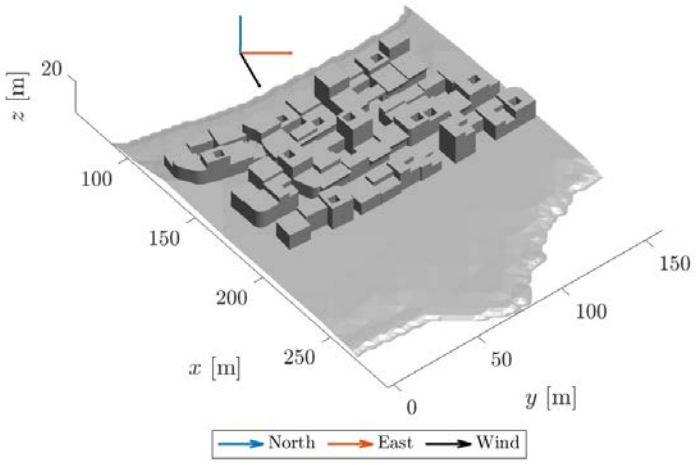

Fig. 1: Geometry used in main simulation, with North, East, and prevailing wind direction indicated.

DOI 10.5258/WES/P0042

The study consists of the following three aspects of investigation. The first aspect involves the bulk thermal response of the whole surface in terms of the temperature and energy balance, for both the buildings and the terrain (Sect. 3.1). In the second aspect, the evolution of the net radiation, the surface temperature, and the sensible heat flux for the various surface facets (roofs, walls, streets, and terrain) are presented (Sect. 3.2). The third aspect aims to understand the behaviour of environmental quantities, including the street-level air temperature and mean radiant temperature (MRT), considering these key SEB quantities and the flow (Sect. 3.3).

3 RESULTS

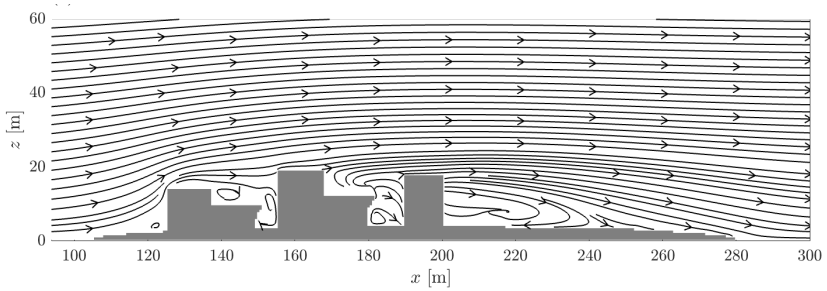

Fig. 2: Streamlines at y=50 m. Note the separation bubble behind the last row of buildings.

3.1 Bulk surface energy balance

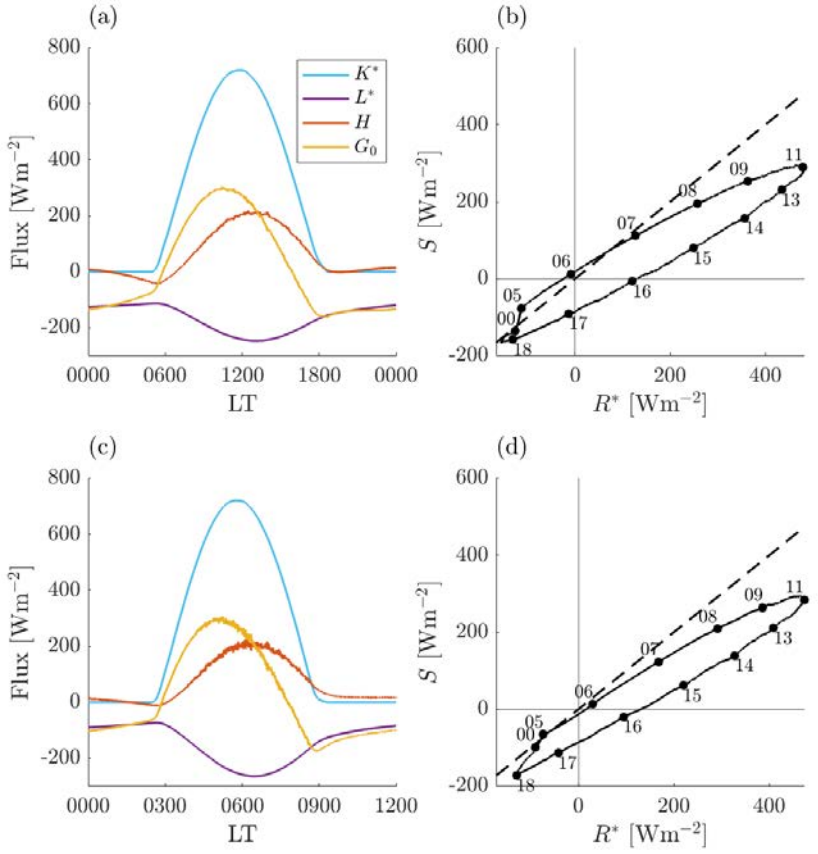

Fig 3: Surface energy fluxes (net shortwave radiation (K^*), net longwave radiation (L^*), sensible heat flux (H), and exterior conduction (G_0)) against local time (LT); and storage ($S = G_0 – G_d$, where G_d is the interior conduction) against net radiation ($R^* = K^* + L^*$) in the form of a Lissajous figure; respectively for the built environment (a,b) and the terrain (c,d).

DOI 10.5258/WES/P0042

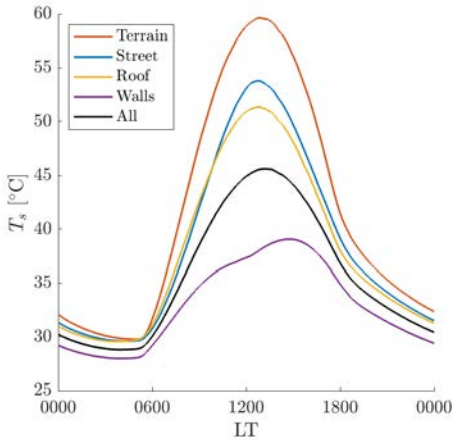

Fig 4: Area-averaged surface temperature (T_s) against local time (LT) for various facet types, where `All' includes the streets, roofs, and walls.

3.2 Spatial variation of surface energy balance

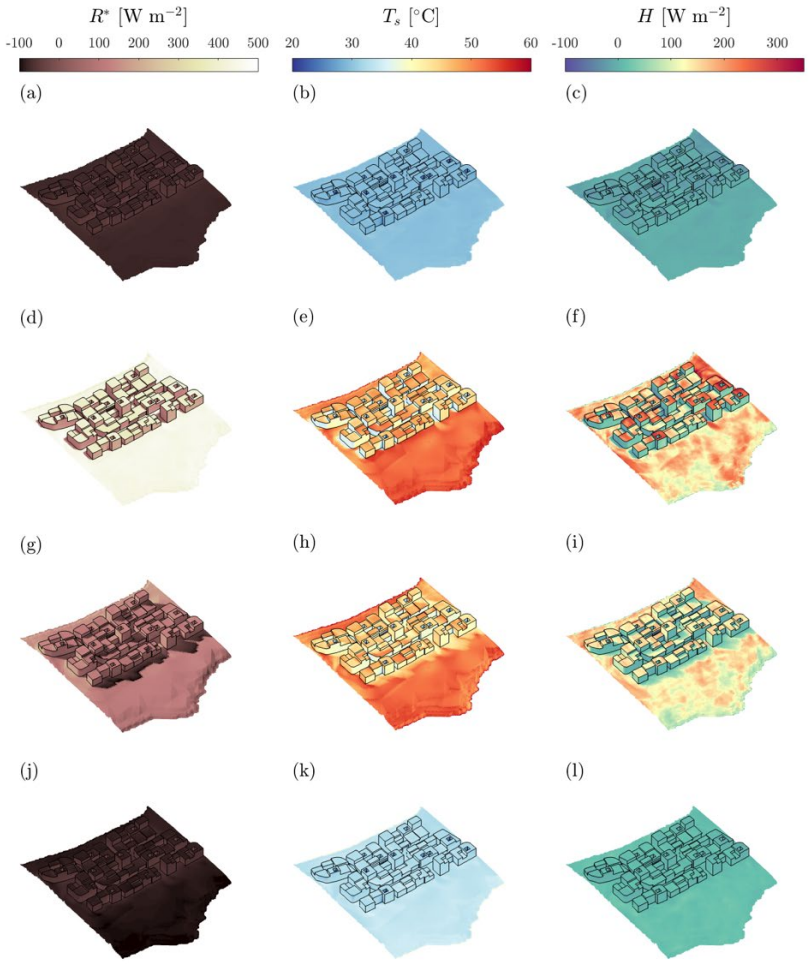

Fig. 5: 3D visualisation of facet net radiation (R^*), surface temperature (T_s), and sensible heat flux (H), respectively at 0400 LT (a-c), 1600 LT (d-f), 1600 LT (g-i), and 2200 LT (j-l).

DOI 10.5258/WES/P0042

3.3 Atmospheric quantities

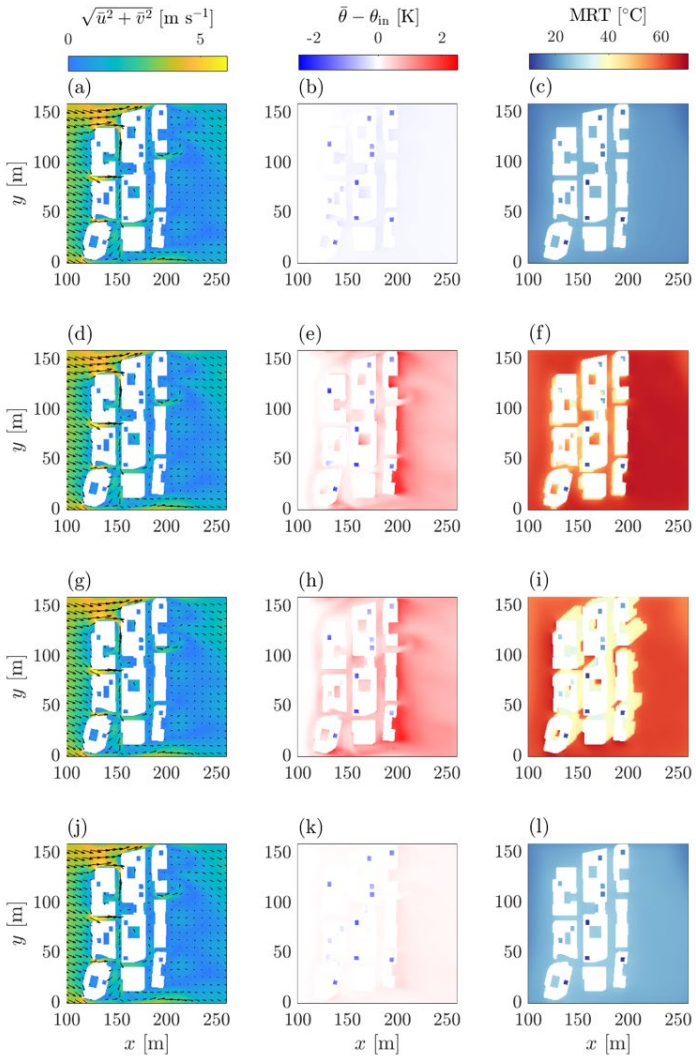

Fig. 6: Street-level wind speed and velocity vectors, and air potential temperature with respect to inflow ($\theta - \theta_{in}$), averaged during time interval: 0300-0400 LT (a-b), 0900-1000 LT (d-e), 1500-1600 LT (g-h), 2100-2200 LT (j-k); and MRT at 0400 LT (c), 1000 LT (f), 1600 LT (i), 2200 LT (l).

4 DISCUSSION

The bulk SEB for the built environment is similar to that of the terrain (Fig. 3), despite the terrain having a higher surface temperature (T_s) throughout the day on average than the built environment, and indeed than any of the facet types that make it up (Fig. 4). This is likely because their effective albedo is similar, resulting in approximately the same shortwave radiation.

The net radiation (R^*) has a strong influence on T_s (Fig. 5) and mean radiant temperature (MRT) (Fig. 6). In particular, the shading of streets results in them having a substantially lower T_s than the terrain, despite having the same material properties. Thermal inertia is important for the evolution: while R^* decreases in the afternoon, T_s does not to the same extent (Fig. 5).

The area of the domain with the highest air temperature is immediately in the wake of the buildings (Fig. 6), even though the local T_s and sensible heat flux (H) are relatively low. This is caused by flow behaviour: there is a separation bubble resulting in recirculation of air from the hot terrain (Fig. 2).

These results have implications for the ability of built environments to provide thermal comfort in hot climates and demonstrate the importance of considering microclimatic processes over a diurnal cycle.

DOI 10.5258/WES/P0042

REFERENCES

[1] Oke T.R., Mills G., Christen A., Voogt J.A. (2017). *Urban climates.* Cambridge University Press.

[2] Angevine W.M., Edwards J.M., Lothon M., LeMone M.A. & Osborne S.R. (2020). "Transition periods in the diurnally-varying atmospheric boundary layer over land". *Boundary-Layer Meteorology* 177:205–223.

[3] Verbeke S., Audenaert A. (2018). "Thermal inertia in buildings: A review of impacts across climate and building use." *Renewable and sustainable energy reviews*. 82:2300–2318

[4] Owens, S.O., Majumdar, D., Wilson, C.E., Bartholomew, P., van Reeuwijk, M. (2024). "A conservative immersed boundary method for the multi-physics urban large-eddy simulation model uDALES v2.0", *EGUsphere* [preprint], https://doi.org/10.5194/egusphere-2024-96.

DOI 10.5258/WES/P0042

Dispersion of Passive and Dense Plumes over a Step-Change in Wall Roughness

C. Deebank[1*], M. Placidi[1], M. Carpentieri[1]
[1]Centre for Aerodynamics and Environmental Flow, University of Surrey
Guildford, United Kingdom
*E-mail:cd00749@surrey.ac.uk

1 INTRODUCTION

Most of the literature on atmospheric dispersion, to date, considers boundary layers with homogenous surface roughness morphologies. However, in many scenarios in nature this is not the case. For example, wind flow over farmland encountering an urban area or ocean winds blowing over a coastline. This discontinuity - or step-change - in surface roughness will generate an internal boundary layer (IBL) within the existing boundary layer as the flow adjusts to the new surface conditions. The IBL (from a smoother to a rougher case) is characterised by a region of more turbulent 'adjusted flow' close to the wall within the existing boundary layer that grows in height with downstream distance [1]. Given that IBLs are so ubiquitous, it is of interest to assess whether they have a significant impact on the dispersion phenomenon.

Currently, there is very little experimental work considering the effect of IBLs on dispersion in boundary layers. Recently, [2] and [3] have performed numerical studies using LES to model dispersion of a passive scalar released within an array of cuboids (which simulate an urban environment) immersed in an boundary layer . Thus, the work herein aims to study the effect of an IBL on the dispersion of both passive and dense gas plumes released both upstream and downstream to the newly-developed IBL.

2 METHODOLOGY

This experiment was performed in the EnFlo Tunnel at the University of Surrey, a suck-down atmospheric wind tunnel. The IBL was generated using the method detailed by [1]; a step-change in roughness length, with an upstream section of relatively smaller roughness length to a downstream section of higher roughness length. Passively buoyant (air) and dense (CO2) plumes are released from a ground level point source in three different locations: 1m upstream from, 1m downstream from and at the step change location. An additional reference case was considered with no step change, so that the smaller roughness elements (i.e. the smaller roughness length here) extended the entire length of the tunnel. Time-resolved concentration measurements were taken via a single Cambustion HFR400 Fast Flame Ionisation Detector mounted on a 3-axis traverse (Figure 1). For brevity, only the case with the plume released upstream of the step change will be considered in this paper.

Concentration profiles were taken at seven streamwise locations, one vertical and two lateral (one within roughness sublayer, one within the log-law region), to observe the plume lateral and vertical growth rate as well as the behaviour of concentration within the plume, both in terms of its mean and higher-order properties. The experiment was carried out with three different sources: a 100mm diameter point source releasing air and CO2 at a flowrate of 10L/min and a third case the same source diameter, with CO2 but a higher flowrate (20L/min to increase the source's buoyancy flux). Given the large diameter of the source (100mm) it can be assumed that momentum effects are negligible in all cases.

DOI 10.5258/WES/P0043

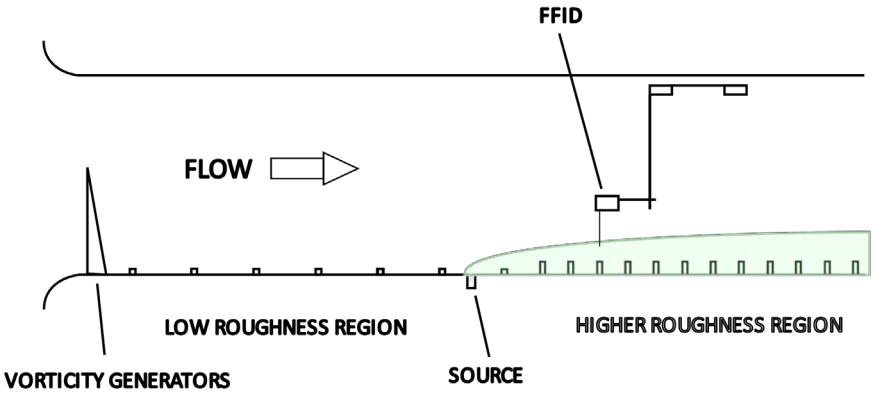

Figure 1: Diagram of EnFlo Tunnel test section showing the experimental setup.

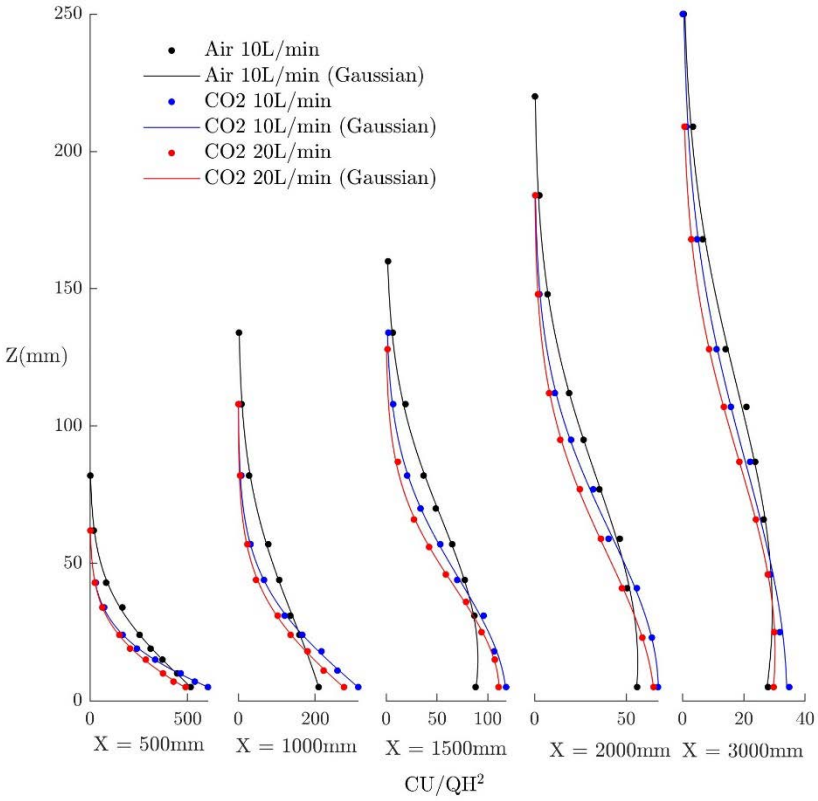

Figure 2: Vertical Profiles of non-dimensional mean concentrations at y = 0. Dots indicate a measurement point and lines show a best-fit single-peaked Gaussian curve. In this case, the step change is located approximately 1m downstream of the source which is defined at the origin.

DOI 10.5258/WES/P0043

3 PRELIMINARY RESULTS

In figure 2, vertical profiles of mean concentration at five streamwise locations are shown. To note that the step-change is located at *X=995*mm. Mean concentration has been nondimensionalized as:

$$\frac{CU}{QH^2}, \tag{1}$$

where C is tracer concentration, U is freestream velocity (1.5ms^{-1}), Q is tracer flowrate and H is boundary layer depth (1m). A single -eaked Gaussian curve has been fitted to each vertical profile. Plume vertical spread, centreline location and maximum concentration can be extracted from this as the coefficients of the fitted Gaussian curves. While this curve generally appears to be a good fit for most profiles, at X = 1000mm it does not appear that the centreline of the plume is at Z = 0, suggesting that the plume does not strictly follow a pure Gaussian profile in vertical spread immediately behind the step-change. This is likely due to the initial growth of the IBL behind the step change changing flow properties only in the region closest to the surface, or a wall reflection from the ground-level source.

When comparing plumes of different densities, they follow expected behaviour both before and after the step change, with the denser plumes exhibiting a lower vertical spread. Despite having the same density, the lower buoyancy flux in the case of the higher-flowrate dense gas case has a significant impact, with this again showing a lower vertical spreading than the lower-flowrate case.

It is notable that the plume appears to show relatively little vertical growth in the region immediately behind the step change (X = 1000 – 1500mm), when compared to the regions immediately before and after this.

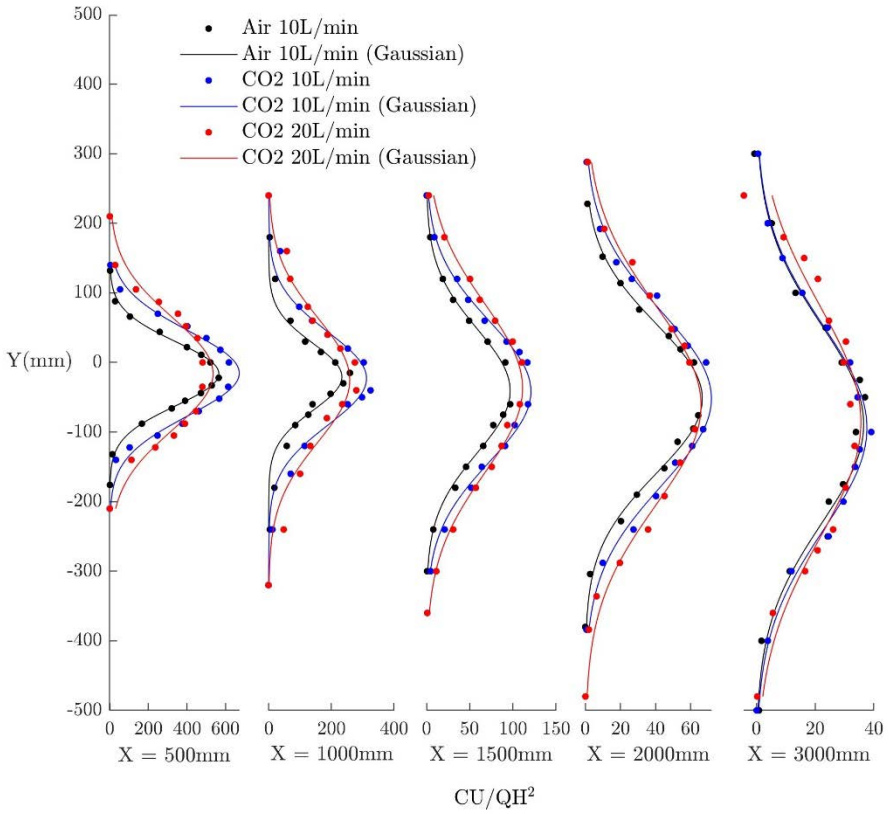

Figure 3: Lateral profiles of non-dimensional mean concentration at Z = 5mm (below the roughness height). As in figure 2, dots denote measured data and lines are a fitted Gaussian curve.

As with the vertical profiles shown in figure 2, Gaussian profiles have been fitted to lateral profiles of mean concentrations and show a good fit of the data. As expected, both downstream and upstream of the step

DOI 10.5258/WES/P0043

change, the dense (CO2) plumes show a greater lateral spreading, with the higher flowrate (i.e. the 20L/min plume) clearly having a significant impact, showing greater lateral extent when compared to the lower flowrate case.

The centreline of the vertical profiles appears to shift in the *Y*-negative direction with increasing streamwise distance. Laterally, this setup was symmetrical with all elements perpendicular to the flow, meaning that any lateral deviation is likely due to flow quality within the tunnel itself, local three-dimensional roughness effects, and vastly unrelated to the presence of the step-change.

From the width of the fitted Gaussian profiles, the plume appears to show a large increase in growth rate immediately behind the step change, in contrast to the lower vertical growth rate seen in figure 2. Ding [1] found that immediately behind the step change, a region of flow with a negative vertical velocity component existed. It is possible that this region acts as to 'squash' the plume downwards, decreasing its vertical growth rate, while increasing its lateral growth rate. Sessa et al. [2] noted similar behaviour, with lower vertical growth and greater lateral growth observed in this region.

Further work on this topic will examine the other two step change locations investigated and examine the fluctuating component of concentration.

References

[1] Ding S S, et al. (2023). Neutrally- and stably-stratified boundary layers adjustments to a step change in surface roughness. *Experiments in Fluids* 64. 86.

[2] Sessa V, Zheng-Tong X, Herring S (2018). Turbulence and dispersion below and above the interface of the internal and the external boundary layers. *Journal of Wind Engineering and Industrial Aerodynamics*. 182: 189-201

[3] Tomas J, et al. (2016) Pollutant Dispersion in Boundary Layers Exposed to Rural-to-Urban Transitions: Varying the Spanwise Length Scale of the Roughness. *Boundary-Layer Meteorology.* 163: 225-251

DOI 10.5258/WES/P0043

CROSS-STORM project: developing a numerical-experimental procedure for evaluating the risk of accident on road vehicles due to the strong crosswinds generated by a thunderstorm

Andi Xhelaj[1], Carlos Esteban Araya Reyes[2], Maria Pia Repetto[1], Luisa Pagnini[1] and Gisella Tomasini[2]
1 Department of Civil, Chemical and Environmental Engineering, University of Genoa, Genoa, Italy
2 Department of Mechanical Engineering, Polytechnic of Milan, Milan, Italy
* E-mail: andi.xhelaj@edu.unige.it

1 INTRODUCTION

Thunderstorm outflows generate intense non-stationary winds that might pose significant risk for road vehicles crossing areas where wind field reaches peak intensity (Fig. 1). Baker and Reynolds [1] reported a high incidence of accidents related to intense storm conditions. Zhang et al. [2] demonstrated that sudden changes in wind intensity and direction can generate high-risk scenarios. Despite this, most studies regarding wind-induced accidents are related to the stability of vehicles under generic synoptic wind conditions (e.g., Winkler et al. [3]).
The CROSS-STORM project aims to address this gap by developing a numerical-experimental procedure to evaluate the risk of accidents on road vehicles traveling through strong crosswinds generated during a thunderstorm downburst event. The methodology is articulated in three main phases: defining the wind velocity field during a thunderstorm downburst, calculating the aerodynamic loads on a road vehicle, and evaluating the dynamic response of the vehicle-driver system to wind actions using a driving simulator (DRISMI).
Given the critical role of driver response to storm-induced winds, key scenarios will be simulated in the driving simulator to study the behaviour of the vehicle-driver system. The ultimate goal of the project is to correlate key parameters with specific levels of accident risk.
Most of the approaches developed in the past for the evaluation of risk associated to crosswind acting on road vehicles, especially those applying deterministic wind profiles, focus on the vehicle characterization with respect to the action of the wind.
The CROSS-STORM project instead shifts the attention to the infrastructure, and to the possibility of defining actions that can mitigate the risk of road accidents: from this point of view, the correct evaluation of the atmospheric phenomenon, that is the real incident wind, is fundamental for the definition of targeted actions, such as the installation of windbreak barriers on highly riskiness sections, or the adoption of systems for reducing the maximum travel speed, to be adopted only in certain weather conditions.
The CROSS-STROM project, which began in September 2023 and is planned to last two years, has already made progress in the initial phase.

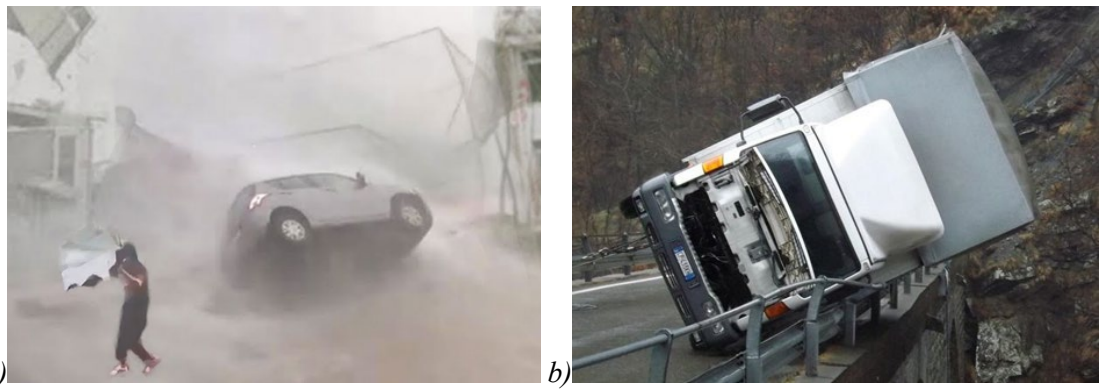
a) b)

Figure 1, Wind-induced overturning of vehicles due to thunderstorm winds

2 METHODOLOGY

2.1 Downburst Wind Field Model

To accurately simulate the wind velocity field experienced by vehicles during a thunderstorm downburst, the CROSS-STORM project adopts a comprehensive four-step modelling procedure. The first step

DOI 10.5258/WES/P0044

involves modelling the horizontal slowly varying mean wind velocity field of a traveling downburst by using a semi-empirical analytical model [4, 5]. This model integrates three primary downburst velocity components: stationary radial velocity, storm motion, and boundary layer background wind. These components collectively represent the fundamental characteristics of the downburst's horizontal wind field.

In the second step, the model simulates the downburst turbulence wind field. Downburst outflow turbulence is characterized as a non-stationary, non-Gaussian, bi-variate and partially coherent random process. The turbulence properties are derived using an extensive database of real-world downburst outflows, which includes data from anemometric and vertical lidar measurements. Once the turbulent structure is defined, synthetic time histories of velocity fluctuations are generated through Monte Carlo Simulations, utilizing prescribed turbulence spectra and horizontal coherence functions. These spectra and coherence functions are calibrated using full-scale data.

The third step involves reconstructing the non-stationary outflow wind velocity field generated by the thunderstorm downburst. This is achieved by considering the wind components obtained in the previous steps. The resulting model provides a detailed representation of the wind field, incorporating both the slowly varying mean wind velocities and the turbulent fluctuations.

Finally, in the fourth step, the model calculates the time history of the relative wind velocity encountered by a moving vehicle. This calculation considers the vehicle's motion, including its speed and direction, as it travels through the downburst. By determining the relative velocity between the vehicle and the wind field, the model provides the data for assessing the aerodynamic loads on the vehicle and its stability under these extreme downburst wind conditions.

Figure 2 illustrates the simulation of a downburst event and its impact on a moving vehicle using the Xhelaj et al. [4] model. The simulation is conducted within a spatial domain of 15,000 × 15,000 meters, with an equal grid resolution of 25 meters in both directions, and a temporal domain from 0 to 600 seconds.

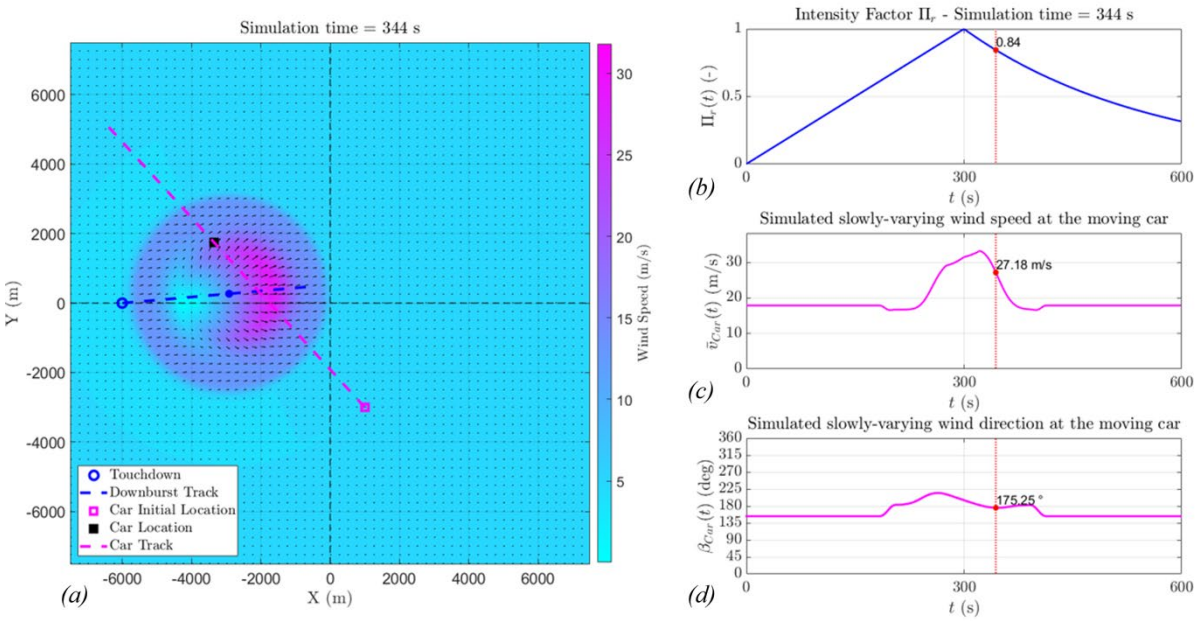

Figure 2, Simulation of the impact of a downburst event on a moving vehicle. Wind velocity filed, downburst and vehicle's trajectory (a). Intensity factor (b). Simulated slowly varying wind speed at the vehicle's location (c). Simulated slowly varying wind direction at the vehicle's location (d).

Key model parameters, including the downburst's touchdown location, maximum radial speed, radial length scale, intensity and decay periods, storm speed, and direction, define the downburst characteristics. In panel (a), the downburst's path over time, based on its translation velocity and direction, is depicted at 344 seconds. The vehicle's kinematics are incorporated by calculating its position over time, considering an initial position (magenta square in Figure 2a). The vehicle moves at a constant speed of 18.75 m/s (60 km/h) and in a fixed direction of 138 degrees from the North, where the Y-axis is aligned with the North, representing the zero-wind direction in meteorological convention. Additionally, the simulation includes

DOI 10.5258/WES/P0044

a constant boundary layer background wind with a speed of 5 m/s and a direction of 245 degrees from the North. Wind velocities at the vehicle's location are interpolated to determine the wind field impacting on the moving vehicle. Panel (b) shows the downburst's radial intensity factor Π_r over time, highlighting a peak intensity at 300 seconds. Panel (c) depicts the simulated slowly varying wind speed at the moving car, while panel (d) illustrates the simulated slowly varying wind direction at the moving car. The model also includes turbulence components which are not shown in Figure 2 but will be presented in the conference.

2.2 Aerodynamic Loads Calculation

The second part of the project concerns the calculation of the aerodynamic loads acting on a road vehicle due to the strong crosswinds during a thunderstorm. Starting from the simulation of the time history of the thunderstorm wind, the aerodynamic loads can be obtained for a given vehicle if the aerodynamics coefficients that characterise its aerodynamic behaviour are known ([6],[7]). In this project, four different types of road vehicles are considered: an articulated lorry, a double-decker bus, a small lorry, and a saloon car. The selected vehicles are presented in Fig. 3-a. These vehicles are representative of a wide range of sizes and shapes, corresponding to the most diffused vehicle categories across Europe. In this way a comprehensive overview is provided of how different road vehicles behaves when exposed to the severe downburst outflow winds.

To characterise the different vehicles that will be analysed in this study, a dedicated experimental campaign is being conducted in the GVPM wind tunnel of Politecnico di Milano. This campaign aims to generate a uniform dataset of aerodynamic coefficients for the selected vehicles. Because thunderstorm winds are naturally not aligned with the vehicle longitudinal axis, and of course the aerodynamic coefficients depend on the angle of attack of the vehicle, it is therefore necessary to measure the aerodynamic coefficients for the vehicles subjected to crosswinds for a range of angles of attack.

For each vehicle, aerodynamic loads will be measured by a dynamometric balance set inside the model, with a uniform (vertical block profile) wind and standard infrastructure (flat ground). As done in the railway field, the effects associated with scenario (wind profile, viaduct, embankment, etc.) are accounted for by applying specific correction formula to wind speed distribution.

In this way, the aerodynamic loads are calculated based on the wind tunnel data and on scenario characteristics. These loads are the input of the dynamic simulations of each vehicle type. This process is crucial for understanding how these loads affect vehicle stability and control.

2.3 Vehicle-driver Dynamic evaluation

The final part of the methodology involves the study of the stability to thunderstorm of the vehicle, considering the influence that the driver has on the system. The DRISMI driving simulator of the Politecnico di Milano (Fig.3-b) permits to evaluate the dynamic response of the vehicle-driver system to the aerodynamic loads calculated in the previous step. The DRISMI simulator replicates real driving conditions, bringing up the possibility to test how vehicle-driver system responds to crosswinds in a controlled environment, thus allowing for repeatability and reproducibility of the tests. The simulator includes sophisticated controls and feedback mechanisms to accurately reproduce real-world driving conditions.

To evaluate the impact on the behaviour of the system under different conditions, some key scenarios are reproduced. To select the most significant conditions and reduce the number of configurations to be tested with the driving simulator, a preliminary virtual testing phase has been carried out by a multi-body vehicle model.

The vehicle dynamics model integrated within the driving simulator is the multibody software VI-CarRealTime, from VI-Grade: it allows to reproduce each vehicle subsystem (wheels, suspensions, body, steering system, brakes, aerodynamic forces, engine and driveline) and all the forces acting on it ([8]).

Different scenarios have been simulated by using this vehicle dynamics model ([8]), without accounting for the driver. By analysing the results obtained by the virtual testing, the more critical configurations, in terms of accident risk, will be identified and finally tested by the driving simulator.

In the last part of the project, through an experimental campaign with a sample of drivers, the effect of wind conditions on vehicle stability and driver behaviour is studied. These scenarios will help to identify critical factors that influence the accident risk, it can be from the driver side, as for example, driver experience or reaction time, but also from the vehicle side like handling characteristics, mass, load

DOI 10.5258/WES/P0044

condition, exposed lateral area. Moreover, by analysing the data from the simulator, it will be possible to correlate specific wind parameters with accident risk levels.

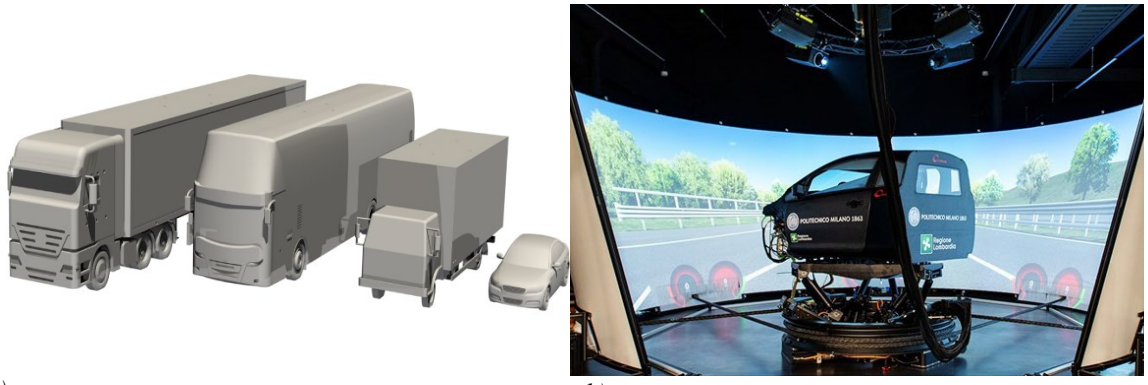

a) *b)*

Figure 3, (a) Vehicle models to be tested in the wind tunnel tests at Politecnico di Milano Wind Tunnel. From left to right: articulated lorry, double-decker bus, small lorry, saloon car. (b) DRISMI Driving simulator of Politecnico di Milano.

3 CONCLUSIONS

In its first year, the CROSS-STORM project has made significant strides in its initial phases, focusing on the development of a comprehensive numerical-experimental procedure to evaluate the risk of vehicular accidents due to thunderstorm-induced extreme winds. The first phase, involving the simulation of wind fields, is currently underway. The second phase, which includes wind tunnel testing, is scheduled to begin in October 2024. The final phase, assessing vehicle-driver responses using the DRISMI driving simulator, has yet to be initiated. As the project progresses, these efforts will be crucial for enhancing vehicle safety and mitigating the risks posed by severe weather conditions.

REFERENCES

[1] Baker C.J. & Reynolds S. (1992). "Wind-induced accidents of road vehicles", *Accid. Anal. Prev*. 24(6), 559–575.

[2] Zhang Z., Li J., Guo W. (2018). "Combined simulation of heavy truck stability under sudden and discontinuous direction change of crosswind with computational fluid dynamics and multi-body system vehicle dynamics software", *Adv. Mech. Eng*. 10(7).

[3] Winkler N., Drugge L., Stensson Trigell A., Efraimsson G. (2016). "Coupling aerodynamics to vehicle dynamics in transient crosswinds including a driver model", *Comput. Fluids*, 138, 26-34.

[4] Xhelaj A., Burlando M., Solari G. (2020). "A general-purpose analytical model for reconstructing the thunderstorm outflows of travelling downbursts immersed in ABL flows", *J. Wind. Eng. Ind. Aerod.,* 207, 104373.

[5] Xhelaj A. & Burlando M. (2022). "Application of metaheuristic optimization algorithms to evaluate the geometric and kinematic parameters of downbursts", *Adv. in Eng. Soft.*, 173, 103203.

[6] Cheli, F., Corradi, R., Sabbioni, E., Tomasini, G., Wind tunnel tests on heavy road vehicles: Cross wind induced loads-Part 1, (2011) Journal of Wind Engineering and Industrial Aerodynamics, 99 (10), pp. 1000-1010, DOI: 10.1016/j.jweia.2011.07.009

[7] Liu, Xianzhi Han, Yan Cai, C. Levitan, Marc Nikitopoulos, Dimitris. (2016). Wind tunnel tests for mean wind loads on road vehicles. Journal of Wind Engineering and Industrial Aerodynamics. 150. 15-21. 10.1016/j.jweia.2015.12.004.

[8] Cheli F., Leo E., Mancosu F., Melzi S. (2006). A 14dof Model for the Evaluation of Vehicle's Dynamics: Numerical - Experimental Comparison. International Journal Of Mechanics And Control, 6, p. 19-30.

DOI 10.5258/WES/P0044

Towards passive scalar reconstruction using data assimilation

Uttam Cadambi Padmanaban[1*], Bharathram Ganapathisubramani[1], Christina Vanderwel[1], Sean Symon[1]
[1]Department of Aeronautics and Astronautics, University of Southampton
Southampton, United Kingdom
[*]E-mail: ucp1n22@soton.ac.uk

1 ABSTRACT

Reconstructing three-dimensional (3D) mean velocity fields using limited observations is valuable for studying pollutant dispersion in urban flows. Data assimilation addresses the challenge of limited experimental observations and the cost-accuracy trade-off of low-fidelity computational models. High-fidelity data is sourced from time-averaged velocity fields in a Detached Eddy Simulation (DES) of flow past a surface-mounted cube in a channel at Reynolds number 40,000. Additionally, pollutant dispersion is modelled by an upstream constant scalar source. DES results for mean scalar fields align well with experiments, validating its utility for pollutant dispersion studies. We use data assimilation to improve imperfect mean velocity predictions from Spalart-Allmaras (SA) Reynolds-Averaged Navier-Stokes (RANS) turbulence model using a single velocity data plane from DES. Improved mean velocity predictions across the domain highlight the potential of using limited observational data to correct RANS models for urban flow studies.

2 INTRODUCTION

RANS turbulence models offer a computationally efficient way of studying 3D flows despite limited accuracy in predicting flow physics in the presence of flow separation, streamline curvature and pressure gradients. Alternatively, the use of field imaging techniques such as particle image velocimetry (PIV) offer a realistic picture of the flow physics but provide only limited observations on discrete planes and not a continuous volumetric field. This paper aims to overcome the inherent limitations of CFD simulations and experimental measurements.

Data assimilation can be used to enhance low-cost simulations by RANS models by incorporating experimental measurements to increase accuracy. Unknown terms in the RANS simulation are tuned by minimizing the discrepancy between high-fidelity reference data and RANS output. This variational data assimilation has been used to assimilate full-field measurements in 2D at a low computational cost [4]. Its extension to 3D flows with limited measurement data is an opportunity that is explored in this paper.

The objective of this study is the assimilation of sparse mean velocity field from a high-fidelity simulation into a low-fidelity model for a 3D flow problem. The assimilation is done for the case of a 3D surface mounted cube in a channel. The geometry represents a simplified model of flow past an isolated tall building which is relevant for urban fluid mechanics. We then apply the variational method to enhance the accuracy of SA turbulence model predictions by integrating limited DES-obtained observations.

3 CASE SETUP

The case consists of a cube mounted on the bottom wall of a channel. The schematic of the case is shown in Figure 1a. The streamwise, vertical and cross-stream directions are along x, z and y respectively. The cube is located $x = 3.5H$ from the inlet and placed centrally between $y = 0$ and $y = 9H$ in the cross-stream direction. The Reynolds number of the flow based on the side of the cube H is $Re_H = 40,000$ which is set by fixing $H = 1m$, $U = 1m/s$ and $\nu = 2.5 \times 10^{-5} m^2 s^{-1}$. The structured 3D mesh consists of 1,216,000 cells with refinement in the wake region as shown in Figure 1b. The scalar is introduced as a source term shaped as a cube of side $0.1H$ that is located in the streamwise mid-plane of $y/H = 4.5$, at a distance of $1.5H$ upstream of the front face of the cube, $0.1H$ units above the bottom wall. The strength of the scalar source is 5 units. The simulations are performed using the open-source finite-volume CFD solver OpenFOAM.

DOI 10.5258/WES/P0045

4 METHODOLOGY

4.1 Detached eddy simulation

The reference data is generated by performing a variant of DES (improved delayed DES or IDDES with SA as the background RANS turbulence model) and then time-averaging the velocity and scalar concentration fields. This model applies RANS in the near wall region and switches to LES to resolve the turbulent eddies in regions away from the wall. The computational details including the boundary conditions can be found in [1].

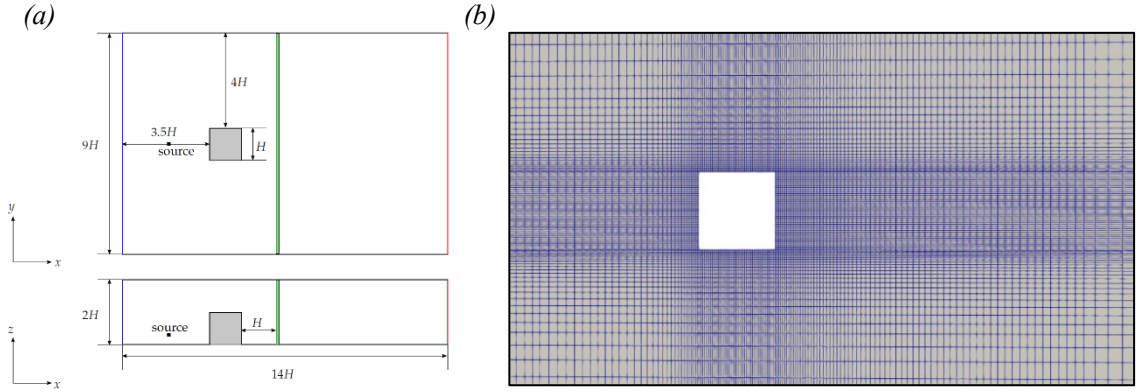

Figure 1. (a) Schematic of the test case. Inlet (—) and outlet (—) boundaries shown with location of reference data plane (—) and scalar source. (b) Close up of transverse section of the mesh at z/H = 0.5.

4.2 Reynolds-Averaged Navier-Stokes

The reference data obtained from DES is assimilated into a low-fidelity RANS turbulence model. The RANS equations are given by,

$$\overline{u}_j \frac{\partial \overline{u}_i}{\partial x_j} = -\frac{1}{\rho}\frac{\partial \overline{P}}{\partial x_i} + \frac{\partial}{\partial x_j}\left(\nu_{eff}\frac{\partial \overline{u}_i}{\partial x_j}\right), \tag{2}$$

where the overbar indicates Reynolds averaging, u is the velocity, P is the combined pressure and turbulent kinetic energy k and $\nu_{eff} = \nu + \nu_T$ is the effective kinematic viscosity which is the sum of molecular viscosity ν and eddy viscosity ν_T. The eddy viscosity can be obtained by solving a transport equation using SA turbulence model, the functional form of which is given by,

$$\frac{D\tilde{\nu}}{Dt} = P(\tilde{\nu}, \boldsymbol{w}) + T(\tilde{\nu}, \boldsymbol{w}) - D(\tilde{\nu}, \boldsymbol{w}), \tag{3}$$

where P, T and D are respectively production, diffusion transport and destruction terms, $\tilde{\nu}$ is the surrogate viscosity and $\boldsymbol{w}$ is the vector of state variables.

4.3 Variational data assimilation

The time-averaged DES velocity data can be used to improve the prediction of the RANS SA model. The goal is find an optimum control variable distribution that minimizes an objective function, formulated as a discrepancy between reference data and RANS model output, subject to constraints given by,

$$f(\boldsymbol{u}, \beta) = \frac{1}{2}\left\| Q(\boldsymbol{u}, \beta) - \widetilde{\boldsymbol{Q}} \right\|^2, \tag{4}$$

where β is the control/design variable of choice, Q is a projection function, $\widetilde{\boldsymbol{Q}}$ is a set of high-fidelity velocity measurements obtained from DES (can also be obtained from PLIF or DNS). The production term of the SA model is pre-multiplied by a spatially varying scalar multiplier $\beta(x, y)$. The modified transport equation for the SA model is given by,

$$\frac{D\tilde{\nu}}{Dt} = \beta P(\tilde{\nu}, \boldsymbol{w}) + T(\tilde{\nu}, \boldsymbol{w}) - D(\tilde{\nu}, \boldsymbol{w}). \tag{5}$$

The baseline SA model can be recovered by setting $\beta = 1$ throughout the domain. We use the discrete adjoint method implemented in DAFoam [3] to obtain the gradient and an interior point method with line search filter implemented in IPOPT to perform the optimization. A single plane of reference data that is located at *x/H = 5.5* or *1H* from the trailing face of the cube (as shown in Figure 1a) is supplied to the assimilation step to perform data assimilation using limited measurements.

DOI 10.5258/WES/P0045

5 RESULTS

5.1 Mean velocity fields

The mean streamwise and vertical velocity fields from DES along planes *z/H = 0.5* and *y/H = 4.5* are presented in Figure 2. The wake recirculation region in Figure 2a is clearly delineated by the $\frac{\bar{u}}{U_\infty} = 0$ contour. Figure 2b suggests that the flow is pushed upward near the trailing face of the cube denoting the presence of recirculation. It is also observed that most of the wake recirculation is confined to a very small region in the vicinity of the cube (~1.5H from the trailing edge). These results are also supported by similar observations made in [5], albeit for a tall building.

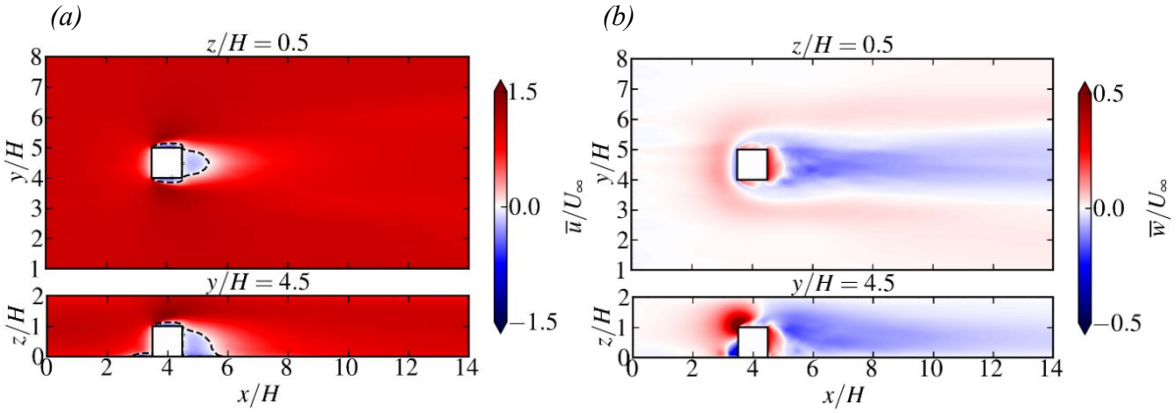

Figure 2. Velocity contours of (a) streamwise (b) wall-normal mean velocity along planes z/H = 0.5 (top) and y/H = 4.5 (bottom). The dashed line is contour of $\frac{\bar{u}}{U_\infty} = 0$.

An interesting point to note is the location of the stagnation point in Figure 2b (the location where the vertical velocity magnitude changes from negative to positive). This is located at *z/H ~ 0.58* which agrees well with [5]. Placing a scalar source below this stagnation point affects the manner in which it diffuses which will become clear upon examining the mean scalar concentration field.

5.2 Mean scalar fields

The mean scalar concentration on two cross-stream planes is presented in Figure 3a. The double peak structure is visible on both planes. The scalar is confined to a region close to the bottom wall with a limited spread in the cross-stream direction. The double peak observation agrees well with experiments performed in [5] where they speculate the distribution to be a result of entrainment in the horseshoe vortex. This is a result of placing the scalar source below the stagnation point of the cube which discourages scalar dispersion over the cube.

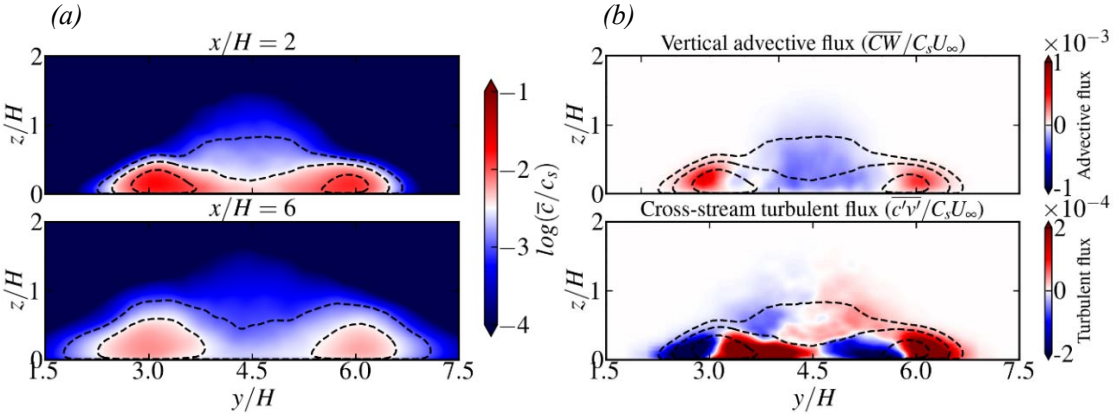

Figure 3. (a) Mean scalar concentration along two cross-stream planes at x/H = 2 and x/H = 6 from the cube trailing face. Dashed contour lines indicate scaled logarithmic scalar concentrations of -3, -2.5 and -2 (b) advective and turbulent fluxes along cross-stream plane at x/H = 2.

The vertical advective and cross-stream turbulent fluxes along a cross-stream plane at *x/H = 2* from the cube trailing face are show in Figure 3b. The advective fluxes are greater than the turbulent fluxes by an order of magnitude. Since the scalar concentration is positive, a negative vertical advective flux indicates a downward transport of the scalar just behind the cube. The positive advective flux shows a double peak

DOI 10.5258/WES/P0045

that coincides with the region of maximum scalar concentration (shown as dashed contours in Figure 3b). The cross-stream turbulent flux shows structures alternating in sign that accumulate the scalar towards the two peaks as can be seen in the dashed isocontours of scalar concentration. In general, these show good agreement with the advective and turbulent fluxes from [5]. The complex flow physics that involve wake recirculation, presence of horseshoe vortex and leading edge flow separation with a shear layer present a good case for data assimilation since they cannot be captured accurately by RANS models.

5.3 Assimilated mean velocity

The comparison of the mean velocity field from baseline SA model with the reference DES result is offered in Figures 4a. The baseline model over predicts the extent of the recirculation bubble as can be seen in Figure 4a. The assimilated mean velocity fields show a very good improvement over the baseline when compared to the reference DES result (Figure 4b). While the reference data was supplied along one cross-stream plane (Figure 1a), the improvement in mean velocity can be observed across other planes in Figure 4b. This encouraging result is particularly beneficial for experiments where it is expensive to image volumetric fields. This result shows that limited planar measurements can be incorporated into RANS models to improve the accuracy of mean flow predictions of 3D flows in the entire domain.

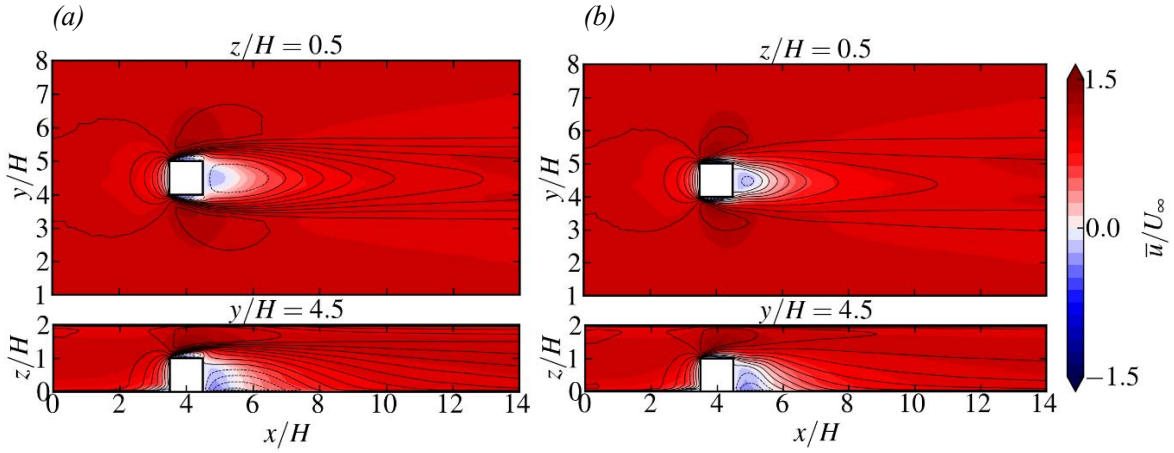

Figure 4. Mean streamwise and vertical components of velocity from (a) baseline RANS SA model and (b) assimilated RANS SA model (solid contours show reference DES velocity field and contour lines show the results from RANS).

6 CONCLUSION AND FUTURE WORK

We performed a DES of a 3D surface mounted cube in a channel with a fixed strength passive scalar source at Re_H = 40, 000. The mean scalar concentration fields, and the advective and turbulent fluxes show good agreement with experiments. Data assimilation using the variational method was performed by supplying a single plane of reference data generated by time-averaging the DES velocity field. The improvement in mean velocity field of a baseline RANS SA model demonstrates the utility of using limited measurements in 3D data assimilation using the variational method. Future work includes scalar source location identification and assimilation of the turbulent scalar flux term (which is typically modelled in RANS models) using reference scalar concentration and mean velocity field from volumetric experimental measurements.

REFERENCES

[1] OpenFOAM Foundation. "Verification and Validation: Turbulent Surface Mounted Cube." https://www.openfoam.com/documentation/guides/latest/doc/verification-validation-turbulent-surface-mounted-cube.html.

[2] He, Ping, Charles A. Mader, Joaquim RRA Martins, and Kevin J. Maki. "DAFoam: An open-source adjoint framework for multidisciplinary design optimization with OpenFOAM." *AIAA journal* 58, no. 3 (2020): 1304-1319.

[3] Thompson, Craig, Uttam Cadambi Padmanaban, Bharathram Ganapathisubramani, and Sean Symon. "The effect of variations in experimental and computational fidelity on data assimilation approaches." *Theoretical and Computational Fluid Dynamics* (2024): 1-20.

[4] Rich, Tomos, and Christina Vanderwel. "Pollutant Dispersion Around a Single Tall Building." *Boundary-Layer Meteorology* 190, no. 8 (2024): 34.

DOI 10.5258/WES/P0045

Exploring wind engineering challenges in super-slender buildings

Stefano. Torre[1*], Edoardo Ruffini[1*]
[1] NOVA Fluid Mechanics Ltd, Teddington, UK
[*] E-mail: Stefano.torre@novafluidmechanics.com

1 INTRODUCTION

In recent years, there has been a remarkable surge in the design of tall and supertall buildings, characterized by increasing heights and slenderer profiles. This trend poses significant challenges to wind and structural engineers in particular with respect to vortex-induced responses that tend to occur well within the design wind speeds (e.g., [1]). Recently, a project for a 2 km skyscraper in Riyadh has commenced which exceeds twice the current height record. This advancement in engineering and architecture could suggests that buildings below 200 m could be designed and constructed without notable challenges in terms of wind action. However, the importance to build structure in prime locations has led developers and designers to build tall building with smaller and smaller footprints introducing therefore a new category of structures of relatively standard height but that can be considered super slender. Moreover, to optimize floor space usage, these buildings often adopt a uniform cross-sectional design, which can lead to enhance wind responses.

This paper presents findings from a series of wind engineering studies based on high-frequency pressure integration wind tunnel tests (HFPI) on similar super slender buildings. These experiments were aimed at evaluating the wind effects relevant to the structural and serviceability design of nine tall and slender buildings located in the same region of South America. All of them share common geometrical features, such as small footprint dimensions, and heights not exceeding 250m, reaching an extremely high slenderness aspect ratio. Additionally, all buildings exhibit structural properties indicating frequencies significantly lower than those predicted by internationally recognised codes and standards. Across all cases, notable vortex-induced vibrations were observed, leading to elevated base loads and accelerations surpassing maximum recommended criteria (e.g., [2]-[4]).

2 CHARACTERISTICS AND PROPERTIES OF THE TALL BUILDINGS

All the structures studied in this paper are residential concreate building characterised by heights ranging from 140 m to 220 m, and mass densities between 300 kg/m^3 to 500 kg/m^3. The cross-sections of the buildings are nearly constant with height, and are characterized by an aspect ratio ranging from 1 to 2.5. Only two of the buildings exhibited aspect ratios significantly greater, approximately equal to 5. Based on the definition reported in [5], the slenderness ratio can be defined as

$$\lambda = \frac{H}{\sqrt{BD}} \tag{1}$$

where H is the reference height of the building, and D and B are the main section dimensions. All the buildings are characterized by a slenderness ratio ranging from 1:6 and 1:11, approximately. BMT Fluid Mechanics (BMT) conducted a study of several tall building in 2017 and have built a large database [6]. The authors have reviewed the slender ratios for the proposed buildings and, comparing these slenderness values with the BMT database, noted that these are significantly lower than the expected ones. In particular, Figure 1-A illustrates the comparison between the buildings object of this study and the BMT's prediction trend line. However, it is important to emphasize that the slenderness definition provided by formulation (1) may be misleading when the cross-sectional aspect ratio is particularly high. For instance, in two cases with an aspect ratio of five, the slenderness ratio can increases substantially using the reference height and the smallest dimension, moving from 6 to 14, and from 8 to 17. Adopting the smallest dimension for slenderness assessment in elongated cross-sections can offer a clearer understanding of the real potential structural issues.

Beyond the notable geometric challenges, these buildings are also characterised by dynamic properties that are considered potentially problematic in terms of wind-induced effects. Indeed, the fundamental bending modes of these structures are associated with natural frequencies ranging from 0.15 Hz to 0.25 Hz, which are significantly lower than the approximated values provided by Eurocode [7], but not so far

DOI 10.5258/WES/P0046

from the expected BMT values ([6]). Figure 1-B shows the comparison between the buildings properties object of this study, the BMT and Eurocode 's expected lines.

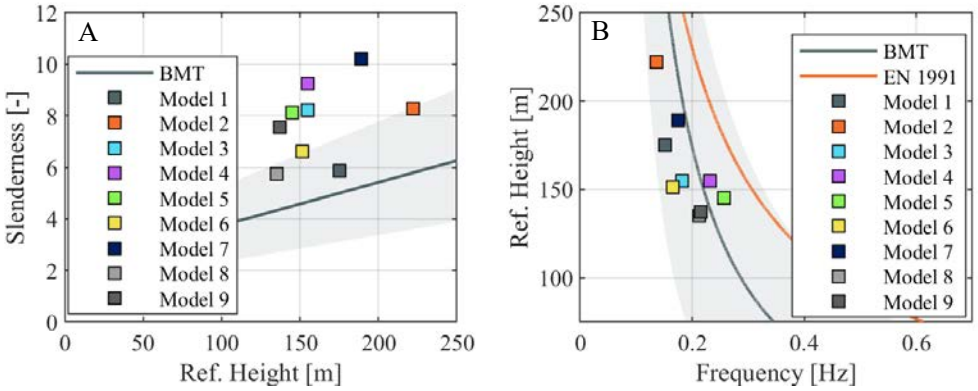

Figure 1, A) Comparison the BMT expected values [6] and the slenderness of the studied buildings. B) Comparison the BMT expected values [6], Eurocode [7], and the provided frequencies

From the outset, preliminary observations of the geometric and structural characteristics of these buildings indicate potential and significant issues associated with wind loading. The pronounced geometric slenderness, coupled with a low structural frequency and a uniform cross-section along the height, creates a potentially critical situation. It is likely that, following the wind tunnel studies, these structures will require substantial structural modifications to mitigate both wind loads and accelerations.

3 LOCATION

These building have been selected for the present study since they were tested in similar wind conditions, both in terms of wind and turbulence profiles, adopting a similar surrounding condition. Indeed, all the structures will be built in the same city area of Brazil. Such city is one of the Brazilian areas that has recently experienced a notable surge in construction activity. This growth has been particularly marked by the rapid increase in luxury residential high-rise towers. Currently, the area is primarily characterized by medium to high-rise residential and commercial buildings situated to the south, southwest, west, and northwest of the town centre. The open sea adjoins the developments to the northeast and east. Figure 2 showed an approximate location for all the studied buildings within the surrounding area.

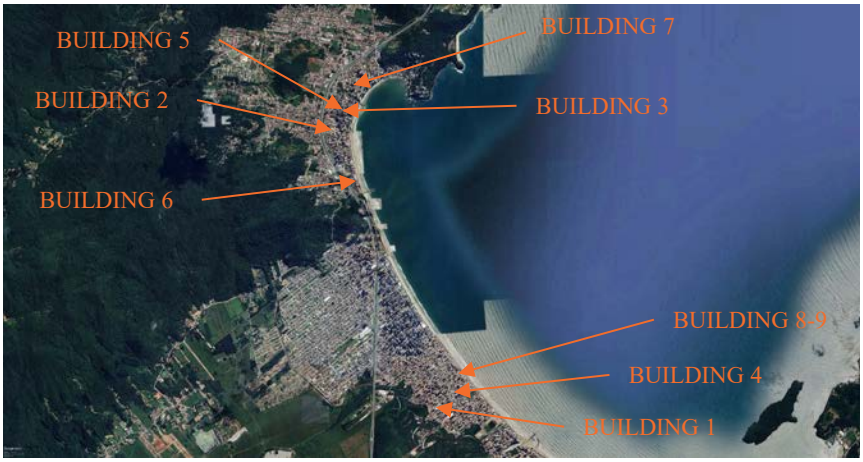

Figure 2 Location of the studied buildings.

4 METHODOLOGY

4.1 Facility and experimental conditions

The wind tunnel experiments were conducted in the closed-loop subsonic wind tunnel at the DICCA laboratory, University of Genoa. This facility features a test chamber with a cross-sectional area of 1.7 × 1.35 m (width × height). The facility is equipped with a simultaneous 368-channels low range pressure

DOI 10.5258/WES/P0046

scanning using Sensor Techniques low range SLP004D differential transducers. The frequency response of the transducers is 2000 Hz.

The wind tunnel tests were conducted by simulating the appropriate boundary layer profiles of the area. Both mean wind and turbulence profiles were reproduced in the wind tunnel, with all dimensional quantities scaled according to the geometric model scale. Measurements were taken for a full range of wind directions in increments of 10°.

4.2 Wind tunnel models

All models were constructed at a geometric scale of 1:300-400. The 3D printed models of the buildings were developed with sufficient details to accurately replicate full-scale flow characteristics and with the highest geometrical precision allowed by the small scale and available prototyping tools. Each model, fabricated using state-of-the-art rapid prototyping (RP) techniques, was fitted with the maximum number of pressures taps appropriate for the chosen scale, capturing all relevant aerodynamic behaviours of the model. Figure 3 shows some examples of wind tunnel models.

Figure 3, Example of wind tunnel models.

5 RESULTS

Design wind loads (in terms of dynamic base and floor-by-floor loads) have been assessed based on 50-year return period, considering a damping ration of 1.5% (fraction of critical) for each building based on the same design wind speed. Regarding serviceability design, namely wind-induced building accelerations, the building responses have been assessed based on the 1- and 10-year return period design wind speeds at the highest occupied level of each building. Both design loads and serviceability have been estimated in conjunction with the use of uniform directional factors.

The along-wind response derived from HFPI technique have been found to be either lower than or comparable with the values derived from a direct code approach. However, the cross-wind response exhibited a significant dynamic amplification, especially for the wind directions orthogonal to the main axes of the structure. Analysing the base load results, the Dynamic Amplification Factor (DAF) was assessed from the peak static and dynamic responses in each direction. Among the buildings described in this paper, a statistical mean DAF value of 3.2 was determined, with the exception of two cases where the buildings exhibited significantly higher values due to their direct exposure to the most severe wind direction.

Similarly, the acceleration values for 1- and 10-year return periods, were found to be substantially above the recommended limits (e.g., [2]-[4]). In most cases, these extreme accelerations values are attributed to the dynamic response induced by vortex shedding for a narrow wind sector in which the wind action is orthogonal to the main axes of the structure. Figure 4 shows the acceleration results for all the buildings compared with the adopted recommended limits.

DOI 10.5258/WES/P0046

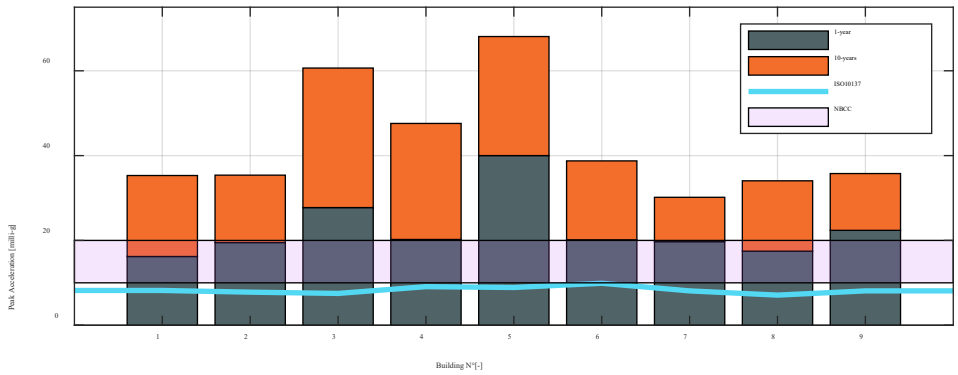

Figure 4, Accelerations results compared with recommended limits for residential buildings ([2]-[4]).

All the aforementioned results pertain to the initial properties of the building as provided by the structural engineers. Additional analyses were conducted based on increased natural frequencies to ensure alignment with relevant standards and code prescriptions. In some cases, revisions to the external envelope of the buildings were implemented to mitigate dynamic responses.

6 CONCLUSION

The primary objective of this paper is emphasizing that slenderness plays a key role in the wind response of a tall building and combined with other factors such as the key dimensions of a footprint, may result in accelerations well above the recommended criteria. Buildings are progressively becoming increasingly slender to maximize the available space, defining new emerging category of super-slender buildings. However, due to these peculiar properties, It would be beneficial for such structures, due to their unconventional design, to be designed based on an aerodynamic shape optimization conducted during the schematic design phase, potentially focusing on corner modifications (e.g., [9], [10]). Implementing these optimizations has the potential to reduce wind loading, resulting in a slimmer structural system that maximizes available footprint space. Furthermore, by integrating aerodynamic principles into the design process, engineers can not only improve structural efficiency but also promote environmentally conscious practices, aligning with global sustainability objectives.

REFERENCES

[1] Irwin, P.A. (2009). "Wind engineering challenges of the new generation of super-tall buildings." *Journal of Wind Engineering and Industrial Aerodynamics* **97**, 328-334.

[2] Task Committee for the Design and Performance of Tall Buildings for Wind. (2020). "Design and performance of tall buildings for wind." *American Society of Civil Engineers*.

[3] National Building Code of Canada (NBCC) (2005). Associate Committee on the National Building Code, National Research Council of Canada, Ottawa.

[4] International Organization for Standardization (2007). “Bases for design of structures - Serviceability of buildings and walkways against vibrations.” *International Standard*, ISO 10137.

[5] International Organization for Standardization (2009). “Wind Action on structures.” *International Standard*, ISO 4354.

[6] Berardi, L., Bagnara, A., Cammelli, S., Solari, G. (2018). “Review of the significance of cross-wind dynamic effects on tall- and supertall- buildings.” *Master Thesis*. University of Genova, Italy

[7] EN 1991-1-4 (2005).”Eurocode 1 – Actions on Structures, Part 1-4: General Actions – Wind Actions”. European Standards.

[8] Kim, Y.C., Tamura, Y., Tanaka, H., Ohtake, K., Bandi, E.K., Yoshida, A. (2014)."Wind-induced responses of super-tall buildings with various atypical building shapes." *Journal of Wind Engineering and Industrial Aerodynamics* **133**,191-199.

[9] Kim, Y.C., Xu, X., Yang, Q., Tamura, Y. (2019) . “Shape effects on aerodynamic and pedestrian-level wind characteristics and optimization for tall and super-tall building design.” *International Journal of High-Rise Buildings* **8**(4), 235-253.

DOI 10.5258/WES/P0046

Increasing high-fidelity modelling efficiency with automated setup and validation of methodologies

Matthew Coburn[1,2*], Zheng-Tong Xie[1]
[1]Faculty of Engineering and the Environment, University of Southampton
Southampton
[2]Royal Academy of Engineering
[*] E-mail: m.r.coburn@soton.ac.uk

1 INTRODUCTION

CFD requires a significant time investment to get accurate, realistic results. The task of the work undertaken here is to significantly reduce the time taken to conduct high-fidelity modelling of chemical plumes through the use of automation. In order to correctly model downstream dispersion, in particular near field dispersion, a good prediction of the flow field is important. Both convection and diffusion processes of the pollutants should be simulated accurately. Convection and diffusion are driven, in urban areas, by large and small turbulent eddies, respectively. Computational Fluid Dynamics (CFD), in the form of Large Eddy Simulation (LES) will be used to resolve the energetic eddies generated within the urban boundary layer. This will make use of Palm4U, an LES code designed for simulation of urban boundary layers. It is possible to run simulations at near real time with small grids (O(1m)) and suitable computing power. To drastically reduce the time required an automation tool will be created. This will include the entire setup process, which includes downloading terrain and building data, creating the mesh file, setting up boundary conditions and generating the required input files.

2 METHODOLOGY

In order to accurately predict downstream concentrations, particularly nearfield dispersion, an accurate prediction of the flow field is required, because the mean flow field and turbulence play significant roles in the downstream development and dispersion of plumes. Palm4U [1] will make it practically possible to adhere to the requirements for simulating urban flow fields, providing accurate results. LES in Palm4U is capable of running CFD simulations at close to, if not at real time, through the application of finite differencing over cartesian grids with horizontal uniform grid spacing, the use of the Fast Fourier Transform or multigrid approaches to solve the Poisson equation, and the use of the efficient synthetic inflow turbulence generation [2]. Palm4U can provide results comparable to that of FVM CFD codes such as OpenFOAM [e.g. 4-7].

In reducing total simulation time it was decided to create a tool to automate the meshing and setup of the simulations. When using Palm4U, setup and meshing time can amount to a significantly larger portion of the time taken to complete a simulation. Automating the procedure will significantly reduce overall time to complete a simulation from start to finish, while maintaining accuracy.

3 AUTOMATION TOOL

The aim of the current project will use Python to create the geometry used in the fluid domain from the Ordnance Survey (OS) BHA data set (Building Height Attribute). and OS 5m resolution terrain data. The code will then produce the _topo file (the topography of region to be investigated). To compliment topology creation, the setup tool creates the run files required by Palm4U. Palm4U requires 4 files to run a simulation. The control file (_p3d & _p3dr) contains runtime parameters, grid size and data output parameters. Inflow conditions (_iprf) provide vertical profiles of mean velocities, Reynolds stresses and integral length scales. Synthetic turbulence generation method [2] uses these profiles to generate inflow turbulence for LES. This part of the project will automate the entire setup and meshing of the simulation. In order to run, only these 4 files would need to be uploaded to an HPC facility or computer powerful enough to run the simulation.

3.1 Outline of the automation process

The current framework is to generate very-large scale geometries specifically for use in Palm4U. For example, Figure 1 shows a (16km by 16km) region of London, with a resolution of 5m. The axes here are grid index, specifically required by the _topo file. Interpolated regions are created to allow the flow

DOI 10.5258/WES/P0048

to develop and provide a smooth transition to the real terrain and buildings. This smoothing region is 1km in the coincident boundary normal direction. The contour is coloured by ALS (Above Sea Level) height (m). This methodology has shown success in creating geometries for current research projects, such as Bristol for the ASSURE project and the City of London for the FUTURE project. Results of which have been presented at the Urban fluid mechanics special interest group meetings [6].

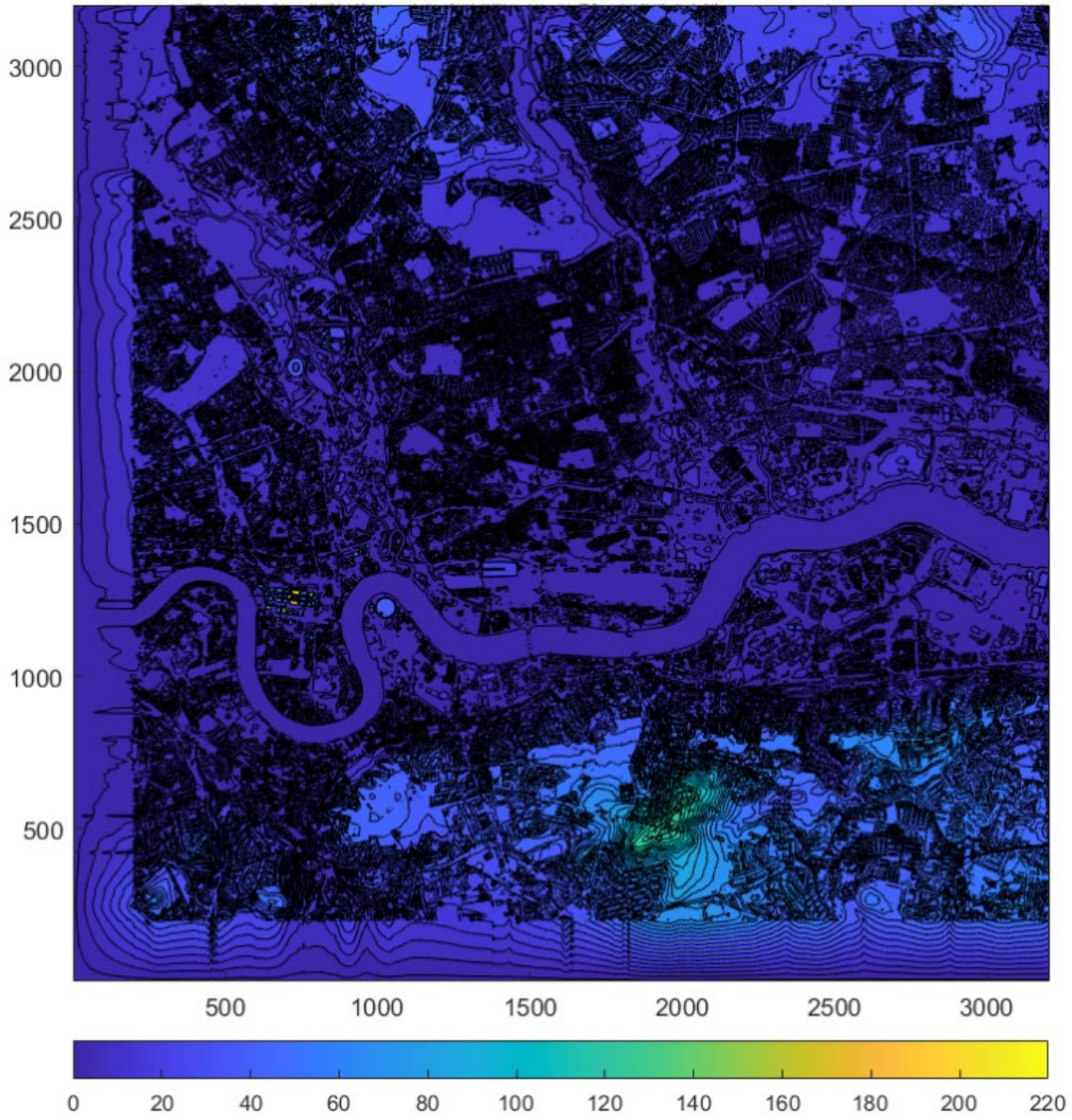

Figure 1: 16km by 16km region with a resolution of 5m, coloured by height (m) above sea level (ASL) for the region centered just north of London City Airport

The input of the data can be any resolution terrain data, here DTM 5 (Digital Terrain Model) with a 5m resolution is used, interpolated onto a 1m grid. The terrain within the domain is created first, which can also be used to compare the effects of buildings on the flow over complex terrain. Building heights are collected from the Ordnance Survey BHA data set (Building Height Attribute). To add buildings, a small region around each building is created, if the building is present within a certain cell, the absolute height of the building is applied to the terrain cell. It is possible to define a minimum, maximum or range of heights for buildings included. This is important when analyzing the effect of building heights. The terrain can also be altered through a multiplying factor to assess the impact of terrain height on flow

DOI 10.5258/WES/P0048

within and above the urban canopy [4,7]. The output is interpolated onto a grid with resolution required for simulation.

One of the challenges of CFD for urban atmospheric flows is the inflow conditions. The wind direction within the urban boundary layer usually changes significantly within short time scales, e.g. 15 minutes [8]. This makes modelling scalar dispersion difficult due to the increased horizontal spreading of the plume, which decreases the mean concentrations downstream, but increases the width of the plume.

3.2 Current Progress

The automation tool take lat/long data for finding the domain centre and defining which buildings are to be included within the domain. The code automatically converts lat/long to eastings/northings and loads the appropriate terrain and building data from the database. Once the grid size is selected, the code then interpolates the terrain data on the new grid with the chosen domain size and resolution. The building creation uses a search function to check which grid points are within the building's perimeter. The cells within the perimeter have the building's ASL height applied to them. The terrain array and building array is rotated separately if required, and a method is used to rotate the buildings without interpolation, so that the plan area of all buildings are conserved and no data is lost.

A GUI has been created to make the input of data simple, fast and efficient. The GUI allows for users with less experience to utilise Palm4U with appropriate setup parameters, inflow conditions and grid sizes, as these are preselected within the code. The GUI displays the final topography files so that no extra steps are required to check the created topography.

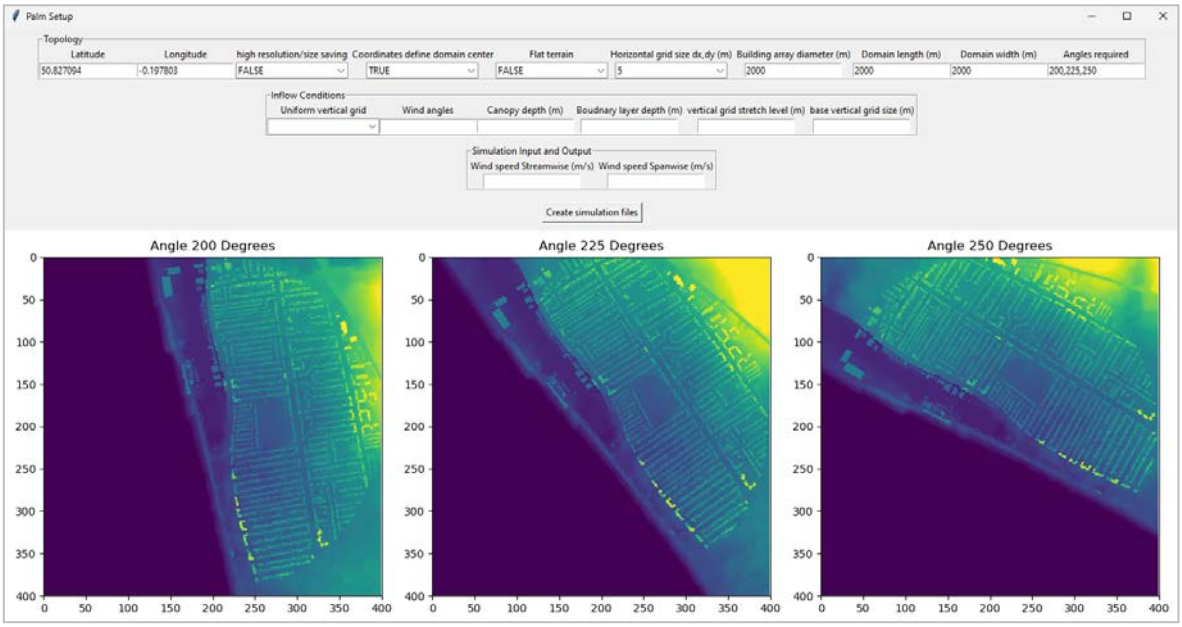

Figure 2: PALM4U Setup tool GUI, post topology creation, showing the three wind angles requested (wind is left to right in each image)

4 PLANNED WORK

The final work package of the 2-years project combines the approaches to carry out a case study to demonstrate the new capability. Field study data (e.g. ASSURE project) will be used to compare to the final data set created using the data driven approach. Dispersion data from field studies are available for Southampton [3] and Bristol [6,9], both from sensor networks. These data sets will be used to validate the methodology proposed here. The data generated through DA will be used to assess the uncertainty of the upstream wind direction compared with the field study results.

Data assimilation has been used to gain knowledge of upstream boundary [10]. Thus it will be possible to quantify the uncertainty in applied boundary conditions. This will lead to a more accurate representation of the upwind condition and thus a more accurate representation of a real world scenario

DOI 10.5258/WES/P0048

with a better prediction of downstream dispersion from the source release location. The results will be able to identify sharp changes in the local wind and scalar concentration from changes in the upstream wind direction.

ACKNOWLEDGEMENT

MC acknowledges a grant from Royal Academy of Engineering (ICRF2324-7-144), ZTX acknowledges a grant support from NERC (grant number NE/W002841/1).

REFERENCES

[1] Maronga et al.(2015) The Parallelized Large-Eddy Simulation Model (PALM) version 4.0 for atmospheric and oceanic flows: model formulation, recent developments, and future perspectives. *Geoscientific Model Development*, 8(8), 2515-2551.

[2] Xie ZT and Castro IP (2008) Efficient generation of inflow conditions for large eddy simulation of street-scale flows. *Flow, turbulence and combustion*, *81*, pp.449-470

[3] Bulot, Florentin MJ, et al. ((2019) "Long-term field comparison of multiple low-cost particulate matter sensors in an outdoor urban environment." *Scientific reports* 9.1 1-13.

[4] Coburn M (2023) "High fidelity modelling of neighbourhood-scale environments." *PhD Thesis,* University of Southampton.

[5] Coburn M, Xie ZT, and Herring SJ. (2022) "Numerical Simulations of Boundary-Layer Airflow Over Pitched-Roof Buildings." *Boundary-Layer Meteorology* 185.3: 415-442.

[6] Coburn M, Xie ZT, and Herring SJ (2022) "LES for wind environments and dispersion at Bristol City", Urban Fluid Mechanics Special Interest Group. https://www.urbanfluidmechanics.org/meetings/metofficereading-sept-1-2-2022.

[7] Coburn M et al. (2023) "Impact of Local Terrain Features on Urban Airflow." *Boundary-Layer Meteorology*, 189, 89–213.

[8] Xie, ZT (2011) Modelling street-scale flow and dispersion in realistic winds—towards coupling with mesoscale meteorological models. *Boundary-layer meteorology*, *141*, 53-75.

[9] Matthews JC (2024) Sensor measurements and large-eddy simulation of point source plumes over a complex urban terrain, *14th UK Conference on Wind Engineering*, Southampton, 4-6th September 2024.

[10] García-Sánchez, C., D. A. Philips, and C. Gorlé (2014) "Quantifying inflow uncertainties for CFD simulations of the flow in downtown Oklahoma City." *Building and environment* 78, 118-129.

DOI 10.5258/WES/P0048

Using a virtual Doppler LiDAR and Large Eddy Simulation to quantify wind velocity measurement errors of ground-based Doppler LiDAR

Author Name(s): Veronica Escobar-Ruiz[1*], Janet F. Barlow[1], and Zheng-Tong Xie[2]
[1]Meteorology Department, School of Mathematical, Physical and Computational Sciences, University of Reading, Reading, Berkshire [2]Faculty of Engineering and the Environment, University of Southampton, Southampton
[*] E-mail: v.escobaruiz@reading.ac.uk

1 INTRODUCTION.

Doppler Wind LiDARs (DWLs) are remote sensing instruments that emit a near-infrared laser pulse at a certain frequency and the frequency shift of the backscattered signal is used to calculate radial velocities along the line of sight of the lidar beam. The ability of DWLs to obtain wind profiles with height or horizontal distance and their relatively easy deployment makes them more popular compared with point measurements such as traditional anemometers [1]. However, DWL scanning techniques assume a homogenous horizontal wind vector over the sensed volume. In cities, this entails a great challenge mainly because the urban building canopy influences the homogeneity of the wind and turbulence [2]. Furthermore, depending on the application, care should be taken with the selection of scanning patterns and their configuration. In the most common scanning method, Velocity Azimuth Display (VAD – see Fig. 3), the beam is scanned around a cone centred on the zenith and is analysed to obtain a 2D vertical wind profile [3]; however, it requires a long time to complete the full 360° measurement and the mean wind vector is assumed to be horizontally homogeneous across the cone. Nonetheless, altering the configuration of the scan can compensate for errors in estimating wind velocity, including the number of beams in a single scanning cycle and the choice of averaging interval.

Large-Eddy Simulation (LES) models provide high spatial resolution unsteady wind velocity fields, allowing realistic turbulent motions. Hence, applying LES in urban environments represents a suitable method to estimate errors derived from different DWL scanning techniques. PALM is a parallelised LES model offering several components for application in urban environments to study atmospheric boundary layers [4]. A virtual Doppler Lidar (VDL) tool for PALM version 6.0 has been developed and applied over a homogenous flat surface ins an attempt to estimate errors related to the VAD scanning technique [5]. The VDL simulates a laser beam path and estimates radial velocities from gridded LES wind vectors over its trajectory. Applying this toolbox in a complex topography urban environment (e.g., Bristol, UK) can provide more insight into possible wind velocity errors in space and time related to the scanning techniques and the underlying flow field. Furthermore, comparing simulated wind profiles with one year of DWL field observations can be used as a form of validation of the VDL-PALM tool.

DWLs have been used in urban environments to provide information about air quality [6], wind speed [1] and knowledge of the urban boundary layer [7] which is useful for a more accurate weather forecast [8]. The city of Bristol (UK) was selected as a study area for the ASSURE Project (Across-Scale Processes in Urban Environments), given its compactness and unique topography. Here, a network of DWLs operating different scanning strategies was deployed in spring/summer 2024 at different locations to characterise the urban boundary layer across space and time. This research aims to: 1) explore errors in measured wind vectors under the VAD scheme, 2) assess VAD performance for measurement of a wind profile climatology under different atmospheric conditions, and 3) aid comparison between PALM simulations and ground-based DWL data, given the flow inhomogeneities caused by the topography. This paper describes the setup and methods for preliminary experiments that will be reported at the WES conference.

2 METHODS

2.1 Study area

The unique physical geography of Bristol, with the long Avon Gorge running from south-east to north-west and south-west to north-east valley in which the city centre lies, provides a suitably high level of complexity for the study of an urban boundary layer with significant topography. The ASSURE field observations comprise a network of five DWLs (Fig. 1) to capture vertical and horizontal wind variations

DOI 10.5258/WES/P0049

across the city. The sites comprise three ground-level locations, to the west (Fenswood Farm, BRFENS), and east (Digital Futures, BRDIFU and Pomphrey Hill, BRPOMP). The remaining DWLs are located on building rooftops, one on Bristol University Physics Building (BRPHYS) and one at the Tobacco Factory building in the city centre (BRTOBA). For this paper, we focused on simulating the BRTOBA DWL.

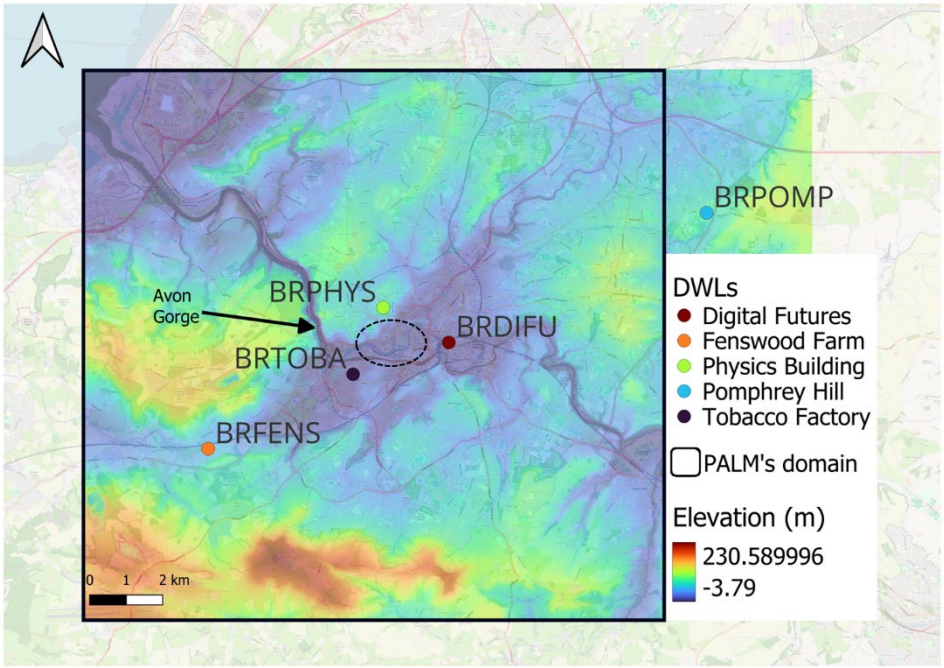

Figure 1, Location of the Doppler Wind LiDARs (DWLs)across Bristol, UK. The city centre is delimited by dotted lines and PALM's domain of 15 km x 15 km.
OpenStreetMap. © Crown copyright and database right 2010-2023.

2.2 Large-Eddy Simulation (LES) simulations and Virtual Doppler Lidar (VDL)

PALM [4] is a parallelized LES model that solves incompressible Navier–Stokes equations using the Boussinesq approximation. Turbulence closure of 1.5 order is used according to [9] for the parametrisation of subgrid-scale (SGS) terms. Discretisation of the domain is accomplished by using finite differences at horizontal-equidistant grid spacing, and time-stepping uses a combination of upwind-biased fifth-order differencing and third-order Runge–Kutta schemes.

Dirichlet or Neuman boundary conditions can be chosen for velocity components (u,v), potential temperature (θ), specific humidity (qv) and perturbation pressure (p^*) at the top and bottom of the domain. PALM follows Monin–Obukhov similarity theory (MOST) in which a constant flux layer can be assumed as a boundary condition between the surface and the first grid level where scalars and horizontal velocities are defined. For resolving solid obstacles (buildings and orography), the method given in [10] is used.

Model setup

The model domain size was 15x15x1 km^3 with a grid size of 5m (x-, y- and z-direction, Fig. 2). Topography in the model domain included buildings and orography of Bristol city. Synthetic turbulence generation (STG) [11] was used at the inlet. The dimensionless mean velocity and the Reynolds stresses for the STG method were obtained from EnFlo wind tunnel experiments in neutral conditions [12]. Along the y-direction, these were set as cyclic boundary conditions. On the bottom boundary, Neumann conditions were selected for the scalar and potential temperature, while for velocities, Dirichlet conditions were used. To consider the thermal stratification effects, a constant surface kinematic sensible heat flux was set on the bottom boundary, and a consistent potential temperature was set at the inlet. A roughness length of 0.1 m was chosen for our case [13]. The model was initialised by horizontally homogenous vertical profiles of temperature and passive scalar. The simulation was run for 2 hrs with a length of time step of 0.5 seconds.

DOI 10.5258/WES/P0049

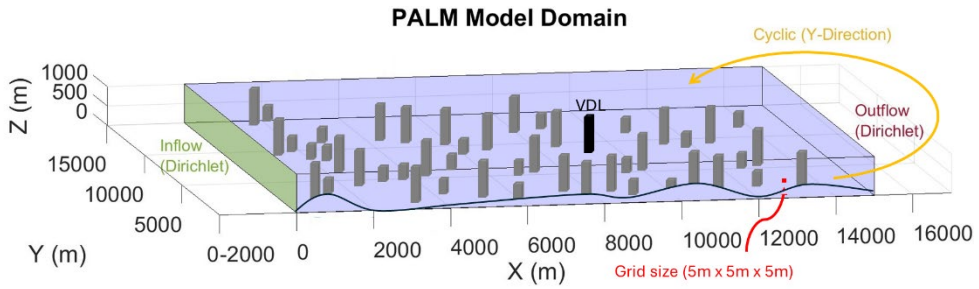

Figure 2, PALM model setup schematic. The Tobacco Factory building (BRTOBA) is represented by a black block in the middle of the domain where VDL is simulated. Topography in the model domain included buildings and the orography of Bristol.

Virtual Lidar

Implementing the VDL was possibly thought a code (user model) integrated with PALM, allowing the customisation of output variables. The VDL was previously developed to simulate VAD and DBS scanning patterns using three zenith angles and simulating different numbers of beams [5]. The VDL code calculates radial velocities from wind velocity data at LES grid points along the laser beam. An average of over 5 seconds of each beam is obtained which is analogous to the integration over several thousand laser pulses in real DWL systems, where a typical pulse repetition rate is around 10 – 20 kHz. Each scan takes 120 seconds to complete. Additionally, the VDL is located at the centre of the domain, and multiple scanning techniques can be run at the same time. For our study area, we adapted the VDL used previously by [5] to represent the field campaign scanning pattern at BRTOBA (see Table 2).

Table 2, Configuration of the Virtual Doppler Lidar scanning pattern (see also Fig. 3)

Scanning Method	VAD
Zenith Angle (∅)	75°
Azimuth Angle Increment (θ)	30°
Number of Beams	12
Time per beam (sec)	5
Cycles	2
Total duration scan (sec)	120

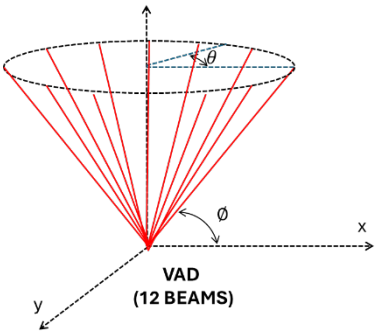

Figure 3, Schematic of the VAD scan technique at BRTOBA. Where ∅ is Zenith Angle, θ the Azimuth Angle Increment and the red lines represent the number of beams (12).

DOI 10.5258/WES/P0049

Error quantification

RMSD will be used to quantify differences between the vertical wind profile derived from a VAD scan using the VDL and the profile directly taken from PALM model values. In future planned work, the Root Mean Square Deviation (RMSD) will be used to compare the retrieved wind profile from the VDL against DWL-measured values for specific case studies. Preliminary results related to the above error quantification based on a single simulated event/scenario will be reported at the conference.

3 FUTURE WORK

Planned future work includes a) assessing LES accuracy against measured data to better simulate Bristol's urban environment, b) case studies of specific meteorological events observed during the ASSURE field campaign and c) simulation of a set of DWLs across the city using different scanning strategies related to the measurement DWL campaign.

REFERENCES

[1] Lane, S.E., Barlow, J.F., & Wood, C.R. (2013). ''An assessment of a three-beam Doppler lidar wind profiling method for use in urban areas'', *Journal of Wind Engineering and Industrial Aerodynamics*, **119**, 53-59.
[2] Drew, D.R., Barlow, J.F., and Lane, S.E. (2013). ''Observations of wind speed profiles over Greater London, UK, using a Doppler lidar'', *Journal of Wind Engineering and Industrial Aerodynamics*, **121**, 98-105.
[3] Werner, C. (2005). ''Doppler Wind Lidar'', *Lidar. Springer Series in Optical Sciences*, *Vol 102*. Springer, New York, NY.
[4] Maronga, B., Banzhaf, S., Burmeister, C., Esch, T., Forkel, R., Fröhlich, D., Fuka, V., Gehrke, K.F., Geletič, J., Giersch, S., Gronemeier, T., Groß, G., Heldens, W., Hellsten, A., Hoffmann, F., Inagaki, A., Kadasch, E., Kanani-Sühring, F., Ketelsen, K., Khan, B.A., Knigge, C., Knoop, H., Krč, P., Kurppa, M., Maamari, H., Matzarakis, A., Mauder, M., Pallasch, M., Pavlik, D., Pfafferott, J., Resler, J., Rissmann, S., Russo, E., Salim, M., Schrempf, M., Schwenkel, J., Seckmeyer, G., Schubert, S., Sühring, M., von Tils, R., Vollmer, L., Ward, S., Witha, B., Wurps, H., Zeidler, J., and Raasch, S. (2022). ''Overview of the PALM model system 6.0'', *Geoscientific Model Development*, **13(3)**, 1335-1372.
[5] Rahlves, C., Beyrich, F., and Raasch, S. (2022). ''Scan strategies for wind profiling with Doppler lidar – an large-eddy simulation (LES)-based evaluation'', *Atmospheric Measurement Techniques*, *15(9)*, 2839-2856
[6] Davies, F., Middleton, D.R., and Bozier, K.E. (2018). ''Urban air pollution modelling and measurements of boundary layer height'', *Atmospheric Environment*, **41(19)**, 4040-4049.
[7] Halios, C.H., and Barlow, J.F. (2018). ''Observations of the Morning Development of the Urban Boundary Layer Over London, UK, Taken During the ACTUAL Project'', *Boundary Layer Meteorol*, **166(3)**, 395-422.
[8] Banks, R.F., Tiana-Alsina, J., Rocadenbosch, F., and Baldasano, J.M. (2015). ''Performance Evaluation of the Boundary-Layer Height from Lidar and the Weather Research and Forecasting Model at an Urban Coastal Site in the North-East Iberian Peninsula'', *Boundary-Layer Meteorology*, **157(2)**, 265-292.
[9] Deardorff, J.W. (1980). ''Stratocumulus-capped mixed layers derived from a three-dimensional model'', *Boundary-Layer Meteorology*, **18(4)**, 495-527.
[10] Briscolini, M., and Santangelo, P. (1989). ''Development of the mask method for incompressible unsteady flows'', *Journal of Computational Physics*, **84(1)**, 57-75.
[11] Xie & Castro (2008). "Efficient generation of inflow conditions for large eddy simulation of street-scale flows", *Flow, turbulence and combustion*, ***81***, 449-470.
[12] Sessa, V., Xie, Z. T., & Herring, S. (2020). "Thermal stratification effects on turbulence and dispersion in internal and external boundary layers", *Boundary-Layer Meteorology*, ***176*****(1)**, 61-83.
[13] Stull (2012). *An introduction to boundary layer meteorology*. Springer Science & Business Media.

DOI 10.5258/WES/P0049

Sensor measurements and large-eddy simulation of point source plumes over a complex urban terrain

James C. Matthews[1], Matthew Coburn[2], M. Anwar H. Khan[1], Dudley E. Shallcross[1,3] and Zheng-Tong Xie[2]
[1]School of Chemistry, University of Bristol, Bristol, U.K.
[2]Faculty of Engineering and the Environment, University of Southampton, Southampton, U.K.
[3]Department of Chemistry, University of the Western Cape, Cape Town, South Africa.
* E-mail: j.c.matthews@bristol.ac.uk

1 INTRODUCTION

The deliberate or accidental release of toxic chemicals in a city can create a threat to public health [1], and therefore the understanding of the dispersion of pollutants through a city is important. A vehicle fire in Bristol, UK, has provided a real example measurement of pollutant dispersion [2,3]. Bristol City Council and University of Bristol measurement sites have seen an elevation of toxic metals, PM_{10} and CO after the vehicle fire.

2 MATERIALS AND METHODS

2.1 Incident and Measurement Site Locations

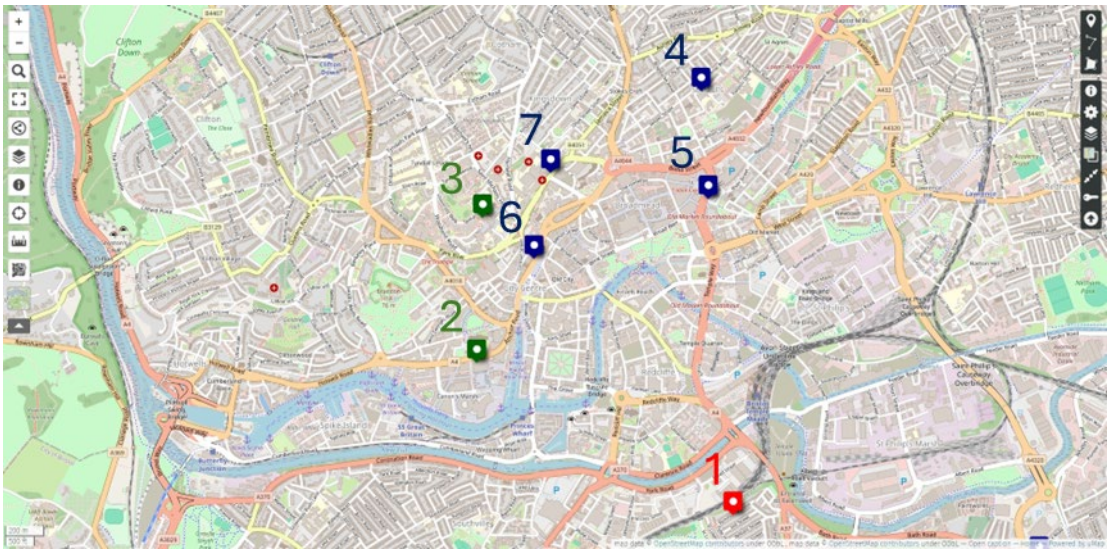

Figure 1, Map of Bristol indicating the position of (1) the car fire (2) the We The Curious measurement position (3) the Biomedical Sciences Rooftop anemometer and (4) the DEFRA AURN Air quality site at St Pauls and (5,6,7) the Bristol City Council air quality stations at Temple Way, Colston Avenue and Marlborough Street respectively. Map generated by OpenStreetmap using uMap © Openstreemap Contributors https://www.openstreetmap.org/copyright.

A vehicle was set alight in Totterdown, Bristol, on 13th January 2022 at 08:45 in the evening (all times UT) with the fire spreading to three other vehicles but extinguished by firefighters that evening [2,3]. The vehicle location was on a domestic street on top of a hill in a residential area (51.441684, -2.570497). Throughout 2021 and into January 2022, metals were sampled onto a quartz filter using a Sven Leckel LVS3 aerosol sampler in a 24-hour sample once a week at the We The Curious science museum (51.450487, -2.600856). The fire increased the level of pollutants measured in the PM_{10} sample; metals including lead, cadmium and chromium increased more than two standard deviations above the previous yearly average [4].

DOI 10.5258/WES/P0052

2.2 Pollutant and Meteorological Measurements

Throughout 2021 and early 2022, a measurement site was set up at We The Curious, Bristol, that recorded CO using a Thermo Scientific 48i TLE , and meteorology using a Gill Maximet throughout the period, with O_3 (Thermo Scientific 49i) added later in the year. Air samples were drawn from an inlet on a first floor balcony and sampled at 1 s intervals, later averaged to 1 hour. Zero checks were made every two hours and span measurements made monthly.

Bristol City Council have several air quality sites that measure NO_x and selected other pollutants. Within our study area, there is one Automatic Urban Monitoring Network site controlled by the UK government Department of Food and Rural Affairs (DEFRA) at St Pauls (51.462839, -2.5844834) [5] which measured O_3, NO_x, PM_{10} and $PM_{2.5}$. Three other sites are run directly by Bristol City Council at Temple Way (51.457968, -2.583975), Colston Avenue (51.455269, -2.5966489) and Marlborough Street (51.459142, -2.5954328) [6].

Wind measurements were made by a Gill GMX501 on the roof of the We The Curious science museum at 1 s sampling intervals, and on the roof of the Biomedical Sciences Building within the University of Bristol using a Gill Windmaster 3d sonic anemometer, measuring at 20 Hz and averaged to 5 s.

2.3 WRF-Chem chemistry simulations

The WRF-Chem-CRI model having a domain covering South and South West England with a 2 km x 2 km resolution and a size of 134 (E-W) by 146 (N-S) grid cells and 41 vertical levels was run from 11 January 2022 00:00 to 21 January 2022 18:00 LT. The meteorology, chemical boundary, biogenic emissions and anthropogenic emissions were adopted in the model from ECMWF ERA5 reanalysis data, WACCM forecast data, MEGAN model data, EDGAR v5.0 emission inventory, respectively.

2.4 Large-Eddy Simulations

In Bristol, field measurements are being compared with large-eddy simulations (LES) using a 15 km x 15 km domain to better interpret the results. Point source releases using inert tracers can be used to measure pollutant dispersion [7] and a tracer point source release in Clifton was compared to an LES point source release. A 5 km x 5 km area was chosen to incorporate the relevant local topography. The model was run in Palm4U, with hour initialisation, a release for 15 minutes and sample for 30 minutes, to align with experimental data. 3D Terrain elevation data was gathered from Ordnance Survey and a 4 km x 4 km area using LIDAR data at 1 m resolution is surrounded by digital terrain model data at a spatial resolution of 5 m, the 2 datasets were then merged.

3 RESULTS

Figure 2(a, b) shows the time series of CO and O_3 measured at We The Curious, PM_{10} measured at two Bristol AQ sites and a selection of metals sampled within 24 hour samples of PM_{10}. Figure 2(c) shows the pollutant metals between Thursday 6th January and Thursday 20th January, including the vehicle fire on 13th January. The CO measured at the We The Curious site was consistently between 100 and 200 ppm before the vehicle fire, and increased after the fire for the following week by several hundred ppm.

The PM10 measurements at the St Pauls and Temple Way air quality measurement sites also increased after the fire. Figure 2(d) shows the observed and WRF-Chem modelled CO and figure 2(e) shows the observed and modelled O_3 for a shorter time. The WRF-Chem model reproduces the variation of CO and O_3 at We The Curious with a reasonable agreement between mixing ratios in the modelled and measured data (biases -114 ppb and -0.25 ppb for CO and O_3, respectively). There is a large discrepancy between model-measurement data of CO during 13-14 January 2022, which could be possibly due to not including the car fire emissions in the model. The CO and Volatile Organic Compounds emitted from the car fire can have a significant impact on ozone levels, but the absence of these emissions in the model increases the discrepancy (bias: -10.7 ppb) between the model and measurement O_3 data during 14-15 January 2022. CO is mainly produced at the surface during incomplete combustion from anthropogenic activity and biomass burning. The car fire on 13 Jan 2022 9 pm can produce a significant amount of CO. Because of its long tropospheric lifetime (about 2 months), it can transport from the fire source to the monitoring station leading to a higher level than the background CO concentration. The

DOI 10.5258/WES/P0052

model underpredicts CO relative to measurement during 13 Jan to 15 Jan 2022 which is to be expected because the model did not include this point source in its emission inventory.

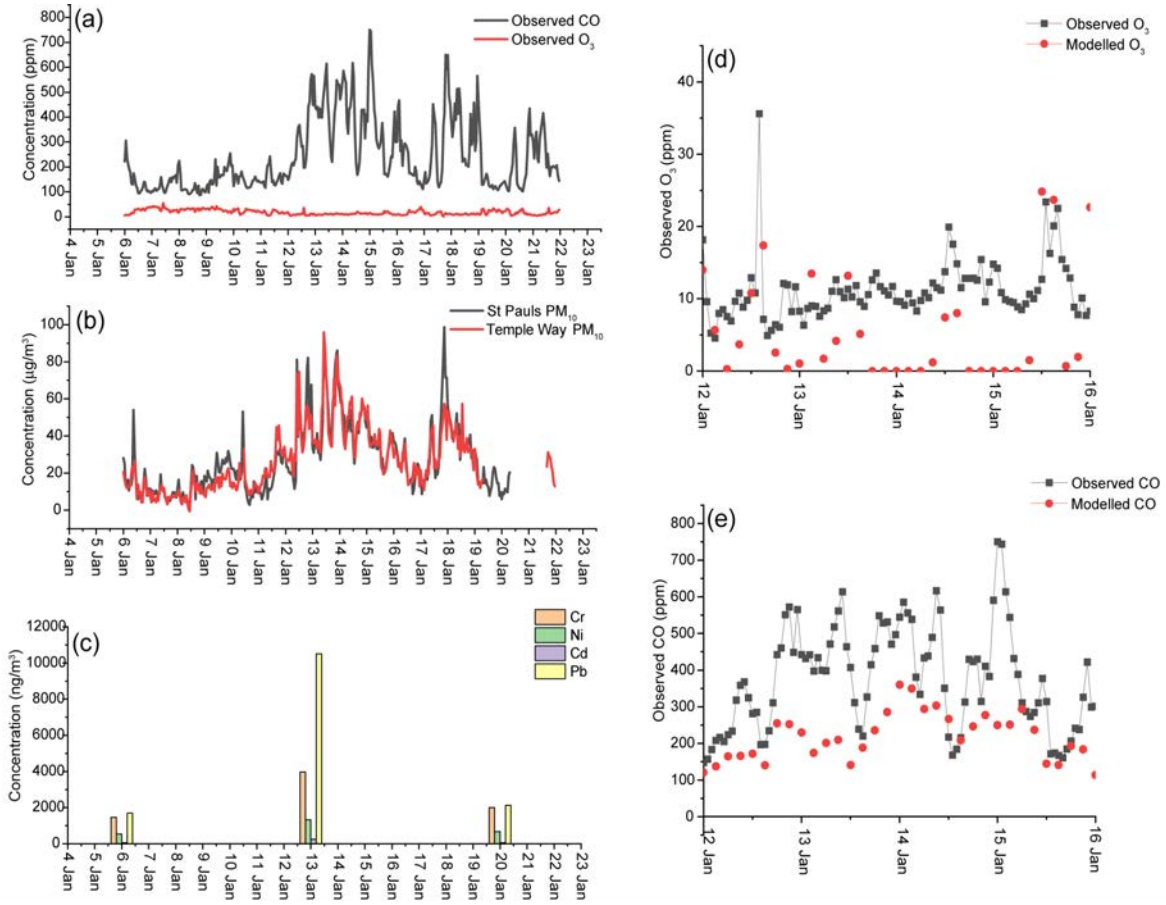

Figure 2, Time series of (a) CO and O_3 measured at We The Curious, (b) PM_{10} measured at two air quality stations and (c) metals bound to PM_{10} measured in 3 24 hour periods, and measurement and WRF-Chem model results of (d) CO and (e)O_3.

Wind speeds and direction on 13th January from the We The Curious weather station show a decrease to low wind speeds into the evening < 1 m/s with wind directions becoming more variable (figure 3). While the wind direction was consistent around SW for most of the day, by the time of the fires at 21:00 it has increased in variability and includes more northern winds. Low windspeeds can cause tracers of pollutant to spread in different directions to the predominant wind [7], and therefore CO as a long-lived pollutant produced by combustion could be seen throughout the city.

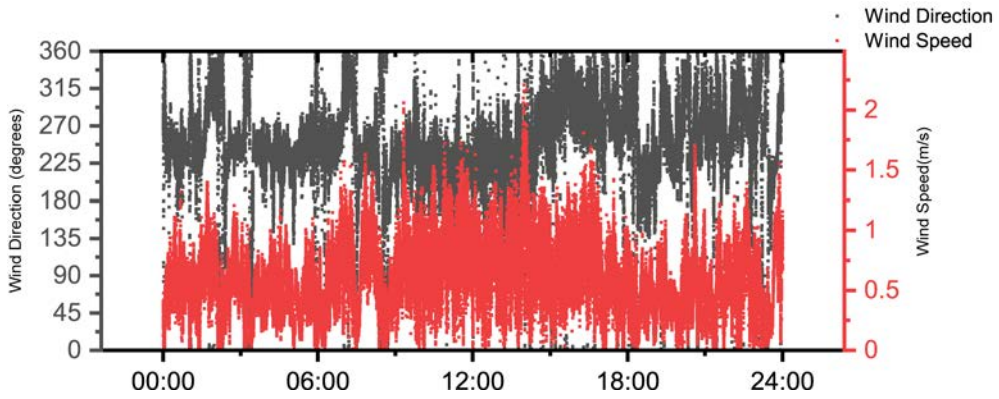

Figure 3, Wind direction (black) and wind speed (red) measured at 1 s sample interval from the roof of the We The Curious measurement site.

DOI 10.5258/WES/P0052

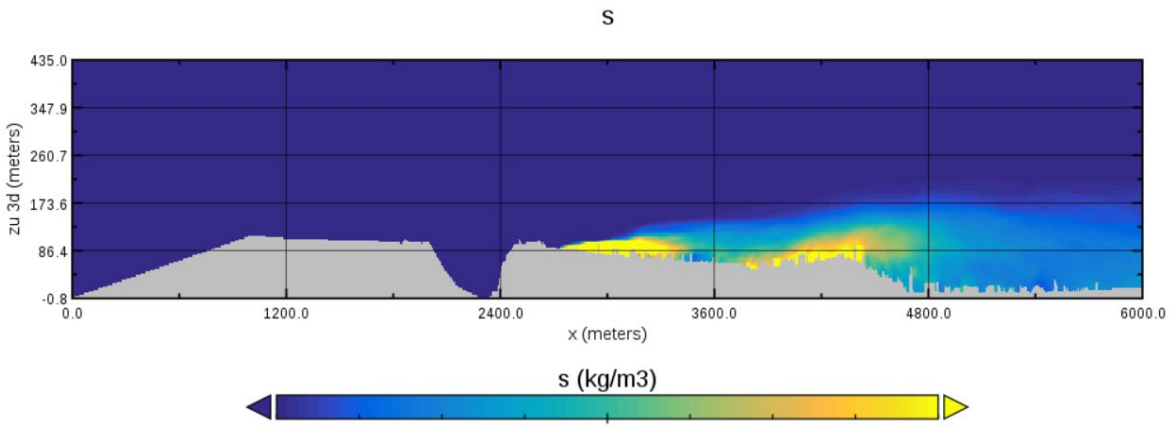

Figure 4, LES modelled source concentration along the source centre line

The LES simulation shown in figure 4 shows the mean concentration contour on the vertical plane across the source along the axial direction with a source release location at approximately 2700 m. The plume shows a second peak downstream likely due to the large buildings and the upslope from approximately 3800 m – 4400 m. The field data undercounts the model data significantly, but there is an evident correlation between the two.

4 CONCLUSIONS

A vehicle fire in South Bristol in January 2022 caused elevated levels of pollutants throughout the city, with CO remaining higher than modelled predictions after the fire had been extinguished. Wind speed and direction were such that pollutants did not clear the city and remained elevated for days after the event. LES simulations can show the importance of the city topography to pollutant dispersion.

REFERENCES

[1] Clements D., Coburn M., Simon J. Cox S.J., Bulot F.M.J. , Xie Z.T. & Vanderwel C. (2024). "Comparing large-eddy simulation and Gaussian plume model to sensor measurements of an urban smoke plume", *Atmosphere*, under review.

[2] https://www.bristolpost.co.uk/news/bristol-news/deliberate-arson-cited-cause-totterdown-6490065 last accessed 29th July 2024

[3] https://www.bristolpost.co.uk/news/bristol-news/police-investigating-totterdown-fire-after-6491602 last accessed 29th July 2024

[4] Matthews J., Khan A., Holland R., Perumal P., Laycock A., Elzein A. & Shallcross D. (2024). "Metal and PAH content in PM10 measured in Bristol in 2021" *EGU General Assembly 2024*, Vienna, Austria, 14–19 Apr 2024, EGU24-13554.

[5] https://uk-air.defra.gov.uk/networks/site-info?site_id=BRS8 Last Accessed 29th July 2024.

[6] https://experience.arcgis.com/experience/bcf5a6312bc04ffeb43db67cd57f5439 Last Accessed 29th July 2024.

[7] Matthews, J.C., Wright, M.D., Martin, D., Bacak, A., Priestley, M., Bannan, T.J., Silva, H.G., Flynn, M., Percival, C.J. and Shallcross, D.E. (2020). "Urban tracer dispersion and infiltration into buildings over a 2-km scale". *Boundary-Layer Met.*, **175**, 113-134.

DOI 10.5258/WES/P0052

Impact of Stably Stratified Boundary Layers on Tall Building Wake

Abhishek Mishra[1], Matteo Carpentieri[1], Alan Robins[1], Marco Placidi[1*]
[1] Centre for Aerodynamics and Environmental Flow, University of Surrey
Guildford, UK, GU2 7XH
[*] E-mail: m.placidi@surrey.ac.uk

1 INTRODUCTION

Tall building clusters are becoming an essential feature of urban areas. These tall buildings disturb the mass, momentum and heat exchange between the urban environment and the atmosphere [1], significantly affecting pedestrian wind comfort, local and macro-scale surface temperature, and pollutant dispersion [2-4]. The wake behind a cluster of tall buildings exhibits different flow behaviour, with near wake dominated by the building geometry, uniformly advected wake in the transition-wake region, and a global wake similar to that of a single building in the far-wake region [5].

Thermally-stratified flows are ubiquitous in the atmospheric flows. Most of the studies on this topic in the literature have focussed on convective conditions, as modelling of stably stratified cases becomes difficult because of intermittent turbulence, the limited size of the turbulent eddies and the generation of the gravity waves [6]. Stable stratification, although less frequently represented in the literature, is equally important in the atmosphere. Wind tunnel studies on urban arrays have shown that stable stratification leads to a reduction in Reynolds stresses, both inside and above the canopy [7]. The measurement of dispersion characteristics within and above a rectangular array of buildings aligned at 45^o to the wind direction has shown that the mean concentration inside the canopy for the stably stratified case can be twice that for the neutral case [8]. Numerical investigations of the effect of thermal stratification on flow over an urban canopy have found that there is a reduction in the drag and heat transfer coefficient as the flow characteristics change from thermally unstable to stable [9]. Study of stratified flow around a building is very limited, however under strong stratification the wake region of a single building is observed to increase [10].

Most of the stably-stratified flow studies have been focused on modelling the urban canopy layer. The study of the building wake is mostly limited to numerical work. The present study aims to understand the characteristics of the wake flows of a tall building exposed to neutral and stable atmospheric flow conditions using laboratory experiments.

2 METHODS

Wind tunnel experiments for the present study have been carried out in the EnFlo wind tunnel facility located at the University of Surrey. The tunnel's test section is 20 m long, 3.5 m wide and 1.5 m high, with a maximum inlet speed of 5 m/s. To attain the vertical thermal gradient, the inlet section is equipped with 15 power heaters stacked vertically. The power heaters are controlled independently so that the desired temperature profile can be achieved. The floor of the tunnel is cooled using recirculating chilled water and a positive vertical temperature gradient was imposed at the tunnel inlet to simulate stable stratification. A set of 7 Irwin spires of height 986 mm were used at the tunnel inlet to produce the boundary layer height (δ) of 1 m at $x = 14$ m from the inlet, where the building is placed for the measurement (Fig 1). The temperature difference between the floor (θ_{floor}) and the freestream flow (θ_{ref}) was kept to 16 ℃. The freestream velocities for neutral and stable cases were 2 m/s and 1.25 m/s, respectively. For the stably stratified case, the bulk Richardson number (Ri_δ) based on quantities at the boundary layer edge ($\delta = 1$ m) was approximately 0.23. The 3 components of velocity were measured using 3D laser Doppler anemometry in the streamwise (x), lateral (y) and vertical (z) directions in the wake of a building which is 60 mm in width (W_A), and 240 mm in height (H_B). The origin of the coordinate system was taken at the centre of the building onto the tunnel's floor, as shown in Fig 1. The vertical profiles were taken at the building centreline ($y = 0$).

DOI 10.5258/WES/P0054

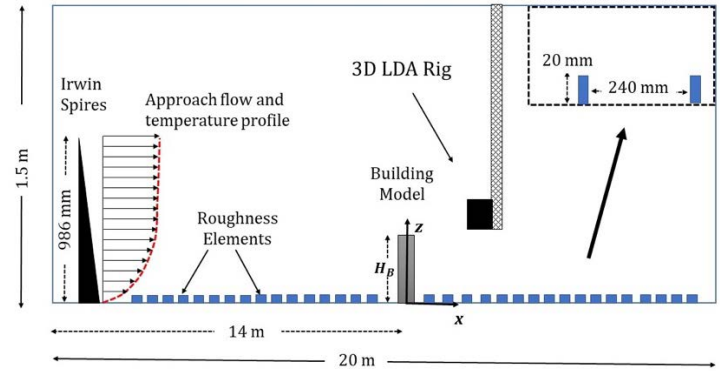

Figure 1: Schematic of the Enflo Wind Tunnel with the relative placement of Irwin spires, roughness elements, and building model.

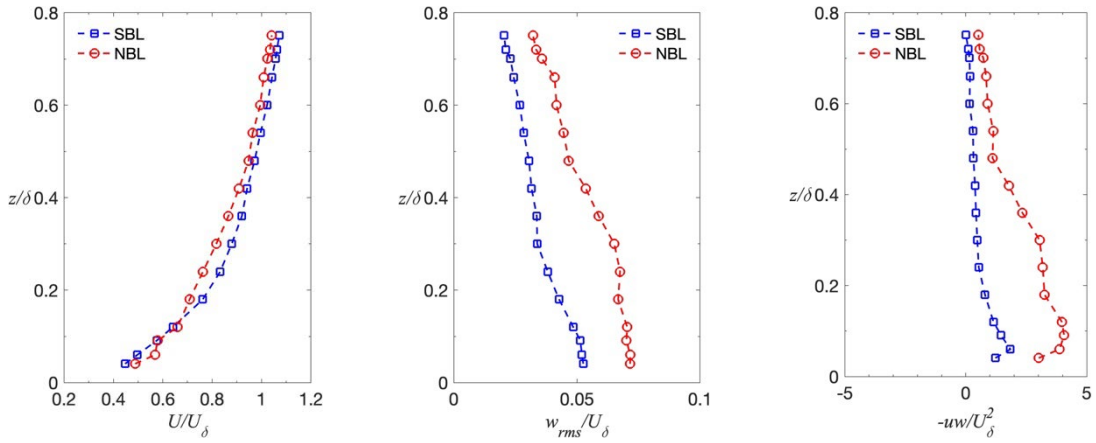

Figure 2: Comparison of flow characteristics between neutral and stably stratified boundary layer upstream of the building, (a) U/U_δ, (b) w_{rms}/U_δ, and (c) $-uw/U_\delta^2$.

3 RESULTS

Fig 2a compares the mean velocity profile, *U,* normalised with the freestream velocity (U_δ) of the approach flow for neutral and weakly-stable flow. The vertical height (z) is normalised with δ. The neutral boundary layer (NBL) is observed to be slightly thicker than that of the stable (SBL) flow, as expected. A comparable reduction in the normal stress (w_{rms}) and Reynolds shear stress (-uw) is also observed for the stable case (Fig 2b, c). The sharp reduction in the stress components in the weakly-stable case compared to the neutral case highlights the turbulence suppression by the buoyancy effects.

The presence of a building significantly changes the flow characteristics in the wake region for the stably-stratified case. Fig 3 compares the vertical profiles of wall-normal velocity (W) and Reynolds shear stress (-uw). The wall-normal distance (z) is normalised with the building height (H_B). Interestingly, W is greater in the SBL than in the NBL up to $x = 3.5W_A$ behind the building, suggesting a higher upwash of the flow from near the ground (Fig 3a and b). This difference subsides for $x = 7.5W_A$ (Fig 3c). For weakly stratified flows, the mechanical turbulence generated by the presence of the building dominates over the suppression caused by the thermal effects. Numerical studies on the effect of stability on the flow around a cubical building have also reported the dominance of shear-generated turbulence for weakly stratified flows [11]. This behaviour is better illustrated by the Reynolds shear stress variation along different

DOI 10.5258/WES/P0054

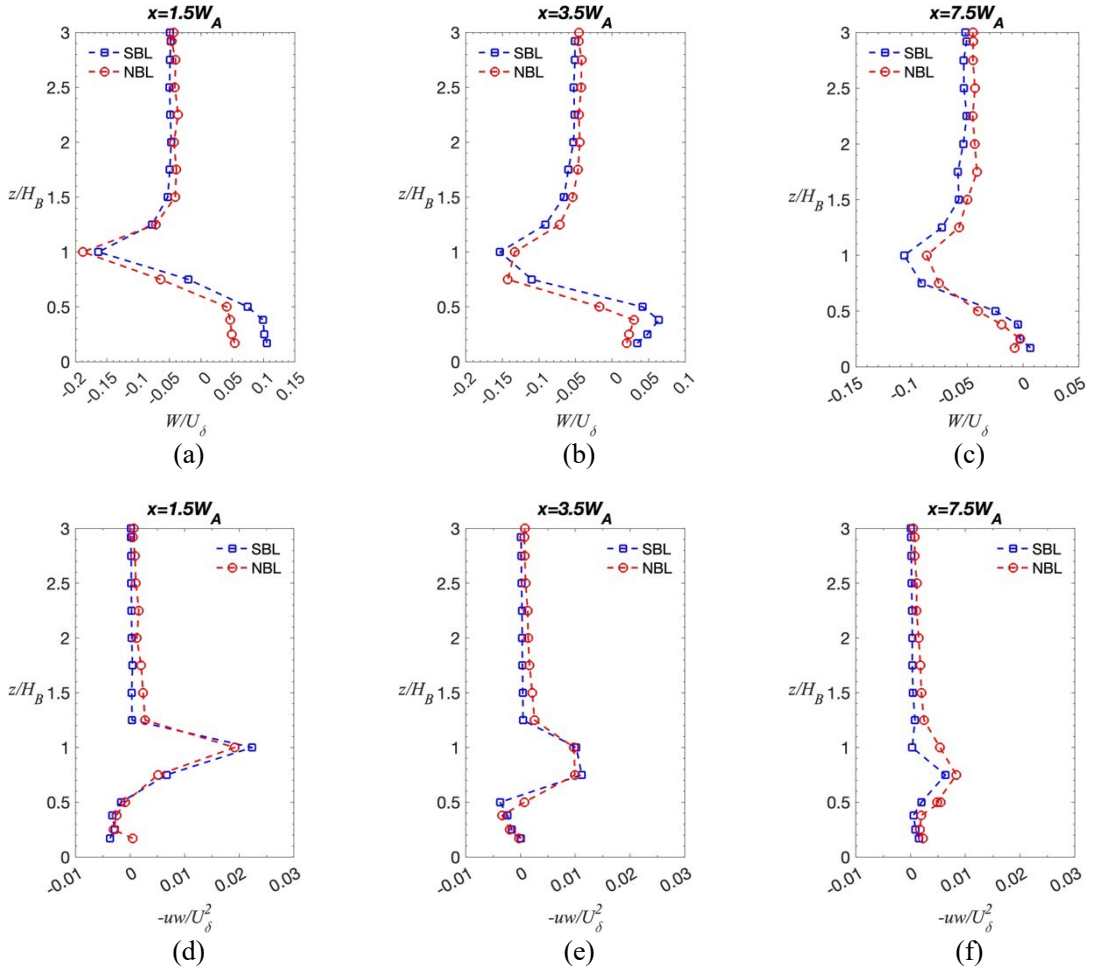

Figure 3: Comparison of vertical wake profiles of a single building in the neutral and stable boundary layer, W/U_δ (a, b, c) and $-uw/U_\delta^2$ (d, e, f).

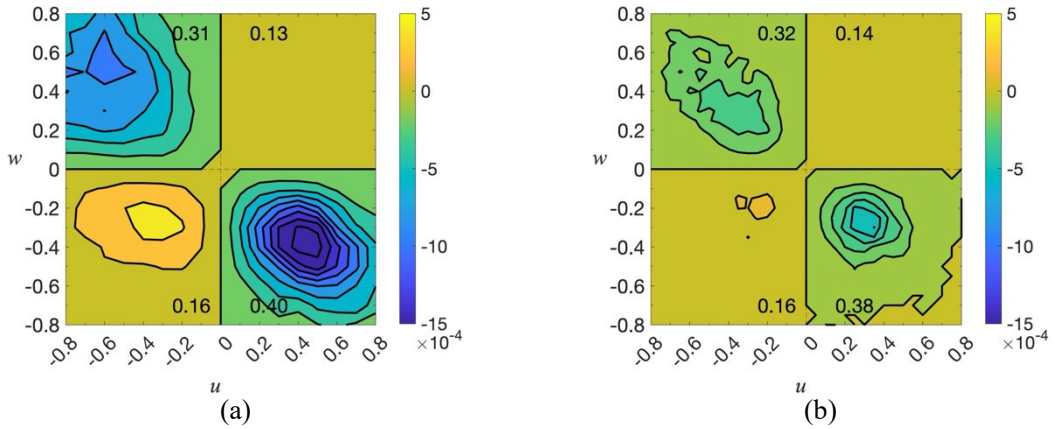

Figure 4: Weighted joint probability distribution function, $uwP(u,w)$, at $z=H_B$ and $x = 1.5W_A$ in (a) neutral boundary layer, and (b) weakly stable boundary layer.

streamwise locations, as shown in Fig 3d-f, which shed some interesting phenomena occurring in the near- and far-wake regions of the building. At $x = 1.5W_A$ and $3.5W_A$ (Figure 3d, e), the Reynolds shear stress variation is almost identical, further validating the dominance of shear-generated turbulence in this region. A slight difference is discerned at $x = 7.5W_A$ (Figure 3f). The Reynolds shear stress for the stable case is smaller than that of the neutral case in the region $0.5 \leq z/H_B \leq 1.25$, highlighting the increasing

DOI 10.5258/WES/P0054

dominance of the buoyancy-driven turbulence suppression in the far region of the wake. Note that we do not have the data beyond $W_A = 7.5W_A$ to further validate this.
To understand the relative contribution of ejection and sweep motion in the wake of a single building, the weighted joint distribution function of streamwise and wall-normal velocity fluctuations (u and w, respectively) for both neutral and stable boundary conditions at $z=H_B$ and $x = 1.5W_A$ is plotted in Fig 4. This gives the relative contribution of each quadrant to the total Reynolds shear stress separately [12]. The probability of occurrence of each event is also reported in each quadrant for both cases. It is observed that ejection and sweep events are almost equally dominating in both cases. The sweeps are more dominant than the ejections, highlighting the downwash of the flow towards the ground. However, the pair of u and w that contribute the most to total stress are concentrated in a smaller region for the SBL case (Fig 4b), while they are more scattered for the NBL case (Fig 4a), though their magnitude is higher as discussed in Figure 3.

4 CONCLUSION

In the present study, we experimentally examined the effect of thermally stratified atmospheric flows on the wake characteristics of a single building using 3D laser Doppler anemometry. It was found that in weakly-stable flow, the mechanical turbulence generated due to the presence of a building dominates over the thermal effects in the near region of the wake. Interestingly, the upwash velocity at $x = 1.5W_A$ is increased when the flow is stably stratified. Quadrant analysis has shown that the probability of the downwash of the flow (sweep) is almost equal in both cases, further highlighting the relative dominance of mechanically generated turbulence over the buoyant production.

REFERENCES

[1] Baik, J. J., Park, S. B., & Kim, J. J. (2009). Urban flow and dispersion simulation using a CFD model coupled to a mesoscale model. *Journal of Applied Meteorology and Climatology*, *48*(8), 1667-1681.

[2] Makedonas, A., Carpentieri, M., and Placidi, M. (2021). Urban boundary layers over dense and tall canopies. *Boundary-Layer Meteorology*, 181:73–93.

[3] Fuka, V., Xie, Z.-T., Castro, I. P., Hayden, P., Carpentieri, M., and Robins, A. G. (2018). Scalar fluxes near a tall building in an aligned array of rectangular buildings. *Boundary-layer meteorology*, 167(1):53–76

[4] Lim, H. D., Hertwig, D., Grylls, T., Gough, H., Reeuwijk, M. V., Grimmond, S., & Vanderwel, C. (2022). Pollutant dispersion by tall buildings: laboratory experiments and Large-Eddy Simulation. *Experiments in Fluids*, *63*(6), 92.

[5] Mishra, A., Placidi, M., Carpentieri, M., & Robins, A. (2023). Wake Characterization of Building Clusters Immersed in Deep Boundary Layers. *Boundary-Layer Meteorology*, *189*(1), 163-187.

[6] van Dop, H., & Axelsen, S. (2007). Large eddy simulation of the stable boundary-layer: A retrospect to Nieuwstadt's early work. *Flow, turbulence and combustion*, *79*, 235-249.

[7] Marucci, D., & Carpentieri, M. (2020). Stable and convective boundary-layer flows in an urban array. *Journal of Wind Engineering and Industrial Aerodynamics*, *200*, 104140.

[8] Marucci, D., & Carpentieri, M. (2020). Dispersion in an array of buildings in stable and convective atmospheric conditions. *Atmospheric Environment*, *222*, 117100.

[9] Boppana, V. B. L., Xie, Z. T., & Castro, I. P. (2014). Thermal stratification effects on flow over a generic urban canopy. *Boundary-layer meteorology*, *153*, 141-162.

[10] Liu, Z., Li, W., Shen, L., Han, Y., Zhu, Z., & Hua, X. (2021). Numerical study of stable stratification effects on the wind over simplified tall building models using large-eddy simulations. *Building and Environment*, *193*, 107625.

[11] Zhang, Y. Q., Arya, S. P., & Snyder, W. H. (1996). A comparison of numerical and physical modeling of stable atmospheric flow and dispersion around a cubical building. *Atmospheric Environment*, *30*(8), 1327-1345.

[12] Wallace, J. M. (2016). Quadrant analysis in turbulence research: history and evolution. *Annual Review of Fluid Mechanics*, *48*(1), 131-158.

DOI 10.5258/WES/P0054

Pollutant Dispersion and Bimodality in Tall Building Clusters

Dianfang Bi[1], Abhishek Mishra[1], Marco Placidi[1], Alan Robins[1], Matteo Carpentieri[1*]
[1]Environmental Flow Laboratory (EnFlo), School of Mechanical Engineering Sciences, University of Surrey
Guildford, Surrey, GU2 7XH, UK
[*] E-mail: m.carpentieri@surrey.ac.uk

1 INTRODUCTION

While tall buildings (TBs) are essential for sustainable city planning and efficient space management [1, 2], they also pose significant challenges regarding the dispersion of harmful pollutants from various sources, such as industrial sites and residential areas [3]. The interaction between the TB cluster and atmospheric boundary layers creates varied dispersion characteristics, which are not yet fully understood [4].

Investigations into the effects of single wall-mounted cylinders, representing individual buildings, have demonstrated the significant impact of shape on aerodynamic and pollutant dispersion characteristics [5, 6]. These studies reveal that TBs considerably influence flow and dispersion, enhancing vertical and lateral plume movement [7]. In homogeneous low-rise building arrays, plume dispersion retains a Gaussian form laterally and a reflected Gaussian form vertically, influenced by building geometry and atmospheric conditions [8].

In real urban settings, non-uniform canopies create complex roughness sublayers that significantly alter airflow and pollutant dispersion [9]. Research on TB clusters as 2D or 3D bluff bodies has focused on aerodynamic characteristics, wake formation, and the phenomenon of bleeding, which affects drag and wake dynamics [10]. As the solidity ratio of the TB cluster increases, wake formations elongate, canopy height increases and both advective and turbulent vertical scalar transport are enhanced.

A previous study by our group investigated wake flow behind varying building clusters, revealing distinct wake characteristics in near-, transition-, and far-wake regimes [11]. This paper extends that work by focusing on how building width W_B influences dispersion characteristics. Section 2 details the experimental setup, Section 3 presents the results, and Section 4 concludes the paper.

2 EXPERIMENT SETUP

The experiment was conducted in the EnFlo wind tunnel at the University of Surrey, with a working section of 20 meters in length, 1.5 meters in height, and 3.5 meters in width. To simulate the atmospheric boundary layer, Irwin spires were placed at the tunnel entrance, creating a boundary layer thickness of 1 meter. The tunnel floor featured a 50% staggered array of rectangular roughness elements to mimic urban conditions.

Building cluster models consisted of wooden cylinders with square cross-sections, each 60 mm wide (W_B) and 240 mm high (H_B), giving an aspect ratio (AR) of 4. The spacing between buildings (W_S) was set at $0.5W_B$, $1W_B$, and $3W_B$, all centrally positioned on a circular turntable 14 meters from the tunnel inlet. Velocity measurements were taken using a three-component Laser Doppler Anemometry (LDA) system with laser wavelengths of 532 nm, 552 nm, and 561 nm. The flow was seeded with sugar particles averaging 1 μm in diameter. Measurement duration at each point was 60 seconds, with a minimum acquisition frequency of 100 Hz. The free stream velocity was 2 m/s, measured by a sonic anemometer located 5 meters from the inlet. For dispersion experiments, propane was released from a ground-level circular source at the cluster centre. Concentrations were measured using a fast-response Flame Ionization Detector (FFID) positioned 5 mm downstream of the LDA measurement volume. Concentrations were sampled at 1000 Hz and averaged over 60 seconds, maintaining standard errors below 5% for mean values and below 10% for variance values.

DOI 10.5258/WES/P0055

3 RESULTS

Building spacing significantly influences plume development from a ground-level source at the cluster centre, as illustrated by the lateral mean concentration profiles at the mid-height of the building cluster ($z/H_B = 0.5$) in Figure 1. The concentration is non-dimensionalized by $\overline{c^*} = \bar{c}U_{ref}H_B^2/Q$, where U_{ref} is the reference velocity (freestream velocity measured by the sonic anemometer) and Q is the volumetric flow rate of the tracer gas.

Flow regions, near-, transition-, and far-wake, are classified based on the impacts of individual buildings as identified in [11]. In the near-wake region, separate wakes form immediately behind the cluster, from the trailing edge to $W_A < 0.45$ (where W_A is the cluster width), and merge into a single wake in the transition region ($0.45 < W_A < 1.5$). In the far-wake region ($W_A > 1.5$), a large cluster wake forms, similar to that behind a single isolated building. Figures 1 illustrate the different dispersion behaviours observed in these regions. Coordinates are normalized by the building width W_B to facilitate comparison across different cluster sizes.

Dispersion characteristics vary across flow regions, with notable bimodality in the near-wake regions for different building spacings, as shown in Figure 1. Further downstream, bimodality transitions to unimodality beyond the transition-wake region. Unimodal profiles in the transition and far-wake regions show similar trends but with decreasing concentration magnitude and wider spread. Notably, the peak value of the mean concentration profile in the near-wake region exceeds those in the transition- and far-wake regions, potentially exacerbating air quality issues at higher elevations.

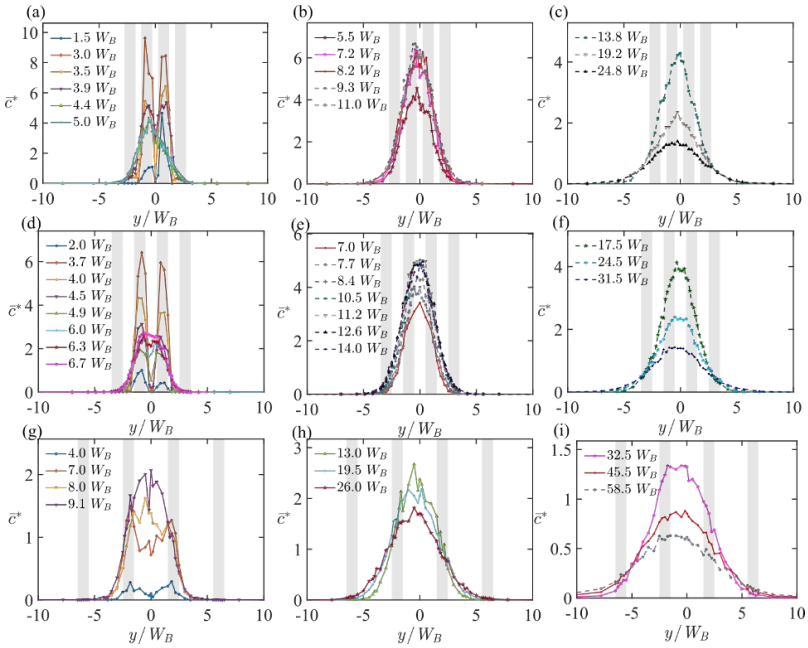

Figure 1, Lateral profiles of the mean concentration at $z/H_B = 0.5$ with three different building spacings: $W_S = 0.5W_B$ (subfigures (a) to (c)), $W_S = 1W_B$ (subfigures (d) to (f)) and $W_S = 3W_B$ (subfigures (g) to (i)). The shaded areas indicate the locations of the buildings

A non-parametric statistical approach, Hartigan's dip test [12], was used to analyse the multimodal characteristics of concentration profiles quantitatively. Due to the limited resolution of the original data, which were measured at discrete locations, a 20 × interpolation was applied, introducing 20 times the number of original data points between existing ones. Figure 2 shows the results of Hartigan's dip test of the different lateral concentration profiles along the streamwise direction at both the one-quarter and half height of the building cluster. Large dip values, indicating bimodality, are primarily observed in the near-wake region for clusters with small spacings ($W_S = 0.5W_B$ and $W_S = 1W_B$) at both $z/H_B = 0.25$ and $z/H_B = 0.5$. These dip values decline rapidly beyond the near-wake region, with only minor fluctuations and low values observed further downstream. For the wide spacing ($W_S = 3W_B$), the dip values approach zero for all streamwise locations at $z/H_B = 0.25$, with only small fluctuations observed at the mid-height of the cluster in the near- and transition-wake regions.

DOI 10.5258/WES/P0055

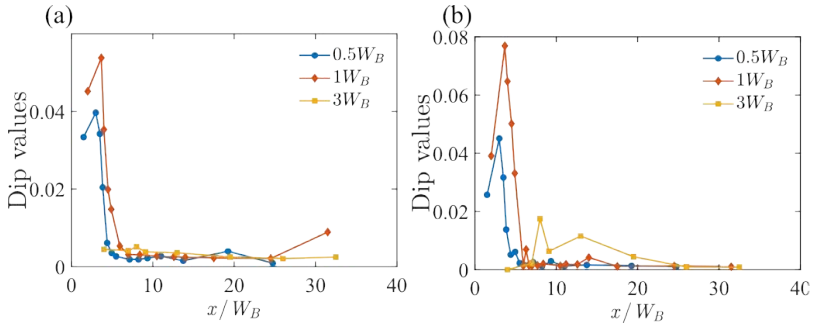

Figure 2, Hartigans' dip values at $z/H_B = 0.25$ and $z/H_B = 0.5$ for the three different building spacings.

To better quantify the effects of spacing on the plume depth, we applied Gaussian distribution fitting to the vertical profiles to determine plume boundaries. The plume boundary at each streamwise position was defined to enclose 90% of the total tracer particles, calculated by integrating the area under the fitted Gaussian curves:

$$90\% = \frac{\int_0^{y_u^*} \bar{c}^* dy^*}{\int_{-\infty}^{+\infty} \bar{c}^* dy^*} \tag{1}$$

where the denominator is the total pollutant tracer under the profile curve, and the numerator is the area enclosed by the upper boundaries y_u^*. Figure 3 shows that with increasing building width, the height of the plume in the far downstream decreases and approaches the plume development observed without any buildings. This indicates that the influence of the building cluster on the plume diminishes with wider spacing. Conversely, for the small spacing ($W_S = 0.5W_B$), the plume is lifted immediately after the cluster.

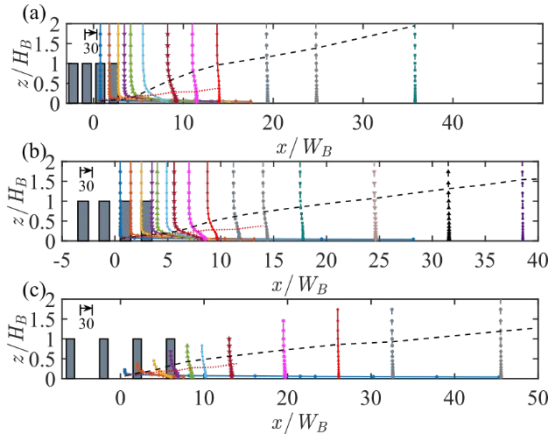

Figure 3, The vertical concentration profiles and the plume's vertical boundaries: (a) $W_S = 0.5W_B$; (b) $W_S = 1W_B$; (c) $W_S = 3W_B$. In each subfigure, the concentration profiles are shifted to the positions where they were measured, and the values are scaled down to 30 times the original values, for better visualization due to the relatively large values near the ground, especially for the measurement points near the source. The scaling magnitude is indicated by the arrow in the top left corner. The black dashed line represents the vertical boundary, and the red dotted line represents the results from an empty tunnel with no buildings for comparison.

In the vertical direction, Figure 4 displays the profiles of advective scalar flux ($\overline{w}\overline{c}^*$) and turbulent scalar flux ($\overline{wc}^*$) in the centre of the wake. For the narrow building spacing ($W_S = 0.5W_B$), $\overline{w}\overline{c}^*$ and $\overline{wc}^*$ have comparable magnitudes. As the building spacing increases, $\overline{w}\overline{c}^*$ decreases and even presents negative values for the cluster with $W_S = 3W_B$. This indicates that in denser clusters, pollutant particles are transported upward from the ground, resulting in higher pollutant levels at greater altitudes and a thicker plume depth. On the other hand, for the turbulent scalar flux ($\overline{wc}^*$), the maximum height of $\overline{w}\overline{c}^*$occurs near the canopy height and gradually decreases with wider building spacing.

DOI 10.5258/WES/P0055

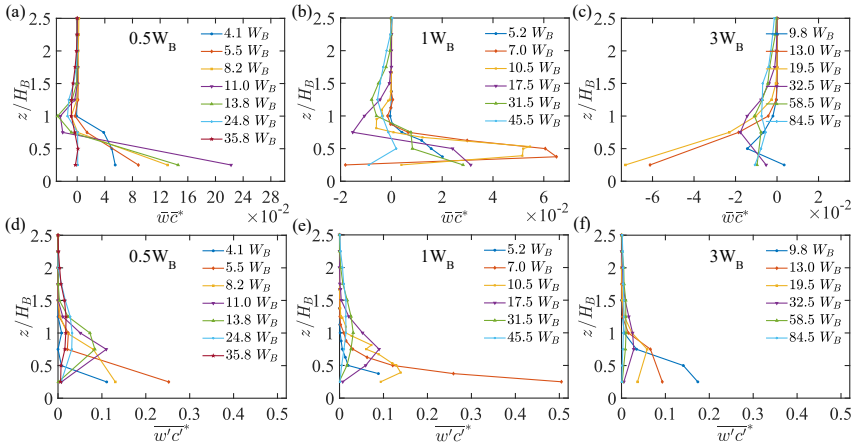

Figure 4, The vertical profiles of advective scalar flux $\overline{w}\overline{c}^*$ and turbulent scalar flux $\overline{wc}^*$ along the centreline of the building cluster.

4 CONCLUSIONS

This study investigates the influence of building spacing (W_S) on pollutant dispersion within tall building clusters. The results show that building spacing significantly impacts plume development and dispersion characteristics. Narrow building spacings ($W_S = 0.5W_B$) enhance vertical plume movement, resulting in higher pollutant levels at greater altitudes and thicker plume depths. In contrast, wider spacings ($W_S = 3W_B$) diminish these effects, leading to a more uniform plume development akin to scenarios without buildings. The use of Hartigan's dip test and Gaussian fitting effectively quantified the bimodality and plume boundaries, revealing that the dispersion complexity decreases with increased building spacing. These findings underscore the critical role of building configuration in urban pollutant dispersion and provide valuable insights for urban planning and air quality management.

REFERENCES

[1] T.R. Oke, G. M. A. C. and J. A. Voo. (2018). Urban Climates. Cambridge University Press.
[2] Brunekreef, B., Holgate, S.T., 2002. Air pollution and health. The lancet 360, 1233–1242.
[3] Cassiani, M., Bertagni, M.B., Marro, M., Salizzoni, P., 2020. Concentration fluctuations from localized atmospheric releases. Boundary-Layer Meteorology 177, 461–510.
[4] Britter, R.E., Hanna, S.R., 2003. Flow and dispersion in urban areas. Annual Review of Fluid Mechanics 35, 469–496.
[5] Wang, H.F., Zhou, Y., Chan, C.K., Lam, K.S., 2006. Effect of initial conditions on interaction between a boundary layer and a wall-mounted finite-length-cylinder wake. Physics of Fluids 18.
[6] Behera, S., Saha, A.K., 2019. Characteristics of the flow past a wall-mounted finite-length square cylinder at low reynolds number with varying boundary layer thickness. Journal of Fluids Engineering 141, 061204.
[7] Heist, D.K., Brixey, L.A., Richmond-Bryant, J., Bowker, G.E., Perry, S.G., Wiener, R.W., 2009. The effect of a tall tower on flow and dispersion through a model urban neighborhood: Part 1. flow characteristics. Journal of Environmental Monitoring 11, 2163–2170.
[8] Marucci, D., Carpentieri, M., 2020. Dispersion in an array of buildings in stable and convective atmospheric conditions. Atmospheric Environment 222.
[9] Wang, L., Li, D., Gao, Z., Sun, T., Guo, X., Bou-Zeid, E., 2014. Turbulent transport of momentum and scalars above an urban canopy. Boundary-Layer Meteorology 150, 485–511.
[10] Wangsawijaya, D.D., Nicolai, C., Ganapathisubramani, B., 2023. Scalar transport in flow past finite circular patches of tall roughness. International Journal of Heat and Fluid Flow 102, 109167.
[11] Mishra, A., Placidi, M., Carpentieri, M., & Robins, A. (2023). Wake Characterization of Building Clusters Immersed in Deep Boundary Layers. Boundary-Layer Meteorology, 189(1), 163-187.
[12] Hartigan, J.A., Hartigan, P.M., 1985. The dip test of unimodality. The Annals of Statistics 13, 70–84.

DOI 10.5258/WES/P0055

Cluster Effects of Tall Buildings

Saad Inam, Cung Nguyen, Changchang Wang, Davide Lasagna and Zheng-Tong Xie
Department of Aeronautics and Astronautics, University of Southampton
Southampton, UK
* E-mail: z.xie@soton.ac.uk

1 INTRODUCTION

Many cities around the world are growing rapidly and tall buildings are being constructed to accommodate the increase in population and commercial activities. These high, slender structures can affect the urban fluid dynamics environment e.g., street-level winds, pollutants, heat, and temperature. When tall buildings are clustered together, a much more complex flow may be observed in the near and far field due to the shedding of asymmetric vortices coupled with the mutual interactions of the individual buildings' wakes. The wake from a cluster of tall buildings lasts for a much longer distance than low-rise buildings and a single tall building [1-2]. In order to understand the wake flow structure of from a cluster of tall buildings, it is crucial to setup a domain much greater than the neighbourhood scale, along with a Reynolds number (based on the building width) greater than a critical threshold, i.e. Re $\approx 2\text{x}10^4$. Many wind tunnel facilities struggle to satisfy the requirement of a large domain due to the scale ratio constraint, suggesting that numerical simulations should play a crucial role for the studies of the cluster effect of tall buildings. These numerical simulations require high computational resources, and their accuracy is inevitably compromised depending on the size of urban area, number of tall buildings and spatial resolution.

The research reported in this paper is part of the project "Fluid Dynamics of Urban Tall building clUsters for Resilient built Environments (FUTURE)''. The present work expands the line of inquiry started in [2], which reported that the characteristic length scale for vortex shedding is close to cluster size of a 2x2 square cylinders in smooth inflow conditions. This phenomenon is known as the "cluster effect''. For instance, in a 45° wind, the dominant dimensionless vortex shedding frequency (i.e., the Strouhal number St) of a 2x2 cluster scaled by 2b is very close to that of a single square cylinder, where b is the cylinder width and the spacing is b. The study [2] raised 4 open questions, 1) whether this scaling could be applied to different numbers of cylinders with different spacings? 2) what is the role of the inflow turbulence? 3) whether this scaling could be applied to a group of finite-height square cylinders (idealised tall buildings)? 4) whether this scaling could be applied to real-life tall building cluster, e.g. the city of London. This paper aims to addressing the first two questions. A conclusive remark is drawn regarding the scaling of dominant vortex shedding frequency for different cluster sizes with various spacings. It also aims to shed light on the effect of free-stream turbulence (FST) as [3] commented that "There is not such an easy rule of thumb for the effects of the length scale". On-going studies [4] and [5] aim to address the third and fourth question above, respectively.

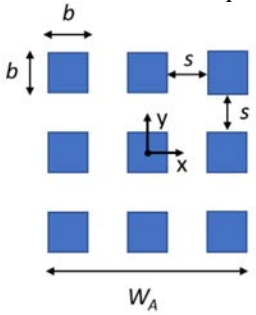

Figure 1 Plan view of the 3x3 cluster of square cylinders

2 COMPUTATIONAL SETUP

Several cases are considered, with 2×2, 3×3 and 4×4 clusters of square cylinders with dimensions of b×b×10b were simulated (Fig. 1), where the height of the cylinder is equal to domain height 10b. The Reynolds number is 6×10^6 based on the freestream velocity (U_∞ = 1m/s) and cylinder width (b=60m)

DOI 10.5258/WES/P0058

for smooth and turbulent inflows. A flow incidence angle α =45° and four spacings 0.5b, b, 1.5b, 2b were simulated. The open source code PALM [6] along with the synthetic inflow generation method [7] was used, which is a parallelized LES model for the atmospheric boundary layer. The audience is referred to [6] for more details, e.g. the governing equations and standard parameters. A periodic boundary condition was applied at the two lateral (north and south) boundaries, while Neuman (free slip) boundary condition was used for the top boundary. No-slip wall boundary condition was used for the bottom boundary including buildings. The computational domain size was 72b×120b×10b. A structured mesh was used, where the total number of cells is 1.06 billion.

3 CLUSTERS OF SQUARE CYLINDERS IN SMOOTH INFLOW

Nguyen et al. (2023) [2] reported that for a 2×2 array of square cylinders with spacing *b* at various flow incidence angles in smooth inflow, the Strouhal number *St* of the vortex shedding process can be scaled by a characteristic cluster size approximately equal to 2*b*. In other words, the shedding frequency is governed by the size of the solid part with such a spacing *b*. The question arises herein whether the characteristic cluster size still holds for other clusters of square cylinders with different spacings and number of cylinders.

First of all, the cluster size W_A is expressed as $W_A = nb + mrb$, where m is the number of spacings across the frontal column of cylinders, n is the number of frontal column cylinders, and r is the ratio of the street width *s* to building width b (Fig. 1). The ratio *r* can be re-written in the following form

$$\epsilon = r - 1 \tag{1}$$

In Eq. (1), ϵ is a small non-dimensional factor, varying from -0.5 to 1 for the spacing *s* from 0.5 to 2. The ϵ can be viewed as a correction factor for considering the cluster porosity (e.g. the total spacing to the physical cluster size W_A), based on the fact that the Strouhal number *St* is governed by the size *2b* of the solid part for a 2×2 array with a spacing *b* resulting in $\epsilon = 0$. From the above equations, a non-dimensional vortex shedding frequency for the cluster St is written as follows,

$$St = \frac{fnb}{U_\infty}\left(1 + \epsilon\frac{m}{n+m}\right). \tag{2}$$

This affirms that the shedding frequency can be scaled by an effective cluster size $W_e = nb(1 + \frac{\epsilon m}{n+m})$, as the primary shedding frequency of an array of infinite-height cylinders normalised by the effective cluster size W_e and the freestream velocity U_∞, i.e., the Strouhal number St, is very close to that of an isolated single cylinder. Equation (2) suggests that the cluster Strouhal number is mostly dependent on the solid part of the cluster, with a small correction required for various spacings.

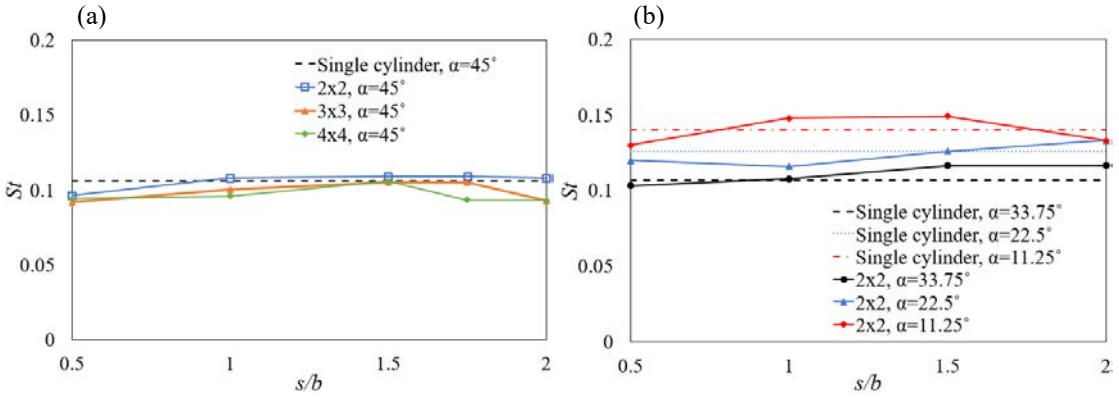

Figure 2. Strouhal numbers St for (a) the clusters of 2×2, 3x3 and 4x4 in smooth inflow flow for different spacings at $\alpha = 45^\circ$ and (b) the cluster of 2×2 cylinders at $\alpha = 33.75°, 22.5°$ and $11.25°$

Fig. 2a shows the cluster Strouhal numbers for a range of the spacings from 0.5 to 2, a range of

DOI 10.5258/WES/P0058

cylinder numbers and in a wind direction $\alpha = 45°$, compared to the isolated cylinder. The Strouhal numbers for the single cylinder and the cluster are almost the same, respectively. This further confirms that the shedding frequency can be scaled by the effective cluster width W_e. Fig. 2b shows the Strouhal numbers of the cluster of 2×2 square cylinders with various spacings in $\alpha = 33.75°, 22.5°$ and $11.25°$ winds, compared with those for isolated square cylinders (Mueller, 2012). Again, the Strouhal numbers for the cluster are almost the same as those for the isolated square cylinder, respectively.

4 CLUSTERS OF SQUARE CYLINDERS IN TURBULENT INFLOW

Table 1 shows the simulated clusters of 2x2 square cylinders in isotropic freestream turbulence (FST) inflows. The turbulence intensity was fixed at 20%, while the integral length scales varied from 1b to 8b.

Table 1. List of simulated clusters of 2×2 cylinders in isotropic freestream turbulence (FST). Turbulence intensity of 20% was specified at the inlet. ILS is the integral length scale. See Eq. (1) for *r*

Case	Size	*s* (*b*)	W_A	*r*	*ILS/b*
N2-1-FST-L1	2x2	1	3	1	1
N2-1-FST-L2	2x2	1	3	1	2
N2-1-FST-L4	2x2	1	3	1	4
N2-1-FST-L8	2x2	1	3	1	8
N2-2-FST-L1	2x2	2	4	1	1
N2-2-FST-L2	2x2	2	4	1	2
N2-2-FST-L4	2x2	2	4	1	4

Figure 3 shows the Strouhal numbers for different cluster configurations and for isolated square cylinders in FST with different isotropic integral length scales in various wind directions. It is evident that St decreases by increasing the eddy size, i.e, the integral length scale of the inflow turbulence. However, the reduction in St, compared to the smooth inflow, is small for the integral length scale smaller than the cluster size i.e., $2b$. For instance, for the 2×2 cluster case N2-1-FST-1 ($s = b, ILS = b$), St reduces to 0.1, whereas for the case N2-1-FST-8 with large integral length scale ($s = b, ILS = 8b$), the reduction in Strouhal number is more pronounced ($St = 0.088$). The latter case suggests that when the FST integral length scale is approximately three times the cluster size W_A, the Strouhal number St is reduced by up to 18%. It is important to note that the St number for spacing $2b$ is not reduced to a similar extent as observed for spacing b. This is due to the reduced ratio of the freestream integral length scale to the cluster size.

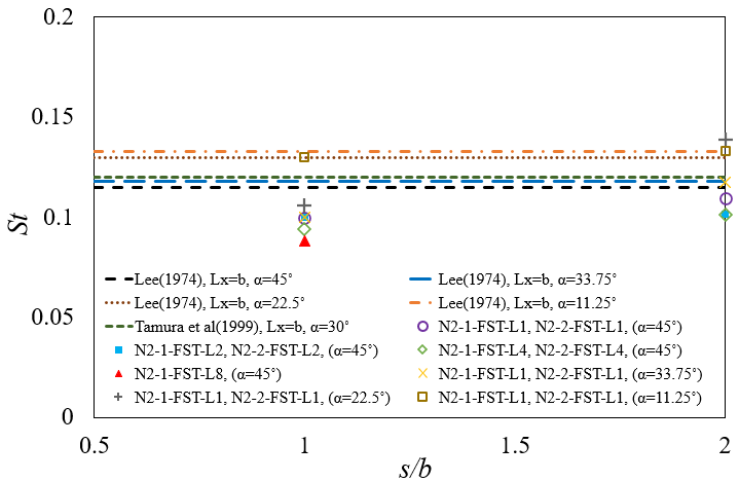

Figure 3. Strouhal number St for the clusters (dots) and for isolated cylinder (lines) for incoming FST for different flow angles and spacings

DOI 10.5258/WES/P0058

5 CONCLUSIONS

This paper investigates the aerodynamical cluster effect of arrays of 2x2, 3x3 and 4x4 square cylinders in smooth and turbulent inflow. Different spacings, i.e., s=0.5b, b, 1.5b, 2b were considered. The primary vortex shedding frequency of infinite height square cylinders can be scaled by the effective cluster size W_e= nb(1+ εm/(n + m)), where n and m are respectively the number of frontal column cylinders and the number of spacings across the frontal column of cylinders, and ε=s/b-1 is the small difference between the spacing (s) to building width (b) ratio and unity. Firstly, the primary shedding frequency of an array of finite-height buildings normalized by the effective cluster size W_e and the freestream velocity U_i, i.e., the Strouhal number St, was very close to that of an isolated single building. The consistency of the data suggests that the aforementioned scaling law can be used for the vortex shedding frequency and for assessing the resulting wake flow behind an array of tall buildings. Second, for incoming free-stream turbulence with a large integral length scale (i.e., greater than the cluster size), the dominant Strouhal number of the arrays of infinite height square cylinders is reduced evidently compared to the smooth inflow.

ACKNOWLEDGEMENT

The authors acknowledge a grant form EPSRC (grant number EP/V010514/1). The computations were carried out on the local computing system Iridis5 at the University of Southampton, and the national computing system Archer2.

REFERENCES

[1] Mishra et al. (2023). Wake Characterization of Building Clusters Immersed in Deep Boundary Layers. *Boundary-Layer Meteorology* 163–187.

[2] Nguyen, et al. (2023) Aerodynamics and wake flow characteristics of a four-cylinder cluster. *Flow, Turbulence and Combustion*, *110,* 1091-1115.

[3] Bearman and Morel (1983) Effect of freestream turbulence on the flow around bluff bodies. Progress in aerospace sciences, 20, pp.97-123

[4] Inam, et al. (2024). Vortex Shedding Frequency of Tall Building Arrays, *9th International Colloquium on Bluff Body Aerodynamics and Applications,* Birmingham, UK, August 2024

[5] Wang, et al. (2024). Turbulence and dispersion in the wake of the tall building cluster in the City of London. *In prep*

[6] Maronga et al.(2015) The Parallelized Large-Eddy Simulation Model (PALM) version 4.0 for atmospheric and oceanic flows: model formulation, recent developments, and future perspectives. *Geoscientific Model Development*, 8(8), 2515-2551.

[7] Xie and Castro, 2008. Efficient generation of inflow conditions for large eddy simulation of street-scale flows. *Flow, turbulence and combustion*, *81*, pp.449-470

DOI 10.5258/WES/P0058

Fluid dynamics of Urban Tall-building clUsters for Resilient built Environments (FUTURE)

Marco Placidi[1*], Matteo Carpentieri[1], Alan Robins[1], Zheng-Tong Xie[2], Davide Lasagna[2], Janet Barlow[3], Sue Grimmond[3], Omduth Coceal[3]

[1]Centre for Aerodynamics and Environmental Flow, University of Surrey, UK
[2]Aerodynamics and Flight Mechanics, University of Southampton, UK
[3]Department of Meteorology, University of Reading, UK
[*] m.placidi@surrey.ac.uk

1 INTRODUCTION AND BACKGROUND

Tall buildings are now ubiquitous in major cities to maximise the provision of housing and commerce. The mean wind field in the wake of a single 100m tall building (TB) can be significantly modified in a region about 500 m long and 300 m wide [1]; its impact on turbulence is even more significant [2], affecting pollutant dispersion and heat transfer. In the wake, the 'classical' description of the Urban Boundary Layer (UBL) no longer applies, severely restricting our ability to predict street-level winds, ventilation, and air quality. Furthermore, the impact of urban climate occurs at local (100m) and city (10km) scales; however, Numerical Weather Prediction models lack adequate representation of TB wakes because of their low spatial resolution, and Computational Fluid Dynamic scale simulations often lack a representation of the full meteorological processes (e.g. UBL scale, heating/cooling effects). Isolated buildings have been considered, but more challenging is the impact of clusters of TBs with complex wake interactions. Pilot numerical simulations around central London (Fig. 1a) highlight non-linear wake interaction effects around the TBs in the Barbican (x,y~1720m,1860m) and Gherkin clusters (x,y~2680m,1200m) in Fig 1b. Project 'Fluid dynamics of Urban Tall-building clUsters for Resilient built Environments' (FUTURE - EP/V010921/1) aims to investigate the issues above via laboratory and field experiments, numerical and analytical modelling.

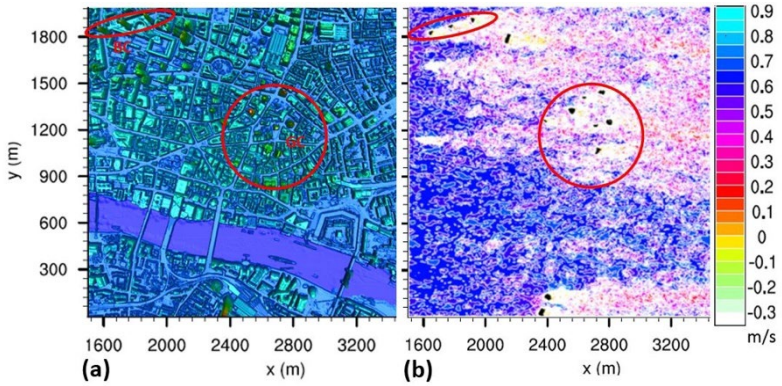

Figure 1, (a) CFD domain of the City of London with Barbican (red ellipse) and Gherkin (red circle) clusters. (b) Low-speed wake downstream of TBs at z=114m (instantaneous streamwise velocity - courtesy Z-T Xie). Flow left to right.

In summary, the aims of the project are:

1. To understand the magnitude/scale of the effects of a cluster of TBs on the UBL;
2. To identify the main parameters that govern the near and far fields within the wake;
3. To assess what can be said generically (i.e. modelled) and what remains site-specific;
4. To develop simplified (analytical) models to describe TB clusters' wakes;
5. To collate this information within a set of publicly available guidelines.

DOI 10.5258/WES/P0059

The project is led by the University of Surrey, academic partners in the Universities of Southampton and Reading and with City of London Corporation, DSTL, Met Office, and RWDI as project partners.

2 PRELIMINARY RESULTS

Though work has organically and synergistically involved all institutions/partners in delivering the aims discussed above, for presentation purposes, results and progress are reported herein per institution.

2.1 University of Surrey

Methodology

Laboratory experiments were conducted within the EnFlo laboratory, with most of the work carried out in the Meteorological EnFlo tunnel (working section 1.5 m × 3.5 m × 20 m). A combination of Irwin spires and wall roughness were used to replicate thick UBLs, while stable thermal stability was achieved by imposing an inlet temperature profile, while cooling the floor of the tunnel. The models are placed on a circular turntable to allow for different wind directions to be considered. 3-D laser Doppler anemometry, cold wire anemometry and thermistors, and fast flame ionization detectors are used to measure velocity, temperature and concentration fields, respectively.

Progress to date

Work has focussed on idealised arrays of TB clusters where different numbers of buildings, aspect ratio, spacing and cluster size (W_A), were considered in both neutral [3,4] and stable thermal conditions [5]. Data analysis has identified characteristic wake regimes (Fig. 2) in both mean [3] and turbulence quantities [4], and their link to dispersion patterns [6]. Alongside idealised cases, a more realistic City of London (CoL) geometry was also tested for comparisons. Data analysis is ongoing.

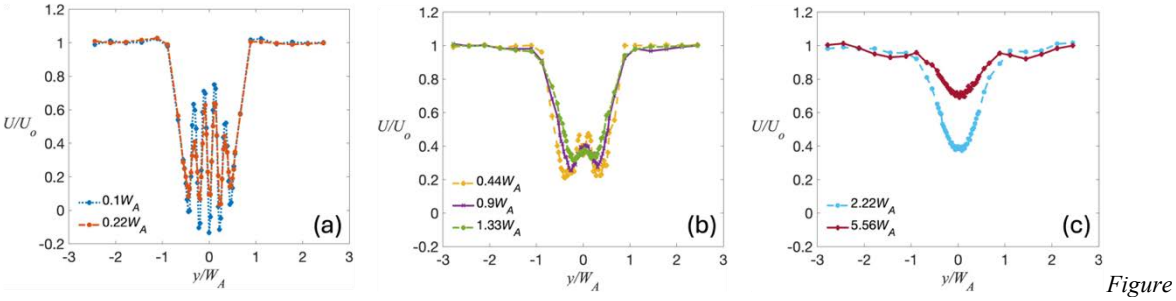

Figure 2, Wake lateral profiles of non-dimensional streamwise velocity, U/U_0, for a 5x5 array in the (a) near-wake regime, (b) transition-wake regime, and (c) far-wake regime. Adapted from [3].

2.2 University of Southampton

Methodology

Large-Eddy Simulations (LES) embedded in PALM [7] and OpenFOAM [8] were used for UBLs. Because the wake from a TB cluster can persist over long distances, large computations (e.g. up to 5 billion cells) were carried out on the national (Archer2) and local (Iridis5) supercomputing facilities, with an efficient synthetic turbulence generation [9] at the inlet. Thermal stratification was considered. An example LES domain is shown below in Fig. 3.

Progress to date

We have designed three types of LES geometries: 1) arrays of square cylinders [10,11]; 2) arrays of idealised tall buildings with a constant [12] and random height [13]; 3) an array of 17 tall buildings (i.e. CoL) [14]. The simulations [12-13] have been compared against the wind tunnel experiments. To date, we observed the following. Firstly, the slenderer buildings were less sensitive to the approaching wind direction as the integral length scale of the turbulence generated by slender TBs is significantly larger than for low-rise buildings. Secondly, for both incoming smooth and turbulent flows, the primary shedding frequencies for infinite height square cylinders, when appropriately scaled, is approximately the same as that of an isolated square cylinder. Thirdly, for incoming free-stream turbulence with an integral length scale greater than the cluster size, the dominant Strouhal number of the arrays of infinite height square cylinders is significantly reduced when compared to the smooth inflow. Finally, the cluster's

DOI 10.5258/WES/P0059

Strouhal number of the arrays of 2×2 finite height buildings is also governed by the effective cluster size despite the 3-D effect and the boundary layer interaction with the TBs.

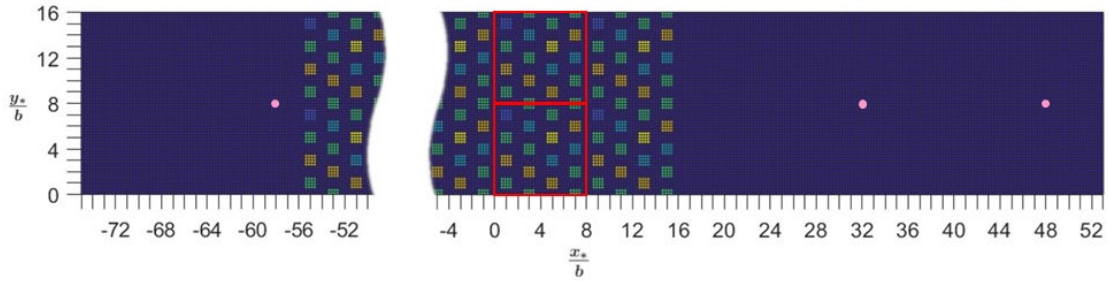

Figure 3: Streamwise-spanwise (x_*, y_*) LES domain with random height buildings (not to scale). Spatially averaged region is outlined in red. b represents the building width.

2.3 University of Reading

Work at Reading includes two separate efforts – fieldwork and simplified (analytical) modelling.

2.3.1 Fieldwork

Methodology

Following previous work studying isolated TB wakes using a Doppler Wind Lidar (DWL) in London, UK [15], wakes around two building clusters in Berlin, Germany (Fig. 4a) were studied using 2 DWLs in collaboration with the urbisphere project [16]. Observations took place from 28.6.22 to 19.9.22. At the SCHO site, a Halo-Photonic Streamline DWL was deployed on a rooftop at 87 m, and at the TUCC site, a Streamline XR DWL was on a rooftop at 80 m. Scans included regular Plan Position Indicator (PPI) at 0° elevation, giving a horizontal slice of the TB wakes at a fixed height (see Fig. 4b).

Progress to date

Analysis of PPI scans is ongoing, including boundary layer depth and vertical wind profiles measured using vertically-pointing scans. An ensemble averaging approach will be applied to instantaneous scans measured for similar wind directions and atmospheric conditions and assumed to be comparable to the relatively long time-averaged wakes measured in the wind tunnel. [15] have shown that a shorter wake was observed under unstable atmospheric conditions due to the stronger vertical mixing that reduced the velocity deficit. This was the case unless turbulence upstream of the building was enhanced (e.g. by the wake of another building). This stability dependence will be tested for TB clusters.

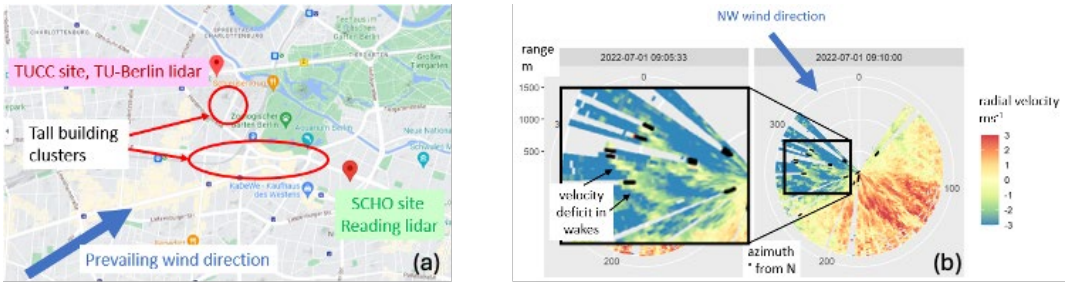

Figure 4: a) Location of DWLs used in urbisphere-Berlin experiment to study wakes around TB clusters (circled in red). b) example of PPI scan at 0° elevation from SCHO DWL, showing radial velocity. Flow coming towards DWL is blue (negative), away is red (positive). Wakes are visible as velocity deficits (yellow, near zero velocity).

2.3.2 Analytical modelling

Methodology

This work focuses on the development of simplified methods for modelling wind profiles in heterogeneous UBLs. Full solution of the PDEs governing the flow (e.g. LES) is expensive. Alternatively, an ODE with position-dependent coefficients can be solved, together with appropriate closure models. A different approach is to put the position dependence not in the coefficients, but in the index of fractional-order derivatives. In this way, the character of the differential equation does not vary spatially and the same solution method can be applied in different flow regimes. This provides a unified and economical treatment of the problem [17].

DOI 10.5258/WES/P0059

Progress to date

Perturbation methods have been developed to provide approximate analytical solutions for the different types of ODEs that emerge [18]. These will be applied and tested with the FUTURE datasets. In addition, a simple fractional order model has been formulated and solved numerically. Comparisons with three different test datasets are shown in Fig 5. With model coefficients fixed for a given geometry, the middle portion of the wind profile can be reproduced. A more sophisticated model is needed to resolve the regions close to the ground and canopy top.

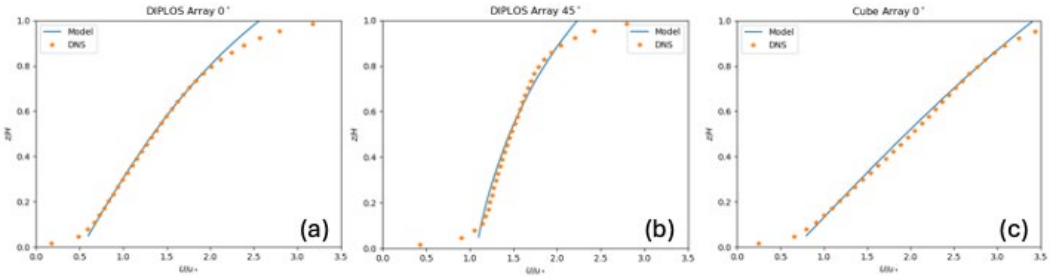

Figure 5: Examples of wind profile solutions of a fractional canopy model compared against DNS data for three different setups (a) cuboid array, 0° (b) cuboid array, 45° (c) cube array, 0°. Lines: model; circles: DNS data.

3 FURTHER INFORMATION

With the project end date of June 2025, work is still ongoing. For further information and up to date progress, please visit our website https://www.surrey.ac.uk/research-projects/future.

REFERENCES

[1] Hertwig et al. (2019). Wake characteristics of tall buildings in a realistic urban canopy. *Boundary-Layer Meteorol*., 172, 239-270.

[2] Goulart et al. (2019). Local and non-local effects of building arrangements on pollutant fluxes within the urban canopy, *Building Environ*., 147, 23-34.

[3] Mishra et al. (2023). Wake Characterization of Building Clusters Immersed in Deep Boundary Layers. *Boundary-Layer Meteorol.,* 189, 163–187.

[4] Mishra et al. (2024). Experimental Study of the Turbulent Characteristics in the Wake of Tall Building Clusters, *Flow*, *In Press.*

[5] Mishra et al. (2024). Effect of Stable Thermal Stratification on Flow around Tall Building Clusters. *In prep*.

[6] Bi et al. (2024). Dispersion characteristics in the wake of tall building cluster. *In prep*.

[7] Maronga et al. (2015). The Parallelized Large-Eddy Simulation Model (PALM) version 4.0 for atmospheric and oceanic flows: model formulation, recent developments, and future perspectives. *Geosci. Model Dev.*, 8, 2515-2551

[8] Weller, et al. (1998). A tensorial approach to computational continuum mechanics using object-oriented 715 techniques. *Computer in Physics* 12, 620–631.

[9] Xie & Castro (2008) Efficient generation of inflow conditions for large eddy simulation of street-scale flows. *Flow, Turbulence and Combustion*, *81*, 449-470.

[10] Nguyen, et al. (2023) Aerodynamics and wake flow characteristics of a four-cylinder cluster. *Flow, Turbulence and Combustion*, *110,* 1091-1115.

[11] Inam, et al. (2024) Effect of free-stream turbulence on wake flows of an array of square cylinders. *In prep*.

[12] Inam, et al. (2024). Vortex Shedding Frequency of Tall Building Arrays, *9th International Colloquium on BBAA,* Birmingham, UK, August 2024

[13] MacGarry, et al. (2024). Slenderness effects on the flow over an array of tall buildings with random heights. *13th International Symposium on TSFP*, Montreal, Canada. 25 - 28 Jun 2024.

[14] Wang, et al. (2024). Turbulence and dispersion in the wake of the tall building cluster in the City of London. *In prep*.

[15] Theeuwes, et al. (2024) Observations of tall-building wakes using a scanning doppler lidar, *preprint in Atmospheric Measurement Techniques*,

[16] Fenner, et al. (2024) urbisphere-Berlin campaign: investigating multi-scale urban impacts on the atmospheric boundary layer, *Bulletin of the AMS*

[17] Coceal (2024). A fractional model for the mean velocity profile within a canopy of roughness elements. *In prep.*

[18] Coceal, et al. (2024). Analytical solution methods for the mean wind profile in canopy flows. *In prep.*

DOI 10.5258/WES/P0059

CFD Methodology for Air Quality Assessment

Vincenzo Sessa[1*], Mingzhe He[1] & Steven Daniels[1]
[1]AKTII
London, United Kingdom
[*] E-mail: vincenzo.sessa@akt-uk.com

1 INTRODUCTION

The 'Air Quality Positive (AQP) approach' is a process of identifying and implementing measures on new developments in London to demonstrate how benefits to local air quality are maximised, and how pollution exposure is minimised [1]. To achieve the AQP target, new developments are pushed beyond compliance with Air Quality Neutral benchmarks and the requirements of the typical air quality assessment.

Dispersion models (i.e., ADMS) are widely used for air quality assessments in support of planning applications. These models are continuously being developed and also used early in the design process to help describe the existing air quality environment within and around the development site [1]. However, dispersion models often struggle to accurately predict the interaction of complex-built environments and local effects on wind microclimate and pollutant concentrations.

During the design process, more advanced prediction tools (i.e., Computational Fluid Dynamics (CFD) or wind tunnel) are needed to quantify the air quality impact of different design options, highlight constraints and opportunities, and inform on how to progress to more detailed design stages. This is especially applicable in the case of larger, complex developments, or tall buildings, which can have major impacts on the local microclimate [1].

This paper describes a methodology to implement the Technical Guidance [2] to advanced prediction tools (i.e., CFD) for modelling air quality impact during the design process, supporting the AQP approach of a real-world case study (125 & 130 London Wall, City of London).

2 METHODOLOGY

2.1 Road vehicle emissions

The Emission Factors Toolkit EFT is published by Defra to allow users to calculate road vehicle emission rates for NO_x, PM_{10}, $PM_{2.5}$ and CO_2 for a specified year, road type, vehicle speed and fleet composition. The toolkit is implemented in several dispersion models and updated yearly.

Table 1, Example of EFT Road emission input.

Road ID	Road Type	AADT	%HDV	Speed (kph)	N° hours	Link (km)
London Wall	London Central	18332	3	20	24	0.7

EFT 2019 was used to calculate the NO_x emissions from light and heavy-duty vehicles on the road network surrounding the application site (Table 1). The annual average daily traffic (AADT) and traffic percentage of heavy-duty vehicles were obtained for each road link [3]. To evaluate the air quality impact of the proposed development, the number of proposed trips generated by the development was added to the AADT and a growth factor was applied for the future opening year [2].

The toolkit calculates the road emissions (g/s) using standard vehicle emission factors, which are converted into hourly or daily NO_x emissions. The values are divided by the volume of the road source created in the CFD model to obtain the volume emission rate (i.e., g/m^3). Road sources were created as closed volumes extending over the road links between 0.2m and 1.5m from the ground [2], and the scalar emission rate was set for each source.

DOI 10.5258/WES/P0060

2.2 Assumptions

A steady-state Reynolds-Averaged Navier-Stokes (RANS) model was implemented in the CFD package OpenFOAM version 7.0. Pollutant concentrations were obtained by solving the transport equation of a non-buoyant passive scalar. The study was limited to the prediction of NO_2 concentrations and thermal stratification effects on turbulent diffusion were assumed negligible compared to advection mechanisms. Following this approach, the prediction of the scalar concentrations is based on the accurate prediction of the wind microclimate.

2.3 Wind Microclimate Assessment

The wind assessment was conducted according to the City of London Guidelines [4].
The CFD wind assessment specifically assumed:

1. Surrounding (context) buildings within at least 400m from the site.
2. Future consented schemes in the surroundings within 300m from the site boundary.
3. No landscape features smaller than 8m.
4. 36 equally spaced wind directions.
5. Maximum cell size near critical locations of 0.3m or lower.
6. Minimum 10 cells across street canyons.
7. k-ω SST turbulence model.

The inflow velocity profile was assumed logarithmic with the equivalent roughness height (z_0) specified at 0.7m (City terrain, ESDU 84011). The remaining inflow characteristics relating to turbulence followed ESDU 01008.
The meteorological data used for the assessment relate to the Weibull parameters specified in [4] - Annex A: Wind climate properties. A reference height of 120m was used (i.e., Scale Factor = 1.0).

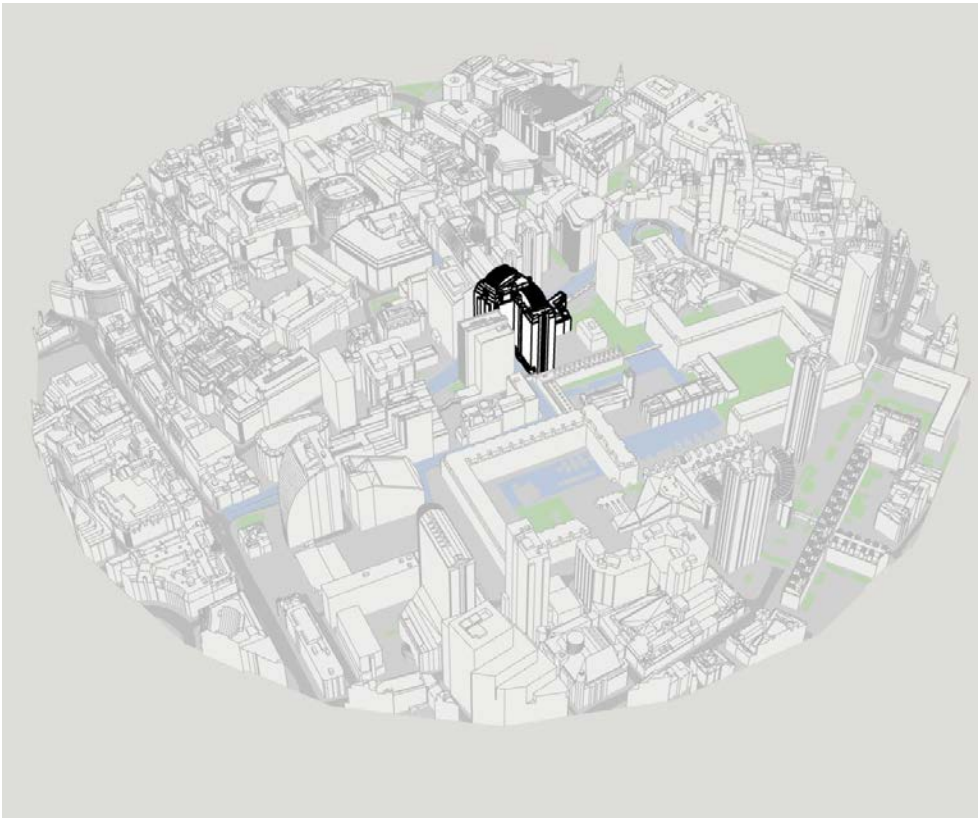

Figure 1, 3D model used for the CFD wind and dispersion assessment.

2.4 Post Processing

The total NO_x concentrations were obtained from the CFD simulations of momentum and transport equations from all road sources and for each of the 36 wind directions. The EFT toolkit 'NO_x-NO_2-calculator' was used to convert NO_x to NO_2 concentrations using the fraction emission at the future opening year in the City of London. Simulated NO_2 concentrations were then 'combined' for all wind

DOI 10.5258/WES/P0060

directions using the probability function of the Weibull distribution. The 'estimated' background concentration was added to the simulated NO_2 scalar field [2]. Finally, simulated NO_2 concentrations were 'calibrated' using an adjustment factor obtained from a linear fitting interpolation of the NO_2 measurements from nearby diffusion tubes and automatic stations (Table 3).

Table 2, Background NO_2 concentration and fraction emission.

Local Authority	**Background NO_2 concentration**	**Fraction NO_x emitted from local road vehicles as NO_2**
City of London	29.8	0.236

Table 3, Local NO2 measurements used for calibration.

Diffusion tube	**Annual Mean concentration (µg/m^3) of NO_2 (2019)**
London Wall	52
Museum of London	55
Brewers Hall Gardens	42

3 RESULTS

The Air Quality Strategy [5] provides the policy framework for local air quality management and assessment in the UK. The policy sets out air quality objectives for key pollutants, which are designed to protect human health and the environment. The annual mean objective for NO_2 is 40µg/m^3 and this value was used as the threshold concentration for 2D and 3D contour plots.
Figure 2 shows NO_2 concentrations at the pedestrian level (1.5m from the ground) in the proximity of the site and within the passageway. During the design stage, the contour plot was used to identify areas of potential air quality risk at the ground level, helping the design of entrances, sitting areas and outdoor amenity spaces.

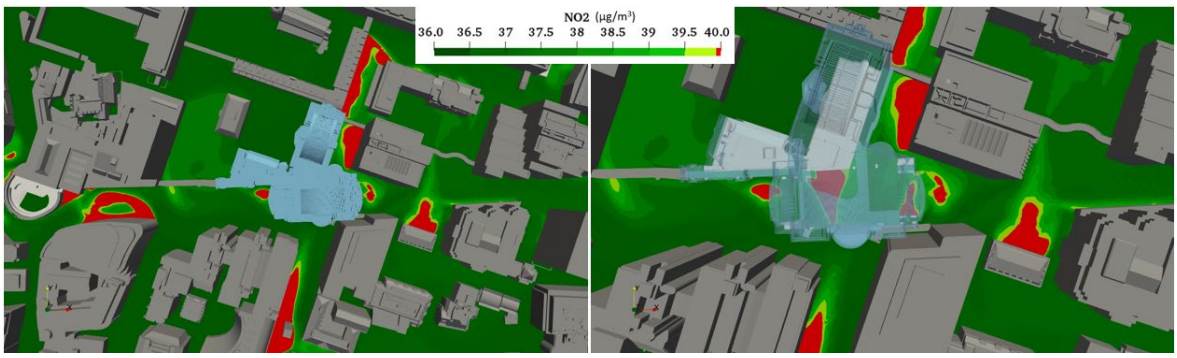

Figure 2, NO_2 mean concentrations at ground level (1.5m from the ground).

Figure 3 shows the 3D contour of the annual NO_2 mean objective (40µg/m^3) within and around the proposed development. The impact of large complex buildings on pollution dispersion is visible, particularly in areas of strong wind recirculation and low wind speed where the plume height is significantly increased. On the other hand, air quality improves in areas where ventilation is enhanced by local wind accelerations (i.e., channelling effects, downdraughts, corner separation, etc.). The 3D analysis was used during the design stage to identify dispersion mechanisms near the building facades, particularly over balconies and terraces. Mitigation measures (i.e., solid balustrades and green walls) were also tested by using CFD and integrated into the final design to improve local air quality conditions.

DOI 10.5258/WES/P0060

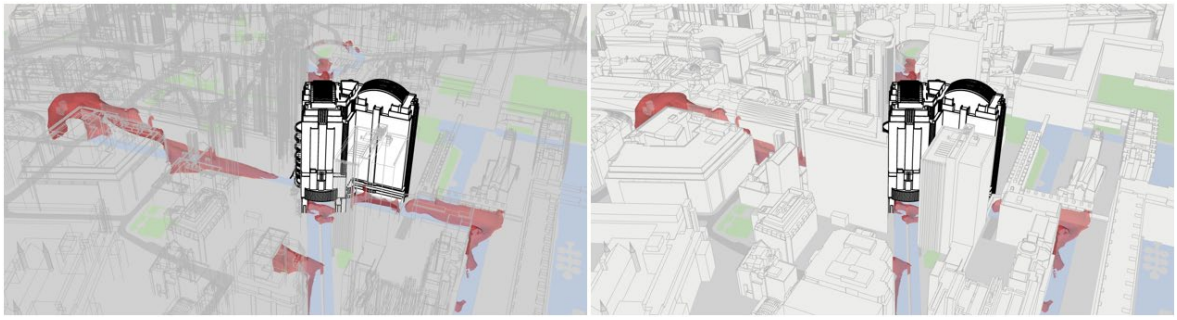

*Figure 3, 3D NO_2 contours (*40µg/m^3*) within and around the site.*

4 CONCLUSIONS

CFD is a valid prediction tool to inform designers how benefits to local air quality are maximised, and how pollution exposure is minimised. CFD is known to predict the interaction of built environments and local effects on wind microclimate and pollutant dispersion more accurately than standard dispersion models, particularly for large, complex developments or tall buildings.
This paper describes a methodology to implement the Technical Guidance [2] into CFD for the key pollutant NO_2. The aim is to expand air quality guidelines to computational tools, which can be used to achieve the Air Quality Positive target and/or be integrated into the standard air quality assessment for new developments in London. The methodology was successfully applied to a real-world case study in the City of London which was granted a planning application. CFD results provided interesting insights and a better understanding of local dispersion mechanisms, which helped the design of the proposed scheme, capturing local benefits to air quality whilst reducing public exposure.

5 AKNOWLEDGEMENT

The completion of this study has been supported by Arax Properties.

REFERENCES

[1] Mayor of London. (2023). “Air Quality Positive”, *London Plan Guidance, London,* Feb. 2023.
[2] Defra (2022). “Local Air Quality Management”, *Technical Guidance (TG22),* Aug. 2022.
[3] Department for Transport (2019). “Road traffic statistics”, *Dft.gov.uk.*
[4] City of London (2019). “Wind Microclimate Guidelines for Developments in the City of London”, Aug. 2019.
[5] Defra (2007). “The Air Quality Strategy for England, Scotland, Wales and Northern Ireland”, *United Kingdom*, 2007.

DOI 10.5258/WES/P0060

Finite element analysis of low-rise non-engineered timber residential buildings in Dominica under hurricane loads

Sarah Esper[1*], Dina D'Ayala[1]
[1]EPICentre, Civil, Environmental and Geomatic Engineering, University College London
London, United Kingdom
[*]sarah.esper.12@ucl.ac.uk

1 INTRODUCTION

Hurricanes may remain the most dominant and destructive natural peril negatively impacting the economies of Caribbean states. Non-engineered private-sector homes are considered subject to the largest risk, with most of their structural data difficult to access for vulnerability assessment.

He et al. [5] note the utility of fragility/vulnerability curves accounting for the critical structural responses quantifying building performance. This requires a complete, validated finite element (FE) building model, preferably stochastic rather than deterministic. Non-engineered wooden buildings are expected to be one of the most fragile typologies to wind; however, previous studies which have built full numerical wind analysis models of low-rise timber buildings have been found to exclude elevated buildings and were mainly concerned with investigating the load paths and load sharing through the structure.

This paper presents an FE methodology developed for the analytical wind vulnerability assessment of low-rise, non-engineered elevated timber buildings with lightweight hip roofs. The objectives of this study include (1) visualising the structural response of an elevated building exposed to hurricane-level wind loads, (2) incorporating three-dimensional system effects, especially but not limited to the hip roof frame assembly, (3) accounting for as-built construction details for the building typology of interest as observed in the field. The ability of the structure to sustain loads beyond the first element failure is also investigated. It is noted by Pan et al. [7] that due to their substantial redundancies, timber structures can usually bear more loads past the initiation of damage at their most vulnerable point. Therefore, the limit states considered must go beyond the first element failure for damage prediction and mitigation.

The proposed FE methodology intends to fill a gap in the existing knowledge base regarding the construction materials, methods, and structural performance of typical non-engineered residential building typologies in the Caribbean and specifically Dominica, by facilitating the study of the initiation and propagation of their structural failure under hurricane loads. Three other common Dominican residential building typologies of varying wind fragility were also covered by this project, including timber and concrete masonry buildings with light hip/hip & valley roofs, concrete masonry buildings with light hip/hip & valley roofs, and concrete masonry buildings with heavy flat roofs. The present paper concentrates on the all timber light hip roof typology because, while is not the most common surveyed typology, it has been identified as the most vulnerable. Moreover, its construction is similar to the upper storey of timber and concrete masonry buildings with light hip/hip & valley roofs, which constitutes a larger class of buildings, across the whole Caribbean, and present similar level of vulnerability. Therefore, results of this analysis can be extrapolated to this second class.

2 METHOD

Given the non-engineered nature of the structures being investigated, the methodology proposed draws on diverse sources of information to identify existing construction practices and building typologies, to reliably underpin a tool for wind vulnerability assessment applicable to any region of interest.

2.1 Parameter Selection

To eventually model the building numerically, measurable quantities, including the sizing and spacing of structural and non-structural elements and connections, as well as their material properties, are required. Some of these parameters can also be found in fragility and vulnerability literature as critical in the definition of particular building typologies. Therefore, the first stage of this methodology is concerned with identifying the construction parameters required. Most of the construction parameters

DOI 10.5258/WES/P0062

identified describe features of the roof construction, which is expected to be of concern due to the roof experiencing considerable uplift forces during hurricane events. The walls, which experience positive pressure or suction in different regions depending on the prevailing wind direction, also have their construction details captured. By comparison, the floor and foundation construction details are less apparent in building typology descriptions for fragility/vulnerability functions.

2.2 Damage Data Analysis

The second stage uses available empirical damage data, which could be beneficial in terms of reference and validation of the study. A desk study exercise is undertaken to locate construction, damage, and/or claim data to identify the typical residential building typologies across the region of interest. In the case of Dominica, a building damage assessment was led by the United Nations Development Program (UNDP) after Hurricane Maria (2017). If the geotagged locations of these buildings are coupled with the available wind speed estimates of a relevant hurricane event, an empirical fragility assessment can be carried out, indicating the relative performance of the typologies against wind hazard. A total of 262 houses were identified (on pillars or shallow foundations), which fell into the timber typology of interest and were most likely to have been solely impacted by wind hazard during the hurricane. Approximately 47% of these homes suffered extensive roof damage, whereas 35% were reported to have suffered extensive wall damage.

2.3 Field Survey

Primary data collection is at the core of this methodology and takes place in the third stage. To address the relative data scarcity on Caribbean residential construction, a detailed field survey was undertaken in Dominica by University College London (UCL). The construction data obtained in the second stage is compared with the required parameters identified in the first stage, to design and undertake a structural survey, which targets the outstanding information. Structural inspections were carried out for three timber frame buildings across the island, and their structural details were used to build a representative single-storey index building. The building is elevated on reinforced concrete pillars, with anchor bolts connecting the timber frame to the foundations. Considering these are non-engineered structures, the compliance of the as-built construction with existing codes/standards is also examined.

2.4 Structural Model

Finally, based on the information collected in the field, a prototype numerical model can be built for the typology of interest. In the likelihood that wind tunnel data is not available to compute the wind loading for the model (as in this study), the structural response of the building against hurricane loads is assessed with wind loading calculated according to ASCE 7-22 Main Wind Force Resisting System (MWFRS) Case 1, which accounts for elevated buildings. The loading is applied incrementally to allow for failure checks against the capacities of the structural and non-structural connections.

3 NUMERICAL ANALYSIS

A 3D frame model is built for the structure using commercial FE software SAP2000 [2], as shown in Figure 1. The joist-to-foundation connections and the joist-to-joist joints are modelled as pinned. As numerical models have yet to be developed in the literature for elevated buildings, the pinned connections for joists are assumed to be similar to the modelling of pinned wall stud-to-wall and sill plate connections by Martin et al. [6]. Timber wall studs are modelled, allowing bending about their major axis. The rafter-to-rafter and rafter-to-wall plate connections are modelled as pinned. As buildings belonging to this typology were encountered in the field both with and without bracing elements at the building corners, this is also incorporated as a sensitivity check. The bracing elements, when present, are modelled, allowing bending about their minor axis, as their placement differs by 90 degrees compared to the wall studs.

During Hurricane Maria (2017), the maximum 3-s gust wind speed over land was recorded as 165mph or 74m/s [4]. In the FE model, distributed wind forces are applied to the frame elements in an incrementally increasing manner from zero to 74m/s, expecting to cause systemic failure. The model is initially assumed to have zero damage. Two basic failure modes for the nailed members are explored: pull-out and slip failure of the nails. The nail capacities are calculated using the following equations in the U.S. National Design Specification [1] and Wood Handbook [3]. Wind loads are calculated and applied to the frame, assuming wind approaches perpendicular to the front elevation. This is done to analyse the windward roof-to-wall junction with a large overhang over the porch. Worst-case single

DOI 10.5258/WES/P0062

values are taken for external pressure coefficients, whilst positive and negative internal pressure coefficients are considered. The analysis is ultimately stopped for a model once enough elements have failed and been removed at the same wind speed value, causing a drop in base shear (V_b) greater or equal to 10%.

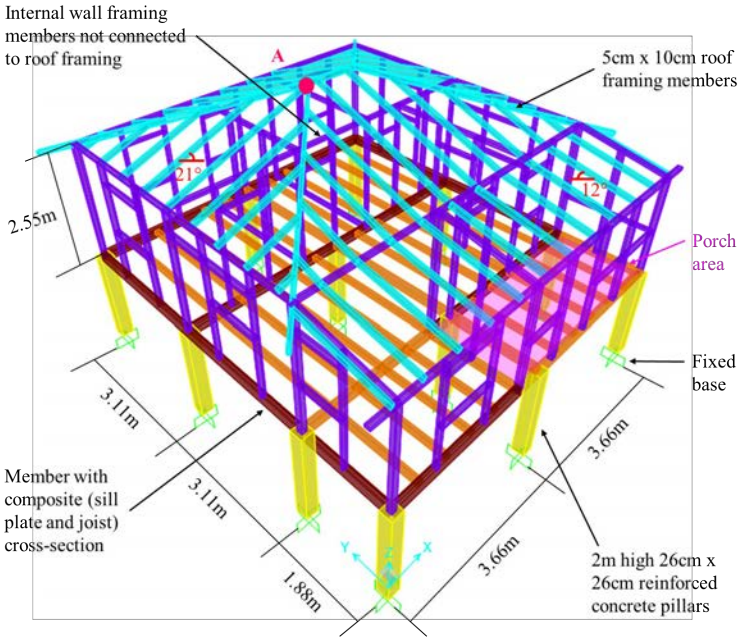

Figure 1: 3D frame model of elevated timber building with hip roof in SAP2000

The cladding, including timber floorboards, wall sheathing, roof sheathing and metal sheeting of the house are not included in the FE model; however, their connection capacities are assessed to determine whether they will fail at wind speeds lower or greater than the frame elements.

4 RESULTS

At each wind speed value, as loading is applied to the structure, horizontal and vertical displacements are extracted at Point A, the highest structural elevation, where the ridge board meets a rear hip rafter. Figure 2 shows that the presence of bracing, as expected, stiffens the structure.

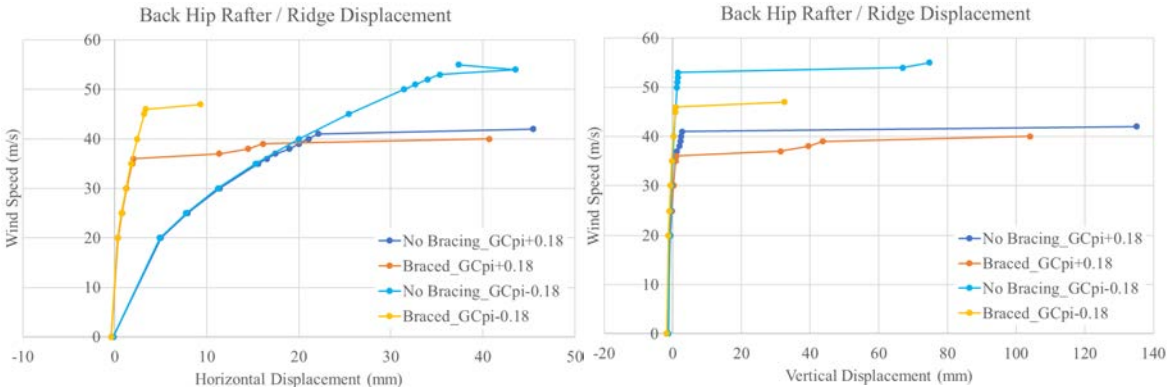

Figure 2: Wind speed vs. horizontal and vertical displacement curves extracted at the Back Hip Rafter / Ridge (Point A) with either positive or negative internal pressure coefficient, GC_{pi}

Positive internal pressures work in concert with the external pressures applied to the roof and floor elements and the wall frame elements at the back and side elevations. Therefore, element failures are expected to occur at lower wind speeds with positive internal pressures. Whether positive or negative internal pressures would develop will depend on the arrangement of the openings across the various elevations. In the field, openings are incorporated on all building elevations for this building typology. As such, no matter the wind direction considered, openings will always predominate in the suction regions, making the development of negative internal pressures the most likely.

DOI 10.5258/WES/P0062

5 CONCLUSIONS

The following conclusions are formed based on research conducted in support of this project and, therefore, pertain only to the specific load applications previously described. It is noted that this differs from a typical building design, which must consider all wind attack angles from 0°-360°. The current study is focused on developing a numerical procedure to investigate the structural performance under given loading conditions.

1. Floor frame elements fail exclusively in slip, whilst wall studs failed exclusively in pull-out, indicating that they are affected significantly more by the uplift forces on the roof rather than the lateral wind loads. The roof frame elements exhibit both pull-out and slip failure.
2. The failure mechanism shown to recur for this building typology under positive internal pressures is the slip failure of the joists under the centre of the building. This study's findings show the importance of considering and modelling the floor and foundation construction details for elevated buildings, as the building envelope may be breached through these elements.
3. The failure mechanism shown to recur for this building typology under negative internal pressures is the rafter-to-ridge pull-out and rafter-to-wall plate slip failure of the front left-hand hip rafter at the connections, which leads to the failure of the attached main and jack rafters due to excessive displacements under wind loading. At this stage, the building envelope would be significantly breached at the roof and front elevation, highlighting further the crucial role of the roof frame connections in the building's response to wind loading.
4. By assessing the UDLs applied to the frame elements and comparing these values to the capacities of the cladding and purlin connections, it is found that these capacities were not exceeded before the frame elements' failures. The majority of the details of the structural elements adopted for the prototype model, as assumed from the field surveys, fall below the minimum requirements specified by Dominica's Housing Standards [8].
5. The inclusion of bracing elements at building corners is shown to slightly reduce the wind speed at which the onset of failure occurs. This indicates that the addition of bracing alone as a possible retrofit measure is not beneficial to improving the building's response against wind loading without also improving the condition and/or connections of the structural frame elements.

ACKNOWLEDGEMENTS

The work employs field data collected by Sarah Esper with the assistance of Issa Alleyne, Edward Charles, Dailah Felix, Edmund Laville, and Oran Sabaroche. Further information and clarifications required on construction practices, cost, and structural details were obtained through personal communications with Eric James of QSC. Ltd.; Isaac Baptiste of Baptiste & Associates Ltd.; Alistair Grell, Lex Jervier; Marcus Philbert of SORELL Consulting Ltd. (SCL); Christopher Sorhaindo of ACE Engineering Ltd.; and Jamie Jno Baptiste. The kind participation of the residents of Dominica in this study is greatly appreciated.

REFERENCES

[1] American Wood Council, 2018. NDS National Design Specification for Wood Construction.
[2] CSI. (2016). Structural Analysis Program SAP2000-NonLinear version 19. Computers and Structures, Inc. (CSI).
[3] Forest Products Laboratory (US), 1999. Wood handbook: wood as an engineering material.
[4] Gibbs, T. (2017). The Wind Speeds in Selected Islands During Hurricanes Irma and Maria in 2017.http://www.unc.edu/ims/luettich/jbikman/01_23_2013/Literature%20dump/StatisticalModelsOfHollandPressureProfileParameter.pdf
[5] He, J., Pan, F., & Cai, C. S. (2017). A review of wood-frame low-rise building performance study under hurricane winds. Engineering Structures, 141, 512–529.
[6] Martin, K. G., Gupta, R., Prevatt, D. O., Datin, P. L., & van de Lindt, J. W. (2011). Modeling System Effects and Structural Load Paths in a Wood-Framed Structure. Journal of Architectural Engineering, 17(4), 134–143. https://doi.org/10.1061/(asce)ae.1943-5568.0000045
[7] Pan, F., Cai, C. S., Zhang, W., & Kong, B. (2014). Refined damage prediction of low-rise building envelope under high wind load. Wind & Structures, 18(6), 669–691.
[8] United Nations Development Program (UNDP), 2018. Guide to Dominica's Housing Standards.

DOI 10.5258/WES/P0062

Title: Proceedings of the 14th UK Conference on Wind Engineering

Editors: Zheng-Tong Xie and Christina Vanderwel

ISBN 978-1-912431-37-3